The Effect of Stellar and Quasar Feedback on the Interstellar Medium: Structure and Lifetime of Molecular Clouds

Davide Decataldo

SCUOLA NORMALE SUPERIORE

Supervisor:
Andrea Ferrara

Co-supervisors:
Andrea Pallottini
Alessandro Lupi

A Thesis presented for the degree of
Doctor of Philosophy

Pisa, Italy, April 2020

The Effect of Stellar and Quasar Feedback on the Interstellar Medium: Structure and Lifetime of Molecular Clouds

Davide Decataldo

The molecular component of the interstellar medium (ISM) is structured in dense clumps and filaments. Stars form in these overdense region, and the emitted radiation affects in turn the properties of the surrounding gas. Radiation in the far ultraviolet (FUV, 6 eV $< h\nu <$ 13.6 eV) and extreme ultraviolet (EUV, $h\nu >$ 13.6 eV) bands respectively dissociates and ionizes the ISM. HII regions form around most massive stars, with temperatures $T \sim 10^{4-5}$ K, while thick transition layers of atomic gas (Photodissociation Regions, PDRs) separate the ionized bubble from the fully molecular component, that is structured in Giant Molecular Clouds (GMC). Due to the increase in pressure in the heated components, radiation has also a dynamical effect on the gas, fostering bulk motions and turbulence.

The inner structure of a GMC often presents pillars and dense globules with bright rims, which can be produced by radiation impinging on molecular gas. Furthermore, some observations attest triggered star formation on the edge of HII regions, where the radiation-driven shock compresses and piles up a gas shell. Stellar feedback can also explain the low star formation efficiency of GMCs, where only a few percent of the total gas mass is converted to stars, by heating the gas and preventing its collapse. Molecular gas is also observed embedded in outflows driven by Active Galactic Nuclei (AGN), moving at hundreds of km s^{-1}. The formation of molecules within hot outflowing gas is a challenging problem, and it is unclear how they can survive up to ∼kpc scale when exposed to the strong AGN flux.

The aim of this Thesis is to study the effect of radiation feedback on the molecular component of the ISM. In order to understand how radiation interacts with the gas and affects its properties, we use both semi-analytic models and numerical radiation-hydrodynamic simulations, including a complex chemical network accounting for the formation and destruction of H_2.

We study the photoevaporation of molecular clumps exposed to a UV radiation field, showing the formation of a hot expanding layer on the surface, while the inner core manages to self-shield from radiation. We find that the clump undergoes an initial shock-contraction phase and a subsequent expansion phase, which lets the radiation penetrate in until the

clump is completely evaporated. Typical evaporation time-scale is 0.1 Myr (0.01 Myr) for clumps of mass $10^3\,M_\odot$ ($0.1\,M_\odot$) embedded in quasar (stellar) radiation. We find that clump lifetimes in quasar outflows are compatible with their observed extension, suggesting that photoevaporation is the main mechanism regulating the size of molecular outflows.

By running a set of simulations considering different clump masses ($M = 10 - 200\ M_\odot$) and impinging stellar fluxes ($G_0 = 2 \times 10^3 - 8 \times 10^4$ in Habing units), we find that most of H_2 mass ($40 - 90\%$) is dissociated during the R-type phase of the dissociation front. The self-shielded core collapses because of the radiation-driven shock and, for all the clump in the simulation suite, it manages to retain enough mass ($M > 2\,M_\odot$) to potentially trigger star formation. This shows that external radiation can only regulate the final clump mass, but it is not able to prevent its collapse.

Finally, we run a simulation of a $10^5\,M_\odot$ molecular cloud, tracking the formation of individual stars with mass $M > 1\,M_\odot$ with a stochastic recipe, and including both radiation feedback and stellar winds. We identify two stages in the cloud evolution: (1) radiation and winds carve ionized, low-density bubbles around massive stars, while FUV radiation dissociates most H_2 in the cloud, apart from dense, self-shielded clumps; (2) rapid star formation (SFR$\simeq 0.1\,M_\odot\,\mathrm{yr}^{-1}$) consumes molecular gas in the dense clumps, so that UV radiation can ionize the remaining HI gas in the GMC. H_2 is exhausted in 1.6 Myr, yielding a final star formation efficiency of 36%. The average intensity of FUV and ionizing fields increases almost steadily with time, with the ionization field showing a more patchy distribution than the FUV. Throughout the evolution, the escape fraction of ionizing photons from the cloud is $f_{\mathrm{ion,esc}} \lesssim 0.03$.

Supervisor: Andrea Ferrara

Co-supervisors: Andrea Pallottini, Alessandro Lupi

Collaborators: Simona Gallerani, Livia Vallini, Laura Sommovigo, Stefano Carniani

Nomenclature

Acronym	Extended name
AGB	Asymptotic Giant Branch
AGN	Active Galactic Nucleus
ALMA	Atacama Large Millimeter-submillmeter Array
AMR	Adaptive Mesh Refinement
ART	Adaptive Refinement Tree
BE	Bonnor-Ebert (sphere)
CD	Contact Discontinuity
CIC	Cloud-In-Cell
CIE	Collisional Ionization Equilibrium
CFL	Courant-Friedrichs-Lewy (condition)
CMB	Cosmic Microwave Background
CNM	Cold Neutral Medium
CO	Carbon Monoxyde
DF	Dissociation Front
EUV	Extreme Ultra-Violet (band): $h\nu > 13.6$ eV
FIR	Far InfraRed
FUV	Far Ultra-Violet (band): $6\,\mathrm{eV} < h\nu < 13.6$ eV
GLF	Global Lars-Friedrich (function)
GMC	Giant Molecular Cloud
HCN	Hydrogen cyanide
HCO	Hydrogencarbonate
HLL	Harten-Lax-van Lee (function)
HIM	Hot Ionized Medium
HPC	High Performance Computing
HST	Hubble Space Telescope
ICM	InterClump Medium
IGM	InterGalactic Medium
IRAM	Institut de RadioAstronomie Millimétrique

IF	Ionization Front
IR	InfraRed
IMF	Initial Mass Function
ISM	InterStellar Medium
LHS	Left-Hand Side
LW	Lyman-Werner (band): $11.2\,\mathrm{eV} < h\nu < 13.6$ eV
MS	Main Sequence
MUSCL	Monotone Upstream-centered Scheme for Conservation Laws
MW	Milky Way
OB	OB (class stars)
ODE	Ordinary Differential Equation
OTSA	On-The-Spot Approximation
PAH	Policyclic Aromatic Hydrocarbons
PDF	Probability Distribution Function
PDR	PhotoDissociation Region
PdBI	Plateau de Bure Interferometer
PM	Particle-Mesh (scheme)
QSO	Quasi-Stellar Object (quasar)
RDI	Radiation-Driven Implosion
RHS	Right-Hand Side
RT	Radiative Transfer
RW	Rarefaction Wave
SED	Spectral Energy Distribution
SF	Shock Front
SFE	Star Formation Efficiency
SFR	Star Formation Rate
SPH	Smoothed Particle Hydrodynamics
SBMH	Super Massive Black Hole
SDSS	Sloan Digital Sky Survey
SK	Schmidt-Kennicutt (relation)
SN	SuperNova
SW	Shock Wave
UFO	Ultra-Fast Outflow
UV	Ultra-Violet
WIM	Warm Ionized Medium
WNM	Warm Neutral Medium
XMM	X-ray Multi-Mirror (mission)

Contents

Declaration

The work in this Thesis is based on research carried out at Scuola Normale Superiore of Pisa, Italy. No part of this thesis has been submitted elsewhere for any other degree or qualification, and it is the sole work of the author unless referenced to the contrary in the text. Some of the work presented in this Thesis has been published in journals and conference proceedings - the relevant publications are listed below.

1. **Decataldo D.**, Ferrara A., Pallottini A., Gallerani S., Vallini L., *Molecular clumps photoevaporation in ionized regions*, 2017, MNRAS, Vol. 471, 4476-4487
2. Pallottini A., Ferrara A., **Decataldo D.**, Gallerani S., Vallini L., Carniani S., Behrens C., Kohandel M., Salvadori S., *Deep into the structure of the first galaxies: SERRA views*, 2019, MNRAS, Vol. 487, 1689-1708
3. **Decataldo D.**, Pallottini A., Ferrara A., Gallerani S., Vallini L., *Photoevaporation of Jeans- unstable molecular clumps, 2019*, MNRAS, Vol. 487, 3377-3391
4. Ferrara A., Vallini L., Pallottini A., Gallerani S., Carniani S., Kohandel M., **Decataldo D.**, Behrens C., *A physical model for [CII] line emission from galaxies*, 2019, MNRAS, Vol. 489, 4476-4487
5. Sommovigo L., Ferrara A., Pallottini A., Vallini L., Gallerani S., **Decataldo D.**, *Warm dust in high-z galaxies: origin and implications*, 2020, MNRAS, submitted
6. Pizzati E., Ferrara A., Pallottini A., Vallini L., **Decataldo D.**, *Outflows and extended [CII] halos in high redshift galaxies*, 2020, MNRAS, submitted
7. **Decataldo D.**, Lupi A., Ferrara A., Pallottini A., Gallerani S., Vallini L., *Shaping the structure of a GMC with radiation and supernova feedback*, 2020, MNRAS, submitted

Introduction

The Interstellar Medium (ISM) is the baryonic matter filling the space among Astrophysical bodies, as stars, planets and stellar remnants. Studying its properties and evolution is a central topic in modern Astrophysics, since it represents the intermediary scale between a galaxy and its stars, determining the properties of both objects.

Dense filaments and clumps collapse to form stars, determining the Initial Mass Function (IMF) of stellar clusters, their kinematics, and the initial properties of newly formed stars (as their metallicity). In turn, stars affect the ISM via radiation feedback, winds and supernovae (SNe). Radiation is able to dissociate, ionize and heat the gas, consequently affecting its thermodynamical state. Together with the injection of momentum by winds and SNe, feedback mechanisms contribute to feeding the level of turbulence of the ISM, altering its structure and possibly quenching future events of star formation. Furthermore winds and SN explosions inject new material in the ISM, and determines its enrichment in heavy elements.

The evolution of the ISM on the small scales of stars and molecular clouds also affects galactic scales. For example, the global star formation rate (SFR) of a galaxy, and hence its being starburst or quiescent, depends on the properties of its substructures, as the distribution of Giant Molecular Clouds (GMCs) and their local SFR. Furthermore, galaxies with rapid star formation can drive warm/cool gas outflows (Steidel et al., 1996; Shapley et al., 2003) as a consequence of momentum injection in the ISM by SN explosions, in turn affecting the morphology and star formation activity of a galaxy (Dressler & Gunn, 1983; Couch & Sharples, 1987) and altering its metallicity, setting a galactic mass-metallicity relation (Tremonti et al., 2004). Finally, the escape fraction of ionising radiation from galaxies, crucial to understand hydrogen re-ionization of the universe at $z \simeq 6$ (Dayal et al., 2020), depends on the escape fraction of single GMCs and on the attenuation from their surrounding medium.

The properties of the ISM also determine the observational features of galaxies. The

dissociation/ionization state of the gas, together with the intensity of the radiation field, affect the level population of the chemical species, hence regulating the line emission intensities. On the other side, ISM is also responsible for the absorption of light coming from distant sources, attenuating the observable flux.

In this Thesis, we focus on the effect of feedback from radiation sources on the molecular component of the ISM, in particular inside GMCs, that are the location where star formation occurs (Blitz, 1993). Observations have shown that GMCs have a rich and complex internal structure, with filaments, pillars and clumps (Bally et al., 1987; Bertoldi & McKee, 1992), thanks to high-resolution CO maps and far-infrared observations (e.g. Genzel & Stutzki, 1989; Williams et al., 1994; Bolatto et al., 2008). The interaction of the radiation field with the gas could help explaining the formation of these substructures.

The effect of UV radiation on the interstellar gas has been studied in-depth in pioneering works (Strömgren, 1939; Tielens & Hollenbach, 1985). The extreme UV portion of the spectrum ($E > 13.6$ eV) is responsible for the ionization of atomic H. As a result, a bubble of ionized hydrogen forms around bright stars, the so-called HII region. The ionization front rapidly reaches the Strömgren radius (whose size depends on the density of the gas and the intensity of the ionizing source) without altering the gas density (R-type ionization front Kahn, 1954). In the following D-type phase, the ionized bubble expands due to its overpressure with respect to the surrounding medium. On the other hand, far-ultraviolet radiation (FUV, 6 eV$< E <$ 13.6 eV) gets through the HII regions and penetrates deeper into the molecular gas. Lyman-Werner radiation (LW, 11.2 eV$< E <$ 13.6 eV) dissociates H_2, forming a thick transition layer between the ionized and the molecular phase, called Photodissociation Region (PDR Tielens & Hollenbach, 1985; Hollenbach & McKee, 1979). This layered composition - molecular phase, PDR and HII region - is typical of any patch of the ISM affected by UV radiation.

Feedback from stars forming within molecular clouds is generally invoked to explain their low star formation efficiency (SFE), i.e. the ratio between the total mass converted to stars and the initial gas mass of the GMC. Indeed, observations show that GMCs surprisingly have SFEs around a few percent (Lada et al., 2010; Ochsendorf et al., 2017). One possible explanation is that GMCs are indeed short-lived, because of the stellar feedback from the first stars, that heats and disperses the gas, preventing further collapse and star formation (Elmegreen, 2000). Another model assumes that GMC are long-lived, but feedback manages to keep the level of turbulence high enough to hinder fast star formation (Federrath & Klessen, 2012). In both cases, stellar feedback appears to be the key mechanism that self-regulates star formation inside GMCs.

Another interesting phenomenon often observed in GMCs is the so-called triggered star formation (or self-propagating star formation), where new stars form at the edge of HII regions of other massive stars (Elmegreen, 2011a). This scenario could be understood con-

sidering the effect of external radiation impinging on a dense clump, generally named photoevaporation (Bertoldi, 1989; Gorti & Hollenbach, 2002). When a dissociation/ionization front propagates towards the center of the clump as D-type, it induces the collapse of its core, while the external surface is heated and dispersed in the surrounding medium. The collapse of the core, provided that it retains enough mass, could hence lead to star formation.

Recent observations have revealed the presence of molecular clouds also in outflowing gas around quasars (Cicone et al., 2014; Bischetti et al., 2018). Quasars are powerful emitting sources, and the radiation pressure drives ultra-fast winds, which in turn impact the surrounding ISM. The shocked gas is heated up to 10^7 K and reaches velocities up to 1000 $\mathrm{km\,s^{-1}}$ (King & Pounds, 2015). Nevertheless, a molecular component is detected within the outflow, as evident from CO and HCN maps in nearby sources (Feruglio et al., 2010; Morganti et al., 2015) and [CII] detections at high redshift (Maiolino et al., 2005). Being exposed to the strong quasar flux, these clouds undergo photoevaporation, and they are an interesting subject to study in the context of radiation feedback. From one side, it has to be understood how these clouds can survive to the large distances – up to 1 kpc – at which they are observed. Moreover, triggered collapse via photoevaporation could comply with the recent hints of star formation within the outflow (Maiolino et al., 2017; Rodríguez del Pino et al., 2019).

The evolution of a cloud affected by radiativion feedback is complex, and its description requires a proper modelling of gas dynamics (including self-gravity), cooling and heating mechanisms, a chemical network and a scheme for radiation transport. It follows that a complete solution cannot be achieved only by analytical means, and numerical simulations are a promising option for theoretical studies. Recent improvements in the computational power allow simulations to include several physical processes, and to reach sub-pc resolution. Early simulations have used approximated recipes to account for stellar photoionization, without the inclusion of radiative transfer calculations: for example, a common approach was to compute the ionization state of the gas and then the corresponding temperature (Dale et al., 2005, 2007b; Ceverino & Klypin, 2009; Gritschneder et al., 2009), or to account for photoionization feedback by injecting thermal energy at stellar locations (Vázquez-Semadeni et al., 2010). On the other hand, more recent works have adopted coupled hydrodynamics and radiative transfer schemes to account for gas-radiation interaction, but using simplified chemical networks (Walch et al., 2012; Raskutti et al., 2016; Howard et al., 2017).

In this work, we aim at making a further step in the understanding of radiative feedback on the ISM, firstly with semi-analytical considerations and then running numerical simulations, extending previous results on this subject. The structure of the Thesis is as follows:

- Chapter 1: we review the main properties of the ISM, and the effects of stellar and quasar radiation;
- Chapter 2: we describe the numerical codes used in this work, focusing on our contribution;
- Chapter 3: we analyse by semi-analytical means the photoevaporation of a dense molecular clump by UV radiation, both in the case of stellar and quasar radiation;
- Chapter 4: we focus on the photoevaporation of a molecular clump by stellar far-ultraviolet radiation with a suite of high-resolution simulations;
- Chapter 5: we study the evolution of a star-forming giant molecular cloud, describing the effect of stellar feedback on the morphology of the cloud and its star formation efficiency.

A final chapter summarizes our conclusions.

Chapter 1

The Interstellar Medium

1.1 The components of the interstellar medium

All baryonic matter inside galaxies, which fills the space around astrophysical bodies (stars, planets, stellar remnants), is referred as interstellar medium (ISM). As a general picture, the ISM is made of gas and solid conglomerates (dust grains), with a dust-to-gas ratio typically of $\langle \rho_{\rm dust}/\rho_{\rm gas} \rangle = 0.01$ (Milky Way value, Bohlin et al., 1978). The gas density spans a range from 10^{-3} cm^{-3} in the diffuse medium to 10^{6} cm^{-3} in dense molecular clouds, showing a non-uniform distribution due to turbulence and gravitational interactions. The gas is mainly hydrogen, with about 10% of atoms being helium, and 0.1% in other elements as carbon, oxygen and nitrogen.

Depending on the density and the possible presence of radiative sources, the interstellar gas can be found in different phases, differing for temperature and ionization state. In the most common classification (Draine, 2011), the ISM can be found in a molecular phase, a neutral atomic phase (which include both a warm and a cold component) and an ionized phase (warm ionized medium, HII regions and hot ionized medium). The following sections describe in details the ISM phases, while Tab. 1.1 summarizes their properties.

ISM phase		T (K)	n (cm^{-3})	$n_{\rm e}/n_{\rm H}$
Molecular Gas		$10-100$	$>10^2$	10^{-4}
Cold Neutral Medium	CNM	~ 100	~ 50	10^{-4}
Warm Neutral Medium	WNM	~ 8000	~ 0.5	10^{-3}
Warm Ionized Medium	WIM	$\sim 10^4$	~ 0.1	0.7
HII regions		10^{4-5}	10^{2-3}	1
Hot Ionized Medium	HIM	$>10^5$	$10{-}3-10^{-1}$	1

Table 1.1: Summary of the properties of the different ISM phases. The columns show the phase name, the common acronym, temperature T, density n and H ionized fraction $n_{\rm e}/n_{\rm H}$ (where $n_{\rm e}$ and $n_{\rm H}$ are the electron and H number densities).

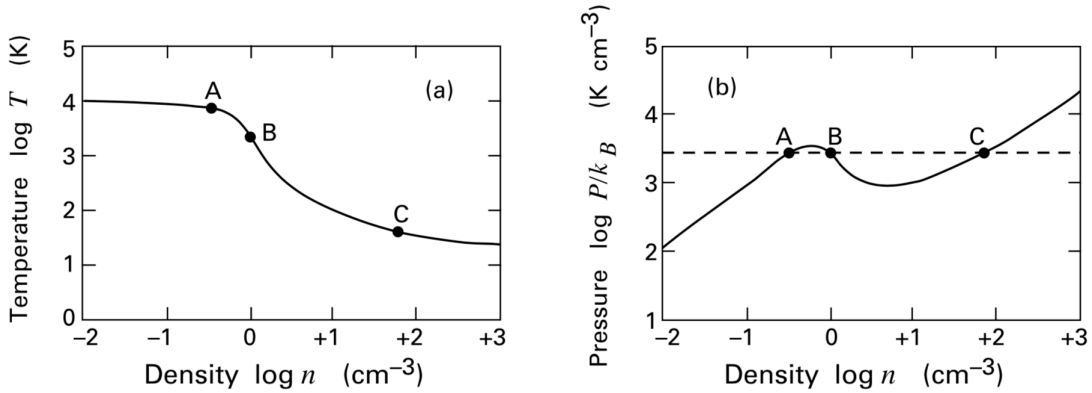

Figure 1.1: **Left**: Diagram of equilibrium temperature of a parcel of neutral gas, as a function of its number density. **Right**: Corresponding thermal pressure of the gas at equilibrium, with dashed line representing a typical empirical pressure. The points A, B and C, are possible states of the gas, with A and C being the only stable states. Figure from Stahler & Palla (2004).

1.1.1 Molecular gas

Massive clouds, with typical masses $M > 10^5$ $M_\odot$ and sizes $\ell > 10$ pc, are self-gravitating rather than in pressure equilibrium with the surrounding medium. As a result, they reach densities higher than 100 cm^{-3} and they are self-shielded from external sources of radiation. The temperature decreases down to 10 K, allowing molecules to form. H_2 is the most abundant molecule, but also CO, HCN and other species form, and their lines are measured and used to determine the properties of the interstellar gas.

Molecular clouds show a turbulent structure, with the consequent formation of substructures with different densities at smaller scales. Filaments, cores and clumps may reach a density higher than 10^5 cm^{-3}, where the gas pressure is not able to keep the gas from collapsing. A collapsing core fragments in smaller patches of gas of a few solar masses, from which individual stars form. An in-depth description of molecular cloud properties is given in Sec. 1.9.

1.1.2 Neutral atomic gas

The neutral atomic phase of the ISM is generally organised in cold HI clouds (cold neutral medium, CNM) and warm intercloud gas (warm interstellar medium, WNM), occupying 1% and 30-40% of the ISM volume respectively (Draine, 2011). The CNM component has a density of about 50 cm^{-3} and a temperature around 100 K, while the WNM is more diffuse (density $n \simeq 0.5$ cm^{-3}) and hotter ($T \simeq 8000$ K). The regions of the neutral medium whose chemistry and structure is dominated by the presence of a non-ionizing radiation field are called Photodissociation Regions, and they will described in details in Sec. 1.8. The main tracers of the atomic phases of the ISM are the HI hyper-fine transition

line at 21 cm, and far-infrared lines as [CII] 158 μm.

The existence of this two-phase structure has been investigated, for instance, by Field (1965) and Wolfire et al. (1995, 2003). The heat-loss function of the gas can be written as

$$\mathcal{L}(n,T) = \sum_i \Gamma_i(n,T) - \sum_i \Lambda_i(n,T) \ , \tag{1.1}$$

where the first RHS term is the sum of all heating rates, and the latter is the sum of cooling rates. The states of thermodynamical equilibrium of the gas are given by the equation

$$\mathcal{L}(n,T) = 0 \ . \tag{1.2}$$

Fig. 1.1 shows the solutions of eq. 1.2 on the $T-n$ plane (left panel) and the $P-n$ plane (right panel), by assuming the equation of state of a perfect gas ($P = nk_{\rm B}T$, with P pressure and $k_{\rm B}$ the Boltzmann constant). The horizontal dashed line on the right panel marks the mean empirical value of $P/k_{\rm B}$, which is crossing the equilibrium curve in three points A, B and C. The pressure equilibrium is granted by the stability criterion for isobare perturbations (Field, 1965):

$$\left(\frac{\partial \mathcal{L}}{\partial T}\right)_P > 0 \ , \tag{1.3}$$

hence it follows that the state corresponding to point B is unstable. On the other hand, points A and C are stable and their temperature and density correspond to CNM and WNM respectively.

1.1.3 Ionized gas

In presence of a radiation field with a spectrum extending beyond 13.6 eV, hydrogen is ionized according to the reaction

$$\mathrm{H} + h\nu \quad \rightarrow \quad p + e \ , \tag{1.4}$$

where p are free protons (or equivalently H^+) and e are free electrons. When a class O or a class B star forms inside a molecular cloud, a spherical bubble of fully ionized gas forms around the new-born star. These regions are called HII regions, and present a density around $10-100$ cm^{-3}. The main heating mechanism is photoionization from UV photons emitted by the central star, and temperatures around $10^4 - 10^5$ K are generally attained. HII regions will be described in-depth in Sec. 1.7. The main observational tracer is the Hα emission line (Zurita et al., 2000; Oey et al., 2007), while the weakness of the [OI] 6300Å line proves that gas is almost fully ionized.

In addition to HII regions, ionized gas is found also in different structures extending up to 1 kpc from the midplane of the Milky Way (Haffner et al., 2009), with temperatures as high as 9000 K and densities around 0.1 cm^{-3}. This gas is called Warm ionized medium

(WIM), and a possible energy input has been identified in supernova-driven turbulence and super bubble structures (Wood et al., 2010).

Finally, extremely hot gas (hot ionized medium, HIM) with $T > 10^{5.5}$ K can be found in low density clouds ($n \simeq 10^{-3}$ cm^{-3}) crossed by shocks produced by exploding supernovae. These regions are detected via line emission of multiply ionized species, as OVI.

1.1.4 Interstellar dust

Dust in the ISM can is responsible for the reddening and the extinction of light coming from distance sources. The reddening dependence on wavelength implies a size distribution of the grains, which has the form given by $n(a) \sim a^{-3.5}$ (Mathis et al., 1977), where a is the grain diameter. The size of dust particles ranges from the molecular domain ($\sim$ 50 nm) up to larger solid grains (~ 0.1 μm). Metals (as C, Si, Mg, Fe, Al, Ti, Ca) are locked into dust particles, so that about 1% of the gas mass is contained into dust. The ISM is also populated by larger molecules with up to 200 carbon atoms (policyclic aromatic hydrocarbon, PAH), showing peculiar IR emission features. These molecules can also stick together, forming conglomerates of $10^4 - 10^5$ C atoms (Hollenbach & Tielens, 1999), locking in total about 10% of carbon. The absorption of photons causes the heating of dust grains, which then re-emit this energy as thermal continuum radiation in the IR band, with a spectrum of a black body.

1.2 Photochemistry of the interstellar medium

The chemical species contained in the ISM take part into chemical reactions that explain the formation of more complex molecules, detected in the cold molecular clouds. Chemical reactions have temperature-dependent rates, which can be studied in laboratories. The formation and destruction rates of each chemical species allow to compute the evolution of their abundance with time. When the timescales of chemical processes are much shorter than other physical timescales of interest, it is possible to approximate the abundance of each species with their equilibrium abundances, by equating their formation and destruction rate.

Radiation has a fundamental role in the chemical evolution of interstellar gas, since radiation can ionize atoms and dissociate molecules. Furthermore, radiation can trigger some chemical reactions that happen only between species in their excited state. Cosmic rays must also be accounted, since they can interact with molecules in the deeper part of molecular clouds, that radiation is not able to reach because of self-shielding of the gas.

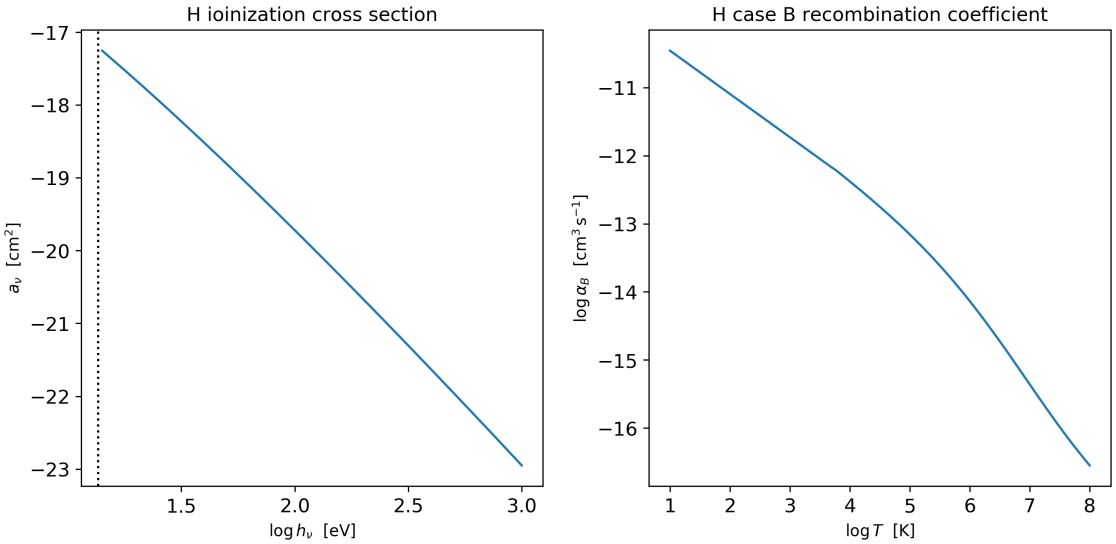

Figure 1.2: **Left**: Cross section of photoionization of hydrogen according to eq. 1.4, with the dotted line marking the ionization potential $h\nu_0 = 13.6\,\mathrm{eV}$ (Osterbrock & Ferland, 2006); **Right**: case B recombination coefficient for hydrogen, fit given by (Abel et al., 1997)

1.2.1 Ionization and recombination of hydrogen

In presence of a radiation field with a spectrum extending beyond 13.6 eV, the basic processes to be considered in the ISM are photoionization and recombination of hydrogen (eq. 1.4). It is important to notice that collisional processes between the chemical species happen with a short timescale (with respect to the reaction 1.4), so that the gas can be globally considered in thermal equilibrium (i.e. characterized by a Maxwellian velocity distribution, parametrized by only temperature T).

A photon with energy greater than $h\nu_0 = 13.6$ eV (h is the Planck constant) is able to ionize a neutral H atoms, producing a free electron, with a rate

$$\Gamma_{\mathrm{ion}} = n_{\mathrm{H}} \int_{\nu_0}^{\infty} \frac{4\pi J_\nu}{h\nu}\, a_\nu \,\mathrm{d}\nu \tag{1.5}$$

where J_ν is the specific mean intensity ($\mathrm{erg\,cm^{-2}\,s^{-1}\,sr^{-1}\,Hz^{-1}}$) and a_ν is the frequency-dependent cross section of the process (assuming that the H atom is initially in the ground state). As a reference value, $a_{\nu=\nu_0} \simeq 6.3 \times 10^{-18}\,\mathrm{cm}^2$. An analytical approximation of a_ν for an hydrogenoic atoms (with charge Z) is given by Osterbrock & Ferland (2006), and plotted in the left panel of Fig. 1.2 for $Z = 1$:

$$a_\nu(Z) = \frac{A_0}{Z^2}\left(\frac{\nu_1}{\nu}\right)^4 \frac{\exp[4 - 4\tan^{-1}(\varepsilon)/\varepsilon]}{1 - \exp(-2\pi/\varepsilon)} \tag{1.6}$$

where

$$A_0 \simeq 6.20 \cdot 10^{-18}\,\mathrm{cm}^{-2}\,, \qquad \varepsilon = \sqrt{\nu/\nu_1 - 1}\,, \qquad h\nu_1 = (h\nu_0)Z^2\,. \tag{1.7}$$

For $\nu > \nu_1$, the photoionization cross section decreases approximately as $a_\nu \sim \nu^{-3}$.

The rate per unit volume of the recombination process, with an electron recombining to the n-th energetic level, is

$$R_n(T) = n_e n_p \alpha_n(T) = n_e^2 \alpha_n(T) \tag{1.8}$$

where n_p and n_e are proton and electron number densities (neglecting species other than H, we have $n_e = n_p$), and $\alpha_n(T)$ is the recombination coefficient to the level n. α_n depends on temperature because (1) the probability to recombine to level n depends on the electron kinetic energy, and (2) the rate of a proton-electron collision depend on electron velocity distribution. α_n can be computed with the integral

$$\alpha_n = \int_0^\infty u\, \sigma_n(u)\, f(u)\, \mathrm{d}u \ , \tag{1.9}$$

where u is the electron speed (more correctly, it is the relative speed between a proton and an electron), σ_n is the recombination cross section and $f(u)$ is the Maxwell-Boltzmann velocity distribution (Maxwell, 1860; Boltzmann, 1872).

The on-the-spot approximation (OTSA) states that direct recombination to the ground state produces a photon that ionizes another H atom in the very same region. Thus the effective recombination rate per unit volume (producing photons which escape from the cloud) is

$$R_{\mathrm{OTSA}}(T) = \sum_{n=2}^{\infty} R_n(T) = n_e^2 \sum_{n=2}^{\infty} \alpha_n(T) = n_e^2 \alpha_{\mathrm{B}}(T) \ , \tag{1.10}$$

where α_{B} is the so-called case B recombination coefficient (see right panel of Fig. 1.2), in contrast with the case A recombination coefficient α_{A} accounting also for the recombination to the ground state. In this approximation we are also assuming that all H atoms are in the ground state, assumption justified by the fact that the decay of an excited atom to ground state (via electric dipole transition, e.g. emitting Balmer lines.) is very fast*. Thus the event of ionizing an already excited H atom is very unlikely.

1.2.2 H_2 formation and photodissociation

The H_2 formation rate is obtained by observing H_2/H column density ratios and assuming equilibrium between H_2 formation and destruction (Jura, 1975):

$$R_{\mathrm{f,H_2}} \simeq 1 - 3 \times 10^{-17}\ n n_{\mathrm{H}}\ \ \mathrm{cm^{-3}s^{-1}} \ . \tag{1.11}$$

Which mechanism can produce such formation rate? Gas phase reactions are not efficient enough, since radiative association of two H atoms ($\mathrm{H + H \rightarrow H_2 + \gamma}$) and neutral-ion

*Reference values for the mean lifetime of an electron at level n are $\tau_n \simeq 10^{-4} - 10^{-8}$ s, with the exception of $\tau_{1\mathrm{s}} \simeq 10^8$ s. In any case, the timescale are shorter than the photoionization timescale $\tau_{ph} \simeq 10^8$ s (Osterbrock & Ferland, 2006).

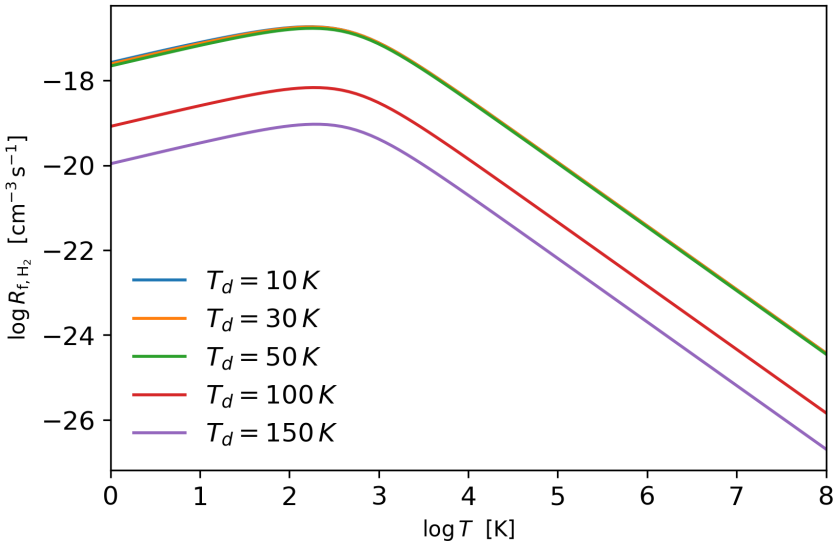

Figure 1.3: Formation rate of H_2 on dust grain surface, using the temperature-dependent expression given from eq. 1.12

reaction ($H + H^- \rightarrow H_2 + e$) have a rate lower than $10^{-23}\ nn_H$ cm^{-3}s^{-1} (Le Teuff et al., 2000). The alternative way of forming H_2 is the formation on dust grains, with a rate (Hollenbach & Salpeter, 1971)

$$R_{f,H_2} = \frac{1}{2} S(T, T_d) \eta \sigma_d n_d n_H v_H \ , \tag{1.12}$$

where $S(T, T_d)$ is the sticking probability of an H atom on a grain surface, if the gas has temperature T and the grain has temperature T_d, η is the probability that an adsorbed H atom will migrate over the grain surface and find another H atom before evaporating again to gas phase, σ_d is a cross section, n_d and n_H are dust and H number density respectively, v_H is the thermal speed of H atoms in gas phase. Plugging in experimental values for S and η at temperatures relevant in astrophysics, explains adequately the rate given by eq. 1.11 (Hollenbach & Salpeter, 1971).

To account for the dependence of H_2 formation rate on temperature, the following more accurate expression can be adopted (Hollenbach & McKee, 1979; Sternberg & Dalgarno, 1989):

$$R_{f,H_2} = 3 \times 10^{-17}\, f_a\, S(T, T_d)\, (T/100)^{0.5}\ \text{cm}^{-3}\,\text{s}^{-1}\ , \tag{1.13}$$

where the factor f_a is the fraction of atoms that do not evaporate before forming H_2:

$$f_a = \frac{1}{1 + 10^4 \exp(-600/T_d)} \tag{1.14}$$

and S is given by

$$S(T, T_d) = \frac{1}{1 + 0.04(T + T_d)^{0.5} + 2 \times 10^{-3} T + 8 \times 10^{-6} T^2}\ . \tag{1.15}$$

Fig. 1.12 shows R_{f,H_2} for different dust grain temperatures, ranging from $T_d = 10$ K to 150 K. Notice that for gas temperatures higher than $T = 10^3$ K the rate decreases significantly with respect to the approximation of constant rate (eq. 1.11).

Photodissociation of H_2 mainly occurs via the Solomon process, triggered by photons in the Lyman-Werner (LW) band (11.2 eV - 13.6 eV). The absorption of LW photons leads an H_2 molecule from the ground electronic state to an excited electronic state. In about 10% of cases, the molecule decays to the vibrational continuum of the ground electronic state, i.e. a dissociated molecule. In the remainder of the cases, the molecule decays to to a vibrationally-excited states of the ground electronic state; then IR fluorence or collisional de-excitation may follow.

The Solomon process rate is often taken to be proportional to the total flux at 12.87 eV (Glover & Jappsen, 2007; Bovino et al., 2016):

$$\Gamma_{H_2} = 1.38 \times 10^9 \frac{J(h\nu = 12.87\,\mathrm{eV})}{\mathrm{erg\,s^{-1}\,Hz^{-1}\,sr^{-1}}}\,\mathrm{s^{-1}}\ . \tag{1.16}$$

This expression is correct only if the flux is approximately constant in the Lyman-Werner band, as pointed out by Richings et al. (2014a). They find that the most general way to parametrise the dissociation rate is

$$\Gamma_{H_2} = 7.5 \times 10^{-11} \left(\frac{n(12.24 - 13.51\,\mathrm{eV})}{2.256 \times 10^4} \right) \mathrm{s^{-1}}\ , \tag{1.17}$$

where $n(E_{bin})$ is the photon density in the energy bin E_{bin}, giving approximately correct results even when the spectrum is a black body or a Draine field. In the case of flat spectrum in the LW band, eq. 1.17 yields

$$\Gamma_{H_2} = 2.97 \times 10^9 \frac{J(h\nu = 12.87\,\mathrm{eV})}{\mathrm{erg\,s^{-1}\,Hz^{-1}\,sr^{-1}}}\,\mathrm{s^{-1}} \tag{1.18}$$

which differs only slightly from eq. 1.16.

1.2.3 H_2 self-shielding

The absorption of radiation in the LW due to photodissociation of H_2 is difficult to treat, because the cross section depends on the ro-vibrational states of H_2, and so a proper radiative transfer calculation taking into account the level population would be required. Nevertheless, it is possible to use fitting expressions, giving the LW flux absorption as a function of H_2 column density. The simpler analytical approximation for the self-shielding factor S_{H_2} is given by Draine & Bertoldi (1996):

$$S_{H_2} = \begin{cases} 1 & N_{H_2} \leq 10^{14}\,\mathrm{cm^2} \\ \left(\dfrac{N_{H_2}}{10^{14}\,\mathrm{cm^2}} \right)^{-0.75} & 10^{14}\,\mathrm{cm^2} < N_{H_2} \leq 10^{21}\,\mathrm{cm^2} \end{cases} \tag{1.19}$$

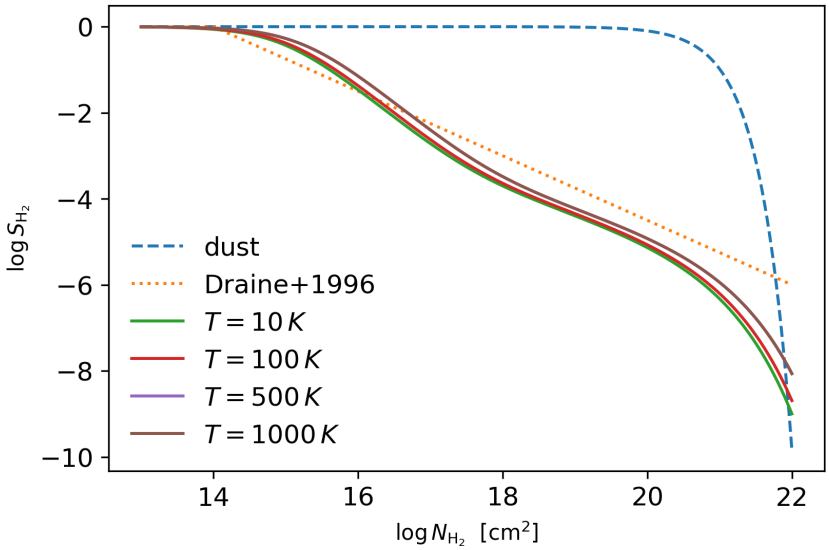

Figure 1.4: Self-shielding factor given by eq. 1.20 for different temperatures (solid lines) and by the simplified eq. 1.19 (dotted line). For reference, absorption by dust is also plotted (dashed line).

where N_{H_2} is the H_2 column density.

A more accurate expression has been obtained by Richings et al. (2014b), taking into account the thermal broadening of LW absorption lines:

$$\begin{aligned} S_{H_2} = & \frac{1-\omega_{H_2}(T)}{(1+x'/b_5)^{\alpha(T)}} \exp(-5\times10^{-7}(1+x')) \\ & + \frac{\omega_{H_2}(T)}{(1+x')^{1/2}} \exp(-8.5\times10^{-4}(1+x')^{1/2}) \end{aligned} \tag{1.20}$$

where $x' = N_{H_2}/N_{crit}$, and

$$\omega_{H_2}(T) = 0.013\left[1+\left(\frac{T}{2700\,\mathrm{K}}\right)^{1.3}\right]^{1/1.3} \exp\left[-\left(\frac{T}{3900\,\mathrm{K}}\right)^{14.6}\right] \tag{1.21}$$

$$\alpha(T) = \begin{cases} 1.4 & T < 3000\,\mathrm{K} \\ \left(\frac{T}{3500\,\mathrm{K}}\right)^{-0.8} & 3000\,\mathrm{K} \le T < 4000\,\mathrm{K} \\ 1.1 & T \ge 4000\,\mathrm{K} \end{cases} \tag{1.22}$$

$$N_{crit} = 10^{14}\,\mathrm{cm}^{-2} \begin{cases} 1.3\left[1+\left(\frac{T}{600\,\mathrm{K}}\right)^{0.8}\right] & T < 3000\,\mathrm{K} \\ \left(\frac{T}{4760\,\mathrm{K}}\right)^{-3.8} & 3000\,\mathrm{K} \le T < 4000\,\mathrm{K} \\ 2.0 & T \ge 4000\,\mathrm{K} \end{cases}. \tag{1.23}$$

Fig. 1.4 shows the self-shielding factor in eq. 1.20 (solid lines) at different temperatures, compared with the simplified self-shielding factor in eq. 1.19 (dashed line). The

dependence on the temperature is not very strong, but taking into account the thermal broadening introduces a significant difference with respect to the simplified expression. In the figure, the dust absorption factor is also plotted, showing that dust is much less efficient in attenuating the LW flux.

1.3 Heating processes

A number of processes in the ISM affects the energy balance of the gas. The efficiency of these processes depends strongly on the properties of the gas, as its density and its chemical composition, and on external factors, as the presence of radiation fields or bulk fluid motions.

In this section, we briefly review the heating processes of the gas, mainly due to the presence of a radiation source. Different processes come into play at different frequency bands in the radiation spectrum.

1.3.1 Photoionization heating

When an ionizing photons (energy higher than 13.6 eV) collides with an H atom, an electron with energy higher than the mean gas temperature is emitted. Then collisions distribute the energy into the gas, and the result is an increase of the gas mean temperature. The heating rate (or energy gain rate) is

$$G_{\rm ph} = n_{\rm H} \int_{\nu_0}^{\infty} \frac{4\pi J_\nu}{h\nu}\, h(\nu-\nu_0)\, a_\nu \,{\rm d}\nu \ . \tag{1.24}$$

Also elements other than hydrogen contribute to photoionization heating, and their contribution is important in particular in presence of a non-ionizing radiation field.

1.3.2 Photoelectric heating on dust

When a photon hits a grain, an electron may be emitted in the grain core and travels towards the surface. If it overcomes the work function W and any electrostatic potential ϕ_c (if the grain is charged), then it is injected in the gas with excess energy. The heating efficiency is

$$\varepsilon_{\rm gr} = \frac{\text{gas heating rate}}{\text{FUV absorption rate}} = Y\left(\frac{h\nu - W - \phi_c}{h\nu}\right) \ . \tag{1.25}$$

The yield Y is the probability that an electron escapes from the grain surface. Tipically $W \simeq 5$ eV and $\varepsilon_{\rm gr} \simeq 5\%$ (Hollenbach & Tielens, 1999).

Photoeletric heating from PAH works with the same model as for grains, but Y is usually higher for planar PAHs and sometimes the ionization potential $\phi_{\rm IP}$ can be higher than 13.6 eV:

$$\varepsilon_{\rm PAH} = \frac{\text{gas heating rate}}{\text{FUV absorption rate}} = Y\left(\frac{h\nu - \phi_{\rm IP}}{h\nu}\right) \ . \tag{1.26}$$

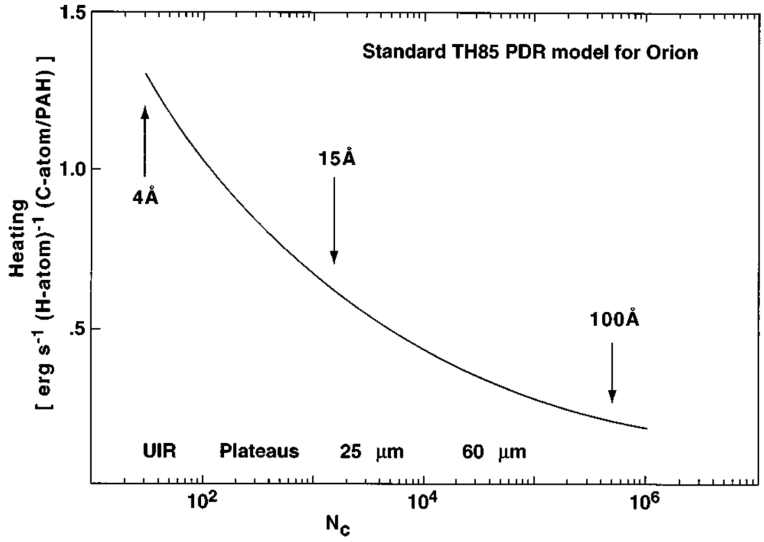

Figure 1.5: Contribution to the heating rate as a function of the number of carbon atoms in the dust molecule / grain. The corresponding size of the dust particle is also indicated. Figure from Hollenbach & Tielens (1999).

Tipically $\phi_{\rm IP} \simeq 7$ eV and $\varepsilon_{\rm PAH} \simeq 15\%$.

Considering both species to have size distribution $n(a) \sim a^{-3.5}$, the total heating rate is given in Fig. 1.5 (Bakes & Tielens, 1994), highlighting the contribution from grains with different sizes: small grains dominate the heating, while the contribution from grains with size larger than 100Åis completely negligible.

1.3.3 Heating from H_2

As we already discussed in Sec. 1.2.2, photodissociation of H_2 occurs via the Solomon process, triggered by photons in the Lyman-Werner band (11.2 eV - 13.6 eV). When a photon has energy in the LW range, the molecule can be dissociate with a 10% probability. The fragments will have some excess kinetic energy, that will be distributed into the gas with the net effect of a heating. This procesess delivers about 0.25 eV per dissociated molecule (Stephens & Dalgarno, 1973).

Most of far UV photon absorptions by H_2 lead to a decay to a bound vibrational excited state of the electronic ground state. Then, the molecule will decay radiatively through the emission of IR photons only if the density is low ($n < 10^4$ cm^{-3}). If the gas is denser, the vibrationally excited molecule can be collisionally de-excited, hence delivering energy to the gas (Sternberg & Dalgarno, 1989; Burton et al., 1990).

Finally, H_2 formation on the surface of dust grains is a heating mechanism as well. In fact, the molecules form in a vibrational and rotational excited state, and this energy can go in gas heating if the molecules are ejected rapidly from the grain surface. Nevertheless,

the heating term due to this mechanism is small if compared to heating produced by LW photons pumping, and it is important only in shocks inside dense clouds (Hollenbach, 1989).

1.3.4 Dust-gas heating

A common feature of the ISM is that the gas and the dust have different temperatures. Hence, they can exchange energy via collisions, resulting in gas heating or gas cooling. The energy exchange rate is (Burke & Hollenbach, 1983; Hollenbach, 1989)

$$G_{\rm gas,dust} \simeq 10^{-33} n T^{1/2} (T_{\rm d} - T) \ {\rm erg\,s^{-1}} \ . \tag{1.27}$$

1.4 Cooling processes

The cooling of the ISM happens through processes that convert kinetic energy into radiation: the photons than escape the gas, with the net effect of decreasing the gas internal energy. This mechanism works as far as the gas is "optically thin", i.e. the emitted photons are not re-absorbed elsewhere in the gas.

The main cooling processes that we treat here in details are

- Line cooling, i.e. cooling via collisional excitation of atoms followed by the radiative de-excitation (1.4.1);
- recombination cooling, when an electron recombines with a proton and a photon is emitted in the process (1.4.2);
- free-free cooling (1.4.3), due to the radiation emitted when charged particles accelerate.

1.4.1 Line cooling in a two-level system

The main cooling process in the interstellar gas is line cooling. The energy is dissipated by atoms and molecules through radiative emission that follows a collisional excitation:

$$\begin{aligned} A + B &\rightarrow A + B^* \\ B^* &\rightarrow B + \gamma \end{aligned} \tag{1.28}$$

It is clear that line cooling will be more efficient if collision are quite frequent (collisional partners are abundant), but not so frequent that a collisional de-excitation occurs before the radiative emission.

The simpler model for line emission is the two-level system, i.e. we consider an atom having only a ground state 0 and an excited state 1. The transition between the two

Species	Transition	Cooling rate
C^+	$^2P_{1/2} \longrightarrow {}^2P_{3/2}$	$7.9 \times 10^{-20}\, T^{-1/2}\, \exp(-92/T)\, n_{C^+} n_e$
Si^+	$^2P_{1/2} \longrightarrow {}^2P_{3/2}$	$1.9 \times 10^{-18}\, T^{-1/2}\, \exp(-413/T)\, n_{Si^+} n_e$
Fe^+	$a^6D_{9/2} \longrightarrow a^6D_{7/2}$	$1.1 \times 10^{-18}\, T^{-1/2}\, [\exp(554/T) + 1.3\exp(-961/T)]\, n_{Fe^+} n_e$
O	$^3P_2 \longrightarrow {}^3P_{1,0}$	$1.74 \times 10^{-24}\, T^{1/2}\, [(1 - 7.6T^{-1/2})\exp(-228/T) + 0.38(1 - 7.7T^{-1/2})\exp(-326/T)]\, n_O n_e$

Table 1.2: Cooling rates for some of the most important fine-structure transitions (Dalgarno & McCray, 1972).

levels $i \to j$ because of collisions is described by the collisional rate coefficient γ_{ij}, while the radiative de-excitation is described by the Einstein coefficient A_{ij}. The statistical equilibrium equation for the population of the two levels, in the optically thin regime, is

$$n_0 n_e \gamma_{01} = n_1 n_e \gamma_{10} + n_1 A_{10} \ , \tag{1.29}$$

where n_i is the number density of species at level i, and we are assuming that electrons are the main collisional partner. Rearranging the terms, we obtain

$$\frac{n_1}{n_0} = \frac{n_e \gamma_{01}}{n_e \gamma_{10} + A_{10}} \ . \tag{1.30}$$

It is useful to consider the limits for high and low density: defining the critical density as $n_{cr} = A_{10}/\gamma_{10}$

$$\frac{n_1}{n_0} = \begin{cases} n_e \gamma_{01}/A_{10} & n_e \ll n_{cr} \\ \gamma_{01}/\gamma_{10} & n_e \gg n_{cr} \end{cases} \ . \tag{1.31}$$

The cooling rate L_{line} is given by the energy carried out by emitted photons. Hence, denoting with ΔE_{10} the energy difference between the two atomic levels,

$$L_{line} = n_1 A_{10} \Delta E_{10} = \begin{cases} n_1 n_e \gamma_{01} \Delta E_{10} & n_e \ll n_{cr} \\ n_1 A_{10} \gamma_{01}/\gamma_{10} \Delta E_{10} & n_e \gg n_{cr} \end{cases} \ . \tag{1.32}$$

This last expression tells us that line cooling goes as $n_1 n_e \sim n^2$ when the gas has low density with respect to the critical value, while it goes as $\sim n$ when the gas is denser. In other words, line cooling is more efficient with increasing density, but the cooling rate grows more slowly when the critical density is reached.

At moderate densities, as in the CNM and in the WNM, fine-structure transitions of metals (as carbon, oxygen, iron and silicon) are the main coolant. This is due to the fact that these transition have relatively high critical densities ($n_{cr} \simeq 10^{2-6}$ cm^{-3} for collisions with H and $n_{cr} \simeq 1 - 10^3$ cm^{-3} for collisions with electrons, see Hollenbach & McKee 1989). The expressions for the cooling rates for the most important metals are summarized in Tab. 1.2.

At higher temperatures, line cooling due to electronic transitions of H and He^+ becomes also effective. The corresponding rates are (Black, 1981):

$$L_{\rm H} = 7.5 \times 10^{-19} \exp(-118348/7)\, n_e n_{\rm H} \ , \tag{1.33}$$

$$L_{\rm He^+} = 5.54 \times 10^{-17} T^{-0.397} \exp(-473638/T)\, n_e n_{\rm He} \ . \tag{1.34}$$

1.4.2 Recombination cooling

When a recombination happens, an electron is subtracted from the electron gas, and its kinetic energy is transformed in binding anergy with the emission of an escaping photon. For recombination to the ground state, there is no net energy loss if we adopt the OTSA. The recombination cooling rate (in $\mathrm{erg\,cm^{-3}\,s^{-1}}$) can be written

$$L_{\rm rec} = n_e n_p k_{\rm B} T \beta_{\rm B}(T) \ , \tag{1.35}$$

where $\beta_{\rm B}$ is the case B recombination cooling coefficient, i.e. the sum of all coefficients β_n for the quantum number $n \geq 2$:

$$\beta_n = \frac{1}{k_{\rm B}T} \int_0^\infty u\, \sigma_n(u) \left[\frac{1}{2} m_e u^2\right] f(u)\, {\rm d}u \ . \tag{1.36}$$

The coefficient β_n can be written as follows:

$$\beta_n = \frac{1}{k_{\rm B}T} \frac{\int_0^\infty u\, \sigma_n(u) \left[\frac{1}{2} m_e u^2\right] f(u)\, {\rm d}u}{\int_0^\infty u\, \sigma_n(u)\, f(u)\, {\rm d}u} \int_0^\infty u\, \sigma_n(u)\, f(u)\, {\rm d}u \simeq \frac{\alpha_n}{k_{\rm B}T} \langle \varepsilon_e \rangle_{\rm th} \ , \tag{1.37}$$

where the $\langle \varepsilon_e \rangle_{\rm th}$ is an average electron thermal energy, weighted on the recombination cross section (then $\langle \varepsilon_e \rangle_{\rm th}$ is actually less than $\frac{3}{2} k_{\rm B} T$, due to the fact that low energy electrons preferentially recombine).

Thus, the cooling rate can be written

$$L_{\rm rec} = n_e n_p \alpha_{\rm B} \langle \varepsilon_e \rangle_{\rm th} \tag{1.38}$$

i.e. the rate of recombining electrons times the energy subtracted from the gas per captured electron.

In the case of recombination of hydrogen, the resulting cooling rate is (Black, 1981):

$$L_{\rm H,rec} = 2.85 \times 10^{-27} T^{-1/2} (5.914 - 0.5 \ln T + 0.01184 T^{1/3})\, n_e n_{\rm H^+} \ . \tag{1.39}$$

1.4.3 Free-free cooling

Bremsstrahlung (free-free radiation) is a cooling mechanism, since a photon is produced and then leaving the gas. The cooling rate is (Black, 1981)

$$L_{\rm ff}(Q) \simeq 1.42 \times 10^{-27} Q^2 T^{1/2} g_{\rm ff} n_e n_+ \ , \tag{1.40}$$

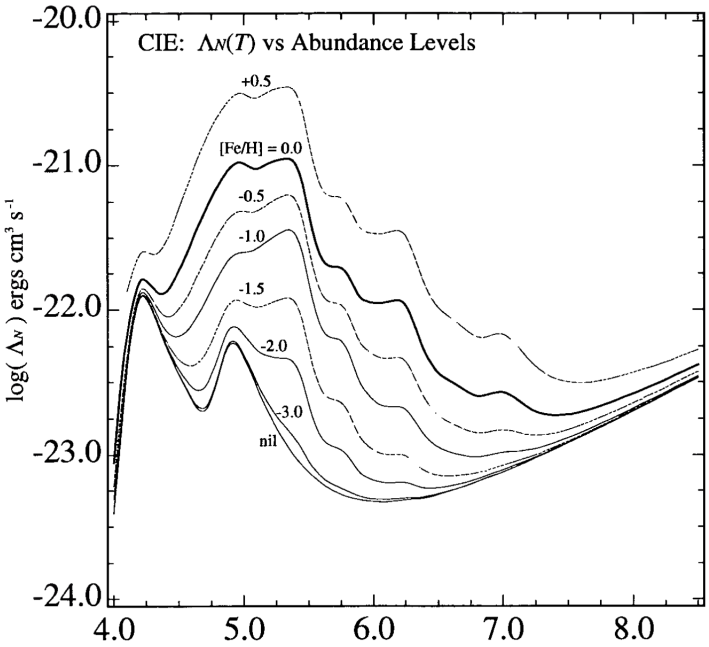

Figure 1.6: Cooling function of a low density gas, at collisional ionization equilibrium (CIE) without an external radiation field, for different metallicities (Sutherland & Dopita, 1993).

where here Q is the charge number (for hydrogen $Q = 1$), $g_{\rm ff}$ is the mean Gaunt factor (slowly varying with n_e, usually $g_{\rm ff} \simeq 1.3$) and n_+ is the ion number density. Free-free cooling becomes important at very high temperatures, otherwise it is negligible with respect to recombination cooling.

1.4.4 Cooling function

The cooling function Λ is defined as

$$n_e n \Lambda(T, n, Z, J_\nu) = L_{\rm rec} + L_{\rm ff} + L_{\rm line} \ , \tag{1.41}$$

where Z is the gas metallicity. $L_{\rm line}$ contains the contribution of all atomic species, from H and He to metal ions. The shape of Λ varies substantially when an external radiation field is present, since the ionized fractions of every species change.

In Fig. 1.6, the standard cooling function of a low density and hot gas ($T > 10^4$ K), by Sutherland & Dopita (1993), is represented as a function of temperature and metallicity (assuming that there is no dependence on density, which is a good approximation), at collisional ionization equilibrium without incident radiation. The most important features are:

- the drop around 10^4 K, due to the fact the the gas is too cold to collisionally excite any line, or ionize any atom (so also recombination cooling is not present);

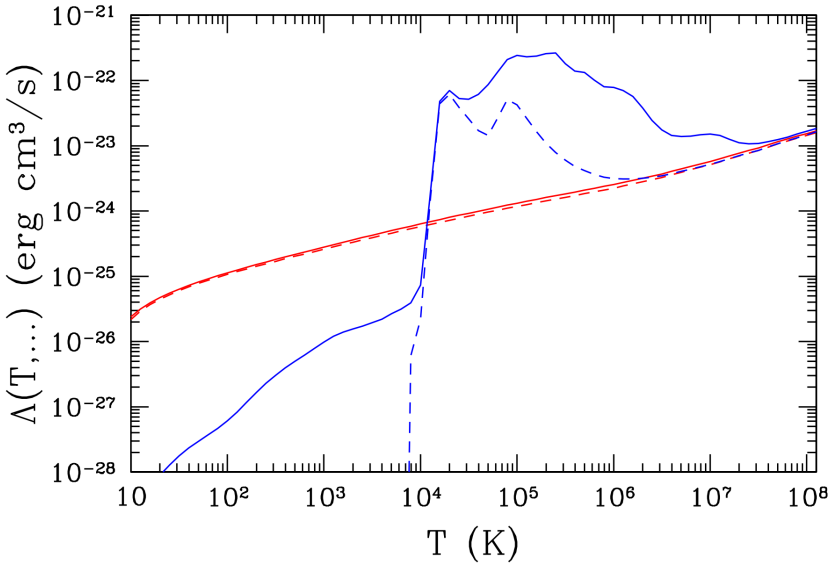

Figure 1.7: Standard cooling function (blue) and cooling function in the presence of a radiation field (red), for a metal-free gas (dashed line) and a solar-metallicity gas (solid line). Figure form Gnedin & Hollon (2012).

- the peak at $10^{4.2}$ K, due to the excitation of Lyα line;
- metals line cooling dominates all the range between the Lyα peak and 10^7 K;
- for very high temperatures, free-free cooling becomes dominating ($\sim T^{1/2}$).

When a radiation field is present, the cooling function changes its shape because the ionized fraction of each species at equilibrium is modified, and thus the cooling rate by line emission is changed accordingly. Fig. 1.7 shows the difference between the standard cooling function with no radiation field (blue lines) and in presence of a radiation field (red lines). For example, the peak at $T \sim 10^4$ K due to Lyα cooling is suppressed, since hydrogen is ionized.

1.5 Shocks and rarefaction waves

The interstellar medium is a very dynamic environment, and the gas is accelerated to very high velocities due to a number of mechanisms. For example, gas at rest is abruptly accelerated by the impact of winds driven by radiation pressure around stars and quasars. Moreover, photoionization and photodissociation heat the gas, that will attain a higher pressure, hence pushing the surrounding medium: this phenomenon occurs around massive stars, in the so-called HII regions. It is therefore fundamental to study the motion of fluids, due to shocks and rarefaction waves.

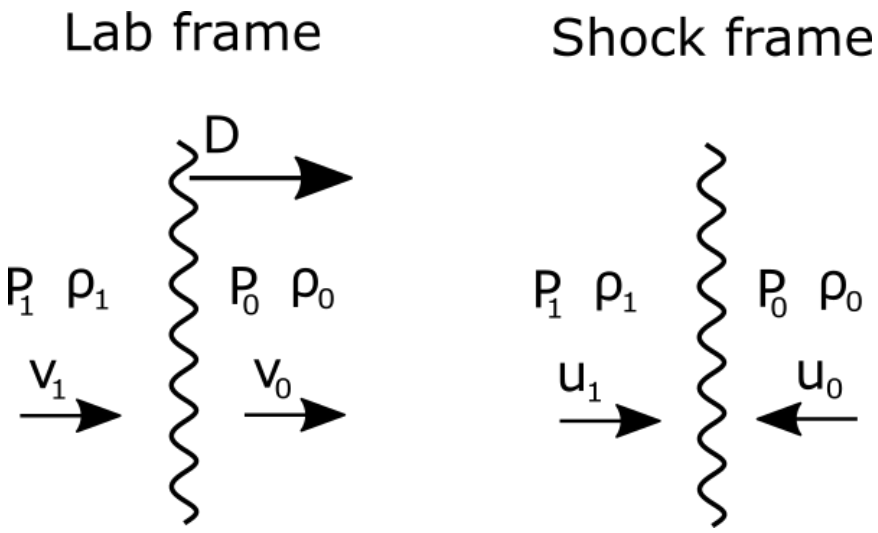

Figure 1.8: Schematic representation of a shock front propagating into a fluid, as seen in the lab reference frame, and the shock front reference frame. The velocity D of the discontinuity, the pre-shock and post-shock velocities v_0 and v_1 satisfy $v_0, v_1 < D$.

A plane shock propagating in a fluid is a discontinuity surface of flow variables ρ, P, T, v, moving at a certain velocity D with respect to the lab frame. Conservation equations of fluids are respected across the discontinuity. We outline the main properties of a shock wave, as developed for the first time in Rankine (1870). It is more convenient to work in the reference frame of the shock front, with the x axis of our Cartesian coordinate system perpendicular to the shock surface, and u is the flow velocity in the x direction this frame. The subscript 0 denotes the variables ahead of the shock, in the unperturbed flow, while the subscript 1 stands for variables in the shocked fluid, as in Fig. 1.8.

For a steady flow, the continuity equation immediately gives

$$\rho_0 u_0 = \rho_1 u_1 \tag{1.42}$$

(u_0 and u_1 are taken positive) and similarly, the Euler equation for a steady, non-viscous fluid gives

$$\rho_0 u_0^2 + P_0 = \rho_1 u_1^2 + P_1 \ . \tag{1.43}$$

The energy transport equation (kinetic and internal) for an adiabatic process is

$$\frac{1}{2}u_0^2 + \varepsilon_0 + \frac{P_0}{\rho_0} = \frac{1}{2}u_1^2 + \varepsilon_1 + \frac{P_1}{\rho_1} \ , \tag{1.44}$$

where ε is the internal energy for unit mass, which for an ideal gas with constant specific heat is

$$\varepsilon = \frac{1}{\gamma - 1}\frac{P}{\rho} \ . \tag{1.45}$$

To sum up, the Rankine-Hugoniot jump conditions are

$$\begin{cases} \rho_0 u_0 = \rho_1 u_1 \\ \rho_0 u_0^2 + P_0 = \rho_1 u_1^2 + P_1 \\ \dfrac{1}{2}u_0^2 + \dfrac{\gamma_0}{\gamma_0 - 1}\dfrac{P_0}{\rho_0} = \dfrac{1}{2}u_1^2 + \dfrac{\gamma_1}{\gamma_1 - 1}\dfrac{P_1}{\rho_1} \end{cases} \tag{1.46}$$

If rest flow variables are known and a parameter describing the strength of the shock is given (for example v_1, u_1, P_1, T_1 or the shock speed D), the jump conditions allow to solve for the state of the post-shock fluid. The following useful relations can be obtained in the case $\gamma = \gamma_1 = \gamma_2$, involving the Mach number $M_i = u_i/c_i$ $(i = 0, 1)$ with c_i speed of sound:

$$\frac{u_1}{u_0} = \frac{(\gamma - 1)M_0^2 + 2}{(\gamma + 1)M_0^2} \tag{1.47}$$

$$\frac{P_1}{P_0} = \frac{2\gamma M_0^2 - (\gamma - 1)}{\gamma + 1} \tag{1.48}$$

$$\frac{T_1}{T_0} = \frac{1 + \dfrac{\gamma - 1}{2}M_0^2}{1 + \dfrac{\gamma - 1}{2}M_1^2} \tag{1.49}$$

$$M_1^2 = \frac{M_0^2 + \dfrac{2}{\gamma - 1}}{\dfrac{2\gamma}{\gamma - 1}M_0^2 - 1} \ . \tag{1.50}$$

Consider a fluid at rest and a piston confining the fluid in the region $x > 0$. A shock wave may be generated if the piston push into the fluid. But if the piston starts moving backwards, then the fluid occupies the region to the left, where the piston is making room. A front propagates to the right, such that the fluid is progressively put into motion toward the piston (the fluid particles close to it move at same velocity of the piston), while pressure and density decrease to lower values. The formalism of characteristics and Riemann invariants allows to find a complete solution of such phenomenon, called rarefaction wave, for a given velocity of the piston. Zel'dovich & Raĭzer (2002) go through a full derivation, and here we present the resulting motion of a rarefied fluid. Assume that the piston starts to move from $x = 0$ at $t = 0$ with velocity $v = -U$, and assume that the system is adiabatic. The fluid has initially a pressure P_o, a density ρ_o and a speed of sound c_o. Then a "wave head" moves at the speed of sound toward the right, followed by a "wave tail" at a velocity

$$v_{\text{tail}} = c_o - \frac{\gamma + 1}{2}U \ . \tag{1.51}$$

The fluid passed by the wave head starts accelerating according to

$$u = -\frac{2}{\gamma + 1}\left(c_o - \frac{x}{t}\right) \ , \tag{1.52}$$

i.e. it accelerates linearly so that it has reached the speed of the piston when crossing the wave tail. The pressure and density throughout the rarefaction wave are

$$\rho = \rho_o \left[1 - \frac{\gamma-1}{\gamma+1}\left(1 - \frac{x/t}{c_o}\right)\right]^{2/(\gamma-1)} \tag{1.53}$$

$$P = P_o \left[1 - \frac{\gamma-1}{\gamma+1}\left(1 - \frac{x/t}{c_o}\right)\right]^{2\gamma/(\gamma-1)} , \tag{1.54}$$

so that the final pressure after the wave has completely passed are

$$\rho_f = \rho_o \left[1 - \frac{\gamma-1}{2}\frac{U}{c_o}\right]^{2/(\gamma-1)} \tag{1.55}$$

$$P_f = P_o \left[1 - \frac{\gamma-1}{2}\frac{U}{c_o}\right]^{2\gamma/(\gamma-1)} . \tag{1.56}$$

It is interesting that U has to be less than $U_{\max} = \frac{2}{\gamma-1}c_o$ for these expressions to make sense. Indeed if U is moving too fast, a vacuum is created between the piston and the fluid. Incidentally, we have thus found the maximum speed of a gas expanding into vacuum.

If a system is not adiabatic, cooling processes modify the post-shock or post-rarefaction temperature. A common case, and a simplifying approximation in some circumstances, is that after the disturbance has passed, temperature goes back to the original value, i.e. the process is isothermal. For a shock, assuming that the gas suddenly cools downstream, the energy equation in (3.14) can be substituted with $T_1 = T_0$, or $P_1/\rho_1 = P_0/\rho_0$. The theory of rarefaction waves can also be adapted to the isothermal case, and the result is that equations (1.53), (1.53) and (1.54) become

$$u = -\left(c_o - \frac{x}{t}\right) \qquad \rho = \rho_0 \exp\left(\frac{x/t}{c_o} - 1\right) \qquad P = P_0 \exp\left(\frac{x/t}{c_o} - 1\right) . \tag{1.57}$$

1.6 Self-gravitating structures

In order to describe the morphology of dense gas in the molecular phase of the ISM, it is useful to analyse the stable configuration of a self-gravitating structure. One of the most common models, applied different scales (from $\sim$ 0.1 pc to tenth of pc), is the Bonnor-Ebert (BE) profile (Bonnor, 1956; Ebert, 1955), describing the radial profile of an isothermal self-gravitating spherical gas cloud of mass M surrounded by a medium with constant pressure P_o. Despite being an idealised model, the BE profile has been proven to fit observed dense molecular globules (Alves et al., 2001; Harvey et al., 2001). In general, clouds tend to have a flat core and then a density profile decreasing as r^{-p} (Beuther et al., 2002; Mueller et al., 2002), with $p \simeq 2$ corresponding to the BE profile (as shown below).

The equation of hydrostatic equilibrium is

$$\frac{d}{dr}P(r) = -\frac{GM(r)}{r^2}\rho(r) = -\frac{d\Phi}{dr}\rho(r) , \tag{1.58}$$

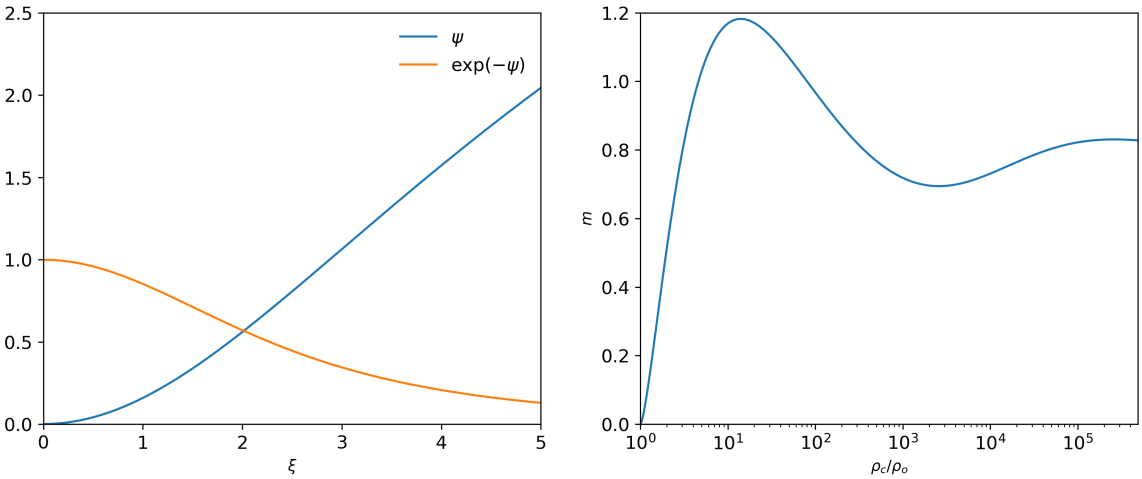

Figure 1.9: **Left**: Solution of the dimensionless Lane-Emden equation (1.64) for a Bonnor-Ebert sphere. **Right**: Dimensionless mass for a Bonnor-Ebert sphere, as a function of density contrast between the centre and the edge of the cloud. At a density contrast $\rho_c/\rho_o \simeq 14.1$ the mass rises to a maximum value, above which the cloud is unstable for collapse. Actually, it can be shown that only clouds with $\rho_c/\rho_o \lesssim 14.1$ are stable, otherwise undergoing a run-away collapse or run-away growth.

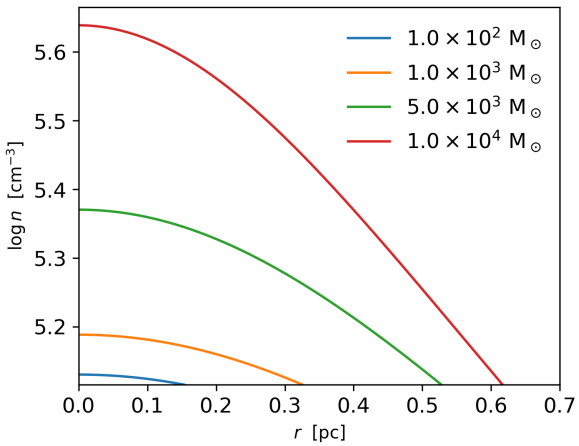

Figure 1.10: Density profiles of Bonnor-Ebert spheres with $T = 10^4\,\mathrm{K}$, $P_o = 1.8 \times 10^{-7}\,\mathrm{erg/cm^3}$ and total mass ranging between $10^2\,M_\odot$ and $10^4\,M_\odot$. We notice that number densities are of the order of $10^5\,\mathrm{cm^{-3}}$ with density contrasts between the centre and the edge not grater then 1.4. For these masses, cloud radii are of the order of some tenths of parsec.

where $M(r)$ is the mass enclosed within radius r, $\Phi(r)$ is the gravitational potential and G is the gravitational constant. The equation of state of an isothermal ideal gas is

$$P(r) = \rho(r) c_s^2 \ , \tag{1.59}$$

where c_s is the isothermal sound speed, constant throughout the sphere. Then we can write (1.58) as

$$\frac{d}{dr} \ln \rho(r) = -\frac{d}{dr}\left(\frac{\Phi}{c_s^2}\right) \ . \tag{1.60}$$

Denoting with ρ_c the central density (that we do not know in our problem) and noting that $\Phi(0) = 0$, the integration yields

$$\rho(r) = \rho_c \exp[-\Phi(r)/c_s] \ . \tag{1.61}$$

The potential satisfies the Poisson equation in spherical coordinates:

$$\nabla^2 \Phi = \frac{1}{r^2}\frac{d}{dr}\left(r^2 \frac{d}{dr}\Phi(r)\right) = 4\pi G \rho(r) = 4\pi G \rho_c \exp[-\Phi(r)/c_s^2] \ . \tag{1.62}$$

In the dimensionless variables

$$\psi = \Phi(r)/c_s^2 \qquad\qquad \xi = \left(\frac{4\pi G \rho_c}{c_s^2}\right)^{1/2} r \ , \tag{1.63}$$

the equation becomes

$$\frac{1}{\xi^2}\frac{d}{d\xi}\left(\xi^2 \frac{d\psi}{d\xi}\right) = \exp(-\psi) \tag{1.64}$$

with the boundary conditions

$$\psi(0) = 0 \qquad\qquad \left.\frac{d\psi}{dr}\right|_{\xi=0} = 0 \ . \tag{1.65}$$

The solution of equation (1.64) can be found numerically: the functions ψ and $\rho/\rho_c = e^{-\psi}$ are plotted in the left panel of Fig. 1.9.

The radius R of the sphere is given by the value ξ_o at which ψ is zero, and the total mass can be expressed as

$$M = \int_0^R 4\pi r^2 \rho(r)\, \mathrm{d}r = 4\pi\rho_c \left(\frac{c_s^2}{4\pi G \rho_c}\right)^{3/2} \int_0^{\xi_o} \xi^2 e^{-\psi}\, \mathrm{d}\xi = 4\pi\rho_c \left(\frac{c_s^2}{4\pi G \rho_c}\right)^{3/2} \left(\xi^2 \frac{d\psi}{d\xi}\right)_{\xi_o} \ , \tag{1.66}$$

using the equation (1.64) in the last passage. The mass M is given, but it's more convenient to use the dimensionless mass

$$m(\xi_o) = \frac{P_o^{1/2} G^{3/2} M}{c_s^4} = \left(4\pi \frac{\rho_c}{\rho_o}\right)^{-1/2} \left(\xi^2 \frac{d\psi}{d\xi}\right)_{\xi_o} \ , \tag{1.67}$$

where ρ_o is the density at the edge of the cloud (easily calculated from $P_o = \rho_o c_s^2$). Plotting $m(\xi) = \left(4\pi e^{\psi(\xi)}\right)^{-1/2} \xi^2 \dfrac{d\psi}{d\xi}$, is possible to find the the value of ξ_o knowing $m(\xi_o)$, which

we have computed from M. Then we get ρ_c and the the density profile from (1.61). Finally, the radius of the cloud is given by

$$R = \left(\frac{4\pi G\rho_c}{c_s^2}\right)^{-1/2} \xi_o \ . \tag{1.68}$$

As an example, we apply this prescription to write the density profile for Bonnor-Ebert spheres of atomic hydrogen with $T = 10^4\,\mathrm{K}$, $P_o = 1.8 \times 10^{-7}\,\mathrm{erg/cm^3}$ and total mass ranging between $10^2\,M_\odot$ and $10^4\,M_\odot$. The results are shown in Fig. 1.10: the profiles show a flat core, with the density dropping as $\sim r^{-2}$ up to the total radius R.

1.7 HII regions

1.7.1 Static HII regions

In presence of an ionizing radiatoin field, the abundance of atomic and ionized hydrogen is determined by the balance between ionization of H and the recombination of electrons with ions H^+ (i.e. protons). We consider a cloud where a new star has formed. The gas is initially neutral, and when the star starts to shine, photons dissociate molecules and ionize atoms around the star, forming a so-called HII region. In the scenario where a star forms at the center of a virtually infinite cloud, a ionization front will propagate radially, so that the HII region has a spherical shape. In this section, we briefly review how the ionisation and the temperature of the HII regions are computed, following the treatment in Osterbrock & Ferland (2006), while the dynamics of its expansion will be covered in Sec. 1.7.2.

We work in the following approximations:

1. All H atoms are initially in the ground state;
2. Recombinations to all levels are immediately followed by a decay to the ground state (see previous section, after eq. 1.10);
3. Photoionization from 1s is balanced by recombination to all levels (i.e. OTSA)

Under only approximation 1 and 2, the photoionization equilibrium equation is obtained by equating hydrogen ionization and recombination rate:

$$n_{\mathrm{H}} \int_{\nu_0}^{\infty} \frac{4\pi J_\nu}{h\nu}\, a_\nu \,\mathrm{d}\nu = n_p n_e \alpha_{\mathrm{A}}(T) \ . \tag{1.69}$$

The mean radiation intensity J_ν has a component $J_{\nu,\star}$ (stellar emission), and a component $J_{\nu,d}$ (diffuse radiation, emitted within the cloud itself). The only source of ionizing diffuse radiation is recombination to the ground state, which is balanced if we adopt the OTSA:

$$n_{\mathrm{H}} \int_{\nu_0}^{\infty} \frac{4\pi J_{\nu,d}}{h\nu}\, a_\nu \,\mathrm{d}\nu = n_p n_e \alpha_1(T) \ . \tag{1.70}$$

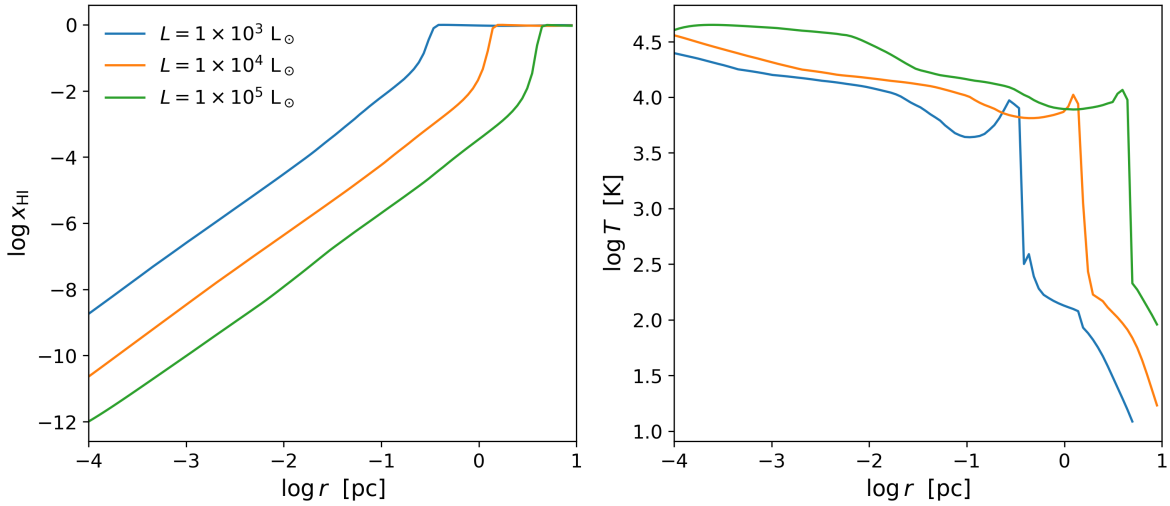

Figure 1.11: Radial profile of an HII region, where the gas has constant density ($n = 100$ cm^{-3}), and star is radiating with a black body spectrum. The left plot shows the neutral fraction $x_{\rm HI} = n_{\rm HI}/(n_{\rm HII} + n_{\rm HII})$ and the right plot shows the temperature profile.

Then, with the full nebular approximation (1, 2, 3), we get

$$n_{\rm H} \int_{\nu_0}^{\infty} \frac{4\pi J_{\nu,\star}}{h\nu} a_\nu \, {\rm d}\nu = n_p n_e \alpha_{\rm B}(T) \ . \tag{1.71}$$

For the stellar component:

$$J_{\nu,\star} = \frac{F_{\nu,\star}(r)}{4\pi} = \left(\frac{r_\star}{r}\right)^2 \frac{F_{\nu,\star}(r_\star)}{4\pi} \, e^{-\tau_\nu(r)} \ , \tag{1.72}$$

where $F_{\nu,\star}$ is the flux (erg cm^{-2} s^{-1} Hz^{-1}), $r_\star$ is the star radius, and $\tau_\nu(r)$ is the optical depth at a distance r from the source, given by

$$\tau_\nu(r) = \int_0^r n_{\rm H}(r') \, a_\nu \, {\rm d}r' \ . \tag{1.73}$$

Thus eq. 1.69 becomes

$$n_{\rm H} \left(\frac{r_\star}{r}\right)^2 \int_{\nu_0}^{\infty} \frac{F_{\nu,\star}(r_\star)}{h\nu} \, a_\nu \, e^{-\tau_\nu(r)} \, {\rm d}\nu = n_p n_e \alpha_{\rm B}(T) \tag{1.74}$$

or

$$(1 - x_e) \left(\frac{r_\star}{r}\right)^2 \int_{\nu_0}^{\infty} \frac{F_{\nu,\star}(r_\star)}{h\nu} \, a_\nu \, e^{-\tau_\nu(r)} \, {\rm d}\nu = x_e^2 n \alpha_{\rm B}(T) \ , \tag{1.75}$$

defining the ionized fraction $x_e = n_p/n = n_e/n$, with n total gas number denisty. Assuming a density profile $n(r)$ and a temperature profile $T(r)$, it is possible to solve the equation numerically for x_e.

In Fig. 1.11, we show the ionization profile (left panel) and temperature profile (right panel) for a gas with uniform density $n = 100$ cm^{-3}. The figure has been realised with a

more refined thermochemical model, described in Sec 2.3, so the temperature profile is also computed accounting for heating and chemical mechanisms. The result is a very sharp transition from an almost completely ionized gas ($x_e \simeq 1$) to an almost neutral medium ($x_e \simeq 10^{-4}$): indeed the $e^{-\tau_\nu}$ term drops rapidly to zero when the integral defining τ_ν starts to grow. Thus, an HII region radius is well defined (the Strömgren radius $R_{\rm S}$) and can be computed analitycally. Multiplying both members of eq. 1.69 by r^2 and then integrating over r:

$$r_\star^2 \int_{\nu_0}^{\infty} \frac{F_{\nu,\star}(r_\star)}{h\nu} \int_0^{\infty} n_{\rm H}(r)\, a_\nu\, e^{-\tau_\nu(r)}\, {\rm d}r\, {\rm d}\nu = \int_0^{\infty} n_p(r) n_e(r) \alpha_{\rm B}(T) r^2\, {\rm d}r \ . \tag{1.76}$$

From the definition of $\tau_\nu(r)$ we have $\dfrac{\rm d}{{\rm d}r}\tau_\nu = n_{\rm H} a_\nu$, which implies

$$\int_0^{\infty} n_{\rm H}(r)\, a_\nu\, e^{-\tau_\nu(r)}\, {\rm d}r = \int_0^1 {\rm d}\left[e^{-\tau_\nu(r)}\right] = 1 \ . \tag{1.77}$$

Now we also apply the approximation

$$\begin{cases} n_p = n_e \simeq n & r < R_{\rm S} \\ n_p = n_e \simeq 0 & r > R_{\rm S} \end{cases} \ . \tag{1.78}$$

As a result, the equation becomes (assuming an average value for $\alpha_{\rm B}$, which is ok when the HII region has a uniform density)

$$r_\star^2 \int_{\nu_0}^{\infty} \frac{F_{\nu,\star}(r_\star)}{h\nu}\, {\rm d}\nu = \frac{1}{3} \alpha_{\rm B}\, R_{\rm S}^3 \ . \tag{1.79}$$

Multiplying by 4π, the integral on the LHS is the number of ionizing photons per second $Q_\star$ ($\rm s^{-1}$). The final expression for the Strömgren radius is then

$$R_{\rm S} = \left(\frac{3 Q_\star}{4\pi \alpha_{\rm B} n^2} \right)^{1/3} \ . \tag{1.80}$$

The easy way to obtain the expression 1.80 is to equate the rate of ionizing photons emitted from the source and recombining atoms in the Strömgren sphere, ignoring the frequency dependence of a_ν:

$$Q_\star = \frac{4\pi}{3} R_{\rm S}^3 (x_e n)^2 \alpha_{\rm B} \ , \tag{1.81}$$

where $x_e \simeq 1$.

1.7.2 Dynamics of HII regions

In the previous Section, we have shown the structure of a static HII region in photoionization equilibrium. However, the gas is heated by photoionization, and the pressure difference will induce a motion in the gas. A complete treatment of the dynamic effect of radiation on neutral gas is done for example in Kahn (1954).

Consider a plane ionization front, due to a source emitting photons with a flux ϕ [$\mathrm{cm^{-2}\,s^{-1}}$]. The subscripts 0 and 1 will respectively denote the values of variables ahead and behind the IF, and the velocities $u_{0,1}$ are measured in the IF reference frame (but taken positive). If χ_0 is the hydrogen ionization potential and χ_r is the mean energy of an ionizing photon, the mean energy of ejected electron is $(\chi_r - \chi_0)$. This energy goes in gas heating, i.e.

$$\frac{1}{2} m_{\mathrm{H}} q^2 = \chi_r - \chi_0 \ , \tag{1.82}$$

where q is the mean velocity gain of hydrogen atoms.

To move the IF from radius r to radius $r + \mathrm{d}r$, as many photons as the number of neutral atoms contained in the shell of thickness $\mathrm{d}r$ have to hit the IF surface:

$$\phi \, 4\pi r^2 \, \mathrm{d}t = n_0 \, 4\pi r^2 \, \mathrm{d}r \ , \tag{1.83}$$

that gives

$$\frac{\mathrm{d}r}{\mathrm{d}t} = \frac{\phi}{n_0} \ . \tag{1.84}$$

Now we can write the jump conditions (eq. 3.14) across the IF (for a monoatomic gas, i.e. $\gamma = 5/3$):

$$\begin{cases} \rho_0 u_0 = \rho_1 u_1 = m_{\mathrm{H}} \phi & (1) \\ P_0 + \rho_0 u_0^2 = P_1 + \rho_1 u_1^2 & (2) \\ \dfrac{1}{2} u_0^2 + \dfrac{5}{2} \dfrac{P_0}{\rho_0} + \dfrac{1}{2} q^2 = \dfrac{1}{2} u_1^2 + \dfrac{5}{2} \dfrac{P_1}{\rho_1} & (3) \end{cases} \tag{1.85}$$

We define the compression ratio as $\varepsilon = \rho_1 / \rho_0$. Then, by (1) and (2)

$$P_1 = P_0 - \frac{\phi}{\varepsilon} \rho_0 u_0^2 (1 - \varepsilon) \ . \tag{1.86}$$

Substituting into (3) u_1 from (1) and P_1 just obtained above, we get the equation

$$(3c_0^2 + u_0^2 + q^2)\varepsilon^2 - (3c_0^2 + 5u_0^2)\varepsilon + 4u_0^2 = 0 \ . \tag{1.87}$$

Computing the discriminant of the equation, we find that there are real solution only if

$$u_0 \geq u_{\mathrm{R}} \equiv \frac{1}{3}(2q + \sqrt{4q^2 + 9c_0^2}) \tag{1.88}$$

or

$$u_0 \leq u_{\mathrm{D}} \equiv \frac{1}{3}(-2q + \sqrt{4q^2 + 9c_0^2}) \ . \tag{1.89}$$

Notice that by their definition $u_{\mathrm{R}} > c_0$ and $u_{\mathrm{D}} < c_0$. Two critical densities correspond to the critical velocities u_{R} and u_{D}, by equation (1) of (1.85):

$$\rho_{\mathrm{R}} = \frac{3\phi}{2q + \sqrt{4q^2 + 9c_0^2}} \qquad \rho_{\mathrm{D}} = \frac{3\phi}{-2q + \sqrt{4q^2 + 9c_0^2}} \ . \tag{1.90}$$

The following classification of IFs can be made:

- **R-type** front: $u_0 \geq u_{\rm R}$ or $\rho_0 \leq \rho_{\rm R}$, the IF advances in the ISM ahead at supersonic speed and there are two possible values of ε (weak and strong R-type fronts);
- **R-critical** front: $u_0 = u_{\rm R}$ or $\rho_0 = \rho_{\rm R}$, with IF sonic w.r.t. the gas ahead and only one possible value of ε;
- **M-type** front: $u_{\rm R} < u_0 < u_{\rm D}$ or $\rho_{\rm D} < \rho_0 < \rho_{\rm R}$, there are no solution for ε and so the IF cannot be in contact with the ionized region (the system cannot remain in this state, and the front has to attain another state);
- **D-critical** front: $u_0 = u_{\rm D}$ or $\rho_0 = \rho_{\rm D}$, with IF sonic w.r.t. the gas behind and only one possible value of ε;
- **D-type** front: $u_0 \leq u_{\rm D}$ or $\rho_0 \geq \rho_{\rm D}$, with the IF subsonic w.r.t. the gas ahead and two possible values of ε (weak and strong D-type fronts).

R stands for "rarified" (an IF of this type happens when the gas density is low), while D stands for "dense" (the density is high).

When the IF is R or D type, there are two solution ε_1 and ε_2. Assuming $\varepsilon_1 > \varepsilon_2$, it is possible to show that the IF is subsonic w.r.t. to the gas behind when $\varepsilon = \varepsilon_1$, while it is supersonic when $\varepsilon = \varepsilon_2$ (Kahn, 1954).

In many references (e.g. Osterbrock & Ferland, 2006), a different approach is taken to write the jump conditions (1.85). Considering that radiation dominates the gas energy balance, it is possible to make the approximation that the gas is heated/cooled behind the IF to some temperature, dependent only on radiation. Thus the radiative jump conditions are

$$\begin{cases} \rho_0 u_0 = \rho_1 u_1 = m_{\rm H}\phi & (1) \\ P_0 + \rho_0 u_0^2 = P_1 + \rho_1 u_1^2 & (2) \\ P_0 = \dfrac{\rho_0}{\mu_0 m_p} k_{\rm B} T_0 \ , \ P_1 = \dfrac{\rho_1}{\mu_1 m_p} k_{\rm B} T_1 & (3) \end{cases} \tag{1.91}$$

Then it is possible to proceed as above, finding different values for the critical velocities:

$$u_{\rm R} = c_1 + \sqrt{c_1^2 - c_0^2} \simeq 2c_1 \ , \tag{1.92}$$

$$u_{\rm D} = c_1 - \sqrt{c_1^2 - c_0^2} \simeq c_0^2/2c_1 \ , \tag{1.93}$$

where the final approximations hold for $c_1 \gg c_0$.

After this analysis of IFs, we want to consider the dynamics of a 1D slab of gas, when a radiation source is present. At first the gas is at rest on the positive side of the plane $x = 0$, while a vacuum is present on the negative side, where radiation is coming from and inciding perpendicularly to the cloud. We want to see what happens for different values of the incident flux ϕ.

IF type	Conditions on ϕ	IF speed	w.r.t HI (ahead)	w.r.t. HII (behind)	Stable?
D-type	$\phi < u_D/m_H$	$V_{IF} < u_D$	sub	Strong: sub Weak: super	No $\rightarrow$ D-critical
D-critical	$\phi = u_D/m_H$	$V_{IF} = u_D$	sub	sonic	Yes
M-type	$u_D/m_H < \phi < u_R/m_H$	/	/	/	No $\rightarrow$ D-critical
R-critical	$\phi = u_R/m_H$	$V_{IF} = u_R$	super	sonic	Yes
R-type	$\phi > u_R/m_H$	$V_{IF} > u_R$	super	Strong: sub Weak: super	No $\rightarrow$ Weak R Yes

Table 1.3: Summary of the properties of IF types, as discussed in the main text. Sub and super are shorthand for subsonic and supersonic.

(a) If $\phi < u_D/m_H$, the conditions at the IF are D-type. This means that the IF propagates at a speed $V_{IF} < u_D < c_0$ into the cloud, subsonically w.r.t. the neutral gas and supersonically/subsonically w.r.t. the ionized gas behind (it depends whether it is a weak or strong IF). However, it is possible to show that a D-type IF is not stable, and a rarefaction wave is driven into the neutral gas, reducing the pressure ahead of the IF and inducing D-critical conditions. Saying it in another way, pressure due to radiation heating is very small, and it is not sufficient to push the cloud gas. As a result, the cloud expands toward negative x, almost as if it was expanding into vacuum.

(b) If $\phi = u_D/m_H$, the conditions at the IF are D-critical. The pressure induced by radiation is just sufficient to keep the cloud from expanding. The IF propagates into the cloud at a speed $V_{IF} = u_D < c_0$, subsonically w.r.t. the neutral gas and sonically w.r.t. the ionized gas behind.

(c) If $u_D/m_H < \phi < u_R/m_H$, the conditions at the IF are M-type. There is no solution for this kind of IF, and indeed it is possible to show that a shock wave starts propagating into the cloud ahead of the IF. The shock front compresses the gas ahead of the IF, inducing D-critical conditions at the IF.

(d) If $\phi = u_R/m_H$, the conditions at the IF are R-critical. The IF is so fast that it catches up with the shock front ahead of it. Thus there is only one front propagating at $V_{IF} = u_R > c_0$, supersonically w.r.t. the neutral gas and sonically w.r.t. the ionized gas behind.

(e) If $\phi > u_R/m_H$, the conditions at the IF are R-type. The systems evolves as in (d), with the IF propagating at $V_{IF} > u_R > c_0$, supersonically w.r.t. the neutral gas and supersonically/subsonically (if it is weak or strong) w.r.t. the ionized gas behind. However, only the strong R-type front is stable.

Tab. 1.3 summarize the properties of 5 types of IFs.

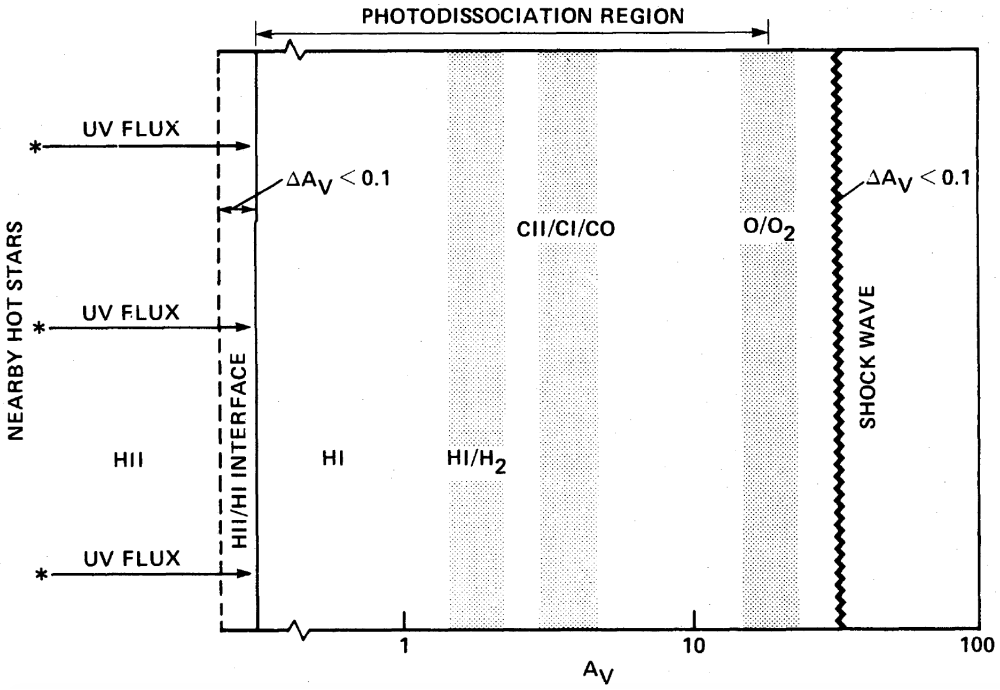

Figure 1.12: Classical scheme of a PDR, from Tielens & Hollenbach (1985). UV radiation comes from the left, and the ionizing flux is absorbed in a thin HII/HI interface. Hydrogen is found in atomic form due to photodissociation by the Solomon process up to $A_v \simeq 2$. At higher visual extinction, we can find the HI/H_2, CII/CI/CO and O/O_2 transitions, until the gas is fully molecular because of complete absorption of the flux.

1.8 Photodissociation regions

A Photo-Dissociation Region (PDR) is a portion of the ISM, whose structure and chemistry are regulated by incident far ultraviolet (FUV) radiation (6 eV $< h\nu <$ 13.6 eV). For example, a PDR forms around the HII region of an OB star, since all ionizing photons are absorbed in the HII region and only FUV photons come out from the ionized bubble. On the other side, a PDR also forms at the edge of a molecular cloud if an external radiation source is present: the dense gas absorbs all ionizing photons in a very thin shell, and only FUV photons get further into the cloud.

The classical stationary (i.e. time-independent) structure of a PDR has been formalized by Tielens & Hollenbach (1985), and it is represented in the scheme of Fig. 1.12. Radiation is coming from the left, and the ionizing portion of the spectrum is absorbed at the left of the HII/HI interface, so that only the FUV radiation determines the structure of the PDR. The depth into the cloud is measured with the visual extinction A_v: an extinction of 1 mag corresponds to an hydrogen column density $N_{\rm H} = 1.8 \times 10^{21}$ cm^{-2}.

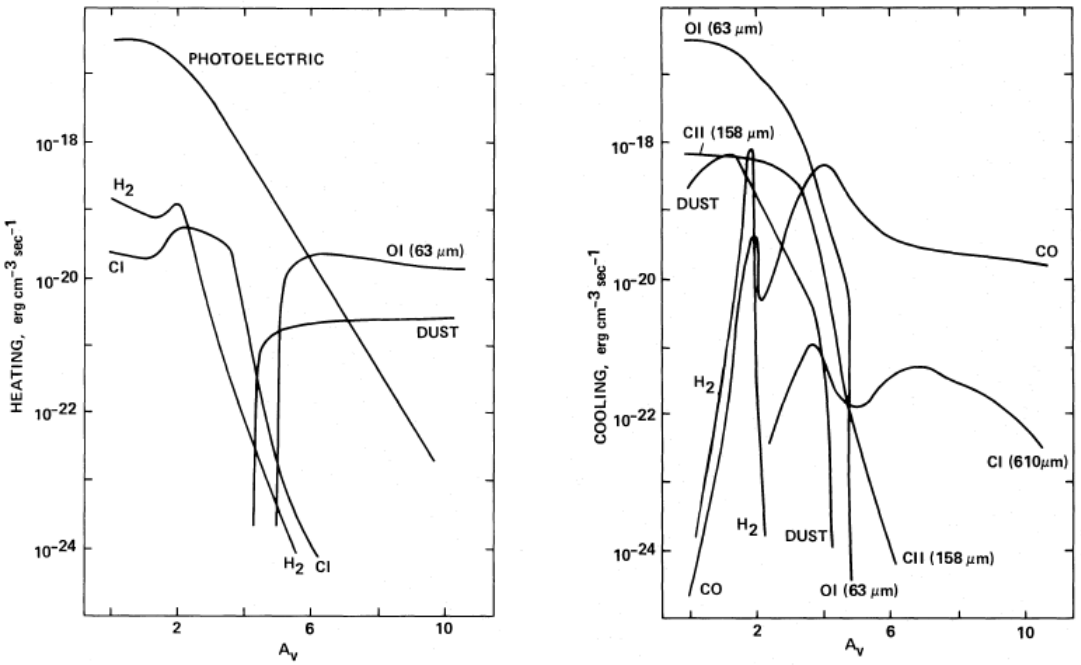

Figure 1.13: Heating (**left**) and cooling (**right**) rate as a function of depth (expressed as a visual extinction) in a PDR, from Tielens & Hollenbach (1985). Photoelectric effect on dust grains dominates the heating, while the gas mostly cools via OI and CII lines (and CO ro-vibrational lines at larger visual extinctions).

In the outer part of the PDR, hydrogen is found in atomic form, since radiation is able to dissociate H_2 molecules. H abundance decreases with depth, since it combines to form H_2 when radiation intensity progressively decreases. For column densities $N < 10^{21}\,\mathrm{cm}^{-2}$, the opacity is dominated by H_2, and the position of the HI/H_2 transition (dissociation front DF) is approximately given by

$$N_{\mathrm{DF}} \simeq 5 \times 10^{14} (G_0/n)^{4/3}\,\mathrm{cm}^{-2}\ , \tag{1.94}$$

where G_0 is the flux in the FUV band in Habing Units*. When $N > 10^{21}\,\mathrm{cm}^{-2}$ (i.e. $G_0/n > 4\times10^{-2}\,\mathrm{cm}^3$) dust absorption becomes important. For $G_0/n \simeq 1\,\mathrm{cm}^3$ the HI/H_2 transition occurs at $A_v \simeq 2$. Whether absorption is dominated by dust or H_2, the attenuation of radiation is such that H_2 piles up rapidly. As a consequence of H_2 self-shielding, the HI/H_2 transition is always sharp.

Analogously to hydrogen, the CII abundance decreases with depth because of FUV flux attenuation. Correspondingly, CI abundance increases, but then starts to decrease again at $A_v \simeq 4$ when CO formation begins (but charge exchange reaction with S and SiO are responsible for another peak at $A_v \simeq 6.5$, after which all CI is completely converted into CO). CO abundance has a small peak at $A_v \simeq 2$ (because of reactions initiated by H_2^*)

*1 Habing corresponds to 1.6×10^{-3} erg s^{-1} cm^{-2}

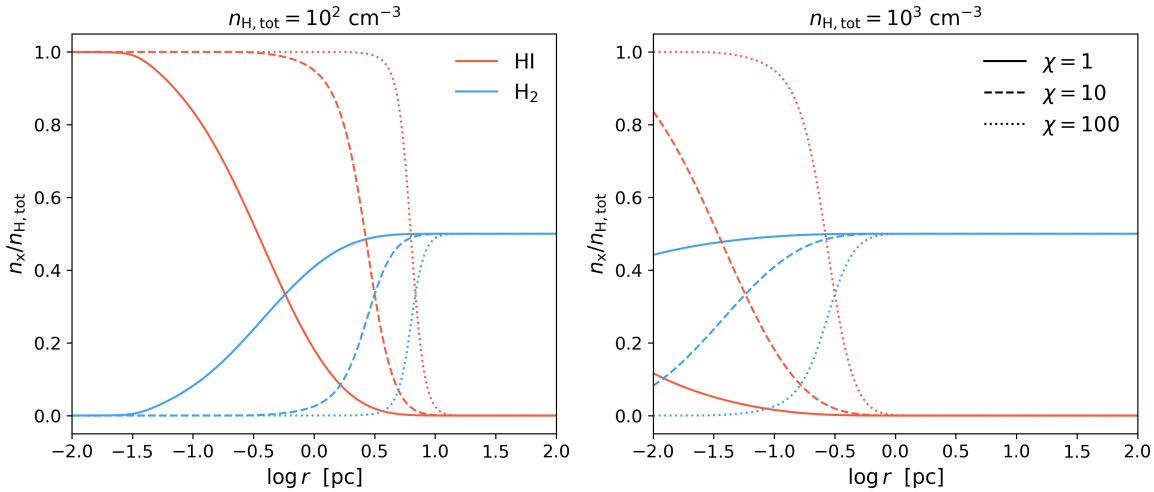

Figure 1.14: Profile of a plane parallel PDR according to Bialy & Sternberg (2016), for different gas densities ($n_{\rm H,tot} = n_{\rm HI} + 2n_{\rm H_2} = 10^2, 10^3$ cm^{-3}) and different fluxes ($\chi = 1, 10, 100$ in Draine units). r is the distance from the edge of the slab where radiation is coming from, the red and blue lines represent the ratio of HI and H_2 densities to the total H density).

and a dip at $A_v \simeq 6.5$ (corresponding to the peak of CI). Since the CO abundance is low (with respect to H_2), its self-shielding is never very strong. As a result, the CII/CI/CO transition occurring around $A_v \simeq 6-7$ is not sharp (see Fig. 14 in Röllig et al., 2007).

These chemical processes also entail corresponding heating and cooling mechanisms, shown in Fig. 1.13. For $A_v < 6$ the heating is dominated by the photoelectric effect on dust grains, with a small contribution from H_2^* collisional de-excitation and C ionization. The cooling is dominated by the OI 63 μm line, with the contribution from CII 158 μm: indeed these two lines, together with OI 145 μm and molecular ro-vibrational lines, are the main observational feature of a PDR. With increasing depth, the photoelectric heating drops because of FUV flux extinction, but less than expected since the grains are now not charged and the efficiency of the process increases. The OI cooling decreases too, for the same reason (FUV flux is weaker and a lower fraction of OI is excited). This tendency of the cooling to drop faster than heating brings to a maximum of temperature around $A_v \simeq 1.2$. For $A_v > 1.2$ the H_2 and CO molecular line cooling becomes important (since H_2 and CO start to appear), and temperature decreases again. For $A_v > 6$ the heating is dominated by IR dust emission ($T_{\rm d} \simeq 50$ K, i.e. $\lambda \simeq 60\,\mu$m): this emission excites the OI 63 μm transition, which is collisionally de-excited: this mechanism tends to couple dust and gas temperature. Gas-grain collisions cool the gas at low depth and heat the gas at high depth. It is generally unimportant, but becomes significant when $n > 10^6$ cm^{-3}.

1.8.1 Analytical profile of a PDR

An accurate description of PDRs is extremely challenging, because their structure is determined by the interaction of radiation with complex chemical species (molecules like H_2, CO, HCN, etc..). For this reason, PDRs are generally studied with 1D numerical simulations: some of the most commonly used codes are CLOUDY (Ferland et al., 1998), COSTAR (Kamp & Bertoldi, 2000), KOSMA-τ (Stoerzer et al., 1996), UCL − PDR (Taylor et al., 1993). However, very useful fitting functions for the profile of a PDR have been obtained in Bialy & Sternberg (2016). Consider a gas slab with constant density, with FUV flux impinging from one side of the slab. At the equilibrium, H_2 formation and destruction by LW photons balance:

$$R\, n_{\rm H,tot}\, n_{\rm H} = \frac{1}{2} D_0 f_{\rm att} n_{\rm H_2} \ , \tag{1.95}$$

where $n_{\rm H,tot} = n_{\rm H} + 2n_{\rm H_2}$, R is the H_2 formation rate (here assumed constant with temperature), D_0 is the unattenuated photodissociation rate, and $f_{\rm att}$ is the attenuation factor (due to both dust and H_2 self-shielding). The factor 1/2 is due to the fact that radiation is coming from one side only of the gas slab (hence from half of the total volume). The formation rate is $R = R_{\rm f,H_2}\tilde{\sigma}_g$ with $R_{\rm f,H_2}$ given by eq. 1.11 for some fixed T and $\tilde{\sigma}_g$ accounting for deviation of the dust grain cross section from the typical value in the Milky Way:

$$\tilde{\sigma}_g = \frac{\sigma_g}{\sigma_{g,\rm LW}} = \frac{\sigma_g}{1.9\times10^{-21}\ {\rm cm}^2} \ . \tag{1.96}$$

The dissociation rate is $\Gamma_{\rm H_2}$ given by eq. 1.16 or more accurately by eq. 1.17. The attenuation factor can be expressed as

$$f_{\rm att} = f_{\rm shield}(N_{\rm H_2})\, e^{-\sigma_g N_{\rm H,tot}} \ . \tag{1.97}$$

$f_{\rm shield}$ is given for example by eq. 1.19 or eq. 1.20. The solution of eq. 1.95 can be written in terms of W_g, a function obtained by fitting 1D simulations of PDRs:

$$\frac{n_{\rm H}}{n_{\rm H_2}}(N_{\rm H_2}) = \frac{\sigma_d}{\sigma_g}\frac{\alpha G f_{\rm shield}(N_{\rm H_2}) e^{-2\sigma_g N_{\rm H_2}}}{\alpha G W_g(N_{\rm H_2}) + 2W_g(\infty)} \ , \tag{1.98}$$

$$n_{\rm H}(N_{\rm H_2}) = \frac{1}{\sigma_g}\ln\left(\frac{\alpha G}{2}\frac{W_g(N_{\rm H_2})}{W_g(\infty)} + 1\right) \ , \tag{1.99}$$

where

$$G = \frac{\sigma_g}{\sigma_d} W_{g,\rm tot} = 3\times10^5 \tilde{\sigma}_g \left(\frac{9.9}{1+8.9\tilde{\sigma}_g}\right)^{0.37} \ , \tag{1.100}$$

$$\alpha = \frac{D_0}{R n_{\rm H,tot}} \ . \tag{1.101}$$

The function W_g is given by

$$W_g(N_{\rm H_2}) = a_1 \ln\left(\frac{a_2+y}{1+y/a_3}\right)\left(\frac{1+y/a_3}{1+y/a_4}\right)^{0.4} \tag{1.102}$$

and

$$W_g(\infty) = \lim_{N_{\rm H_2}\to\infty} W_g = \frac{8.8\times10^{13}\,{\rm Hz}}{(1+8.9\tilde{\sigma}_g)^{0.37}}\ , \tag{1.103}$$

with $y = N_{\rm H_2}/10^{14}\,{\rm cm^{-2}}$, $a_1 = 3.6\times10^{11}\,{\rm Hz}$, $a_2 = 0.62$, $a_3 = 2.6\times10^3$, $a_4 = 1.4\times10^7(1+8.9\tilde{\sigma}_g)^{-0.93}$. Using this analytical formulation, we have plotted in Fig. 1.14 some examples, for different densities ($n_{\rm H,tot} = 10^2, 10^3$ cm^{-3} in the left and right panel respectively) and different fluxes ($\chi = 10, 100, 1000$ in Draine units*). At lower density, the FUV radiation is able to penetrate up to 10 pc, in the case of $\chi = 10^3$. When the density is higher, the PDR is at least a factor of 10 thinner, with radiation able to only partially dissociate the molecular hydrogen in the lowest flux case.

1.9 Molecular clouds

Most of the molecular gas in our Galaxy is organized in clouds (Giant Molecular Clouds, GMCs), which can be gravitationally bound, or marginally unbound due to turbulence driven by stellar feedback (Dale et al., 2005; Matzner, 2002; Haid et al., 2018b) or large scales phenomena in the galaxy (Brunt et al., 2009; Hughes et al., 2013; Colombo et al., 2014; Dobbs, 2015; Walch et al., 2015). The "boundness" of a cloud is generally parametrized with the virial parameter $\alpha_{\rm vir}$, defined as

$$\alpha_{\rm vir} = \frac{2E_k}{U_g} = \frac{5}{3}\,v_{\rm rms}^2\,\frac{R}{GM}\ , \tag{1.104}$$

where E_k is the kinetic energy associated with the turbulent motion with (3D) root mean square velocity $v_{\rm rms}$, and U_g is the gravitationally potential of a uniform sphere with mass M and radius R. According to virial theorem, $\alpha_{\rm vir} = 1$ corresponds to a cloud at equilibrium, $\alpha_{\rm vir} > 1$ to an unbound cloud and $\alpha_{\rm vir} < 1$ to a collapsing cloud. Nevertheless, an initially unbound cloud could collapse if the turbulence is not fed continuously, since it will dissipate in a time $t_{\rm diss} \simeq 2R/v_{\rm rms}$ (Mac Low et al., 1999). The timescale for the collapse of a gravitationally unstable cloud with mean density ρ is given by the free-fall time:

$$t_{\rm ff} = \sqrt{\frac{3\pi}{32G\rho}} = 1.2\times10^6\,{\rm yr}\left(\frac{n}{10^3\ {\rm cm^{-3}}}\right)^{-0.5}\ , \tag{1.105}$$

assuming a mean molecular density $\mu = 3.32\times10^{-24}$ g.

GMCs have typical masses ranging from $10^3\,{\rm M_\odot}$ to $10^6\,{\rm M_\odot}$, while the size can be as small as 5 pc, or larger up to ~ 200 pc (Blitz, 1993). It follows that average number densities are $n \simeq 1 - 10^3$ cm^{-3}, but internal structure driven by turbulent motions can be very complex, presenting low density voids ($n < 1$ cm^{-3}) and high density structures, as clumps and filaments ($n > 10^{4-5}$ cm^{-3} Bally et al., 1987; Bertoldi & McKee, 1992). Small dense

*1 Draine corresponds to 2.736×10^{-3}erg s^{-1} cm^{-2}

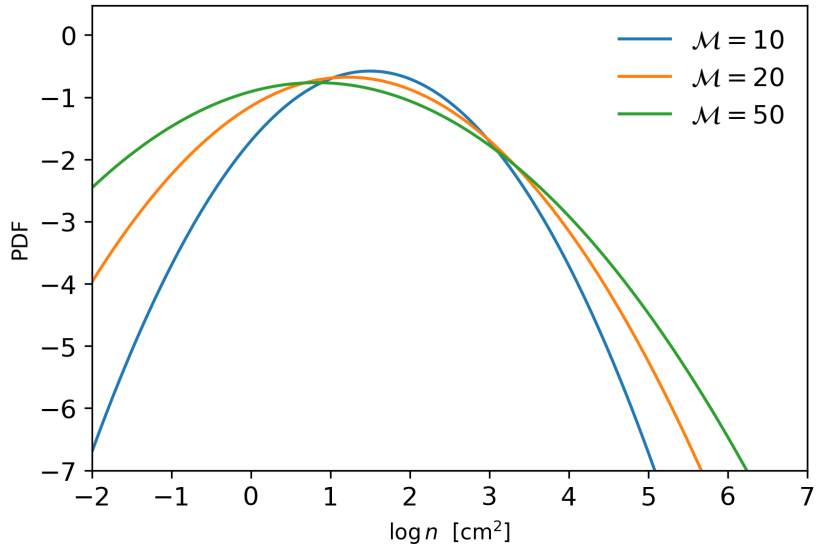

Figure 1.15: Density PDF in a GMC with average number density $n = 100$ cm^{-3}, as found by Padoan & Nordlund (2002), for a factor $b = 0.3$ (see text) and negligible magnetic pressure ($\beta \to \infty$). The three curves stand for different Mach numbers for the turbulence ($\mathcal{M} = 10, 20, 50$). Most of the gas has density $n \simeq 1$ for $\mathcal{M} = 10, 20$, while the peak of the PDF shifts towards $n \simeq 10$ for $\mathcal{M} = 50$. With stronger turbulence, the PDF is more spread, with gas collapsing to higher densities ($n > 10^7$ cm^{-3}).

clumps are the location where gravitational collapse brings to star formation, which in turns affects the gas structure, by means of different feedback effects: photoionization and photodissociation (Whitworth, 1979; Gorti & Hollenbach, 2002), radiation pressure, winds (Castor et al., 1975; Weaver et al., 1977) and supernova explosions (Sedov, 1958; Ostriker & McKee, 1988). The internal structure developing as a consequence of turbulence, gravity and magnetic fields has been studied numerically (Padoan & Nordlund, 2002; Federrath & Klessen, 2013). These studies find a log-normal Probability Distribution Function (PDF):

$$g(s) = \frac{1}{(2\pi\sigma^2)^{1/2}} \exp\left[-\frac{1}{2}\left(\frac{s - s_0}{\sigma}\right)\right] , \tag{1.106}$$

where $s = \ln(n/n_0)$, with n_0 being the mean GMC density, $s_0 = -\sigma^2/2$, and σ a parameter quantifying the pressure support. Turbulent and magnetic contribution to gas pressure can be parametrized by the Mach number $\mathcal{M}$ and the thermal-to-magnetic pressure ratio β, respectively; then σ is given by

$$\sigma^2 = \ln\left(1 + b^2\mathcal{M}^2\frac{\beta}{\beta + 1}\right) , \tag{1.107}$$

where $b \simeq 0.3 - 1$ is a factor taking into account the kinetic energy injection mechanism which is driving the turbulence (Molina et al., 2012). Plots of the PDF $g(s)$ are shown in Fig. 1.15, for mean cloud density $n = 100$ cm^{-3} and Mach numbers $\mathcal{M} = 10, 20, 50$. For larger Mach numbers, the PDF has a larger variance, hence overdensities reach higher

values ($> 10^6$ cm^{-3}). Including self-gravity, the high-density end of the PDF is modified with a power-law tail $g(n) \sim n^{-\kappa}$, with $\kappa \sim 1.5 - 2.5$ (Krumholz & McKee, 2005; Padoan & Nordlund, 2011; Federrath & Klessen, 2013; Schneider et al., 2015).

From an observational point of view, GMCs were initially discovered as patches in the galaxy with absence of stars (Herschel, 1785), due to their high visual extinction. The most common way to study GMCs is through molecular line emission, as CO ro-vibrational transitions, parametrized by the quantum number J. For example, the $J = 1 \rightarrow 0$ transition has been used to study the H_2 structure in the Milky Way and nearby galaxies (Nakanishi & Sofue, 2003, 2006; Nieten et al., 2006), by assuming a value for the CO-to-H_2 conversion factor $X_{\rm CO}$. The intensity of the CO line together to its radial velocity can be used to delineate the internal structure of a GMC (e.g. Genzel & Stutzki 1989 for the Orion compex, Williams et al. 1994 for the Rosette and Maddalena Clouds, Bolatto et al. 2008 for extragalactic clouds). Nevertheless, the $X_{\rm CO}$ is very uncertain, since it depends on the values adopted for the gas density and the CO excitation temperature, and determinations in the MW may not be representative of other galaxies. Another useful tool to observe GMCs is the far-infrared (FIR) and sub-mm thermal emission from dust grains, characterized by temperatures of few tens of K (Scoville & Good, 1989; Calzetti et al., 2000; Kriek & Conroy, 2013). From the IR flux, it is possible to obtain the dust mass and hence the cloud mass, for an assumed dust-to-gas ratio (Dame et al., 2001; Draine et al., 2007).

Star formation happens in dense cores inside GMCs, so that a fraction of the mass of the cloud is converted into stars. The two key quantities describing this process are the star formation efficiency (SFE), defined as the ratio of the stellar mass and the initial cloud mass, and the star formation rate (SFR), defined as the mass going into stars per unit time ($M_\odot\,{\rm yr}^{-1}$). Observations show the existence of a relation between the gas mass (HI and H_2) and the local SFR over a galaxy. These measurements are based on several proxies: HI density is inferred from the 21 cm emission, H_2 from the CO line emission (and an assumed conversion factor $X_{\rm CO}$) and the SFR from Hα emission, FUV continuum or IR emission from dust. The resulting Schmidt-Kennicutt (SK) relation (Schmidt, 1959; Kennicutt, 1998) states that

$$\Sigma_{\rm SFR} \propto \Sigma_{\rm gas}^{1.4} \,, \tag{1.108}$$

where the $\Sigma_{\rm SFR}$ is the SFR surface density and $\Sigma_{\rm gas}$ is the gas surface density, with the exponent rising to 1.7-1.8 when considering the differences of $X_{\rm CO}$ in galaxies with properties different from the Milky Way (Narayanan et al., 2012). The relation as measured from a collection of observed galaxies is shown in the left panel of Fig. 1.16. An attempt to apply a SK-like relation at smaller scales, as individual GMCs in the Milky Way, shows significant deviations due to the local conditions of the gas. In particular, Krumholz et al. (2012) demonstrate that a universal law for star formation is found when accounting for

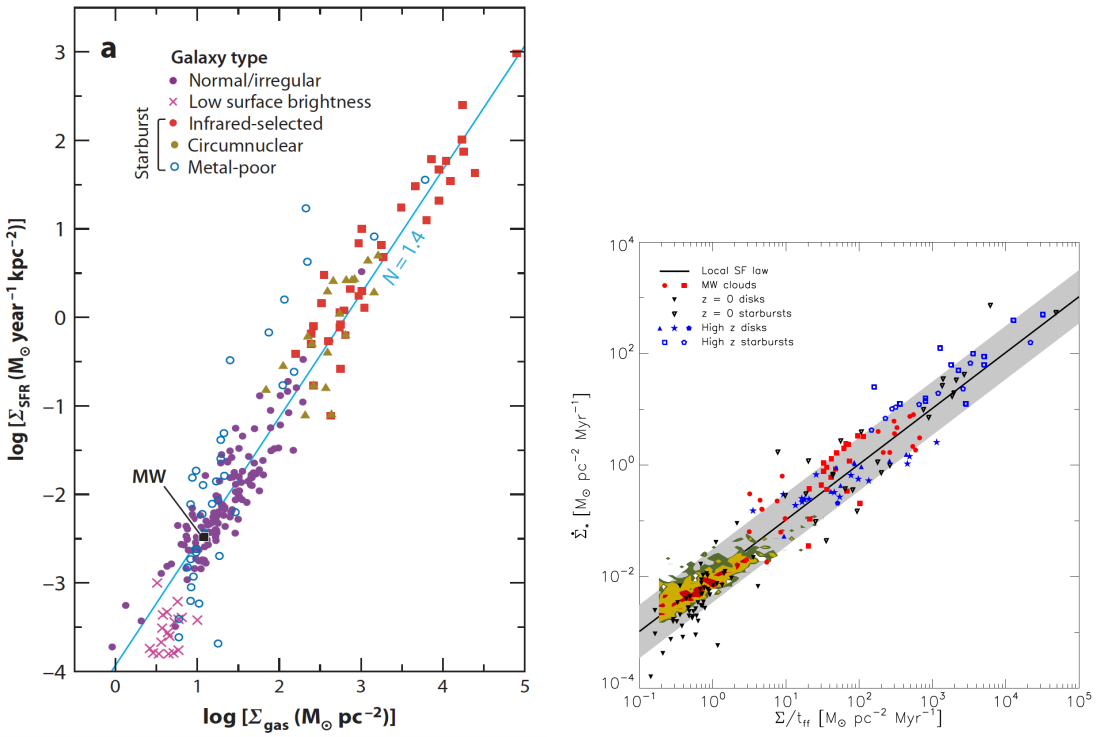

Figure 1.16: **Left**: Relation between $\Sigma_{\rm SFR}$ and $\Sigma_{\rm gas}$ for a sample of galaxies (Kennicutt & Evans, 2012). The values are integrated over the whole galaxy. **Right**: Relation between $\Sigma_{\rm SFR}$ and $\Sigma_{\rm gas}/t_{\rm ff}$ including also molecular clouds (Krumholz et al., 2012)

the local gas density, parametrized with the free-fall time $t_{\rm ff}$. The plot in the right panel of Fig. 1.16 shows the existence of a relation of the form

$$\Sigma_{\rm SFR} \propto \frac{\Sigma_{\rm gas}}{t_{\rm ff}} \ , \tag{1.109}$$

including galaxies of different kinds and GMCs in the Milky Way.

Star formation proceeds as long as there is cold gas available. However, radiation from newly formed stars heats the gas preventing its collapse, while winds and supernovae can destroy completely the parent GMC. Hence, we expect SFE to be significantly lower than 100%, and observations confirm that only a few per cent of the initial gas mass is converted into stars (Williams & McKee, 1997; Carpenter, 2000; Evans et al., 2009; García et al., 2014; Lee et al., 2016; Chevance et al., 2019). There are two theories to explain such an inefficient star formation: (1) GMCs are short-lived, destroyed by the effect of feedback in less than 10 Myr (Elmegreen, 2000; Hartmann et al., 2001; Kruijssen et al., 2019; Chevance et al., 2019) (2) GMCs can be long-lived, but turbulence is constantly nourished so that the gas is not able to collapse (simulations with driven turbulence are shown by Federrath & Klessen, 2012; Padoan et al., 2012). This point will be explored with a numerical simulation in Cap. 5.

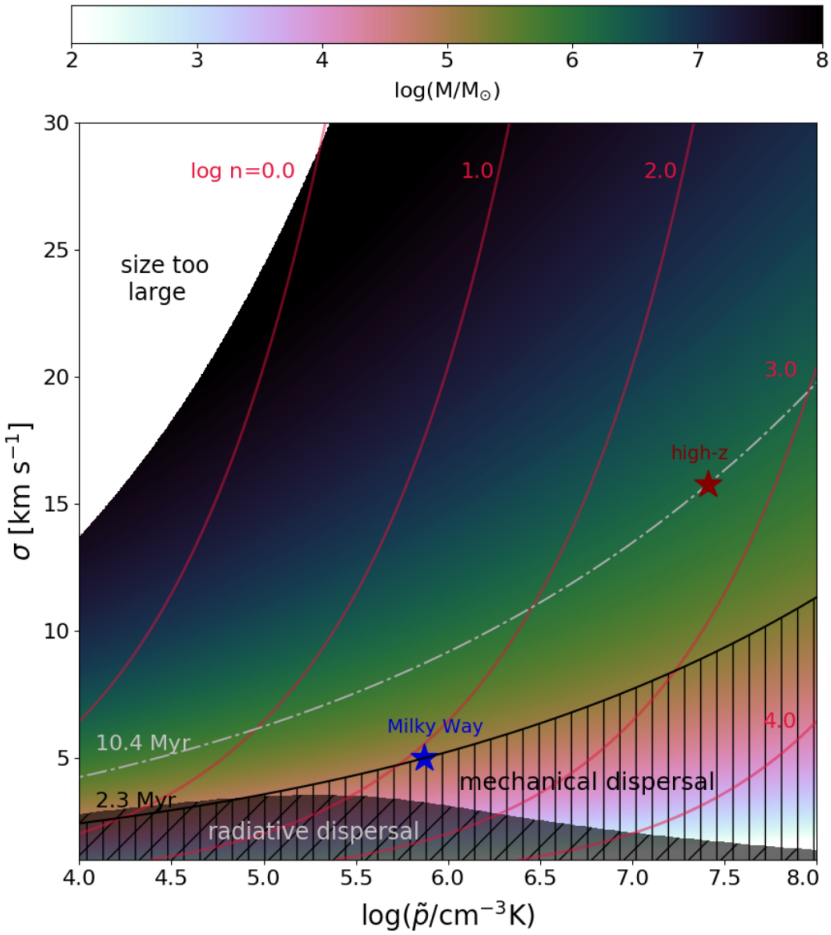

Figure 1.17: Summary of GMC properties in the $P - \sigma$ plane, with the colorbar showing the cloud mass. The white region corresponds to cloud with unrealistic size (> 1 kpc). The dark grey region highlights clouds dispersed by the development of an HII region within 4 Myr, and the vertically hatched region stands for clouds mechanically (winds and SNe) dispersed within 2.3 Myr. Red lines mark the clods with number density $\log n = 0, 1, 2, 3$ and 4. Finally, the two star symbols mark the position in the diagram of a typical Milky Way cloud ($\sigma = 5\,\mathrm{km\,s^{-1}}$, $\tilde{P} = 10^{5.87}\,\mathrm{cm^{-3}K}$). See text and Sommovigo et al. (prep) for a more detailed description of the plot.

1.9.1 Analytical model for cloud dispersal

In Sommovigo et al. (prep), we have developed a simple analytical model to estimate the cloud lifetime and the cloud emission properties, focusing in particular on dust distribution and temperature. A GMC is modeled as a homogeneous sphere with density ρ, r.m.s. velocity dispersion σ and thermal pressure P. Assuming that cloud mass M is exactly the Jeans mass at density ρ, and $\alpha_{\rm vir} = 5/3$, the following relations can be derived:

$$M = \frac{1}{2}\frac{\sigma^4}{\sqrt{G^3 P}} \qquad R = \frac{1}{2}\frac{\sigma^2}{\sqrt{GP}} \qquad n_{\rm H} = \frac{1}{2\mu m_p}\sqrt{\frac{P}{G}} \tag{1.110}$$

where $\mu = 2$ is the mean molecular mass (considering only H_2). The SFR inside the cloud is given by the Schmidt-Kennicutt relation:

$$\mathrm{SFR} = \eta \frac{M}{t_{\mathrm{ff}}} = \frac{1}{2}\eta \frac{\sigma^3}{G} = 10^{-5.9} \sigma_{\mathrm{kms}}\, \mathrm{M}_\odot\, \mathrm{yr}^{-1} \ , \tag{1.111}$$

where σ has been expressed in units of $\mathrm{km\,s^{-1}}$. Here the value $\eta = 0.01$ is assumed for the efficiency of gas conversion into stars (Krumholz & Tan, 2007). Using the population synthesis code STARBURST99 (Leitherer et al., 1992) and the Geneva tracks (Schaerer et al., 1993) to derive the rate of ionizing photons emitted, we obtain a Strömgren radius (eq. 1.80)

$$R_{\mathrm{s}} = 0.14 \sigma^{7/3} P^{-2/3} = 3.7 \times 10^{-3} \sigma_{\mathrm{kms}}^{7/3} \tilde{P}_8^{-2/3} \ , \tag{1.112}$$

with P in units of $10^8\, k_{\mathrm{B}}\, \mathrm{K}$. If $R_{\mathrm{s}} > R$, the GMC is destroyed by the ionization front itself in a timescale given by the recombination time $t_{\mathrm{rec}} \simeq (n_e \alpha_{\mathrm{B}})^{-1} < 2 \times 10^4$ yr. Otherwise, when $R_{\mathrm{s}} < R$, the HII region starts expanding and the GMC could be dispersed in the D-type phase of the ionization front. The analytical model by Raga et al. (2012) gives the stalling radius of the ionization front, that must be compared with R to determine whether the cloud is dispersed or not.

Stellar winds and supernovae (SNe) are also able to destroy the GMC. The number of SNe as a function of time is

$$N_{\mathrm{SN}}(t) = \nu_{\mathrm{SN}} \mathrm{SFR} t \simeq 0.02 \sigma_{\mathrm{kms}}^3 t_{\mathrm{Myr}}\, \Theta(t - t_{\mathrm{SN}}) \ , \tag{1.113}$$

using $\nu_{\mathrm{SN}} \simeq (53\, M_\odot)^{-1}$ for the number of SNe per solar mass (Ferrara & Tolstoy, 2000). Θ is the Heavyside step function, which is zero for all times $t > t_{\mathrm{SN}}$, where $t_{\mathrm{SN}} \simeq 3$ Myr is the time at which the first SNe explode. It follows that the total energy released in SNe is

$$E_{\mathrm{SN}}(t) = f_{\mathrm{SN}} E_0 N_{\mathrm{SN}}(t) \simeq 2 \times 10^{48} \sigma_{\mathrm{kms}}^3 t_{\mathrm{Myr}}\ \mathrm{erg} \ , \tag{1.114}$$

where $f_{\mathrm{SN}} \simeq 0.1$ is the kinetic-to-total energy efficiency and $E_0 = 10^{51}$ erg. Concerning the winds, $E_{\mathrm{w}} = \frac{1}{3} E_{\mathrm{SN}}$ is often assumed (for example in STARBURST99). The condition for the cloud destruction is

$$E_{\mathrm{SN}}(t) + E_{\mathrm{w}}(t) \leq \frac{1}{2} M v_e^2 \ , \tag{1.115}$$

where v_e is the cloud escape velocity, and from this expression a destruction timescale can be derived. Typical clouds in the Milky Way ($\tilde{P} \simeq 7 \times 10^5$ and $\sigma_{\mathrm{kms}} \simeq 5$) are dispersed by winds and SNe in around $t_{\mathrm{MW}} = 2.3$ Myr. On the other side, clouds in high redshift galaxies are more compact and turbulent ($\tilde{P} \simeq 3 \times 10^7$ and $\sigma_{\mathrm{kms}} \simeq 16$), so that the mechanical dispersal time is longer ($t_{\mathrm{high-z}} \simeq 10.4$ Myr).

Fig. 1.17 gives an overview of GMC properties, with pressure and velocity dispersion on the axis, color-coding for the cloud mass. The white area on the upper left corner corresponds to clouds with an unrealistic size ($R > 1$ kpc), and red lines indicate the cloud number

density. The dark grey region highlights clouds which are dispersed within 4 Myr (an arbitrary value between $t_{\rm MW}$ and $t_{\rm high-z}$): only relatively small and low turbulence clouds are dispersed by radiation. The vertically hatched region corresponds to mechanically dispersed clouds (by winds and SNe) within $t_{\rm MW}$, and finally the white line marks clouds mechanically dispersed within $t_{\rm high-z}$.

At high redshift ($5 \leq z \leq 10$), the SFR is usually probed via UV observations (Oesch et al., 2012; Finkelstein et al., 2012; Bouwens et al., 2016). Nevertheless, the observed UV flux will be attenuated by dust, and detailed calculations accounting for the dust density distribution in the cloud and its wavelength-dependent opacity show that $\tau_{\rm UV} \gg 1$ for typical high-z clouds. Therefore, it's only after the dispersal time $t_{\rm d}$ that radiation is free to escape, and this factor must be taken into account when inferring the SFR from UV measurements. An estimate of the obscured UV fraction is given by the following equation

$$f_{\rm UV}(t_{\rm d}) = \frac{\int_0^{t_{\rm d}} L_{1500\,{\rm nm}}(t)\,{\rm d}t}{\int_0^{\infty} L_{150\,{\rm nm}}(t)\,{\rm d}t}\ , \tag{1.116}$$

which gives $f_{\rm UV} \simeq 0.42$ for our fiducial high-z GMC.

1.10 Galaxies and outflows

A galaxy is an astrophysical system consisting of baryons, in the form of gas (as the ISM) and stellar matter (stars and stellar remnants), and the dark matter halo. From a morphological point of view, different types of galaxies are observed:

- Spiral galaxies have a disk-like appearance, and in some cases a central spheroidal component (called bulge) or dynamical features as bars are found
- Elliptical galaxies do not show any structural features in their brightness distribution, with total luminosities ranging from the most bright galaxies observed to dwarf galaxies;
- Lenticular galaxies with intermediate properties between spiral and elliptical galaxies, showing a large scale disk but no spiral arms.
- Irregular galaxies, lacking both a dominant bulge and a rotational symmetry.

Some galaxies show a central region with peculiar features, as a high bolometric luminosities ($10^{45-48}\,{\rm L}_\odot$) and a broad spectrum extending up to X and γ rays, called Active Galactic Nucleus (AGN). According to the most widely accepted model, an AGN consists of a super massive ($M > 10^5\,{\rm M}_\odot$) black hole (SMBH) accreting material through an accretion disk (Netzer, 2015).

Analysing the distribution of galaxies in the color-magnitude diagram, two families can be identified (Madgwick et al., 2002; Kauffmann et al., 2003; Wyder et al., 2007):

- Red sequence: high-mass spheroidal galaxies, with low star formation rate and high bolometric luminosity (absolute magnitude < -20);
- Blue sequence: star-forming low-mass galaxies, generally dominated by a disk component.

Observations seem to give evidence that the blue sequence galaxies are more abundant at redshift $z > 1$ (Wolf et al., 2003; Bell et al., 2004), hence suggesting an evolution of galaxies with cosmic time, from the blue sequence to the red sequence. A possible explanation for the transition between the two sequences, at least for more massive galaxies, consists in quenching due to feedback from the stars and the SMBH.

Furthermore, the kinematical properties of galaxies are seen to be connected to SMBH hosted at their center: for example, there are relations between the SMBH mass and the stellar velocity dispersion, known as $M - \sigma$ relation (Ferrarese & Merritt, 2000; Gebhardt et al., 2000; Kormendy & Ho, 2013), or between the SMBH mass and the bulge mass (Häring & Rix, 2004). The emergence of these correlations suggests and interplay between the SMBH and its host galaxy, that can happen for example through outflows from the central region of the galaxy. AGN-driven outflows could sweep the surrounding gas and affect the properties of the whole galaxy, and this process could be able to quench star formation, hence explaining the transition from gas-rich starburst galaxies to quiescent elliptical galaxies (Bell et al., 2003; Faber et al., 2007; Gutcke et al., 2017).

1.10.1 AGN-driven outflows

Galactic outflows are thought to be a possible mechanism to quench star formation in galaxies, by sweeping away the gas from the central region, and hence being responsible for the transition of galaxies from the blue to the red sequence. Observational evidence of the existence of AGN-powered outflows has become possible thanks to the modern high-resolution X-ray observatories, such as Suzaku, Chandra and XMM-Newton. Observations have detected the so-called ultra fast outflows (UFOs), consisting in ionized gas moving at velocities up to 10% the speed of light. The first UFO was found by XMM-Newton analysing radiation with energy above 1 keV of PG1211+143. The main features of the spectrum were blue-shifted absorption lines of highly ionized metals, providing evidence of fast ionized outflows: in particular, the Doppler shifted Lyα line of iron indicated a speed of about $0.09\,c$ (Pounds et al., 2003). After this first example, many other observations reported evidences for the existence of UFOs, and lists of the related objects are for example included in Cappi et al. (2006) and Tombesi et al. (2010).

More recent observations have been able to asses the presence of a cold phase in AGN-driven outflows. In the local universe it's possible to obtain, via interferometric techniques, maps of CO millimiter emission (Feruglio et al., 2010; Dasyra & Combes, 2012; Morganti et al., 2013; Combes et al., 2013; Sakamoto et al., 2014; García-Burillo et al., 2015; Mor-

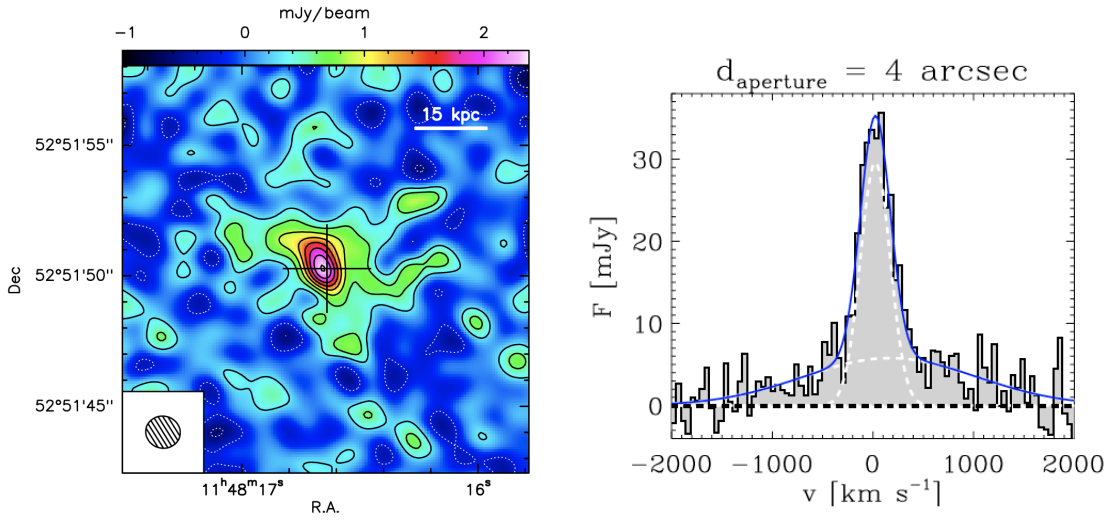

Figure 1.18: Observation of the [CII] 158 μm emission line in the galaxy SDSS J1148+5251, obtained with high sensitivity IRAM Plateau de Bure Interferometer in Cicone et al. (2015). **Left**: Continuum-subtracted of the total [CII] emission, integrated within $v \in (-1400, 1200)\,\mathrm{km\,s^{-1}}$. Right: velocity profile of the continuum-subtracted [CII] emission, obtained with the 4 arcsec aperture. The profile can be fitted using a Gaussian for the narrow component, tracing quiescent gas, and a Gaussian for the broad component, tracing the outflowing gas.

Object	$\log M_{\mathrm{H_2,OF}}$ $[\mathrm{M_\odot}]$	$\dot{M}_{\mathrm{H_2,OF}}$ $[\mathrm{M_\odot\,yr^{-1}}]$	R_{OF} [kpc]	$v_{\mathrm{OF,avg}}$ $[\mathrm{km\,s^{-1}}]$	$v_{\mathrm{OF,max}}$ $[\mathrm{km\,s^{-1}}]$	Refs.
(1)	(2)	(3)	(4)	(5)	(6)	(7)
IRAS F08572+3915	8.61	1210	0.82	800	1200	1
IRAS F10565+2448	8.37	300	1.10	450	600	1
IRAS 23365+3604	8.17	170	1.23	450	600	1
Mrk 273	8.24	600	0.55	620	900	1
IRAS F23060+0505	≤ 9.56	≤ 1500	≤ 4.05	(550)	(1100)	1
Mrk 876	≤ 9.48	≤ 1830	≤ 3.55	(700)	(1700)	1
I Zw 1	≤ 7.67	≤ 140	(0.50)	(500)	(750)	1
Mrk 231	8.47	1050	0.60	700	1000	2
NGC 6240	8.61	800	0.65	400	500	3
NGC 1068	7.26	84	0.10	150	250	4

Table 1.4: Information inferred by observation of a set of active galaxies. Columns: (1) name, (2) mass of the molecular gas in the outflow, (3) molecular outflow mass rate, (4) radial extension of the outflow, (5) average speed of the outflow, (6) maximum speed of the outflow, (10) references: 1. Cicone et al. (2014) 2. Cicone et al. (2012), 3. Feruglio et al. (2013), 4. Krips et al. (2011). Table from Cicone et al. (2014).

ganti et al., 2015) and also other molecules, as OH (Fischer et al., 2010; Sturm et al., 2011; Veilleux et al., 2013; Spoon et al., 2013; Stone et al., 2016; González-Alfonso et al., 2017), H_2O (Alatalo et al., 2011; Feruglio et al., 2015) and HCN (Aalto et al., 2012a, 2015; Walter et al., 2017). Furthermore, the high-resolution spectroscopy allows to map the emission in space, thus giving information on the mass and the radial extension of the molecular outflow. Molecular lines are too weak to be observed in distant sources, as high redshift galaxies. Nevertheless, the [CII] 158 μm line has been detected in many objects (Maiolino et al., 2005; Janssen et al., 2016), and it is believed to be a tracer of neutral gas, such as the gas present in PDRs (Pineda et al., 2013). Some observations have also been able to spatially resolve the [CII] (Maiolino et al., 2012; Cicone et al., 2015), showing extended structures up to ~ 1 kpc. An example is given by the observation of the source SDSS J1148+5251 by Cicone et al. (2015), shown in the left panel of Fig. 1.18. On the right panel, the velocity distribution of [CII]-emitting gas is shown: a single Gaussian is not able to fit the velocity profile, meaning that an additional gas component is present which is not co-rotating with the galactic disk. The so-called broad wings are fitted with a Gaussian with larger σ, and represent gas moving at very high velocity, indeed interpreted as outflowing gas. A review of current observation of molecular outlflow properties has been done for example by Cicone et al. (2014) and Fluetsch et al. (2019): as we can see from Tab. 1.4, molecular gas is present up to radii of about 1 kpc, with a mass rate of many hundreds of solar masses per year.

The presence of molecular gas within a hot outflow is a challenging problem, and both its origin and its evolution are still not understood. Concerning the origin of the molecular gas, there are two possible scenarios:

1. molecular clouds are already present in the surrounding of the AGN, and are accelerated from the AGN-driven wind;
2. gas manages to cool within the outflow, and patches of gas condense to form molecular clouds.

The first picture appears problematic because GMCs could be destroyed in the acceleration process. Ferrara & Scannapieco (2016) show that dense clouds are rapidly ablated when hot gas flows past them, in a timescale much shorter than the outflow lifetime. Hence it would be impossible to explain the presence of molecular gas far from the central region (Richings & Faucher-Giguère, 2018a,b). On the other hand, the second scenario provides a mechanism to form cold clumps in the outflow as it moves further from the center. The following section shows a theoretical model for the structure of an outflow, inspecting the possibility of fast cooling and condensation of gas into clumps. Nevertheless, even if a model for molecular gas formation is provided, it must be considered that the radiation

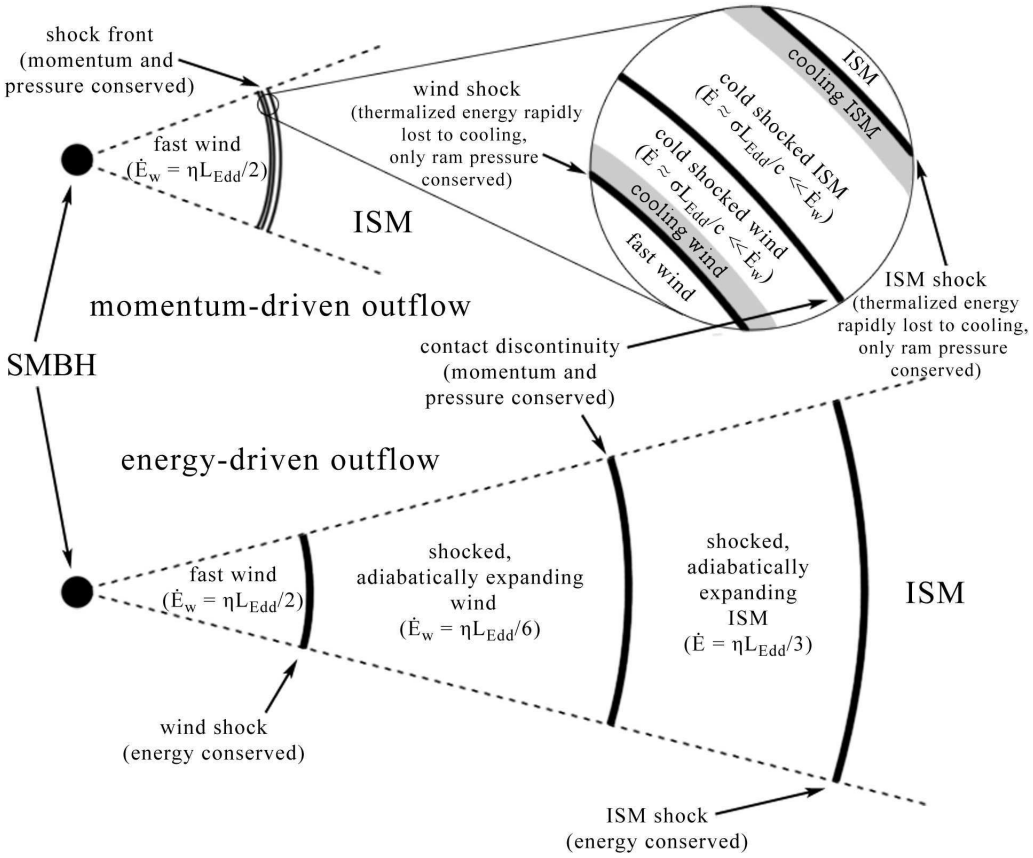

Figure 1.19: Representation of an isothermal (top figure) and an adiabatic (bottom figure) outflow. In the isothermal outflow, the reverse-shocked wind cools rapidly and doesn't expand, so that the thin layer just communicates the ram pressure of the wind to the ISM. In the adiabatic case energy is not lost, resulting in a powerful outflow with higher momentum. Figure from King & Pounds (2015).

field form the AGN can dissociate and ionize the gas. Hence, in order to explain the observation of molecular gas within outflows, the photoevaporative effect of radiation must be taken into account: an in-depth analysis of this issue is pursued in Chap. 3.

1.10.2 King model of an outflow

A theoretical model for the structure of an AGN outflow has been proposed by King (2003); King & Pounds (2003). In this model, radiation pressure pushes the gas in the immediate vicinity of the AGN, generating an ultra-fast wind, which in turn impacts the outer ISM initially at rest. The ISM is then put into motion by the shock wave due to the collision, and this gas makes up the large-scale AGN outflows.

Consider a quasar with luminosity approximately the same as its Eddington luminosity, i.e. such that radiation pressure exactly balance the gravitational attraction on the

surrounding gas:

$$L_{\rm EDD} = \frac{4\pi G M m_p c}{\sigma_{\rm T}} \simeq 3.2 \times 10^4 \left(\frac{M_{\rm BH}}{M_\odot}\right) L_\odot \ , \tag{1.117}$$

where m_p is the proton mass, c is the speed of light, $\sigma_{\rm T}$ is the cross section of Thomson scattering and $M_{\rm BH}$ is the SMBH mass. The momentum transferred to the surrounding gas via radiation pressure is

$$\dot{M}_w v \simeq \frac{L_{\rm EDD}}{c} \ , \tag{1.118}$$

where $\dot{M}_w$ is the wind mass flux and v is the terminal wind velocity, assuming that the scattering optical depth is $\tau \sim 1$ (King, 2003), i.e. each photon scatters once before escaping. This wind impacts the interstellar medium (ISM) of the galaxy, which is initially uniform and at rest, with a velocity $v \simeq \eta c$. The collision generates a shock propagating into the ISM, speeding it up, and a reverse shock into the wind itself, while the contact discontinuity between the wind and the ISM continues to move forward. Depending on the efficiency of cooling mechanisms in the gas, the reverse shock can be considered isothermal or adiabatic. Because of the very high temperature of the reverse-shocked wind and the presence of an intense radiation field, we expect inverse Compton cooling to be very a efficient way of cooling the gas. King (2003) computes the shocked wind temperature ($10^{10} \div 10^{11}$ K) and the timescale for Compton cooling of the electrons in the wind:

$$t_{\rm C} \simeq 10^5 \, R_{\rm kpc}^2 \left(\frac{c}{v}\right)^2 M_8^{-1} \, {\rm yr} \ , \tag{1.119}$$

where $M_8 = M_{\rm BH}/10^8 \, M_\odot$ and $R_{\rm kpc}$ is the distance from the black hole expressed in kpc. If the flow timescale is

$$t_{\rm F} = 8 \times 10^6 \, R_{\rm kpc} \sigma_{200} M_8^{-1/2} \, {\rm yr} \tag{1.120}$$

cooling is efficient only when $t_{\rm C} < t_{\rm F}$, that means within a critical radius

$$R_{\rm C} \simeq 500 \, M_8^{1/2} \sigma_{200} \, {\rm pc} \ . \tag{1.121}$$

It is then possible to identify two different regimes of the outflow: an isothermal momentum-driven outflow when $R < R_{\rm C}$ and an adiabatic energy-driven outflow when $R > R_{\rm C}$. Since an outflow can originate close to the black hole, we expect it to be isothermal and then to switch to being adiabatic when it reaches the critical radius.

The total mass within a radius is given by

$$M(R) = 4\pi \int_0^R \rho(r) r^2 {\rm d}r = \frac{2 f_g \sigma^2 R}{G} \ , \tag{1.122}$$

assuming an isothermal density distribution $\rho(r)$ (Keeton & Kochanek, 1998) with velocity dispersion σ. If considering only the gas mass, a factor $f_g \simeq 0.16$ (Spergel et al., 2003) is introduced: $M_g(R) = f_g M(R)$. When the wind reaches radius R, it means that all the ISM gas mass up to R has been swiped by the wind, and then it is compressed in a shell

ahead of the wind. The pressure in the post-shock wind gas for a strong isothermal shock is (see Dyson & Williams (1997))

$$P = \rho_w v_w^2 \ , \tag{1.123}$$

so that the force on the shell is given by

$$F = 4\pi R^2 P = (4\pi R^2 \rho_w v_w) v_w = \dot{M}_w v_w = \frac{L_{\rm EDD}}{c} \ . \tag{1.124}$$

Thus, the equation of motion of the gas shell is

$$\frac{\mathrm{d}}{\mathrm{d}t}[M_g(R)\dot{R}] + \frac{GM_g(R)[M_{\rm BH} + M(R)]}{R^2} = \frac{L_{\rm EDD}}{c} \tag{1.125}$$

which simplifies to

$$\frac{\mathrm{d}}{\mathrm{d}t}(R\dot{R}) + \frac{GM_{\rm BH}}{R} = -2\sigma\left(1 - \frac{M_{\rm BH}}{M_\sigma}\right) \tag{1.126}$$

defining

$$M_\sigma = \frac{f_g \kappa}{\pi G^2}\sigma^4 \simeq 3.2 \times 10^8 \, M_\odot \sigma_{200}^4 \ . \tag{1.127}$$

For large R the equation gives

$$\dot{R}^2 \simeq -2\sigma^2\left(1 - \frac{M_{\rm BH}}{M_\sigma}\right) \ . \tag{1.128}$$

Notice that this is impossible if $M_{\rm BH} < M_\sigma$, which means that the outflow doesn't make it to large R at all. Nevertheless the black hole is accreting mass, then it will be able to swipe the surrounding gas away when it is grown to a mass M_σ. This also means that, once the black hole reaches M_σ, then it stops accreting because all the gas is swiped away. The relation (1.127) is very close to the observational $M - \sigma$ relation, suggesting that outflows can regulate the SMBH growth.

When the mass of the SMBH is larger than the critical mass M_σ, outflows are able to reach an arbitrary large radius. This means that for $R > R_{\rm C}$ the gas wind is no longer efficiently cooled, and the outflow can be approximated to be adiabatic. The equation of motion is

$$\frac{\mathrm{d}}{\mathrm{d}t}[M_g(R)\dot{R}] + \frac{GM_g(R)M(R)}{R^2} = 4\pi R^2 \ , \tag{1.129}$$

where this time we have neglected the black hole mass. P is determined by the energy conservation equation:

$$\frac{\mathrm{d}}{\mathrm{d}t}U_{\rm th} = \dot{E}_{w,\rm kin} - P\frac{\mathrm{d}V}{\mathrm{d}t} - F_{\rm grav}\dot{R} \ , \tag{1.130}$$

where (defining $\eta = v/c$):

$$U_{\rm th} = \frac{4}{3}\pi R^3 \cdot \frac{3}{2}P \, , \tag{1.131}$$

$$\dot{E}_{w,\rm kin} = \frac{1}{2}\dot{M}_w v^2 = \frac{\eta}{2}L_{\rm EDD} \ , \tag{1.132}$$

$$F_{\rm grav} = \frac{GM_g(R)M(R)}{R^2} = 4f_g\frac{\sigma^4}{G}\dot{R}\ . \tag{1.133}$$

Substituting P from (1.129) into (1.130), after some algebra we get

$$\frac{\eta}{2}L_{\rm EDD} = \frac{2f_g\sigma^2}{G}\left[\frac{1}{2}R^2\dddot{R} + 3R\dot{R}\ddot{R} + \frac{3}{2}\dot{R}^3\right] + 10f_g\frac{\sigma^4}{G}\dot{R}\ . \tag{1.134}$$

The equation has a solution of the form $R = v_e t$ with v_e satisfying

$$2\eta c = 3\frac{v_e^3}{\sigma} + 10v_e\ . \tag{1.135}$$

The assumption $v_e \ll \sigma$ leads to the contradiction $v_e \simeq 0.01c \gg \sigma$, then assuming $v_e \gg \sigma$ we get the following expression for v_e:

$$v_e \simeq \left[\frac{2}{3}\eta\sigma^2 c\right]^{1/3} \simeq 925\,\sigma_{200}^{2/3}\,{\rm km/s}\ . \tag{1.136}$$

From the physics of shocks, Zubovas & Nayakshin (2014) compute post-shock ISM temperature and density:

$$T_{\rm sh} \simeq 2.2\times10^7\,\sigma_{200}^{4/3}f^{-2/3}\,{\rm K}\ , \tag{1.137}$$

$$n_{\rm sh} \simeq 60\,\sigma_{200}^2 f R_{\rm kpc}^{-2}\,{\rm cm}^{-3}\ , \tag{1.138}$$

where f is the ratio of f_g to the cosmological mean value 0.16 (Spergel et al., 2003).

1.10.3 Molecular gas in outflows

The presence of molecular gas in quasar outflows (in the adiabatic phase, so that the gas can reach kpc-distance from the central region) is a problem in principle, because the temperature of the shocked gas is so high that molecules would be collisionally dissociated (the binding energy in H_2 is roughly 4.52 eV, which corresponds to about $50,000$ K). Thus, efficient cooling mechanisms must operate, so that a fraction of gas is put in molecular form, and in the following we will see the conditions for the gas to be stable in two different phases.

Following Zubovas & Nayakshin (2014), cooling mechanisms that should be taken into account are Compton cooling, bremsstrahlung and line cooling. However, the shocked gas is at a temperature similar to Compton temperature for radiation in the extreme UV

$$T_C(h\bar{\nu}\simeq10^3\,{\rm eV}) = \frac{h\bar{\nu}}{4k_{\rm B}} \simeq 3\times10^6\,{\rm K}\ . \tag{1.139}$$

Then we do not expect Compton cooling to be relevant to the purpose of decreasing the gas temperature to about 10^4 K .

Zubovas & Nayakshin (2014) integrated the cooling function by Raymond et al. (1976), appropriate for a fully ionized optically thin plasma, over a dynamical time R/σ, to find the final temperature of the gas for values of gas fraction f_g from 1.6×10^{-3} to 1 and for

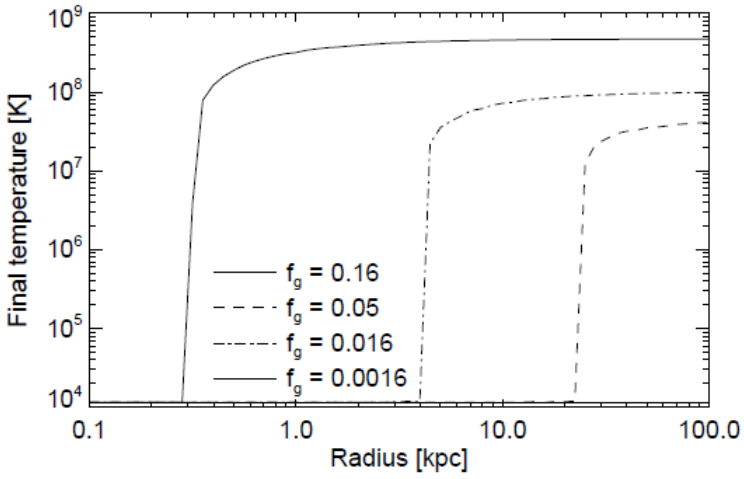

Figure 1.20: Final temperature of the shocked ISM gas as a function of radius for different values of gas fraction f_g. We can see that two-body processes are able to cool the gas to temperatures lower than 10^5 K to a certain radius, depending on the gas fraction. Figure from Zubovas & Nayakshin (2014).

distances R from 0.1 kpc to 100 kpc. The result for the final temperature as a function of the radius is plotted in Fig. 1.20. The radius up to which gas efficiently cools is found to be

$$R_{\rm cool} = 100 f^{1.5} \text{ kpc} . \tag{1.140}$$

The outflow becomes energy-driven at a distance $R_{\rm C}$ given by eq. 1.121, and clump formation could indeed happen at the discontinuity-interface because of Raylegh-Taylor instabilities. Since $R_{\rm cool} \gg R_{\rm C}$, then clumps can form just as the outflow becomes energy-driven and then be carried with it to an arbitrary distance.

Zubovas & Nayakshin (2014) also computed the gas temperature as a function of time, and the results are shown in Fig. 1.21. The gas cools to sufficiently low temperatures (as molecules formation concerns) in a sufficient short time with the respect to its dynamical timescale. The cooling time found in this way can be expressed as

$$t_{\rm cool} \simeq 0.017\, R_{\rm kpc}^2 f^{-1.75} \text{ Myr} . \tag{1.141}$$

After that bremsstrahlung and ion line cooling have sufficiently cooled the gas, atomic and molecular line cooling comes into play. In fact it is efficient at temperatures lower than 10^4 K, and operates to further cool the gas, putting it in molecular form. As an order of magnitude $\Lambda_{\rm at}(T) \simeq 10^{-25}$ erg cm^3 s^{-1}, and the cooling rate is given by $n_{\rm at}^2 \Lambda_{\rm at}(T) \simeq$, where the number density of the cooling patches in the post-shocked gas is approximately $n_{at}(T) \sim (T_{\rm sh}/T) n_{\rm sh}$ with the $n_{\rm sh}$ and given $T_{\rm sh}$ in eqs. 1.138 and 1.137. Then we have

$$n_{\rm at}^2 \Lambda_{\rm at}(T) = 3.6 \times 10^{-22}\, R_{\rm kpc}^{-4} f^2 \left(\frac{T_{\rm sh}}{T}\right)^2 \sigma_{200}^4 \text{ erg s}^{-1} \tag{1.142}$$

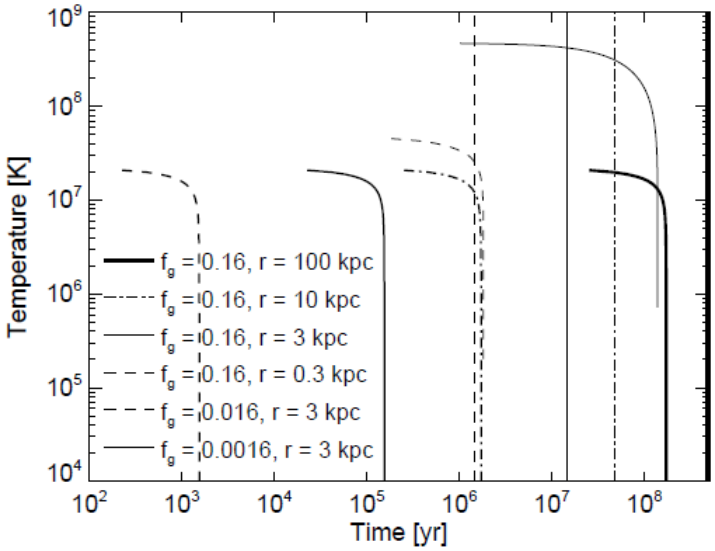

Figure 1.21: Temperature of the shocked ISM gas as a function of time for different values of gas fraction f_g and radii r. Vertical lines represent the dynamical times for corresponding values of radii (with the same line style). The gas cools in a time shorter than the dynamical timescale. Figure from Zubovas & Nayakshin (2014).

and a corresponding approximate cooling timescale

$$t_{\rm cool,at} \simeq \frac{3n_{at}kT}{\Lambda_{at}} \simeq 24 \left(\frac{T}{10^4\,{\rm K}}\right)^2 R_{\rm kpc}^2 f^{-1/3} \sigma_{200}^{-10/3}\ {\rm yr}\ , \tag{1.143}$$

which is much shorter than the dynamical timescale for any value of R of interest, implying that gas cooling to few K could indeed occur in the outflow.

Nevertheless, a low temperature is not a sufficient condition for the formation of molecules, since the formation of H_2 requires the presence of dust grains (see Sec. 1.2.2). Ferrara & Scannapieco (2016) show that dust is destroyed in the outflow, though a two-step process. Initially, dust undergoes an erosion due to the passage of the wind-driven shock wave: from the results obtained by Dwek et al. (1996), it follows that only 45% of dust mass survives after 340 yr during the passage though a 2000 km s^{-1} shock. When the dust grains are embedded in the hot post-shock gas, they are eroded because of thermal sputtering. The size decrease of a dust grain is described by the following equation close to results by Dwek et al. (1996), Draine & Salpeter (1979) and Tsai & Mathews (1995):

$$\frac{{\rm d}a}{{\rm d}t} = -AnT_6^{-1/4} e^{BT_6^{-1/2}}\ , \tag{1.144}$$

where T_6 is the temperature in units of 10^6 K and the values of the parameters are $A = 1.2 \times 10^{-5}\,\mu{\rm m\,yr^{-1}}$ and $B = 3.85$. Ferrara & Scannapieco (2016) implemented dust grain destruction in their simulation of quasar outflows, obtaining that dust is completely destroyed in $\sim 10^4$ yr. Since H_2 cannot form in absence of dust grains, molecule formation within the outflow remains a challenging problem which is currently not yet understood.

Chapter 2

Numerical Simulations

2.1 Hydrodynamical simulations with ramses

Astrophysical systems, from the small scales of planets and stars to large scale structures, are too complex to allow for an analytical description. The number of physical effects to be included spans from fluid dynamics, gravitational interaction, cooling and heating processes, radiation emitted by stars, chemical reactions, as we have seen in the previous section. As a consequence, it is impossible to give a satisfying description of any system with simple models, and numerical simulations are becoming the new work-horse in theoretical studies. Thanks to the increasing computational power available, it is now possible to run simulations including a large number of physical effects and with an unprecedented resolution.

Many codes have been developed in the last 50 years, exploiting different algorithms and numerical techniques. Hydro codes are mainly classified in two great families: (1) smoothed-particle hydrodynamics (SPH) codes, as for example GASOLINE (Wadsley et al., 2004), GADGET (Springel et al., 2001), GIZMO (Hopkins, 2015), and (2) grid-based codes, as for example RAMSES (Teyssier, 2002), ATHENA (Stone et al., 2008), FLASH (Fryxell et al., 2000), ENZO (Bryan et al., 2014). In SPH codes, the fluid is discretized in a a number of elements, called particles, and the properties of the fluid in a particular position are computed from a weighted average over the properties of nearby particles. On the other side, grid codes base on a fixed grid with fluid properties computed at each cell center and evolved with time according to fluid equations. Adaptive mesh refinement (AMR) codes are an improvement of standard grid codes, where the resolution is increased in specific spatial regions according to some refinement criterion.

RAMSES is an AMR code developed by Teyssier (2002), based on the same N-body solver of the ART code (Kravtsov et al., 1997). Interstellar gas is treated as a fluid, obeying

Euler equations with pressure and gravitational terms:

$$\partial_t \rho + \nabla \cdot (\rho \mathbf{v}) = 0 \tag{2.1a}$$

$$\partial_t (\rho \mathbf{v}) + \nabla (\rho \mathbf{v} \otimes \mathbf{v}) + \nabla P = -\rho \nabla \Phi \tag{2.1b}$$

$$\partial_t (\rho \mathrm{e}) + \nabla \left[\rho \mathbf{v} \left(\mathrm{e} + \frac{P}{\rho} \right) \right] = -\rho \mathbf{v} \cdot \nabla \Phi \tag{2.1c}$$

where ρ, $\mathbf{v}$, P, e and Φ are respectively density, velocity, pressure, total energy per unit mass and gravitational potential. The system is closed by the equation of state

$$P = (\gamma - 1) \left(\mathrm{e} - \frac{1}{2} \mathbf{v}^2 \right) \rho \ , \tag{2.2}$$

with Γ adiabatic index, assumed constant. Defining $U = (\rho, \rho \mathbf{v}, \rho \mathrm{e})$, the numerical discretization of the Euler equations is

$$\frac{U_i^{n+1} - U_i^n}{\Delta t} + \frac{F_{i+1/2}^{n+1/2} - F_{i-1/2}^{n+1/2}}{\Delta x} = S_i^{n+1/2} \ , \tag{2.3}$$

with the lower index indicating the cell, and the upper index indicating the timestep. The time-centered fluxes at the cell interfaces $F_{i\pm1/2}^{n+1/2}$ are computed using a second-order Godunov method (Godunov, 1959), and the source term is given by

$$S_i^{n+1/2} = \left(0, \frac{\rho_i^n \nabla \Phi_i^n + \rho_i^{n+1} \nabla \Phi_i^{n+1}}{2}, \frac{(\rho \mathbf{v})_i^n \cdot \nabla \Phi_i^n + (\rho \mathbf{v})_i^{n+1} \cdot \nabla \Phi_i^{n+1}}{2} \right) \ . \tag{2.4}$$

This scheme for the numerical solution of Euler equations is called MUSCL (Monotone Upstream-centered Scheme for Conservation Laws), and it is detailed in Colella (1990), Saltzman (1994) and Toro (2009).

Stars are considered as point particles, and their motion is predicted through an N-body solver.* The -Poisson equations

$$\frac{\mathrm{d}}{\mathrm{d}t} \mathbf{x}_\mathrm{p} = \mathbf{v}_\mathrm{p} \qquad \frac{\mathrm{d}}{\mathrm{d}t} \mathbf{v}_\mathrm{p} = -\nabla \Phi \qquad \nabla^2 \Phi = 4\pi G (\rho_\mathrm{gas} + \rho_\mathrm{stars}) \tag{2.5}$$

are solved on a grid using a standard PM (particle-mesh) scheme: (1) the mass density assigned to a cell is computed with a CIC (cloud-in-cell) interpolation scheme (Hockney & Eastwood, 1981), (2) Φ is computed on the grid, (3) the acceleration is computed with using a finite-difference approximation for the gradient, (4) the acceleration of every particle is computed with an inverse CIC scheme, (5) the velocity and then the position of each particle are updated with a second-order midpoint scheme (which is an evolution of the standard leapfrog scheme by Hockney & Eastwood, 1981).

*In cosmological simulations, particles are also used to represent dark matter.

In RAMSES, the time evolution is computed recursively, starting from the coarsest level $\ell_{\rm min}$ down to the finer level $\ell_{\rm max}$. At each level ℓ, the timestep is constrained by the CFL (Courant, Friedrich, Levy) stability condition:

$$\Delta t_\ell \leq C_{\rm cfl} \Delta x_\ell / \max(|v_x| + c_{\rm s}, |v_y| + c_{\rm s}, |v_z| + c_{\rm s}) \ , \tag{2.6}$$

where $c_{\rm s}$ is the sound speed, $C_{\rm cfl} < 1$ is the Courant factor, and the max is computed over all the cells. Since both the gas speed and the sound speed limit the simulation timestep, it follows that the simulation becomes very heavy when dealing with very fast flows (stellar winds, outflows) or very hot gas (radiation-heated gas, shocked gas).

2.2 Radiation hydrodynamic codes: ramsesrt

A first approach to analyse the effect of radiation sources in simulations is to post-process hydro simulations, assuming that each source emits a certain flux which is attenuated by the surrounding gas. Nevertheless this approach fails to account for the gas-radiation interaction, or radiative feedback: radiation heats the gas, producing a pressure increase, hence affecting the dynamics of the gas. In fact, the physics of radiative feedback is crucial to reproduce accurately many astrophysical phenomena in simulations, as outflows, the formation of HII regions and PDRs (see Sec. 1.7 and 1.8) or the re-ionization of the universe. However, coupled radiation-hydro simulations are computationally expensive, because of (1) the high-dimensionality of radiative transfer (spatial, angular and frequency-wise) and (2) the small timescale dictated by the speed of light (because of the CFL stability condition, eq. 2.6).

Radiative transfer (RT) has been implemented in astrophysical simulations following three approaches:

- ray-tracing (e.g. C^{2}RAY Mellema et al., 2006): each source shoots a number of rays, and the flux along each path is computed considering the optical depth of the cells crossed;
- Monte Carlo (e.g. CRASH Maselli et al., 2003): radiation is sampled with photon packets, the emission angle and the interaction point with the gas are determined statistically;
- Momentum-based (e.g. RAMSES-RT Rosdahl et al., 2013): taking angular moments of the RT equation, conservation laws similar to the Euler equations for fluids are obtained, and so they are solved in a similar way.

The RT version of RAMSES includes a momentum-based implementation of RT (Rosdahl et al., 2013), that we explain in more details in the following. The RT equation has the

form (Mihalas & Mihalas, 1984)

$$\frac{1}{c}\frac{\partial}{\partial t}I_\nu + \mathbf{n}\cdot\nabla I_\nu = -\kappa_\nu I_\nu + \eta_\nu \ , \tag{2.7}$$

where I_ν is the radiation specific intensity (in $\mathrm{ergs}^{-1}\mathrm{cm}^{-2}\mathrm{sr}^{-1}\mathrm{Hz}^{-1}$), κ_ν is an absorption coefficient and η_ν a source function. Taking the zero-th and first momenta over the angles, the equations for the evolution of the photon number density N_ν and the flux $\mathbf{F}_\nu$ are obtained:

$$\frac{\partial}{\partial t}N_\nu + \nabla\cdot\mathbf{F}_\nu = -\sum_j n_j\sigma_{\nu,j}cN_\nu + N_\nu^\star + N_\nu^{\mathrm{rec}} \tag{2.8a}$$

$$\frac{\partial}{\partial t}\mathbf{F}_\nu + \nabla\cdot\mathbb{P}_\nu = -\sum_j n_j\sigma_{\nu,j}c\mathbf{F}_\nu \tag{2.8b}$$

where $\mathbb{P}_\nu$ is the radiation pressure tensor, and the sum j is over the chemical species contributing to absorption. The photon source terms are due to stellar emission ($N_\nu^\star$) and recombination radiation (N_ν^{rec}). To close the set of differential equations, an expression for $\mathbb{P}_\nu$ is needed. In RAMSES-RT the M1 closure relation is adopted (Levermore, 1984): $\mathbb{P}_\nu = \mathbb{D}_\nu N_\nu$, where $\mathbb{D}_\nu$ is the Eddington tensor given by

$$\mathbb{D}_\nu = \frac{1-\chi_i}{2}\mathbf{I} + \frac{3\chi_i - 1}{2}\mathbf{n}_i\otimes\mathbf{n}_i \tag{2.9}$$

with

$$\mathbf{n}_i = \frac{\mathbf{F}_i}{|\mathbf{F}_i|} \qquad \chi_i = \frac{3+4f_i^2}{5+2\sqrt{4-3f_i^2}} \qquad f_i = \frac{|\mathbf{F}_i|}{cN_i} \ . \tag{2.10}$$

In the RAMSES-RT implementation, the solution of the RT equations is handled in threee steps (operator splitting strategy):

1. *Photon injection step.* Photon are injected from sources into the grid, updating the number of photons by $N^\star\Delta t$ at every timestep Δt in the cell where the source is located.
2. *Transport step.* Equations 2.8a and 2.8b are solved with RHS=0, using the following formulation: the general equation

$$\frac{\partial}{\partial t}\mathcal{U} + \frac{\partial}{\partial x}\mathcal{U} = 0 \tag{2.11}$$

is discretized as (for simplicity in 1D)

$$\frac{\mathcal{U}_\ell^{n+1} - \mathcal{U}_\ell^n}{\Delta t} + \frac{\mathcal{F}_{\ell+1/2}^n - \mathcal{F}_{\ell-1/2}^n}{\Delta x} = 0 \ , \tag{2.12}$$

where Δx is the cell size, the upper index is the timestep index and the lower one is the cell index. The 1/2 denotes an intercell flux, which can be computed in different ways: for example, in RAMSES-RT the HLL (Harten et al., 1983) and GLF (Global Lars Friedrich) functions are implemented.

3. *Thermochemical step.* Photons in each energy bin are absorbed in every cell, according

to its optical depth. The new chemical abundances are computed according to the flux in the cell: the original version of RAMSES-RT includes HI, HII, HeI, HeII and HeIII, but in the following sections we will show our custom version with more chemical species using the thermochemistry package KROME (Grassi et al., 2014).

2.3 The krome thermochemical package

An accurate treatment of chemistry is fundamental in modern astrophysical simulations. Not only it is interesting for the purpose of tracking the evolution of individual chemical species (and therefore giving an insight on line emission properties), but it also allows (1) to compute opacities and hence perform more accurate RT calculations, (2) to get a more accurate thermal state of the gas by including detailed cooling and heating mechanisms, with an effect also on gas pressure and hence its dynamics. Nevertheless, the inclusion of a chemical network often represents a challenging task. In the first place, even including a few species, the number of possible reactions can be huge, implying a complex set of coupled differential equations to be solved. As a consequence, the computational cost can be very high, especially when chemistry is included in an already complex code accounting for hydrodynamics and radiative transfer. KROME is a package which allows to solve chemical rate equations for a network provided by the user: a PYTHON pre-processor generates the FORTRAN subroutines that can be called from another code (in our case RAMSES).

The time evolution of the abundances of the different species is regulated by a system of ordinary differential equations (ODEs), which includes an equation for every species:

$$\frac{\mathrm{d}n_i}{\mathrm{d}t} = \sum_{j,\mathrm{form}} k_j \prod_r n_r - \sum_{j,\mathrm{destr}} k_j \prod_r n_r \ , \tag{2.13}$$

where n_i is the number density of the i-th species, which is increased by formation reactions (the first summation) and decreased by destruction reactions (the last summation). Each reaction has a rate coefficient k_j and can involve a different number of reactants with densities n_r. Rate coefficients are in general temperature-dependent, so that the equations for the species abundances are also coupled with the equation for the temperature:

$$\frac{\mathrm{d}T}{\mathrm{d}t} = (\gamma - 1)\frac{\Gamma(T, \mathbf{n}) - \Lambda(T, \mathbf{n})}{k_\mathrm{B} \sum_i n_i} \ , \tag{2.14}$$

where Γ and Λ are respectively the heating and cooling function ($\mathrm{erg\,cm^{-3}\,s^{-1}}$), dependent on temperature and the vector of all species densities ($\mathbf{n}$). γ is the adiabatic index and it is computed according to the abundance of each chemical species. For photoionizations and photodissociations respectively of the form

$$\mathrm{A} + h\nu \rightarrow \mathrm{A}^+ + \mathrm{e}^- \tag{2.15}$$

$$\mathrm{A} + h\nu \rightarrow \mathrm{B} + \mathrm{C} \tag{2.16}$$

the rates are given by (Glover & Abel, 2008; Grassi et al., 2012, 2014)

$$k = 4\pi \int_{E_0}^{\infty} \frac{I(E)\sigma(E)}{E} e^{-\tau(E)} \, \mathrm{d}E \ , \tag{2.17}$$

where E_0 is the activation (photon) energy of the reaction, $I(E)$ is the energy distribution of radiation, $\sigma(E)$ is the cross section, $\tau(E)$ is the gas optical depth and E is the photon energy.

The system of ODEs is often stiff, meaning that the values of dependent variables change with different scales, as a function of independent variables. Hence, a tailored solver is required to solve efficiently these kind of systems. KROME employs the DLSODES (Hindmarsh, 1983), which takes advantage of the sparsity of the Jacobian matrix associated to the system of ODEs (i.e. most of elements are zero). The solver requires a certain number of timesteps to find the solution for the species abundances, which depend on the initial densities of the species, the initial temperature and the radiation flux. This implies that in a 3D simulations, the solver could employ a different amount of time to perform the integration on each cell. This means that cells where the chemistry requires more timesteps act as a bottleneck, increasing considerably the computational load of the simulation.

KROME allows to set up any chemical network with an arbitrary number of species. In this Thesis, we are mainly interested in the evolution of the molecular component of the ISM, and its interaction with the radiation field from stars and quasars. Hence, we implemented with KROME a network focused on the formation and destruction on H_2. In total, 9 species are included: H, H^+, H^-, H_2, H_2^+, He, He^+, He^{++} and free electrons. The chemical network includes 46 reactions in total, featuring neutral-neutral reactions, charge-exchange reactions, collisional dissociation and ionization, radiative association reactions and cosmic ray-induced reactions (we consider a cosmic ray ionization rate $\zeta_{\mathrm{H}} = 3 \times 10^{-17}\,\mathrm{s}^{-1}$, the reference value in the Milky Way Webber, 1998). The reactions and the respective rates are taken from Bovino et al. (2016): reactions 1 to 31, 53, 54 and from 58 to 61 in Tab. B.1 and B.2, photoreactions P1 to P9 in Tab. 2. H_2 formation on dust is based on the Jura rate at solar metallicity $R_{\mathrm{f,H_2}} = 3.5 \times 10^{-17} n_{\mathrm{H}} n_{\mathrm{tot}}$ (see eq. 1.11). There are 9 reactions involving photons, listed in Tab. 2.1: photoionization of H, He, He^+, H^- and H_2 to H_2^+, direct photodissociation of H_2^+ and H_2 and the two-step Solomon process, with the rate by Richings et al. (2014a), as explained in Sec. 1.2.2. Photons emitted by recombination processes are neglected (on-the-spot approximation).

2.4 The coupling between ramses-rt and krome

KROME provides a pre-processor producing FORTRAN modules that can be implemented in any other framework code. In the present work, we have coupled such chemistry module

Photochemical reactions	
$H + \gamma \rightarrow H^+ + e$	$H_2^+ + \gamma \rightarrow H^+ + H$
$He + \gamma \rightarrow He^+ + e$	$H_2^+ + \gamma \rightarrow H^+ + H^+ + e$
$He^+ + \gamma \rightarrow He^{++} + e$	$H_2^+ + \gamma \rightarrow H + H$ (direct)
$H^- + \gamma \rightarrow H + e$	$H_2^+ + \gamma \rightarrow H + H$ (Solomon)
$H_2 + \gamma \rightarrow H_2^+ + e$	

Table 2.1: List of photochemical reactions included in our chemical network.

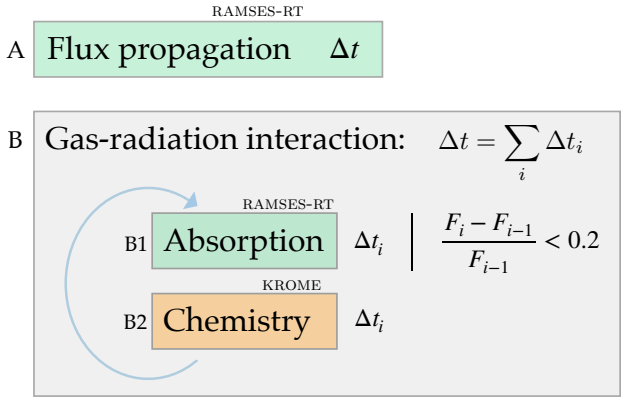

Figure 2.1: Diagram of the RAMSES-RT and KROME coupling. In each time step Δt, first the flux F is propagated without attenuation (A). Then, the gas-radiation interaction step is carried out (B), by sub-cycling in radiation absorption (B1) and chemical evolution (B2) steps (Decataldo et al., 2019). Each sub-step is evolved for a time Δt_i, that is chosen to assure a fractional variation <20% for the impinging flux.

with the radiative transfer module in RAMSES-RT. With respect to the default implementation of chemistry in RAMSES-RT, this approach allows (1) to include more chemical species (default RAMSES-RT evolves only H, He and corresponding ionized states), and (2) to propagate more accurately the radiation in each energy bin, by including all photoreactions involving the chemical species.

Fig. 2.1 summarises the approach we used to couple RT module with the chemical network (Decataldo et al., 2019; Pallottini et al., 2019; Decataldo et al., prep). At each timestep of the simulation (Δt), photons are first propagated from each cell to the nearest ones by RAMSES-RT (A). Then, the gas-radiation interaction step (B) is executed, sub-cycling in absorption (B1) and chemical evolution (B2) steps with a timestep $\Delta t_i < \Delta t$, such that the flux is not reduced by more than 20% at each substep (Δt_i).

In step B1, we account for (1) photons that take part in chemical reactions, (2) H_2 self-shielding and (3) dust absorption. The optical depth of a cell in the radiation bin i (excluding the Solomon process) is computed by summing over all photo-reactions:

$$\tau_i = \sum_j n_j \Delta x_{\rm cell} \sigma_{ij} \ , \tag{2.18}$$

where n_j is the number density of the photo-ionized/dissociated species in the reaction j, $\Delta x_{\rm cell}$ is the size of the cell, and σ_{ij} is the average cross section of the reaction j in the bin i. For the Solomon process, the self-shielding factor $S_{\rm self}^{\rm H_2}$ is taken from Richings et al. (2014b), and it is related to the optical depth by $\tau_{\rm self}^{\rm H_2} = -\log(S_{\rm self}^{\rm H_2})$. Absorption from dust is included, with opacities taken from Weingartner & Draine (2001). We have used the Milky Way size distribution for visual extinction-to-reddening ratio $R_V = 3.1$, with carbon abundance (per H nucleus) $b_C = 60$ ppm in the log-normal populations*. After every absorption substep, KROME is called in each cell (step B2): photon densities in each bin are passed as an input, together with the current chemical abundances and the gas temperature in the cell, and KROME computes the new abundances after a timestep accordingly.

In the following subsections, we perform two tests to validate our scheme for the coupling between RAMSES-RT and KROME:

- An ionized region, comparing the results with the analytical solution;
- The structure of H_2 in a PDR, compared with the standard benchmarks of Röllig et al. (2007).

2.4.1 Test A: HII region

As a first test of our version of RAMSES-RT coupled with KROME, we run a simulation of 1D slab of atomic gas invested by ionizing radiation. The test is aimed to check the coupling between radiative transfer and chemistry, hence we run in static mode, i.e. forcing the gas velocity in every cell to zero. The 1D computational domain has a size $L = 0.2$ pc, resolved with 1024 cells, and it is filled with neutral hydrogen, at a density of 100 $\rm cm^{-3}$.

The radiation field comes from the left side of the slab, with the spectrum of a black body source at a distance of 1 pc, discretised in 10 bins (delimited by 13.6, 18.76, 23.9, 29.1, 34.2, 39.4, 44.5, 49.8, 54.8, 60.0, 1000.0 eV). The geometrical flux reduction is not considered, while dust cross section is set to $\sigma_d = 2.94 \times 10^{-22}\,\rm cm^2$. We note that dust is not relevant since the column density in the whole slab is lower than $10^{20}\,\rm cm^{-2}$. The simulations are stopped at 1 kyr, i.e. longer than the recombination time $t_{\rm rec} \simeq n/\alpha_{\rm B}$.

The result is compared with a semi-analytical solution, obtained by dividing the slab of gas in 1024 cells and proceeding from the first cell to the n-th cell as follows:

1. compute the temperature T in the n-th cell, using heating and cooling function provided by Gnedin & Hollon (2012);

*https://www.astro.princeton.edu/~draine/dust/dustmix.html

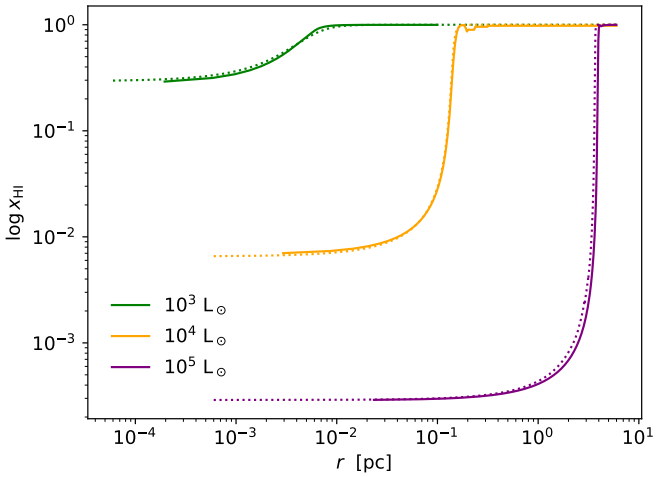

Figure 2.2: Neutral fraction as a function of depth, for a 1D gas slab with radiation coming from the left side. The source is a black body at a distance of 1 pc, and different colours stand for different bolometric luminosities. The solid lines show the results obtained with a simulation using the code RAMSES-RT coupled with KROME, while the dotted lines are obtained with a semi-analytical model. Plot from Decataldo et al. (2019).

2. compute the ionization fraction $x(T)$ in the n-th cell, according to

$$x(t) = \left(\frac{1}{n\alpha_{\rm B}(T)} \int_{13.6\,eV}^{\infty} F_\nu \, a_\nu \, {\rm d}\nu \right)^{1/2} , \tag{2.19}$$

   where n is the H nuclei number density, $\alpha_{\rm B}(T)$ is the case B recombination coefficient (taken from Abel et al., 1997), F_ν is the specific flux at the cell and a_ν is the photoionization cross section (values in Verner & Ferland, 1996).

3. compute the total H I column density $N_{\rm HI}$ from cell 1 to n

4. reduce radiation according to absorption due to $N_{\rm HI}$

The comparison between the simulation and the semi-analytical model is shown in Fig. 2.2, showing the neutral fraction $x_{\rm HI}$ as a function of the depth into the gas slab, for black bodies sources with different bolometric luminosities (10^3, 10^4, 10^5 L$_\odot$). The solid lines shows the results of the simulations, while the dotted lines are obtained with the semi-analytical model. The curves for the 10^3 and 10^4 L$_\odot$ are in very good agreement, while there is a small difference for the the 10^5 L$_\odot$ source near the Strömgren depth $\delta_{\rm Str}$. We have verified that this is due to slightly different gas temperatures around $\delta_{\rm Str}$, which in turn implies a difference in the recombination coefficient. Indeed, KROME and Gnedin & Hollon (2012) do not use the same coefficients to compute heating and cooling functions.

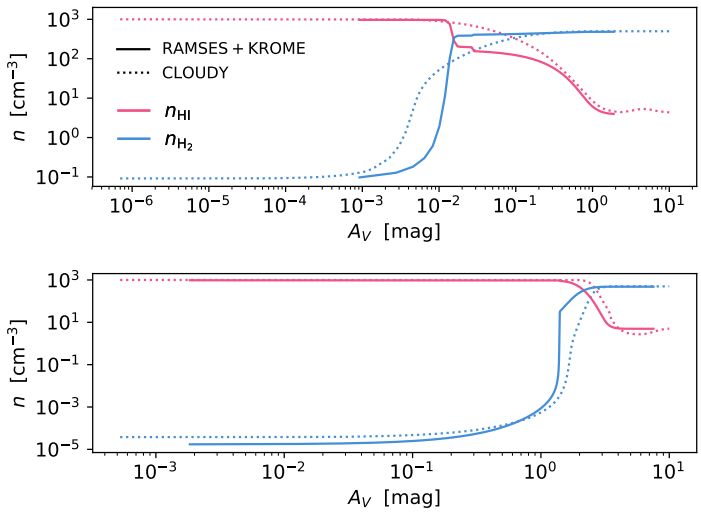

Figure 2.3: Atomic (red) and molecular (blue) hydrogen density as a function of visual extinction, for a PDR-like gas slab with FUV radiation coming from the left side. The solid lines show the result obtained with RAMSES-RT coupled with KROME, while the dotted lines show the result obtained with CLOUDY in the context of PDR code comparison (Röllig et al., 2007). Plot from Decataldo et al. (2019).

2.4.2 Test B: PDR

In order to test the chemistry of molecular hydrogen, we have carried out a 1D simulation of a slab of molecular gas, with radiation coming from one side. The setup is the same of typical simulations carried out with 1D time-independent PDR codes, as KOSMA-τ (Stoerzer et al., 1996), CLOUDY (Ferland et al., 1998), UCL_PDR (Bell et al., 2005) and many others. A PDR-code comparison has been done by Röllig et al. (2007), that benchmarks the results obtained with the different codes starting from the same setup conditions.

In particular, here we compare the results of our code with the models V1 and V2 in Röllig's work. In the V1 and V2 models, the gas filling the computational domain has an H density $n_{\rm H} = 10^3$ cm^{-3}, with He elemental abundance $A_{\rm He} = 0.1$. The flux is coming from the left side, and it is given by χ times the Draine spectrum (Draine, 1978) in the FUV (6.0 - 13.6 eV); the V1 model has $\chi = 10$, while V2 has $\chi = 10^5$.

The dust cross section is $\sigma_d = 1.75 \times 10^{-21}$ cm^2 and does not depend on frequency, the cosmic ray H ionization rate is $\zeta_{\rm H} = 5 \times 10^{-17}$ s^{-1} and the H_2 formation and dissociation rates are set to $R_{\rm H_2} = 3 \times 10^{-18} T^{1/2}$ and $\Gamma_{\rm H_2} = 5.10 \times 10^{-11}\,\chi$) respectively. Note that in Röllig et al. (2007), such prescription on the dissociation rate is adopted only for the codes that do not compute explicitly it by summing over all oscillator strengths.

We prepare our simulation to match the setup of the V1 and V2 models in the PDR benchmark, in particular by setting the same H_2 formation and dissociation rate of molecular

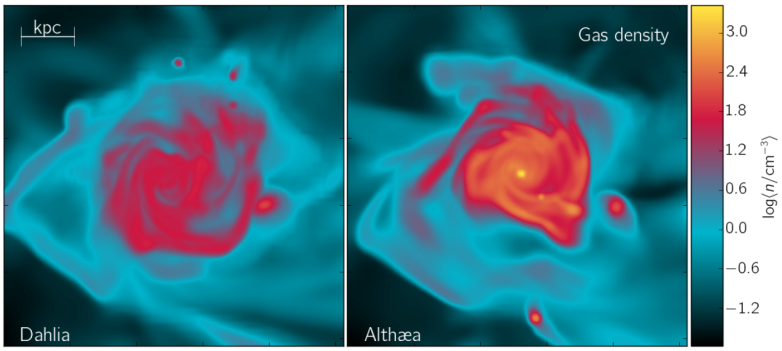

Figure 2.4: Face-on maps of gas density (line-of-sight mass averaged values) in Dahlia and Althæa at $z = 6$. From the maps, it is already evident that Althæa present a more clumpy structure, with density peaks $10\times$ larger than the typical density in Dahlia.

hydrogen. The main drawbacks with respect to PDR codes are that (1) we use only the two FUV bins [6.0-11.2] eV and [11.2-13.6] eV to sample the Draine spectrum, and (2) we do not track C, O and Si as separate species.

The results of the comparison are displayed in Fig. 2.3, for model V1 (upper panel) and model V2 (lower panel). The H_2 number density and the HI number density are represented with a blue and a red line respectively; with solid lines we plot the result from our RAMSES-RT + KROME simulation; with dashed lines we plot results* for the CLOUDY test. The depth into the gas slab in the x axis is measured as a visual extinction A_V, which is proportional to the H column density, according to $A_V = 6.289 \times 10^{-22}\, N_H$. We obtain a good agreement with CLOUDY, matching the HI and H_2 abundances at low/high A_V. The small difference in the residual H_2 abundance in the V2 test is due to a difference in the temperature, affecting the H_2 formation rate. The position of the HI $-$ H_2 transition is well captured in the simulations, with a steeper transition profile due to the different H_2 self-shielding recipe.

2.5 The impact of chemistry and RT on cosmological simulations

The relevance of the inclusion of chemistry and RT on the evolution of the ISM has been investigated in a suite of cosmological simulation by Pallottini et al. (2017a,b, 2019). Three galaxies have been simulated, by zooming-in a dark matter halo of $\sim 10^{11}\,M_\odot$ at redhshift $z = 6$. Star formation is implemented following a a linearly H2-dependent Schmidt-Kennicutt relation (Schmidt, 1959; Kennicutt, 1998), drawing the mass of new star particles from a Poisson distribution (Rasera & Teyssier, 2006). A subgrid model for feedback due to stellar winds, supernovae (SN) and radiation pressure is adopted, injecting

*Data from Röllig et al. (2007) are available at http://www.ph1.uni-koeln.de/pdr-comparison.

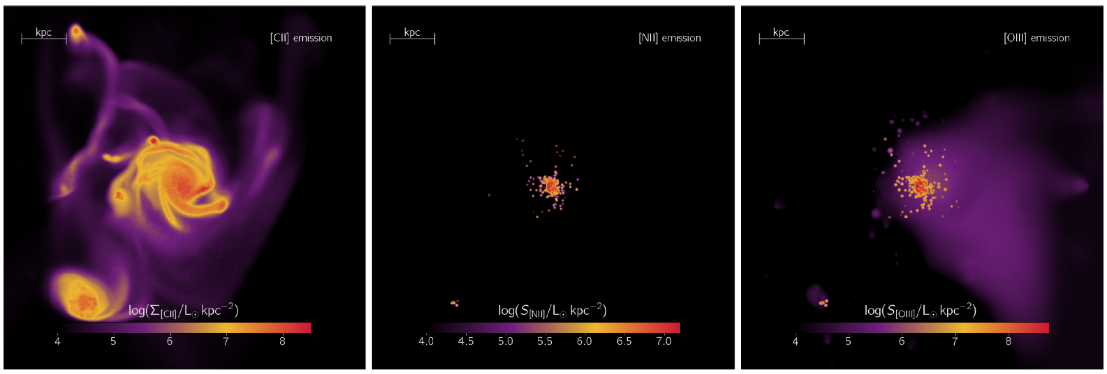

Figure 2.5: Surface line emission of far-infrared lines (from left to right, [CII], [OII] and [NII]) from Freesia. The maps are obtained by post-processing the simulation snapshots with CLOUDY.

thermal and turbulent energy according to the SN blastwave model (Ostriker & McKee, 1988) and the OB/AGB stellar wind model (Weaver et al., 1977). The three simulations differ for the implementation of chemistry and radiation:

- Dahlia (Pallottini et al., 2017a): equilibrium thermo-chemistry, with H_2 abundance derived from a subgrid model (Krumholz et al., 2009); stellar radiation is not included on runtime.
- Althæa (Pallottini et al., 2017b): a non-equlibrium chemical network of primordial species is implemented via KROME (see Sec. 2.3, and a radiation field is assumed through the galaxy in order to trigger photochemical reactions; even in this simulation, there is no on-the-fly radiative transfer.
- Freesia (Pallottini et al., 2019): the same chemical network as in Althæa is adopted, but with the chemistry fully coupled to an RT scheme, as detailed in Sec. 2.4.

A comparison between the properties of the two galaxies Dahlia and Althæa allows to asses the importance of including a proper chemical network for the formation and destruction of H_2. Both galaxies show a similar star formation rate (SFR) history, increasing all the way up to $z = 6$, when the simulations is interrupted. Nevertheless, Dahlia shows a consistently higher SFR, by a factor ~ 1.5. Furthermore, the morphological structure is also different, with Althæa featuring a more clumpy and fragmented structure, while Dahlia has more uniform density distribution and in general lower density (see Fig. 2.4). These differences can be explained with the fact that the density for the formation of H_2 is different in the two simulations: in Althæa H_2 forms at higher density ($n \simeq 300$ cm^{-3}) than in Dalhia ($n \simeq 30$ cm^{-3}). Since the star formation recipe is based on H_2, it follows that the star formation threshold is higher in Althæa, so that stellar clusters form more massive and in close isolated regions. This results in stronger and spatially coherent supernova explosions,

and feedback is more effective, hence decreasing the SFR. Thanks to this refined model, Althæa sits on the Kennicutt -Schmidt relation, while Dahlia was 3σ off.

In Althæa, the interstellar radiation field was assumed spatially constant and proportional to the SFR. On other hand, Freesia is a simulation with on-the-fly radiative transfer, so that the distribution of the flux throughout the galaxy can be studied: the flux is naturally higher close to stellar clusters, and decreasing further because of geometrical dilution and absorption. In particular, the far-ultraviolet field has a smooth spatial distribution ($G_0 \simeq 8$ in Habing units), while the ionizing flux has a large variation (ionization parameter varying in the range $U_{\rm ion} = 1 - 20 \times 10^{-3}$). Together with the information on the chemical abundances in each cell, this allows to compute in post-processing the intensity of emission lines, as [CII], [OIII] or [NII] (see Fig. 2.5). In this case, we have used a grid of models obtained with the photoionization code CLOUDY (Ferland et al., 1998), in a similar fashion as Vallini et al. (2017, 2018). Far-infrared lines are the main tool to observe high-redshift galaxies, therefore estimating their intensity is crucial to guide future observations of these objects. Furthermore, peculiar properties of these lines are visible from the simulation, as the spatial offset between [CII] and [OIII] which is sometimes observed at high-z (Carniani et al., 2017). In conclusion, the inclusion of fully coupled RT and chemistry in this new generation of simulations, allowed by an increasing availability of computational power, is a promising tool to understand many of the properties observed in astrophysical systems, both at galactic and molecular cloud scales, as we aim to do in this Thesis.

Chapter 3

Analytical model of a photoevaporating clump

3.1 Dense clumps and filaments in GMCs

CO maps have revealed that Giant Molecular Clouds (GMCs) contain a very rich internal structure featuring filaments and clumps (Bally et al., 1987; Bertoldi & McKee, 1992). The typical sizes of the detected clumps range from 1 to 10 pc. Temperature and density of the gas can be estimated by combining line intensities with radiative transfer calculations. Such studies yield kinetic temperatures in the range $T = 15 - 200$ K, associated with H_2 densities of $n = 10^{3-4}$ cm^{-3} (Parsons et al., 2012; Minamidani et al., 2011). A correlation between clump temperature and Hα flux suggests that denser clumps are warmer because of a larger UV radiation intensity, likely provided by external sources or internal star-formation activity.

Dense molecular clumps have also been detected within the Photo Dissociation Regions (PDRs) of OB stars, through observations in the infrared and millimiter bands (Van der Werf et al., 1993; Luhman et al., 1998). Detections of fine-structure lines of [CI] and [CII], high-J CO rotational lines, and $J = 3 - 2$ lines of HCN and HCO, show that PDRs are made of a low-density, more diffuse component ($n \simeq 10^{2-4}$ cm^{-3}), and high-density structures ($n \simeq 10^{6-7}$ cm^{-3}), such as in M17SW (Hobson, 1992; Howe et al., 2000), and in the Orion bar (Lis & Schilke, 2003). These clumps must have sizes as small as one tenth or a hundredth of pc, often showing elongated shapes. The presence of such clumps affects significantly the emission spectrum of stellar PDRs.

According to recent observations (Cicone et al., 2014), molecular clumps are also detected in outflowing gas around quasars. As detailed in Sec. 1.10.2, the radiation pressure drives a powerful wind ($v \sim 0.1c$ with c speed of light) which collides with the ISM, so that a shock propagates forward into the ISM and a reverse shock propagates back into the

wind (model by King, 2010). The outflowing gas is heated by the shock to very high temperatures ($T \sim 10^7$ K), so that it is expected to be completely ionized. Nevertheless, detections of the CO, OH and H_2O lines (e.g. Alatalo et al., 2011; Aalto et al., 2012b; Feruglio et al., 2015) show that the outflow is in molecular form up to a radius of $1 - 10$ kpc. To reach such distances, the molecular gas has to be structured in clumps, able to provide sufficient self-shielding against the strong quasar radiation field.

The structure of a molecular clump is significantly determined by the presence of an ionizing/photo-dissociating radiation field, since incident photons with different wavelengths alter the chemical composition of the gas and its physical properties. Far ultraviolet (FUV) radiation (6 eV$< h\nu <$ 13.6 eV) is responsible for the dissociation of molecules, determining the formation of a PDR (Tielens & Hollenbach, 1985; Kaufman et al., 1999; Röllig et al., 2007; Bisbas et al., 2012) at the surface of the clump itself. Furthermore, radiation above the Lyman limit ($h\nu > 13.6$ eV) ionizes neutral atoms, and it is completely absorbed within a shallow layer.

The goal of this Chapter is to understand the evolution of radius and the density profile of molecular clumps exposed to a UV radiation field including hydrogen-ionizing photons produced by massive stars or quasars. The key point is that an ionized shell *and* an atomic shell form at the edge of the clump. The dynamics of this layered structure is determined by the fact that each layer is at a different temperature and pressure. For a clump with initial density $n_0 \simeq 10^5$ cm^{-3}, typical temperatures deep into the clump are $T \simeq 10 - 100$ K, while an atomic (ionized) region can be heated up to around $T \simeq 10^3$ K ($T \simeq 10^4$ K). We denote this type of ionization/photodissociation regions as iPDR.

In particular, we apply our model to two scenarios.

- Stellar case: a molecular clump is in pressure equilibrium within a GMC in the proximity of an OB star, and it is suddenly engulfed by the expanding HII region.
- Quasar case: a clump forms as a result of thermal instabilities within the outflow, finds itself embedded in the ionized wind and exposed to the quasar radiation.

Previous works in the literature concentrated mostly on the effects of non-ionizing photons on photoevaporation of clouds (Gorti & Hollenbach, 2002; Adams et al., 2004; Champion et al., 2017). The evolution in their case is simplified by the fact that the clump is exposed only to radiation below the Lyman limit. As a result, the clump develops a single shell structure.

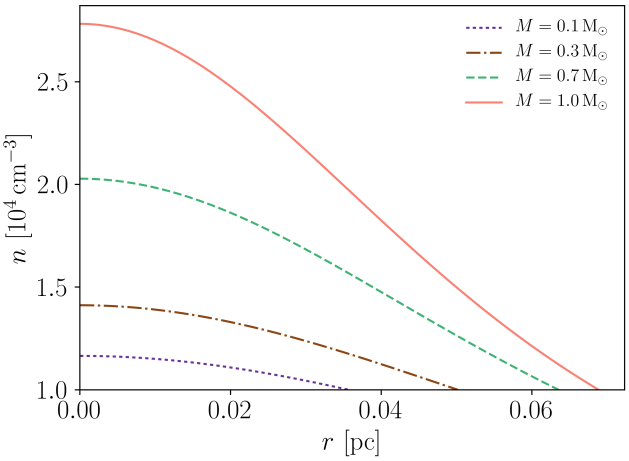

Figure 3.1: Density profile of molecular spherical clumps at temperature $T_{H_2} = 10$ K, confined by a medium with $T_{ICM} = 100$ K and $n_{ICM} = 10^3$ cm^{-3}, computed with the BE model The outer density depends only on T_{H_2} and the confining ICM pressure, while the mass sets the density at the centre of the clump.

	n_{ICM} [cm^{-3}]	T_{ICM} [K]	T_{H_2} [K]
Stellar case	10	$100 - 1000$	10
Quasar case	60	2.2×10^7	100

Table 3.1: Clump and ICM properties at the onset of the photoevaporation process.

3.2 Analytical Model

3.2.1 Gaseous environment

The gaseous environment where clumps are located plays a crucial role in determining properties such as temperature, density and confining pressure. We now describe the interclump medium (ICM) which surrounds clumps in the stellar and quasar case. The ICM properties are summarized in Tab. 3.1.

We assume that clumps in a stellar surrounding are in pressure equilibrium with atomic gas, whose temperature depends on the distance and luminosity from the stellar source. We take $n_{AT} \simeq 10^3$ cm^{-3} as a typical density for this surrounding gas, and we compute the corresponding temperature according to the FUV flux, using the same method used to compute the temperature of the atomic phase in the clump (see Sec. 3.2.3). Such temperature ranges between 10^2 K and 10^3 K. The clump is exposed to the radiation of the massive star when it is engulfed in the growing HII region, for which the density is taken to be $n_{ICM} \simeq 10$ cm^{-3}.

In the case of quasars, molecular clumps likely form from thermal instabilities within the outflow. Clumps detach from the hot phase at the discontinuity between the fast wind

and the ISM (Zubovas & King, 2014), starting from the distance at which the outflow has become energy-driven. This critical radius has been estimated by Zubovas & King (2012):

$$R_c = 520\,\sigma_{200} M_8^{1/2} v_{0.1}\,\mathrm{pc}\ , \tag{3.1}$$

where σ_{200} is the velocity dispersion in the host galaxy in units of 200 km s^{-1}, M_8 is the mass of the SMBH in units of $10^8\,\mathrm{M}_\odot$ and $v_{0.1}$ is the wind velocity in units of 0.1 times the speed of light. In the outflow, the gas is heated to $T_{\rm ICM} \simeq 2.2 \times 10^7$ K and has a typical density $n_{\rm ICM} \simeq 60$ cm^{-3} (Zubovas & King, 2014; Costa et al., 2014). The outflow fragments (King, 2010; Nayakshin & Zubovas, 2012) because of thermal instabilities, so that one component cools to a low temperature. The existence of an equilibrium between a 10^4 K and a 10^7 K phase has been studied by Krolik et al. (1981), while Zubovas & King (2014) show that an atomic clump requires a very short time to cool and turn to molecular form (see Sec. 1.10.3). Molecule formation can occur in the overdensities generated via thermal instabilities, since radiation is efficiently self-shielded and the gas deep into the clump is allowed to cool*. When a clump starts to cool, we assume that it maintains pressure balance with the ICM until its temperature is $T \gtrsim 10^4$ K. Below such temperature the cooling time-scale is very short, and the evaporation process detailed in the next Sections happens before the clump can readjust to the external pressure. The final temperature of the molecular gas is about 100 K, in agreement with detections with CO and water vapour line emission (Cicone et al., 2012; Aalto et al., 2012a; González-Alfonso et al., 2010).

3.2.2 Radiation field

Radiation affects the structure of a clump according to the shape of the emitted spectrum. In particular we are interested in ionizing (energy $h\nu \geq 13.6$ eV) and FUV photons (6 eV $< h\nu <$ 13.6 eV), whose flux G_0 is measured in units of the Habing flux†.

For stellar sources, we use black body spectra with different effective temperatures T_{eff}. In terms of solar luminosity ($\mathrm{L}_\odot$), OB stars have typical luminosities ranging between $10^3\mathrm{L}_\odot$ and $10^5\mathrm{L}_\odot$. Then, the effective temperature is given by

$$T_{eff} = \left(\frac{L}{4\pi R_\star^2 \sigma_{\rm SB}}\right)^{1/4}\ , \tag{3.2}$$

where $\sigma_{\rm SB}$ is the Stefan-Boltzmann constant, $R_\star$ is the star radius and L is the bolometric luminosity. We compute $R_\star$ through the mass-luminosity and radius-luminosity relations by Demircan & Kahraman (1991), which for an OB star give

$$R_\star = 1.33\,\mathrm{R}_\odot \left(\frac{L}{1.02\,\mathrm{L}_\odot}\right)^{0.142}\ , \tag{3.3}$$

*This conclusion has been re-examined by Ferrara & Scannapieco (2016), who pointed out that molecule formation is problematic due to the efficient dust destruction by the outflow shock.

†The Habing flux ($1.6 \times 10^{-3}\,\mathrm{erg\,s^{-1}cm^{-2}}$) is the average interstellar radiation field of our Galaxy in the range [6 eV, 13.6 eV] (Habing, 1968).

where $R_\odot$ is the solar radius. Integrating the black body spectrum in the FUV band, typical values of the FUV flux are $G_0 = 10^2 - 10^4$ for gas at 0.3 pc from sources with luminosities in the range $L = 10^3 - 10^5\,L_\odot$. In the same way, we integrate the spectrum for $h\nu \geq 13.6$ eV to obtain the ionizing flux.

In the case of quasars, the fundamental difference is the wide extension of the spectrum to the X-rays, so that ionizing radiation is much more intense in this case. An analytical expression for the ionizing flux can be found with the same approach as in Ferrara & Scannapieco (2016), thus obtaining that the specific (ionizing) luminosity for $\nu > \nu_L \simeq 3.3 \times 10^{15}$ Hz is:

$$L_\nu = 6.2 \times 10^{-17} \left(\frac{\nu}{\nu_L}\right)^{\alpha-2} \left(\frac{L}{\mathrm{erg\,s^{-1}}}\right) \mathrm{erg\,s^{-1}\,Hz^{-1}}\ , \tag{3.4}$$

where $\alpha = 0.5$ for a radio-quiet quasar (Mortlock et al., 2011). We assume eq. 3.4 to be valid for energies below the cut-off value $E_c = 300$ keV (Sazonov et al., 2004; Yue et al., 2013). Furthermore, we can easily infer a relation between the bolometric and FUV luminosity, setting $\nu = \nu_L$ in eq. 3.4. The spectrum is almost flat in the FUV band, with typical values $G_0 \simeq 10^{3-5}$ at 1 kpc, for $L = 10^{45-47}\,\mathrm{erg\,s^{-1}}$.

We investigate the evolution of clumps irradiated by stars or quasars, with L as the only free parameter determining the flux in the bands we are interested in.

3.2.3 Clump structure

We have modeled a clump as a Bonnor-Ebert (BE) sphere (Ebert, 1955; Bonnor, 1956), which is isotropically affected by an external impinging radiation field. Given the clump mass, the clump temperature and the confining pressure, the BE sphere model allows to compute the radial density profile inside the clump and its radius. The algorithm to compute the profile is detailed in Sec. 1.6. In Fig. 3.1 we show the density profile for clumps of different mass, with the same temperature $T = 10$ K and a confining pressure $P = 10^{-11}$ erg cm^{-3} (corresponding to a confining medium with $T_{\rm ICM} = 100$ K and $n_{\rm ICM} = 10^3$ cm^{-3}). The clumps have different radii and same outer density, set by the pressure equilibrium between the clump and the surrounding gas. The density increases towards the centre, with a steeper profile for larger values of the mass. A clump undergoes a collapse if its mass is larger than the BE mass:

$$M_{\rm BE} \simeq 1.18 \frac{c_s^4}{\sqrt{P_0 G^3}}\ , \tag{3.5}$$

where P_0 is the confining pressure, c_s is the isothermal sound speed and G is the gravitational constant. We are considering only the thermal contribution to pressure, not accounting for turbulent and magnetic pressure. We underline that, apart from the use of a BE density profile, gravity is not included in the hydrodynamical equations for the clump evolution presented in Sec. 3.2.4.

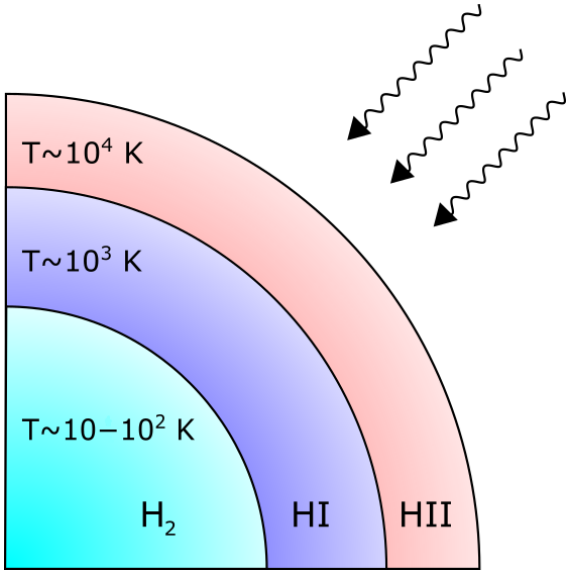

Figure 3.2: Schematic structure of a clump exposed to UV radiation. In the sudden heating approximation, a molecular clump instantaneously develops a shell structure, with an ionized (HII) shell and a neutral (HI) shell, surrounding a cold and dense molecular core (H_2).

Given the clump density profile, we assume that the impinging radiation induces a shell-like structure, before any dynamical response of the gas to the photo-heating occurs (sudden heating approximation, see Fig. 3.2). The FUV radiation is responsible for the formation of an atomic layer (HI shell). The more energetic part of the spectrum partially or totally ionizes an outer shell (HII shell), depending on the intensity of the source. This sets up the initial condition for the subsequent hydrodynamical evolution of the clump.

The sudden heating approximation means that radiation dissociates and ionizes particles and heats the gas to its final temperature instantaneously, while the clump shape is unaltered. This situation is often referred to as a R-type ionization front (Spitzer, 1998). To justify this assumption, we compare the sound-crossing time-scale t_{cross} with the ionization timescale t_i and the heating time-scale t_h. The Strömgren theory adapted for plane geometry (which can be assumed when the radius of the clump is much smaller than the distance from the source) allows to compute the HII shell thickness,

$$\delta_{\rm HII}(t) = \delta_{\rm HII}(1 - e^{-n\alpha_{\rm B}t}) \ , \tag{3.6}$$

where n is the gas number density, and $\alpha_{\rm B}$ is the case B recombination coefficient (values in Verner & Ferland, 1996). Thus, we have $t_i = 1/n\alpha_{\rm B}$. On the other hand, the sound-crossing time-scale is $t_{cross} = r_c/c_s$ where r_c is the clump radius and $c_s \sim \sqrt{k_{\rm B}T/m_p}$ is the sound speed. Plugging in typical values, it is easily seen that the condition $t_i \ll t_{cross}$ is always satisfied for physically reasonable values of r_c ($0.01 - 1$ pc) and c_s (0.11 km s^{-1}

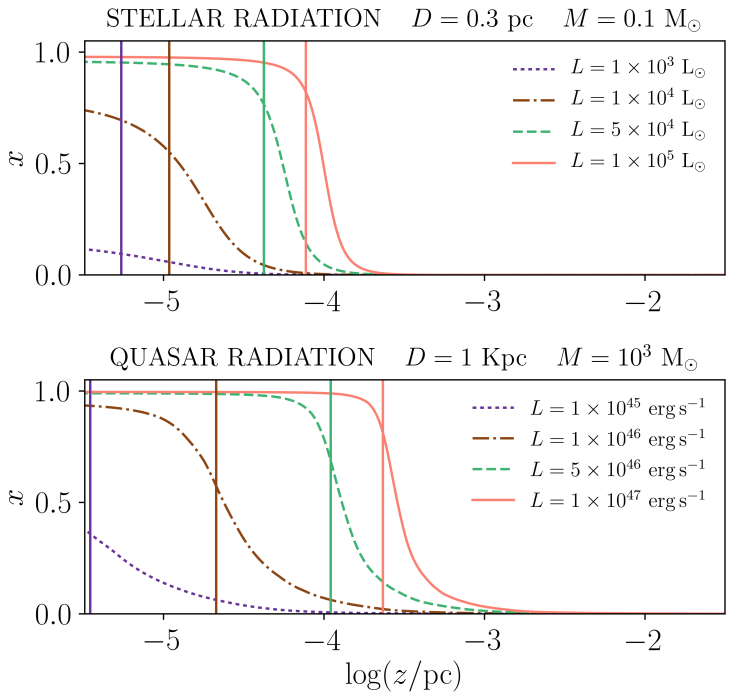

Figure 3.3: The ionized fraction x in the HII shell is plotted as a function of depth ($z = 0$ is the surface of the clump) for different luminosities of the sources. Both the stellar case (**upper** panel) and quasar case (**lower** panel) are represented. Clumps have mass $0.1\,M_\odot$ and $10^3\,M_\odot$ for stars and quasars respectively, and their density in the HII shell is computed with a BE density profile. The confining ICM is as described in Sec. 3.2.1. Vertical lines mark the thickness of the HII shell computed as if the transition between ionized and neutral phase was a step function.

in the cold phase). Regarding the gas heating time-scale (t_h), a simple estimate gives us:

$$t_h = \frac{k_B T_f}{\Gamma(T_f)} \ , \tag{3.7}$$

where k_B is the Boltzmann constant, T_f is the final gas temperature and $\Gamma(T_f)$ is the heating rate (in erg/s), mainly due to photoionization. To give some examples, Γ/n varies from $\sim 10^{-23}$ erg cm^3 s^{-1} at a distance of 1 pc from a star with $L = 10^3\,L_\odot$, to $\sim 10^{-16}$ erg cm^3 s^{-1} at 0.5 kpc from a quasar with $L = 10^{47}$ erg s^{-1} (using the heating function by Gnedin & Hollon, 2012). The result is that for any value of r_c and c_s of interest, the condition $t_h \ll t_{cross}$ holds.

In what follows, we discuss how we compute the thickness and the temperature of each shell in the clump. The thickness of the HI shell (δ_{HI}) is defined as the depth at which hydrogen is found in molecular form. Tielens & Hollenbach (1985) find how such depth (expressed as hydrogen column density) scales with the gas density and the FUV flux:

$$N_H \propto n^{-4/3} G_0^{4/3} \ , \tag{3.8}$$

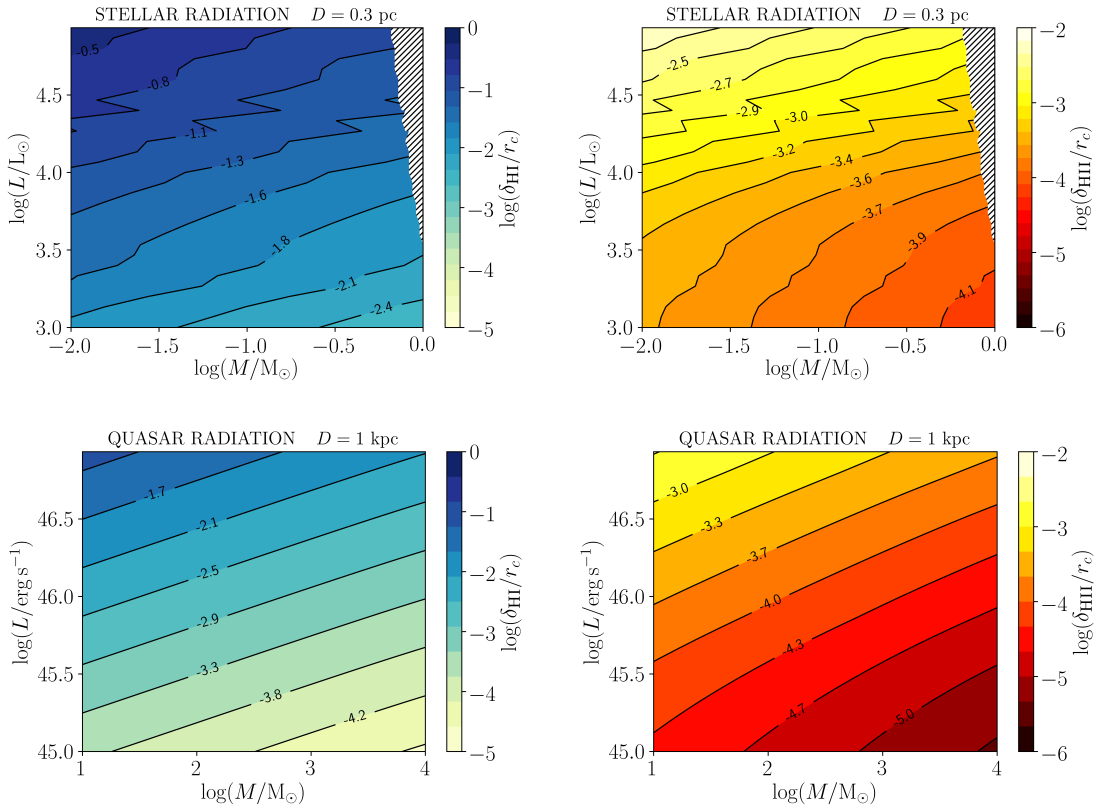

Figure 3.4: Plots of the ratio of the shell thickness to the initial clump radius r_c, as a function of clump mass and source luminosity. **Upper** panels: HI shell thickness $\delta_{\rm HI}$ (**left**) and HII shell thickness $\delta_{\rm HII}$ (**right**) when the clump is located in the surroundings of a massive star, at a distance of 0.3 pc. Clumps in the shaded region are not considered, since their mass is larger than the BE mass for collapse (eq. 3.5). **Lower** panels: HI shell thickness $\delta_{\rm HI}$ (**left**) and HII shell thickness $\delta_{\rm HII}$ (**right**) when the clump is illuminated by a quasar at a distance of 1 kpc. See the text for more details.

and that the thickness for $n = 2.3 \times 10^5$ cm^{-3} and $G_0 = 10^5$ is $\delta_{\rm HI} = 1.5 \times 10^{16}$ cm. Then from eq. 3.8 we find for the shell thickness

$$\delta_{\rm HI} = 0.034 \left(\frac{n}{10^5\,{\rm cm}^{-3}}\right)^{-7/3} \left(\frac{G_0}{10^5}\right)^{4/3} {\rm pc}\ . \tag{3.9}$$

Kaufman et al. (1999) outline that the PDR temperature is rather constant before it drops to the low values of the molecular core. They plot the temperature for different values of the density and the FUV flux, and we use a fit of their model to estimate the temperature of the HI shell.

The outer shell presents a partial or total ionization, depending on its density and the intensity of the impinging radiation field. We compute the equilibrium temperature as a function of depth into the shell by balancing photoionization heating (Sec. 1.3.1), recombination cooling (Sec. 1.4.2), metal line cooling (Sec. 1.4.4) and bremsstrahlung

(Sec.1.4.3). As we already noticed in Sec. 1.4.4, the presence of a radiation field alters the heating and cooling rate: 1) the ionized fraction of each species is modified and thus the cooling rate by line emission is changed accordingly; 2) injection of photoionized electrons in the gas provides an extra heating term. Approximate heating and cooling functions, assuming collisional equilibrium but non-zero radiation field, are provided by Gnedin & Hollon (2012). We assume a fiducial value for metallicity, i.e. the mass fraction of elements heavier than helium, of $Z = 0.02$ (close to the solar value from Anders & Grevesse, 1989), noticing that metals are important for the energetics of the gas, but their contribution to its dynamics (determined by gas pressure) is negligible. Moreover, we account for Compton heating, which we expect to be important for hard radiation fields:

$$H_C = \frac{\sigma_T F}{m_e c^2}(\langle h\nu \rangle - 4k_{\rm B}T) \ , \tag{3.10}$$

where σ_T is the Thomson cross section, m_e is the electron mass, F is the total flux and $\langle h\nu \rangle$ is the average photon energy beyond the Lyman limit.

Once the temperature profile is computed, we obtain the ionization profile by balancing photoionization, collisional ionization and recombination:

$$\gamma(T) n_e n_p + n_{\rm H} \int_{\nu_L}^{\infty} \frac{F_\nu}{h\nu} e^{-\tau_\nu} a_\nu(T) d\nu = \alpha_{\rm B}(T) n_e n_p \ , \tag{3.11}$$

where n_e, n_p and $n_{\rm H}$ are the electron, proton and neutral hydrogen density, respectively; F_ν is the specific flux from the source, τ_ν is the optical depth, a_ν and γ are the photoionization cross section and the collision ionization coefficient, respectively (analytical fits by Verner & Yakovlev, 1995; Cen, 1992). In Fig. 3.3 we plot the ionization fraction $x = n_e/n = n_p/n$, as a function of the depth into the clump, for different source luminosities. The ionization profile varies smoothly throughout the HII shell, between the edge of the clump and the PDR, both in the stellar and quasar case. Nevertheless, the region where x is varying is of the order of 10^{-5} pc, which is negligible with respect to typical clump radii ($0.01 - 1$ pc). Then we adopt a reference value for the HII shell thickness $\delta_{\rm HII}$, computed with the approximation of a sharp boundary between ionized and phase, in the same way as done for the Strömgren radius for a stellar HII region. Further assuming that the clump radius is much smaller than the distance from the source and that it is illuminated isotropically, the HII shell depth is

$$\delta_{\rm HII} = \frac{1}{x_{max}^2 n^2 \alpha_{\rm B}(T)} \int_{\nu_L}^{\infty} \frac{F_\nu}{h\nu} \, {\rm d}\nu \ , \tag{3.12}$$

where x_{max} is the maximum ionization fraction, at the edge of the clump. The thickness $\delta_{\rm HII}$ is shown with dashed lines in Fig. 3.3.

We restrict our analysis to clumps where the shell thickness is much smaller than the molecular core radius. This allows us to determine the densities of the HI and the HII shells by using the outer density of the BE sphere. Furthermore, it simplifies our calculations,

because we can consider separately the evolution of the shells and the core, since the dynamical time-scale of the former is much shorter than the core one. In Fig. 3.4 we plot the ratio of the HI shell thickness (left panels) and the HII shell thickness (right panels) to the total clump radius r_c as a function of the clump mass, for stars and quasars with different luminosities. The atomic shell is always thicker than the ionized shell, showing a large self-shielding effect of the ionized gas. The typical masses of clumps are different for stars and quasars, and we consider only masses smaller than the BE mass for collapse. The distances of clumps from the source are fixed in the two scenarios, and are reasonable for molecular gas engulfed by an expanding stellar HII regions (the distance scale is given by the Strömgren radius) and clumps forming in quasar outflows (critical radius given in eq. 3.1).

Clumps presenting a ratio $\delta_{\rm HI}/r_c = 1$ are completely dissociated on a time-scale t_i, and our analysis restricts to clumps where $\delta_{\rm HI} \ll r_c$. From the plot, we see that such condition is usually verified and breaks only in the stellar case for small clumps ($M < 0.01\,{\rm M}_\odot$) and very intense sources ($L \simeq 10^5\,{\rm L}_\odot$).

3.2.4 Shock dynamics inside the clump

Having set the initial conditions on a clump, i.e. a core-double shell structure, now we can study its dynamical evolution for $t > 0$. The different layers in the clumps have different pressures, so that a shock or rarefaction waves originate, enforcing a continuous value of pressure and velocity across the contact discontinuity between two layers.

The cooling time-scale of a gas at temperature T is

$$t_{cool} = \frac{k_{\rm B} T}{\Lambda(T)}\ , \tag{3.13}$$

with Λ being the cooling function given by Neufeld et al. (1995) for molecular gas and by Tielens & Hollenbach (1985) for PDRs. For the range of temperatures and n, r_c and c_s values of interest here, $t_{cool} \ll t_{cross}$. Thus the fluid motion and the propagation of any disturbance in the gas (as shock and rarefaction waves) can be safely considered as isothermal processes.

A qualitative diagram of the possible outcomes at an arbitrary discontinuity is shown in Fig. 3.5. In the situation considered in the upper inset, a gas has a pressure $P_{\rm R}$ to the right of an interface, and a pressure $P_{\rm L}$ to the left (with $P_{\rm L} > P_{\rm R}$). The velocity to the right is $v_{\rm R} = 0$, while we consider different values $v_{\rm L,1}$, $v_{\rm L,2}$ and $v_{\rm L,3}$ for the velocity to the left. The solid lines connect to the initial state all the possible final states of the gas, when it is crossed by a rarefaction wave (RW) or a shock wave (SW). For example, the points on the blue line represent the possible final states of the gas to the right when it is crossed by a rarefaction wave. The solution of the discontinuity problem is obtained when the lines departing from the two initial states of the gas to the left and to the right

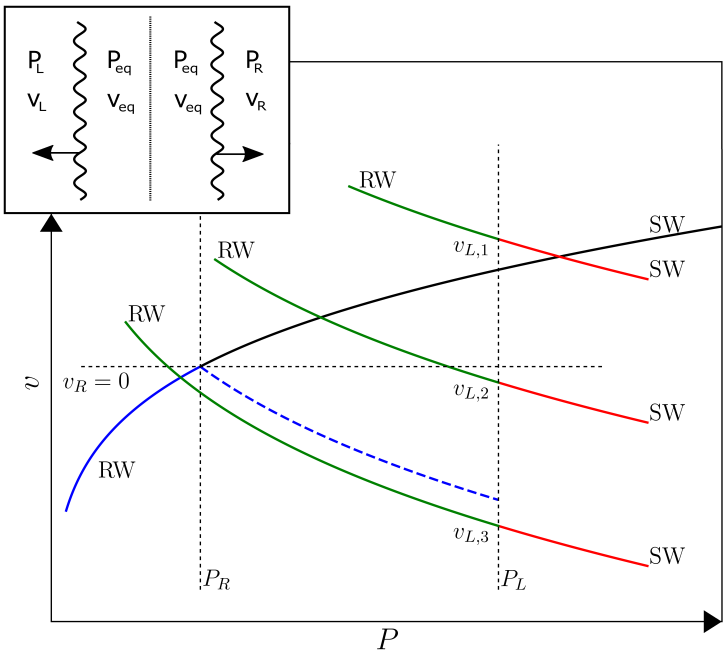

Figure 3.5: The sketch in the upper right corner shows the general arbitrary discontinuity problem: a gas has initial conditions ($P_{\rm L}$, $v_{\rm L}$) and ($P_{\rm R}$, $v_{\rm R}$) to the right and to the left of the discontinuity (dotted line) respectively. Wavy lines are shock waves (SW) or rarefaction waves (RW) originating from it, in order to set a continuous value P_{eq} and v_{eq} of pressure and velocity. The plot shows the qualitative solution of the problem with $P_{\rm L} > P_{\rm R}$ and $v_{\rm R} = 0$. The blue-black line connects all the possible final states on the right side, achieved through a SW or a RW. Similarly, the green-red lines the possible final states to the left side, for different values of $v_{\rm L}$. The intersection of the lines for the regions to the left and to the right gives the solution, and different types of waves (shock or rarefaction waves) are required to get to the final state, according to the value of $v_{\rm L}$.

intersect, since the final values of P and v must be the same across the discontinuity. This also determines which kind of wave is required, i.e. a SW or a RW.

The solution of the problem for given values of the initial pressure, density and velocity across the discontinuity is obtained numerically, imposing the final pressure and velocity to be continuous. The post-shock values are obtained solving the isothermal Rankine-Hugoniot conditions (Rankine, 1870)

$$\rho_0 v_0 = \rho_1 v_1 \tag{3.14a}$$

$$\rho_0 v_0^2 + P_0 = \rho_1 v_1^2 + P_1 \tag{3.14b}$$

$$T_0 = T_1 \tag{3.14c}$$

where the subscript 0 is used for pre-shock values and the subscript 1 for post-shock values, with v velocity in the shock front frame. Rearranging the equations 3.14, it is possible to

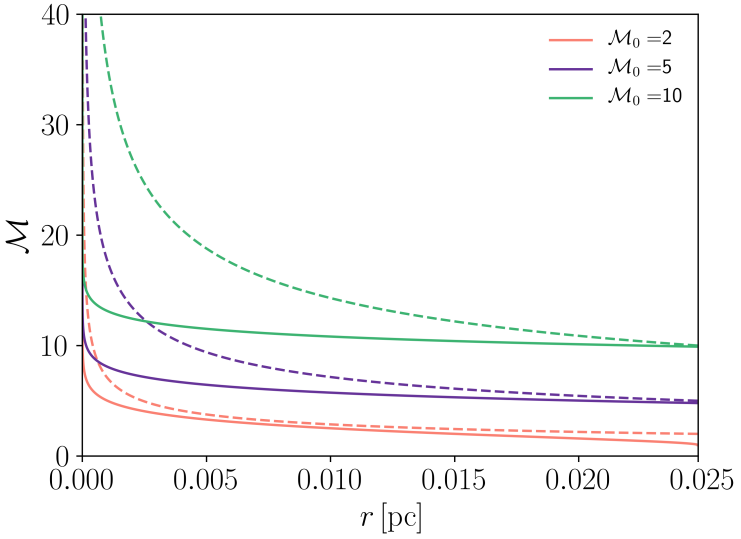

Figure 3.6: Mach number radial profile, $\mathcal{M}(r)$, for different initial Mach numbers $\mathcal{M}_0$ of isothermal shocks at the clump surface, computed considering the density variation in the clump (**solid** line) according to eq. 3.19 or using the power law of eq. 3.20 (**dashed** line) valid for homogeneous density and adiabatic shocks (analytical solution by Guderley, 1942). The clump considered in the plot has mass $0.1\,\mathrm{M}_\odot$ and radius 0.025 pc, and it is made of molecular gas (so that the power law index is $n(\gamma) \simeq 0.394$).

write the following relations

$$\rho_1 = \rho_0 \mathcal{M}^2 \tag{3.15a}$$

$$P_1 = P_0 \mathcal{M}^2 \tag{3.15b}$$

$$v_1 = v_0 / \mathcal{M}^2 \tag{3.15c}$$

with $\mathcal{M} = v_0/c_s$ being the shock Mach number.

On the other hand, rarefaction waves are not discontinuities and values of flow variables across such waves are obtained following Zel'dovich & Raĭzer (2002) and adapting the calculations to the isothermal case. Consider a wave originating at $x = 0$ and propagating toward $x > 0$, such that the final velocity after the wave has completely passed is $v_f = -U$. The profile between the "wave head", moving at the initial sound speed $c_{s,0}$ in the gas, and the "wave tail", moving at speed $v_{\mathrm{tail}} = c_{s,0} - (\gamma + 1)U/2$, is

$$v(x) = -\left(c_{s,0} - x/t\right) \tag{3.16a}$$

$$\rho(x) = \rho_0 \exp\left(x/c_{s,0}t - 1\right) \tag{3.16b}$$

$$P(x) = P_0 \exp\left(x/c_{s,0}t - 1\right) \tag{3.16c}$$

where ρ_0 and P_0 are the values of density and pressure before the rarefaction has passed.

Since shock waves are discontinuities, an interaction between two shocks can be treated as an arbitrary discontinuity between post-shock values of flow variables. To simplify our analysis, we also consider interactions involving rarefactions as discontinuities, by accounting only for the post-rarefaction values of flow variables. This approach introduces only a negligible error (see Appendix in Decataldo et al., 2017).

To compute the shock speed inside the clump, we have to account for the spherical geometry and for the density gradient given by the BE profile. Following Whitham (1958), the flow equations can be written as

$$\partial_t \rho + \partial_r(\rho v) + \rho v \frac{\partial_r A(r)}{A(r)} = 0 \tag{3.17a}$$

$$\partial_t v + v\partial_r v + \frac{1}{\rho}\partial_r P - \frac{1}{\rho_0(r)}\partial_r P_0(r) = 0 \tag{3.17b}$$

where r is the radial coordinate, $A(r) = 4\pi r^2$ in the spherical case, $\rho_0(r)$ and $P_0(r)$ are the initial density and pressure profiles for a BE sphere. Eq. 3.17a and eq. 3.17b can be combined to give the equivalent equation valid along the curves $dr/dt = r + c_s$ in the (r, t) plane (called the C_+ characteristics):

$$\mathrm{d}P + \rho c_s \mathrm{d}v + \frac{\rho c_s^2 v}{v + c}\frac{A'(r)}{A(r)} - \frac{\rho c_s}{v + c_s}\frac{1}{\rho_0(r)}P_0'(r) = 0 \ , \tag{3.18}$$

where the prime denotes the derivative with respect to r. According to Whitham (1958) the shock trajectory in the (r, t) plane is approximately a C_+ characteristic, so that eq. 3.18 can be applied along the shock. Then we can write eq. 3.18 as a function of the Mach number $\mathcal{M}$, substituting the post-shock values P, ρ, v from eq. 3.15:

$$\frac{d\mathcal{M}}{dr} = -\frac{1}{2}\frac{\mathcal{M}^2}{\mathcal{M}^2 - 1}\frac{A'(r)}{A(r)} + \frac{1}{2}\frac{\mathcal{M}^3}{\mathcal{M} + 1}\frac{P_0'(r)}{P_0(r)} \ , \tag{3.19}$$

which is a differential equation for $\mathcal{M}$ as a function of r.

In Fig. 3.6, the solid lines show the the numerical solution of eq. 3.19 for a molecular clump with mass $M = 0.1\,\mathrm{M}_\odot$ and radius $r_c = 0.025\,\mathrm{pc}$, for different values of the initial Mach numbers $\mathcal{M}_0$ of the shock at the edge of the clump, assuming an isothermal shock. For comparison, the dashed line is the classical analytical solution obtained by Guderley (1942) for a homogeneous density distribution, and in the limit of a strong adiabatic shock:

$$\mathcal{M}(r) = \mathcal{M}_0 \left(\frac{r_0}{r}\right)^{n(\gamma)} \ , \tag{3.20}$$

where r_0 is the radius of the bubble, and $n(\gamma)$ is an exponent depending on the adiabatic coefficient γ (e.g. $n(5/3) \simeq 0.543$ for monoatomic gas and $n(7/5) \simeq 0.394$ for diatomic gas). As opposed to Guderley solution, the isothermal shock speeds up considerably only at a smaller radius. After the shock wave has reached the centre, a reflected shock will travel outwards. The velocity as a function of radius has the same profile of the focusing shock.

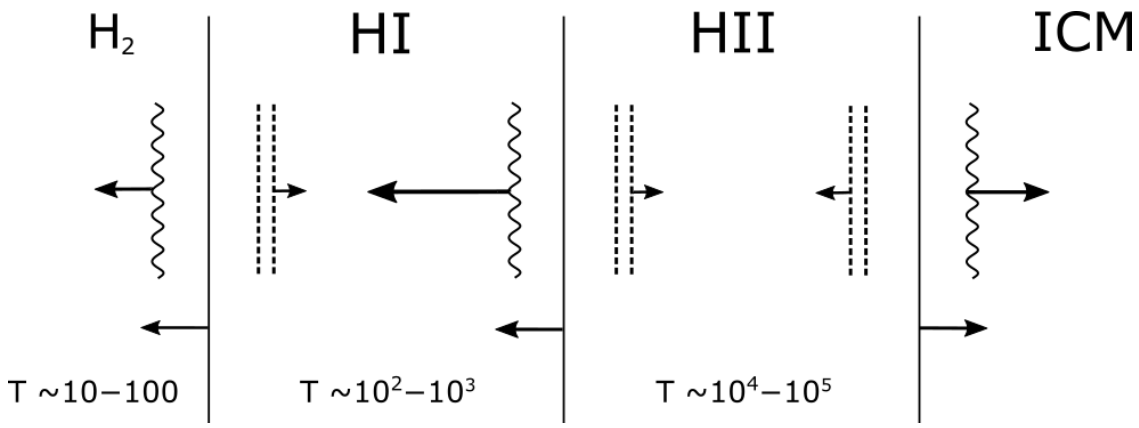

Figure 3.7: Schematic representation of waves propagating in a clump suddenly heated by radiation, where wavy lines are shock waves and double dashed lines are rarefaction waves. High pressure shells drive a shock into adjacent inner shells, and as a result a rarefaction wave propagates back. Discontinuity interfaces move in the same direction of shock waves, at the post-shock speed. The result is an expansion of the two shells and a contraction of the core. See text for the a detailed description.

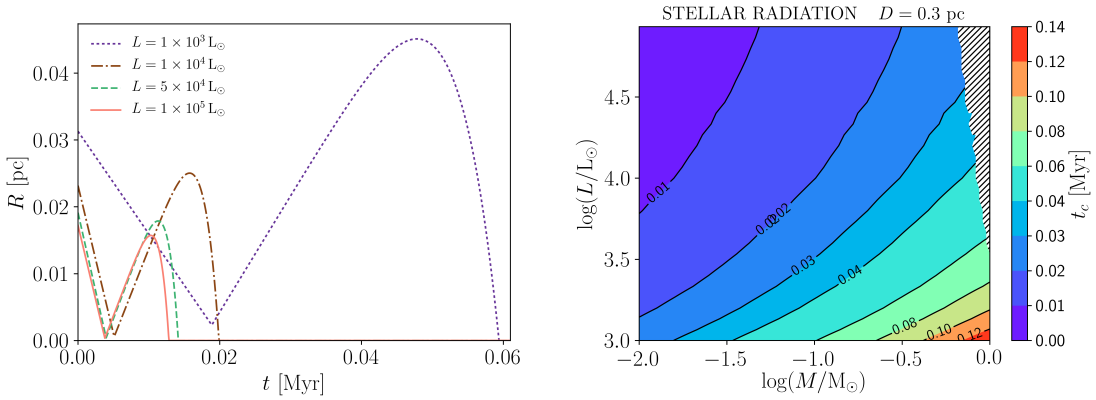

Figure 3.8: **Left**: radius, R, of the molecular core of a clump as a function of time, when the clump is exposed to stellar radiation of different luminosity L. The clump has a mass of $0.1\,M_\odot$, initial radius $r_c \simeq 0.02\,\mathrm{pc}$, and is located 0.3 pc away from the source. **Right**: Lifetime (t_c) of the clumps (located at 0.3 pc from the source) as a function of their mass and stellar source luminosity. Clumps in the shaded region are not considered, since their mass is larger than the BE mass for collapse (eq. 3.5).

3.3 Results

In our model, a clump exposed to UV radiation develops an ionized PDR (iPDR) at its surface. First, we inspect the qualitative behaviour of the structure simply using the arbitrary discontinuity criterion. Fig. 3.7 shows a diagram of shock and rarefaction waves propagating inside the clump because of the pressure difference between adjacent layers.

The HII shell pressure (P_{HII}) is higher both than the pressure of the HI shell (P_{HI}) and

the pressure of the confining ICM ($P_{\rm ICM}$), hence two rarefaction waves cross the HII shell, originating from its edges. Since $\delta_{\rm HII} \ll r_c$, the evolution of the HII shell has a much shorter time-scale than the clump evaporation time. The rarefaction waves which propagate into it interact and reflect at its edges, determining a complex density profile. Nevertheless, the global effect is that the HII shell expands decreasing its density, eventually becoming completely transparent to the ionizing radiation (i.e. the mean free path of photons is much larger than the shell thickness).

On the other hand, $P_{\rm HI}$ is lower than $P_{\rm HII}$, but higher than $P_{\rm H_2}$. Thus, a shock is driven from the HII shell into the HI shell, and a rarefaction wave propagates from the discontinuity with the core (see Fig. 3.7). Once the shock has crossed the HI shell, it reaches the core surface and speeds up its contraction. As a result, the inner boundary of the HI shell moves faster than the outer boundary, and the HI shell is also expanding and becoming transparent on a time-scale shorter than the core evolution time-scale.

The cold ($T_{\rm H_2} \simeq 10 - 100$ K) molecular core is compressed because of the shock wave originating at the discontinuity with the atomic shell and propagating towards the centre. In addition, the shock wave originating at the HII/HI boundary reaches the core surface and catches up with the shock already propagating in the core, resulting in a single stronger converging shock wave.

The shock wave is reflected at the centre of the clump, and eventually gets back to the core edge. The contraction is almost halted, and since the core has a much higher density than the surrounding medium, it starts to expand. The expansion velocity v_{exp} is computed considering the discontinuity between the core compressed by the reflected shock wave and the ICM at rest, using the arbitrary discontinuity algorithm.

We have explicitly verified that the core is so dense ($n \simeq 10^{5-6}$ cm^{-3}) during the contraction phase that the FUV radiation penetrates to a negligible depth with respect to its radius. Thus we can ignore photoevaporation during the contraction phase. When the clump starts expanding, we have computed for each time t the thickness $\delta_{\rm HI}(t)$ of an HI shell (see eq. 3.9) for the corresponding core gas density. We get the core radius at t by subtracting $\delta_{\rm HI}(t)$ to the radius $R(t) = R_0 + v_{exp}t$ (R_0 is the core radius at the end of the shock-contraction phase).

3.3.1 Stellar case

As a first application of our analysis, we consider molecular clumps photoevaporating because of stellar radiation. We consider a cold clump ($T_{\rm H_2} = 10$ K) located in the surrounding of a star, embedded in an atomic region with density $n_{\rm AT} = 10^3$ cm^{-3}. Then we assume that the expanding HII region of the massive star engulfs the clump (the density of the HII region gas is $n_{\rm ICM} = 10$ cm^{-3}, see Tab. 3.1), and we apply the machinery we developed in Sec. 3.2. We consider stars with bolometric luminosities $L = 1 \times 10^3\,{\rm L}_\odot$,

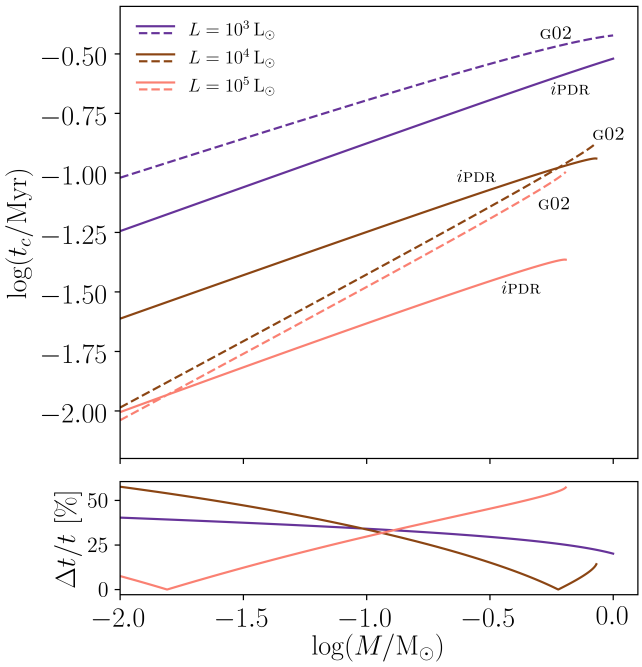

Figure 3.9: **Upper**: Clump evaporation time as a function of clump mass in the stellar case for different source luminosities, for fixed distance from the source (0.3 pc). The solid line representes our modified iPDR model, where we neglect ionizing radiation, the dotted line is the Gorti & Hollenbach (2002) model. **Lower**: Relative difference between the two models $\Delta t/t = (t_{\mathrm{G02}} - t_{i\mathrm{PDR}})/\max(t_{\mathrm{G02}}, t_{i\mathrm{PDR}})$.

$L = 1 \times 10^4\,\mathrm{L}_\odot$, $L = 5 \times 10^4\,\mathrm{L}_\odot$ and $L = 1 \times 10^5\,\mathrm{L}_\odot$. We assume the clump is located 0.3 pc from the source, since this distance is smaller than the Strömgren radius for every star in our set (for the fainter star the Strömgren radius is $R_{Str} \simeq 0.75$ pc for a gas density $n = 10\ \mathrm{cm}^{-3}$). The BE masses for the collapse of molecular clumps at 10 K are around few tenths of solar masses, and for each luminosity we consider only clumps with mass below that limit.

The time evolution of the molecular core radius is shown in Fig. 3.8 (left panel), where a clump of initial mass $M = 0.1\,\mathrm{M}_\odot$ is exposed to the stellar radiation field for the different luminosities considered. The radius has a similar evolution for the different luminosities, with a shorter time-scales for larger luminosities. Consider for example the (brown) curve for $L = 10^4\,\mathrm{L}_\odot$. A clump with mass $0.1\,\mathrm{M}_\odot$ at the distance of 0.3 pc has an initial radius of 0.023 pc when it is in pressure equilibrium with the ICM. In the shock contraction phase, the radius reduces to 6×10^{-4} pc in about 6000 yr because of the shock waves driven by the heated HI and HII shells. Then the expansion phase follows, and the core expands allowing the impinging radiation to penetrate and dissociate the molecules. This occurs

significantly after the radius reaches its maximum value $r \simeq 0.025$ pc.

While the contraction phase has almost the same duration for the tracks of the three more intense sources, we see that it takes more time for the $10^3\,L_\odot$ star. In fact for this source the ionization fraction is low (see Fig. 3.3), since the temperature of the HII shell is only about 900 K. The shock driven by the HII shell is weak for this star, and needs more time to reach the centre of the core.

The lifetime of a clump (t_c) is defined as the time when the core radius goes to zero. In Fig. 3.8 (right panel) we show t_c as a function of the clump mass and the source luminosity, at the same distance to the source (0.3 pc).

Gorti & Hollenbach (2002, hereafter G02) compute the lifetime of clumps located in a stellar PDR, in the absence of ionizing radiation. They account for photoevaporation by assuming that the clump continuously loses mass at a rate

$$\frac{\mathrm{d}M}{\mathrm{d}t} = -4\pi\rho_c r_c^2(t) c_{\mathrm{PDR}} \ , \tag{3.21}$$

where ρ_c is the mean mass density of the clump, and c_{PDR} the sound speed in the PDR of the clump. This implies that the clump loses mass also in the shock-compression phase. G02 do not account for the shock reflection at the centre of the clump, so that the core does not expand after the compression phase. On the other hand, in our treatment, photoevaporation is negligible while the clump is being compressed, and the shock reflection allows for the following expansion of the core. As a result, radiation is allowed to penetrate and dissociate the molecules only when the gas is sufficiently expanded and diluted. Furthermore, G02 find that under certain initial conditions* there is no shock-compression, since the shock suddenly stalls just after its formation, and the clump directly expands and photoevaporates. In our treatment, we do not recover this scenario, since we always allow the shock to reach the centre of the core. Magnetic and turbulent contribution to pressure are included by G02, but not in this work.

In Fig. 3.9 we compare our predictions for the photoevaporation time (without ionizing radiation) with those from the G02 model. A range of clump masses between $0.01\,M_\odot$ and the BE mass is considered, at a distance of 0.3 pc, for three different source luminosities, A modification in our code for iPDR is required, since the HII shell is not present when ionizing radiation is absent. In the G02 model, the $10^4\,L_\odot$ and the $10^5\,L_\odot$ sources induce a shock-compression in the clump, while instead they predict an initial expansion for the $10^3\,L_\odot$ case. The evaporation time-scale for the low-L case differs by an order of magnitude with respect to the other two. In our model we do not find such dichotomy, and the

*According to Gorti & Hollenbach (2002), a clump undergoes a shock-compression only if its mean column density is

$$n r_c < 2.7 \times 10^{21}\,\mathrm{cm}^{-2}\,(c_{\mathrm{PDR}}/c_{\mathrm{H_2}})^3 \ .$$

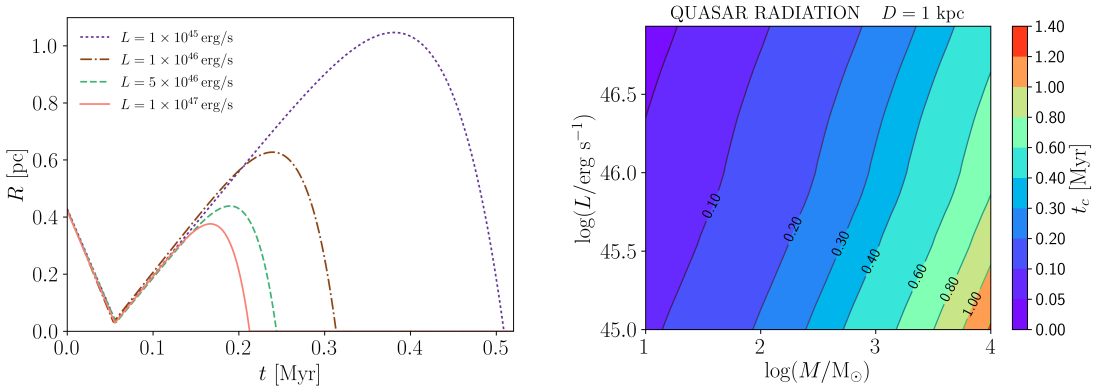

Figure 3.10: **Left** panel: radius (R) of the molecular core of a clump as a function of time, when the clump is exposed to quasar radiation. The clump has a mass of $10^3\,\mathrm{M_\odot}$ and different luminosities are considered. **Right** panel: Lifetime (t_c) of a clump exposed to the radiation of a quasar, for a range of values of the initial clump mass and different source luminosities. The distance of the clump from the source is fixed at 1 kpc.

	L	F_{ion} ⋆	G_0
OB star (0.3 pc)	$10^3\,\mathrm{L_\odot}$	0.006	80
	$10^4\,\mathrm{L_\odot}$	0.5	1.2×10^3
	$10^5\,\mathrm{L_\odot}$	14	9.5×10^3
Quasar (1 kpc)	$10^{45}\,\mathrm{erg\,s^{-1}}$	3.4	6×10^2
	$10^{46}\,\mathrm{erg\,s^{-1}}$	34	6×10^3
	$10^{47}\,\mathrm{erg\,s^{-1}}$	340	6×10^4

Table 3.2: FUV and ionizing fluxes at a distance $D = 0.3$ pc in stellar and $D = 1$ kpc in the quasar case. F_{ion} is in units of $\mathrm{erg\,s^{-1}\,cm^{-2}}$, G_0 is in units of the Habing flux.

evaporation time smoothly increases with L. However, the lifetimes are in agreement within a factor of 2 with those found in G02.

Finally, we make a comparison between the evaporation times obtained with our full iPDR model (see Fig. 3.8) and our model without ionizing radiation, i.e. with no HII shell (see Fig. 3.9). Clump lifetimes are always shorter when we consider the ionizing part of the spectrum, generally by a factor between 2 and 4 depending on clump mass and luminosity. This behaviour is expected, since the outer shell of the clump is heated to an high temperature and a stronger and faster shock propagates into the clump, decreasing its evolution time-scale.

3.3.2 Quasar case

We now describe the evolution of a clumps forming in the ionized outflows of quasars. We choose 1 kpc as a typical distance of a molecular clump from the source, that is of the order of the critical radius (eq. 3.1). The mass of clumps has been estimated by

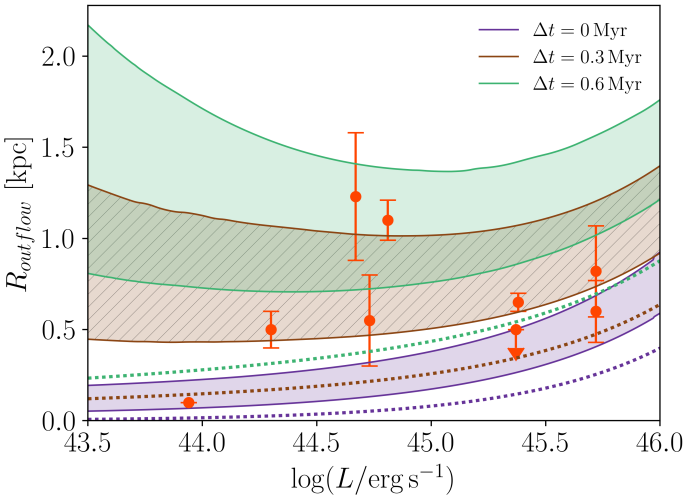

Figure 3.11: Extension of the molecular outflow for quasars with a range of luminosities, according to our photoevaporation model, assuming that clumps with masses in the range $M_c = 0.1 - 0.9\ M_{\rm BE}$ ($M_{\rm BE}$ is the BE mass for collapse) form at the contact discontinuity (CD) between the wind and the ISM around the quasar. The violet dotted line is the initial position of the CD (i.e. the critical radius of the outflow), while the brown dotted and the green dotted lines are the position of the CD after a time $\Delta t = 0.3$ Myr and $\Delta t = 0.6$ Myr respectively. Shaded regions are the maximum distance that a clumps with masses in the considered range can travel before being completely photoevaporated, as a function of quasar luminosity, assuming that they form at the corresponding (same line color) CD position.

Zubovas & King (2014) to be around $8600\,\mathrm{M}_\odot$, thus we consider masses up to $10^4\,\mathrm{M}_\odot$. The ICM is the hot ionized medium of the wind, with temperature $T_{\rm ICM} \simeq 2.2 \times 10^7$ K, and density $n_{\rm ICM} \simeq 60$ cm^{-3} at 1 kpc from the source. As explained in Sec. 3.2.1, we assume that the clump is in pressure equilibrium with the ICM until its temperature reaches 10^4 K (when the clump gas is still in atomic form). Afterwards, the gas turns into molecular form ($T_{\rm H_2} = 100$ K) in a very short time-scale, so that the density profile remains unchanged with respect to the 10^4 K BE sphere. We apply our model to quasars with bolometric luminosities $L = 1 \times 10^{45}\,\mathrm{erg\,s^{-1}}$, $L = 1 \times 10^{46}\,\mathrm{erg\,s^{-1}}$, $L = 5 \times 10^{46}\,\mathrm{erg\,s^{-1}}$ and $L = 1 \times 10^{47}\,\mathrm{erg\,s^{-1}}$, with a spectral energy distribution given by eq. 3.4.

The evolution of the molecular core radius of the clump is shown in the left panel of Fig. 3.10, while the right panel shows the lifetime of a clump at a distance of 1 kpc from a quasar, as a function of clump mass and source luminosity. Similarly to clumps around stars, the core radius presents a contraction phase followed by an expansion phase, where the core is dissociated and then ionized. Notice that the evaporation time is about ten times longer than in the stellar case, although the clump mass considered is about 10^4 times larger. This is because both the FUV and ionizing radiation field are much more

intense since the quasar spectrum extends to very high energies (see Tab. 3.2 for reference values of the fluxes). This implies a higher temperature of the HII and HI shells, and a stronger compression ratio of the shock waves originating at the discontinuities.

Observations have detected molecular gas only up to a maximum distance of few kpc from quasars (Cicone et al., 2014, hereafter C14). Photoevaporation has sometimes been invoked as an explanation for such limited extension. We have slightly modified our code to account for the fact that radiation intensity decreases as the clump moves away from the source, being carried by the outflow. Ferrara & Scannapieco (2016) have shown that molecular clumps forming at the base of the adiabatic outflow are ablated in a short time because of the friction by hot flowing gas. Therefore, we analyse the alternative scenario in which clumps form within the outflow, so that they are at rest with the outflow and they are not subject to a strong acceleration. In this way our model is able to predict the distance travelled by a clump during its lifetime, and we can compare this length with observations of molecular outflow extensions.

We consider a subset of active galactic nuclei (AGNs) listed in C14 (Table 1.4). In Fig. 3.11 we plot the outflow extension obtained with our photoevaporation model as a function of source luminosity. We study clumps with 90% of their BE mass for collapse (i.e. the most massive clumps that do not collapse), forming at the contact discontinuity (CD) between the quasar wind and the surrounding ISM. According to King (2010) model, the initial position of the CD coincides with the critical radius R_c given in eq. 3.1, and it moves at a speed

$$v_{\rm CD} = 875\,\sigma_{200}^{2/3}\,{\rm km\,s^{-1}} \tag{3.22}$$

in the energy-driven phase. In Fig. 3.11 the dotted lines correspond to the position of the CD at different times, while the shaded regions represent the maximum distance that clumps with a range of masses (0.1-0.9 times their Bonnor-Ebert mass) can travel before photoevaporating. The observed extension of the outflows in the considered quasar sample exceed the maximum distance travelled by clumps before they are photoevaporated, if they form at R_c. This implies that there is no mechanism more efficient than photoevaporation in destroying molecular clumps. On the other hand, the existence of outflows with large extensions (up to 1 kpc) suggests that clumps continue to form within the outflow, when the CD moves outwards from its initial position. This can bee see from the other two cases shown in Fig. 3.11 where we consider also clumps formed at a later times when the CD has moved to a radius $R_c + v_{\rm CD}\Delta t$, with $\Delta t = 0.3, 0.6$ Myr. It appears that such delayed formation via thermal instabilities in the outflow can match the observed extensions.

3.4 Summary

In this Chapter, we have studied the evolution of molecular clumps exposed to radiation having both a far ultraviolet (FUV) and an ionizing component, determining the formation of an ionization/photodissociation region (iPDR) at the surface of clumps. The cases of a clump forming in the surroundings of an OB stars and a clump forming in the fast outflow of a quasar are studied separately. The clump is assumed to be an isothermal Bonnor-Ebert sphere with a mass lower than the critical mass for collapse. We assume a sudden heating scenario, inducing a shell structure in the clump, and then we analyse the evolution of its radius and density profile as a function of time, finally computing the clump lifetime (i.e. the time at which the molecular gas in the clump is completely dissociated). The clump evolution is solely determined by two parameters: its mass, M, and the bolometric luminosity L of the source.

We show that the pressure difference between adjacent layers causes the propagation of shock and rarefaction waves into the clump. The core shrinks until the shock wave hits the centre and reflects back, while the external layers expand and become eventually transparent to radiation. The dense core is thus surrounded by a diluted medium and it starts an expansion phase. As a result, the core density decreases and the radiation propagates in the interior, progressively evaporating the whole core. In this analysis we have not included gravity effects which could limit the expansion following the shock-contraction phase of clumps. Gravity may also play a role for the clumps that become gravitationally unstable during the contraction phase, possibly triggering star formation (Bisbas et al., 2011; Walch et al., 2012).

In the stellar case, we find that a higher luminosity speeds up considerably the shock-contraction phase: clumps of 0.1 $M_\odot$ at 0.3 pc from the source evaporate in 0.01 Myr for the brightest star considered ($10^5\,L_\odot$), while it takes 0.06 Myr in the case of the $10^3\,L_\odot$ star. Indeed, the radiation from the fainter star is not able to completely ionize the surface layer of the clump, resulting in a lower pressure of the HII shell and a weaker shock-induce contraction phase.

Our model agrees within a factor of 2 with the Gorti & Hollenbach (2002, G02) model, in the case of clumps embedded in the PDR of a massive star and in absence of ionizing radiation. The main difference between the two models is the evaporation channel. In G02 evaporation is due to a constant mass flow from the clump surface; in our model the clump evaporates as a consequence of the expansion and dilution driven by the reflected shock wave. We also notice that, in the absence of ionizing radiation, evaporation times are always longer by a factor $2-4$ with respect to the full iPDR model including both FUV and ionizing radiation. Therefore, considering ionizing radiation is important, since the evolution history of clumps is significantly modified.

In the context of high-redshift galaxies, this is significant for far infrared (FIR) emission, as [CII]. Indeed, most of the [CII] emission from high-redshift galaxy seems to be due to molecular clumps (Yue et al., 2015; Vallini et al., 2015; Pallottini et al., 2017a) and because of the high radiation field observed in such galaxies (Inoue et al., 2016; Carniani et al., 2017), photoevaporation can play an important role. While Vallini et al. (2017) analyses the effect of clump photoevaporation using a time evolution based on G02, we argue that shorter photoevaporation time-scales obtained with our iPDR model could further affect the detectability of high-redshift galaxies. However, we underline that other effects are also important: the contrast with cosmic microwave background (CMB) attenuates the observed FIR emission for redshift $z \gtrsim 5$ (Da Cunha et al., 2013; Zhang et al., 2016), which is relevant for low density gas ($n < 0.1\,\mathrm{cm}^{-3}$, Vallini et al., 2015; Pallottini et al., 2015), while CO destruction by cosmic rays may enhance [CI] and [CII] emission (Bisbas et al., 2015).

The evolution in the quasar context is characterized by a similar behaviour. The duration of the contraction phase is roughly constant for different L, since all the quasars in the set are able to completely ionize and heat to about 10^4 K the outer shell of the clump. We obtain evaporation times of 0.21 Myr for the $10^{47}\,\mathrm{erg\,s}^{-1}$ quasar and 0.51 Myr for the $10^{45}\,\mathrm{erg\,s}^{-1}$ quasar. With comparison to the stellar case, the evaporation times are longer only by a factor ~ 10, even though the clumps in the quasar case are $\simeq 10^4$ times more massive. This is consistent with the higher UV fluxes produced by quasars in spite of the larger spatial scales of the problem (see Tab. 3.2).

Applying our algorithm to clumps embedded in quasar outflows, we have been able to predict the outflow extension. This is set by the maximum distance travelled by clumps before photoevaporating, assuming that they form at the contact discontinuity (CD) between the quasar wind and the ISM. We find that the observed molecular outflow extensions are always larger than the distance travelled by clumps forming at the initial position of CD, but they are compatible with clumps forming at the CD with a time delay $\Delta t \simeq 0 - 0.6$ Myr after the outflow has entered the energy-driven phase. Therefore, we argue that:

- photoevaporation must be a crucial mechanism involved in the evolution of molecular gas structures in quasars, since none of the observed outflows has a smaller extension than what predicted with our photoevaporation model;
- clumps need to form continuously within outflows, when the CD has moved farther from the quasar, in order to explain the most extended outflows.

A more comprehensive analysis of quasar outflows should consider a distribution of clump masses, the contribution of scattered light in a clumpy medium and the possible occurrence

of star formation within the outflow (Maiolino et al., 2017; Gallagher et al., 2019; Rodríguez del Pino et al., 2019).

Chapter 4

Numerical simulations of photoevaporating clouds

4.1 Introduction

Stars are known to form in clusters inside giant molecular clouds (GMCs), as a consequence of the gravitational collapse of overdense clumps and filaments (Bergin et al., 1996; Wong et al., 2008; Takahashi et al., 2013; Schneider et al., 2015; Sawada et al., 2018). The brightest (e.g. OB) stars have a strong impact on the surrounding interstellar medium (ISM), since their hard radiation field ionizes and heats the gas around them, increasing its thermal pressure. As a result, the structure of the GMC can be severely altered due to the feedback of newly formed stars residing inside the cloud, with the subsequent dispersal of low density regions. Collapse can then occur only in dense regions able to self-shield from impinging radiation (Dale et al., 2005, 2012a,b; Walch et al., 2012).

The ISM within the Strömgren sphere around a star-forming region is completely ionized by the extreme ultra-violet (EUV) radiation, with energy above the ionization potential of hydrogen ($h\nu > 13.6$ eV). The typical average densities of H II regions are $\langle n \rangle \simeq 100$ cm^{-3}: this results in ionization fractions $x_{\rm HII} < 10^{-4}$ and a final gas temperature $T > 10^{4-5}$ K. Far-ultraviolet (FUV) radiation (photon energy $6\,\mathrm{eV} < h\nu < 13.6\,\mathrm{eV}$) penetrates beyond the H II region, thus affecting the physical and chemical properties of the ISM up to several parsecs. This region is usually referred to as the Photo-Dissociation Region (PDR; Tielens & Hollenbach, 1985; Kaufman et al., 1999; Le Petit et al., 2006; Bron et al., 2018). Typical fluxes in the FUV band due to OB associations may have values as high as $G_0 = 10^{4-5}$ (Marconi et al., 1998), in units of the Habing flux[†]. As detailed in Sec. 1.8, PDR is characterised by a layer with neutral atomic hydrogen, photo-dissociated by Lyman-Werner photons ($11.2\,\mathrm{eV} < h\nu < 13.6\,\mathrm{eV}$), and a deeper layer where gas self-

[†]The Habing flux ($1.6 \times 10^{-3}\,\mathrm{erg\,s^{-1}cm^{-2}}$) is the average interstellar radiation field of our Galaxy in the range [6 eV, 13.6 eV] (Habing, 1968)

shielding allows hydrogen to survive in molecular form. There are many observational evidences that the structure of PDRs are not homogeneous, with gas densities spanning many orders of magnitude from 10^2 cm^{-3} to 10^6 cm^{-3}. In particular, small isolated cores of few solar masses and sizes ~ 0.1 pc are commonly observed (Reipurth, 1983; Hester et al., 1996; Huggins et al., 2002; Mäkelä & Haikala, 2013). Radiative feedback by FUV radiation could explain their formation via shock-induced compression (Lefloch & Lazareff, 1994).

The effect of FUV radiation on clumps is twofold: (1) FUV radiation dissociates the molecular gas, which then escapes from the clump surface at high velocity (photoevaporation); (2) radiation drives a shock which induces the clump collapse (radiation-driven implosion, RDI), as we have analysed in-depth in Chap 4. The first effect reduces the clump molecular mass, hence decreasing the mass budget for star formation within the clump. Instead, the latter effect may promote star formation by triggering the clump collapse. Hence, the net effect of radiative feedback on dense clumps is not trivial and deserves a careful analysis.

The flow of gas from clumps immersed in a radiation field has been studied by early works both theoretically (Dyson, 1968; Mendis, 1968; Kahn, 1969; Dyson, 1973) and numerically (Tenorio-Tagle, 1977; Bedijn & Tenorio-Tagle, 1984). Bertoldi (1989) and Bertoldi & McKee (1990) developed semi-analytical models to describe the photoevaporation of atomic and molecular clouds induced by ionizing radiation. In their models they also include the effects of magnetic fields and self-gravity. They find that clumps settle in a stationary cometary phase after the radiation-driven implosion, with clump self-gravity being negligible when the magnetic pressure dominates with respect to the thermal pressure (i.e. $B > 6\,\mu$G), or when the clump mass is much smaller than a characteristic mass $m_{\rm ch} \simeq 50\,{\rm M}_\odot$. They focused on gravitationally stable clumps, thus their results are not directly relevant for star formation.

Later, the problem was tackled by Lefloch & Lazareff (1994), who performed numerical simulations which however only included the effect of thermal pressure on clump dynamics. Gravity was then added for the first time by Kessel-Deynet & Burkert (2003). For an initially gravitationally stable clump of 40 M$_\odot$, they find that the collapse can be triggered by the RDI; nevertheless, they notice that the collapse does not take place if a sufficient amount of turbulence is injected ($v_{\rm rms} \simeq 0.1\,$km/s). Bisbas et al. (2011) also ran simulations of photoevaporating clumps, with the specific goal of probing triggered star formation. They find that star formation occurs only when the intensity of the impinging flux is within a specific range ($10^9\,{\rm cm}^{-2}{\rm s}^{-1} < \Phi_{\rm EUV} < 3\times10^{11}\,{\rm cm}^{-2}{\rm s}^{-1}$ for a $5\,{\rm M}_\odot$ initially stable clump [*]). All these works include the effect of ionizing radiation only, while FUV

[*] Assuming for example the spectrum of a $10^4\,{\rm L}_\odot$, this EUV flux corresponds roughly to a flux $G_0 = 10 - 3\times10^4$ in the FUV band.

radiation feedback is instead relevant for clumps located outside the H II region of a star (cluster).

In our previous work (Decataldo et al., 2017, see Chap. 3), we have constructed a 1D numerical procedure to study the evolution of a molecular clump, under the effects of both FUV and EUV radiation. We have followed the time evolution of the structure of the iPDR (ionization-photodissociation region) and we have computed the photoevaporation time for a range of initial clump masses and intensity of impinging fluxes. However, since Decataldo et al. (2017) did not account for gravity, H_2 dissociation is unphysically accelerated during the expansion phase following RDI. Those results have been compared with the analytical prescriptions by Gorti & Hollenbach (2002), finding photoevaporation times in agreement within a factor 2, although different simplifying assumptions where made in modelling the clump dynamics.

The same setup by Decataldo et al. (2017) has been used by Nakatani & Yoshida (2018) to run 3D simulations with on-the-fly radiative transfer and a chemical network including H^+, H_2, H^+, O, CO and e^-. Without the inclusion of gravity in their simulations, they find that the clump is confined in a stable cometary phase after the RDI, which lasts until all the gas is dissociated and flows away from the clump surface. Nevertheless, they point out that self-gravity may affect the clump evolution when photoevaporation is driven by a FUV-only flux, while the EUV radiation produces very strong photoevaporative flows which cannot be suppressed by gravity.

In the current Chapter, we attempt to draw a realistic picture of clump photoevaporation by running 3D hydrodynamical simulations with gravity, a non-equilibrium chemical network including formation and photo-dissociation of H_2, and an accurate radiative transfer scheme for the propagation of FUV photons. We focus on the effect of radiation on Jeans-unstable clumps, in order to understand whether their collapse is favoured or suppressed by the presence of nearby stars emitting in the FUV range.

4.2 Simulation suite

For our simulations, we have used a customised version of RAMSES-RT in order to add a more accurate treatment of the chemistry of the ISM, by coupling the radiative transfer module with KROME. The details on the chemical network implemented and the coupling between RAMSES-RT and KROME are discussed in Sec. 2.3 and 2.4.

Given the chemical network and the included reactions, KROME can be set with an arbitrary number of photon energy bins. In the particular context of photoevaporating clumps, we decided to make only use of two bins with energies in the FUV (far ultra-violet) domain, i.e. [6.0 eV, 11.2 eV] and [11.2 eV, 13.6 eV]. As we consider molecular clumps located

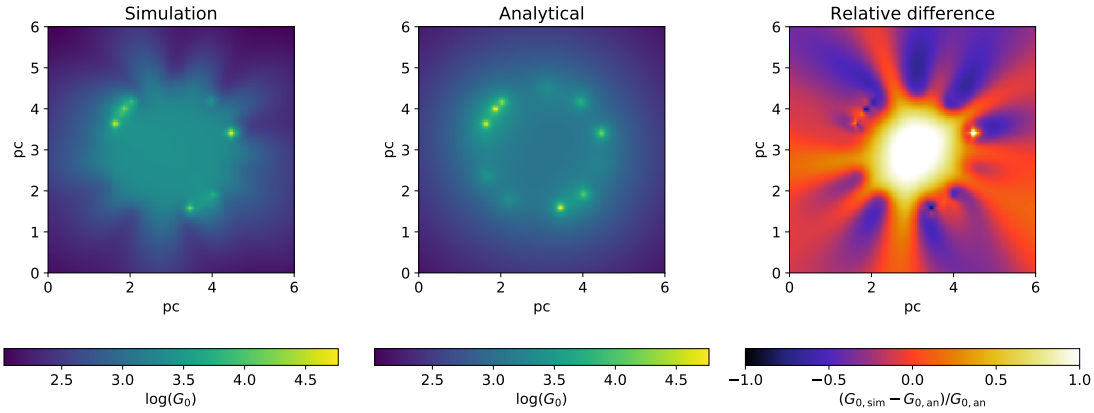

Figure 4.1: Comparison between the radiation field obtained in the simulation and the radiation field obtained analytically, for a domain with homogeneous gas density (100 cm^{-3}) and no dust. **Left**: Total flux in the FUV band in a slice of the computational domain. **Middle**: analytical result for the same configuration of the simulation. **Right**: relative difference between simulated and analytical radiation fields.

outside stellar H II regions, we expect that EUV radiation does not reach the surface of the clump. On the other hand, we neglect photons with energies < 6.0 eV since they do not take part in any chemical reactions of interest in our case.

4.2.1 Opposite colliding beams problem

Radiative transfer codes based on the M1 closure relations give unexpected results when radiation beams that travel in opposite directions collide (see González et al. 2007; Aubert & Teyssier 2008 and Rosdahl et al. 2013, in particular their Fig. 1). The flux in the computational domain can be different to what expected by summing the flux of the single beams, showing an excess in the direction perpendicular to the beams.

With the purpose of testing the behaviour of the radiation field for the setup of our simulations, we have run a simulation with resolution 128^3, with 50 stars with luminosity $10^4\,\mathrm{L}_\odot$ at a distance of 1.5 pc from the box centre and constant gas density inside the whole domain ($n = 10^{-3}$ cm^{-3}). Dust is not included and gas absorption is negligible at this density, so the Habing flux can be easily calculated analytically for comparison: the flux in every cell is computed by summing the contribution to the flux from all sources, by scaling it with the square root of the distance.

The result after a time sufficient for radiation to cross the whole domain is showed Fig. 4.1, where flux in the FUV band (left panel) is compared with the analytical solution for the same setup (middle panel). From the map of the relative difference between the two (right panel), we observe that there is a factor of 2 at most. Nevertheless, in the region inside the spherical shell where stars reside, the flux is rather homogeneous. Hence, despite the opposite colliding beams problem, we can carry out our simulations accounting

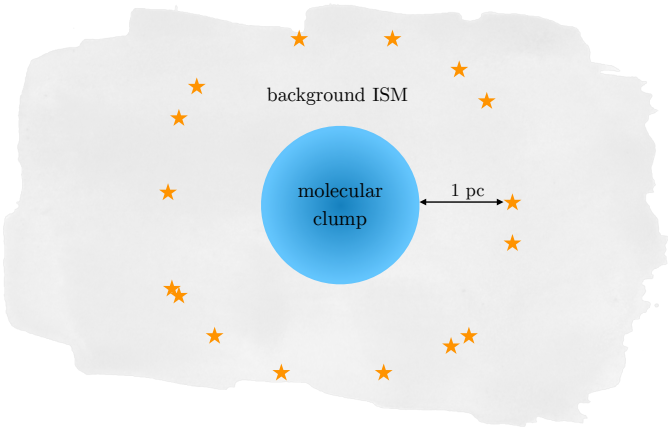

Figure 4.2: Sketch of the simulation set-up. The clump is located at the centre of a box with size 6 pc, filled with a background medium with number density 100 cm^{-3}. 50 stars are placed at a distance of 1 pc from the surface of the clump, randomly distributed on the surface of a sphere.

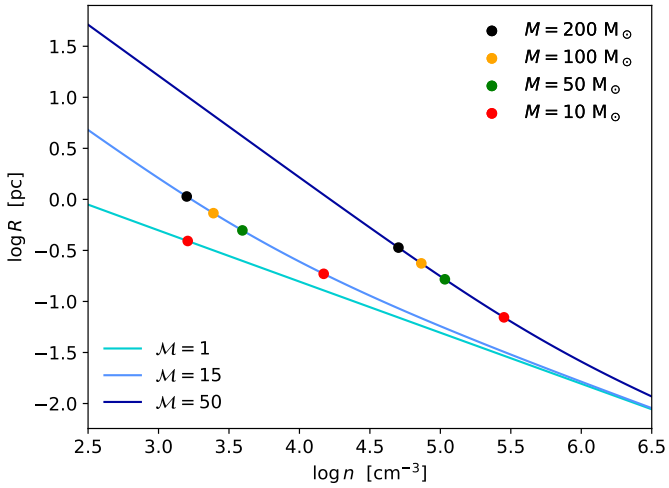

Figure 4.3: Relation between the radius R and the number density n of clumps residing in the parent Giant Molecular Cloud (GMC) with different Mach numbers $\mathcal{M}$. The GMCs have all the same size $L = 25$ pc and temperature $T = 10$ K. For each GMC, the position in the diagram of clumps with different masses is shown with coloured points.

for the fact that the flux on the clump is higher than what expected from an analytical prescription.

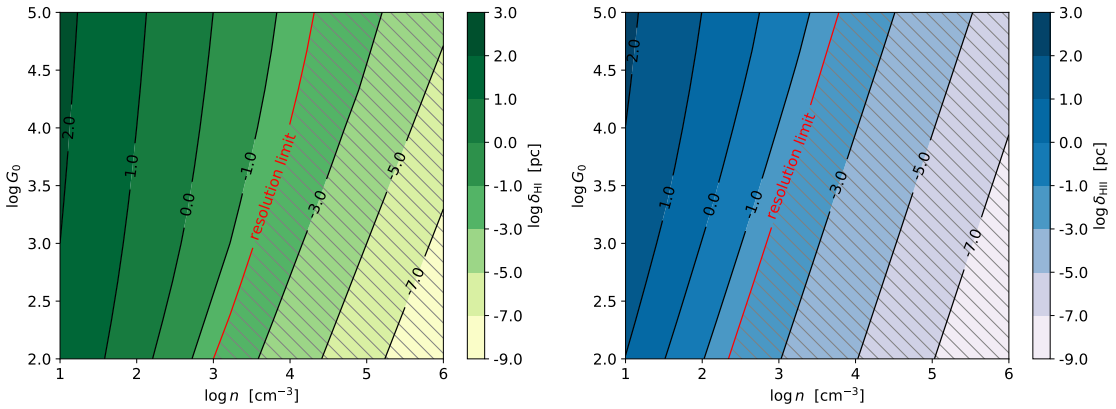

Figure 4.4: **Left**: Depth of the H I /H_2 transition (δ_{HI}) in a slab of molecular gas, as a function of the gas number density (n) and the FUV flux (G_0). The red solid line marks the maximum resolution of our simulations $\Delta x = 0.023$ pc (corresponding to 2^8 cells). The hatched region highlights the portion of the G_0-n diagram where our simulations would not be able to properly resolve δ_{HI}. **Right**: Same plot with the depth of the H II /H I transition (δ_{HII}) in a slab of neutral atomic gas.

	M [$M_\odot$]	R [pc]	$\langle n \rangle$ [cm^{-3}]	n_c [cm^{-3}]	t_{ff} [Myr]	G_0
`clump_M50_noRad`	50	0.5	3.9×10^3	6.6×10^3	0.81	0
`clump_M50_G2e3`	50	0.5	3.9×10^3	6.6×10^3	0.81	2×10^3
`clump_M50_G3e4`	50	0.5	3.9×10^3	6.6×10^3	0.81	3×10^4
`clump_M50_G8e4`	50	0.5	3.9×10^3	6.6×10^3	0.81	8×10^4
`clump_M10_G3e4`	10	0.2	1.5×10^4	2.1×10^4	0.41	3×10^4
`clump_M100_G3e4`	100	0.7	2.5×10^3	4.4×10^3	1.01	3×10^4
`clump_M200_G3e4`	200	1.0	1.6×10^3	3.3×10^3	1.26	3×10^4

Table 4.1: Summary of the 3D simulation run in this work. Given a mass M, the corresponding radius R and density (average number density $\langle n \rangle$ and central number density n_c) are determined, as detailed in Sec. 4.3.1. Simulations of clumps with the same mass differ for the intensity of the external source of FUV radiation G_0, that is calculated at the clump surface (see Sec. 4.3.2). The free-fall time is also reported for reference.

4.3 Set-up of the simulations

4.3.1 Gas

The computational box is filled with molecular gas* of density $n = 100$ cm^{-3} and metallicity $Z = Z_\odot$. A dense clump ($n = 10^3 - 10^4$ cm^{-3}) is then located at the centre of the domain, with the same initial composition of the surrounding gas (Fig. 4.2).

Clumps in GMCs are self-gravitating overdensities. Observations of GMCs of different sizes and masses (Hobson, 1992; Howe et al., 2000; Lis & Schilke, 2003; Minamidani et al., 2011; Parsons et al., 2012; Liu et al., 2018; Barnes et al., 2018) show that clumps have a

*The gas has helium relative mass abundance $X_{He} = 25\%$.

wide range of physical properties: radii range from $0.1 - 10$ pc, densities can be $10 - 10^4$ times the average density of the GMC; typical masses range from few solar masses to few hundreds $M_\odot$.

The density distribution of clumps in GMCs has been studied with numerical simulations of supersonic magnetohydrodynamic turbulence (Padoan & Nordlund, 2002; Krumholz & McKee, 2005; Padoan & Nordlund, 2011; Federrath & Klessen, 2013), yielding a log-normal PDF (eq. 1.106) with variance given (eq. 1.107). Including self-gravity, the high-density end of the PDF is modified with a power-law tail $g(n) \sim n^{-\kappa}$, with $\kappa \sim 1.5 - \breve{}2.5$ (Krumholz & McKee, 2005; Padoan & Nordlund, 2011; Federrath & Klessen, 2013; Schneider et al., 2015). If a value n of the density is drawn from the PDF $g(s)$, the corresponding radius of the clump can be estimated with the turbulent Jeans length (Federrath & Klessen, 2012):

$$R = \frac{1}{2}\lambda_{\rm J} = \frac{1}{2}\frac{\pi\sigma^2 + \sqrt{36\pi c_s^2 G L^2 m_p \mu n + \pi^2\sigma^4}}{6GLm_p\mu n} \tag{4.1}$$

where c_s is the isothermal sound speed, L is the size of the GMC, m_p the proton mass and μ the mean molecular weight. The corresponding clump mass is estimated by assuming a spherical shape and uniform density.

In Fig. 4.3 the clump radius is plotted as a function of the number density, for different Mach numbers $\mathcal{M}$, GMC size fixed at $L = 25$ pc and c_s computed with a temperature $T = 10$ K and molecular gas ($\mu = 2.5$). The coloured points correspond to the position of clumps with different masses $M = 10 - 200\,M_\odot$ in the R-n diagram. In GMCs with the same Mach number, clumps with larger mass are less dense: indeed, as a rough approximation, we have that $R \propto n^{-1}$ and $M \sim m_p\mu n R^3 \propto n^{-2}$. It is also interesting to check how the properties of clumps with the same mass vary for different parent GMCs. Considering the 10 $M_\odot$ clump (red point), we notice that decreasing $\mathcal{M}$, its position in the R-n diagram shifts towards lower density and larger radius. Thus, in a $\mathcal{M} = 1$ cloud, clumps with mass higher than 10 $M_\odot$ would have a density as low as the average cloud density, implying that clumps more massive than 10 $M_\odot$ do not exist at all in such a cloud.

Here we consider clumps residing in a GMC with size $L = 25$ pc, average temperature $T = 10$ K and Mach number $\mathcal{M} = 15$. In particular, we explore the range of masses represented in Fig. 4.3, i.e. $M = 10, 50, 100, 200\,M_\odot$. Masses, radii and average densities of these clumps are summarised in Tab. 4.1. Clumps are modelled as spheres located at the centre of the computational box; their initial density profile is constant up to half of the radius, and then falls as a power law:

$$n(r) = \begin{cases} n_c & r < R/2 \\ n_c(2r/R)^{-1.5} & R/2 \leq r < R \end{cases}. \tag{4.2}$$

where for each clump the core density n_c is chosen such that the total mass is the selected one (Tab. 4.1). The profile in Eq. 4.2 has been used in simulations of molecular clouds (e.g. Krumholz et al., 2011) and it is physically motivated by observations of star-forming clumps (Beuther et al., 2002; Mueller et al., 2002). The choice of this profile implies that there is a discontinuity in the gas density (and so the pressure) at the interface with the external ISM. In the simulations, this will produce a slight expansion of the clump just before the stellar radiation hits the clump surface.

A turbulent velocity field is added to the clump in the initial condition. We generate an isotropic random Gaussian velocity field with power spectrum $P(k) \propto k^{-4}$ in Fourier space, normalising the velocity perturbation so that the virial parameter $\alpha = 5\, v_{\rm rms}^2\, R_c / G\, M_c$ is equal to 0.1, as measured for some clumps with mass around $10^2\,{\rm M}_\odot$ (e.g. Parsons et al., 2012). In three dimensions, the chosen power spectrum gives a velocity dispersion that varies as $\ell^{1/2}$ with ℓ the length scale, which is in agreement with Larson scaling relations (Larson, 1981).

4.3.2 Radiation sources

We set up a roughly homogeneous radiation field around the clump by placing 50 identical point sources (i.e. stars), randomly distributed on the surface of a sphere centred on the clump and with radius larger than the clump radius ($R_{\rm sources} = R_{\rm clump} + 1\,{\rm pc}$)*, as depicted in Fig. 4.2. Each star has a black body spectrum and a bolometric luminosity in the range $L_\star = 10^4 - 10^6\,{\rm L}_\odot$, according to the desired FUV flux at the clump surface (Tab. 4.1).

In our simulations we use the GLF scheme† for the propagation of photons, since it is more suitable for isotropic sources (while the HLL scheme introduces asymmetries, see Rosdahl et al. 2013). Our configuration of sources is prone to the problem of "opposite colliding beams" (Sec. 4.2.1), so the photon density is higher than expected in the cells where two or more fluxes come from opposite directions. To circumvent this issue, we compute the average flux on the clump surface at the beginning of the simulation, which could be higher than that expected from an analytical calculation. In Tab. 4.1 we list the resulting FUV flux at the clump surface, for the different setups.

4.3.3 Resolution

The coarse grid has a resolution of 128^3 cells, which implies a cell size $\Delta x_{\rm cell} \simeq 0.047$ pc. We include one AMR level according to a refinement criterion based on the H_2

*The choice of 1 pc as a distance of the sources from the clump is arbitrary. In fact the aim is to get a specific G_0 at the clump surface, which can be obtained either varying the source luminosity or the source distance. The number of sources is also not relevant, provided that it is large enough to ensure a nearly isotropic flux on the clump surface.

†To solve numerically the propagation of photons, different function for the intercell photon flux can be used. RAMSES-RT implements the Harten-Lax-van Lee (HLL) function (Harten et al., 1983; González et al., 2007) and the Global Lax Friedrich (GLF), obtained by setting the HLL eigenvalues to the speed of light.

abundance gradients: a cell is refined if the H_2 abundance gradient with neighbouring cells is higher than 10%. Thus the effective resolutions is increased up to 256^3 cells with size $\Delta x_{\rm cell} \simeq 0.023$ pc. For the control run without radiation, the resolution is increased by 4 additional levels of refinement in a central region of radius 0.05 pc.

The expected timescale of photoevaporation is of the order of 1 Myr (Gorti & Hollenbach, 2002; Decataldo et al., 2017). Simulations are carried out with a reduced speed of light $c_{\rm red} = 10^{-3}\,c$, where c is the actual speed of light, in order to prevent exceedingly small timesteps, which would result in a prohibitively long computational time. Indeed, timesteps are settled by the light-crossing time of cells in the finest grid, hence in our simulations $\Delta t \simeq 75$ yr with reduced speed of light. The reduced speed of light affects the results of simulations when $c_{\rm red}$ is lower than the speed of ionization/dissociation fronts (Deparis et al., 2019; Ocvirk et al., 2019), which is given by $v_{\rm front} = \phi/n$, where ϕ is the photons flux in $\rm cm^{-2}s^{-1}$. In our set of simulations, `clump_M50_G8e4` has the highest $G_0/\langle n\rangle$ ratio, yielding

$$v_{\rm front} = \frac{\phi}{n} \simeq \frac{1.6\times10^{-3}G_0}{\langle n\rangle\langle h\nu\rangle_{\rm FUV}} \simeq 10^9\,{\rm cm\,s^{-1}} > c_{\rm red} \tag{4.3}$$

This points out that the propagation of the dissociation front is not treated accurately in our simulations. Nevertheless, the dissociation front propagates at $v_{\rm front}$ only for a time around few kyr, after which the front stalls and the photoevaporation proceeds for about 0.1-1 Myr. Hence, most of the simulation is not influenced by the reduced speed of light approximation, and the error concerns only the speed of the dissociation front (and not the thermochemical properties of the photo-dissociated gas).

We have checked that the resolution of our simulation is sufficient to describe the effect of radiation on dense gas. In fact, FUV radiation dissociates and heats a shell of gas at the clump surface, hence the simulation is physically accurate only if the thickness of this layer is resolved. The thickness of the dissociated shell corresponds to the depth $\delta_{\rm HI}$ of the H I /H_2 transition in a PDR. An analytic approximation for the column density of the transition ($N_{\rm trans} = \delta_{\rm HI} n_{\rm H}$) is given by the expressions (Bialy & Sternberg, 2016)

$$N_{\rm trans} = 0.7\,\ln\left[\left(\frac{\alpha G}{2}\right)^{1/0.7} + 1\right]\left(1.9\times10^{-21}\,Z\right)^{-1}\,{\rm cm^{-2}} \tag{4.4}$$

$$\alpha G = 0.35 G_0 \left(\frac{100\ {\rm cm^{-3}}}{n_{\rm H}}\right)\left(\frac{9.9}{1+8.9\,Z/{\rm Z_\odot}}\right)^{0.37}. \tag{4.5}$$

This expression is obtained by considering the H_2 formation-dissociation balance in a slab of gas with constant density, accounting for H_2 self-shielding (Sternberg et al., 2014) and dust absorption, without the effect of cosmic rays.

In Fig. 4.4, we have plotted $\delta_{\rm HI}$ as a function of the FUV flux and the gas density. The SED of the impinging radiation is that of a $10^4\,{\rm L_\odot}$ star, with a distance scaled to obtain

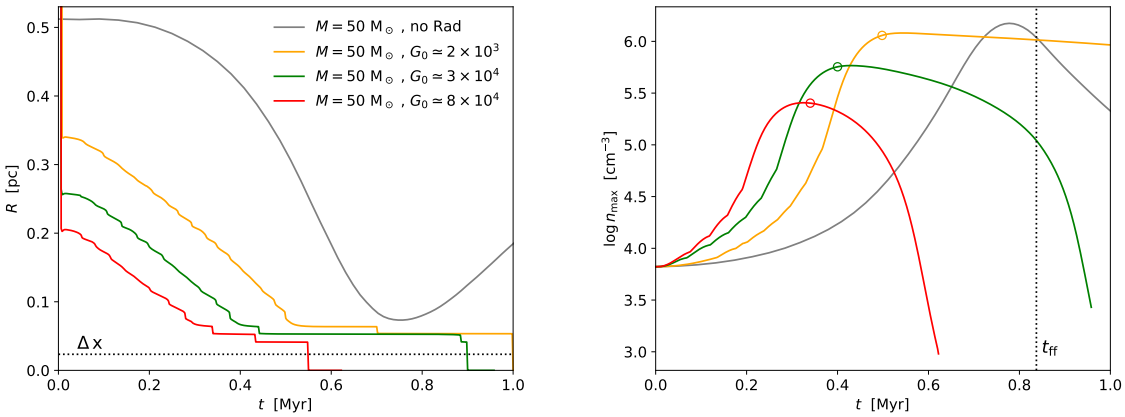

Figure 4.5: Comparison of the evolution of the $50\,M_\odot$ clump in the four simulations without radiation and with $G_0 \simeq 2\times10^3$, 3×10^4, 8×10^4. **Left**: variation with time of the clump radius. The radius is defined as the distance from the centre where 99.7% of the molecular gas mass is enclosed (apart from `clump_M50_noRad`, where it is defined as the distance from the centre where the density drops to 10% of the maximum value). **Right**: variation with time of the clump maximum density, with circles marking the time when the clump reaches its minimum radius, and gravitational collapse begins. The black dotted line marks the free fall time, computed with the initial average clump density.

the flux G_0 shown in the x axis of the plot. The red line marks the contour corresponding to the maximum resolution of our simulations, i.e. $\Delta x = 0.023$ pc. Hence, referring to Tab. 4.1 for the values of the mean density, $\langle n \rangle$, we can see that the effect of radiation on clumps with mass larger than 50 $M_\odot$ is well resolved for every value of G_0 of interest. Simulations with $M = 10, 50 M_\odot$ are close to the resolution limit if $G_0 < 10^4$. Keep in mind, though, that due to the imposed profile Eq. 4.2, the density in the outer regions is smaller than $\langle n \rangle$.

4.3.4 Set of simulations

We run in total seven 3D simulations of photoevaporating dense molecular clumps (Tab. 4.1). The first simulation of a 50 $M_\odot$ clump does not include radiation and it is used for comparison. Then we run a set of simulations of clumps with the same mass ($M = 50\,M_\odot$) and different intensities of the radiation field ($G_0 = 2\times10^3 - 8\times10^4$). Finally, in the last set of simulations, we consider clumps with masses varying in the range $M = 10 - 200\,M_\odot$ and constant impinging radiation ($G_0 \simeq 3\times10^4$).

4.4 Results - Fiducial clumps (50 $M_\odot$)

We study first the evolution of a fiducial clump with initial mass of $50\,M_\odot$. The clump has an initial radius $R = 0.5$ pc and a profile described by Eq. 4.2 with a core density

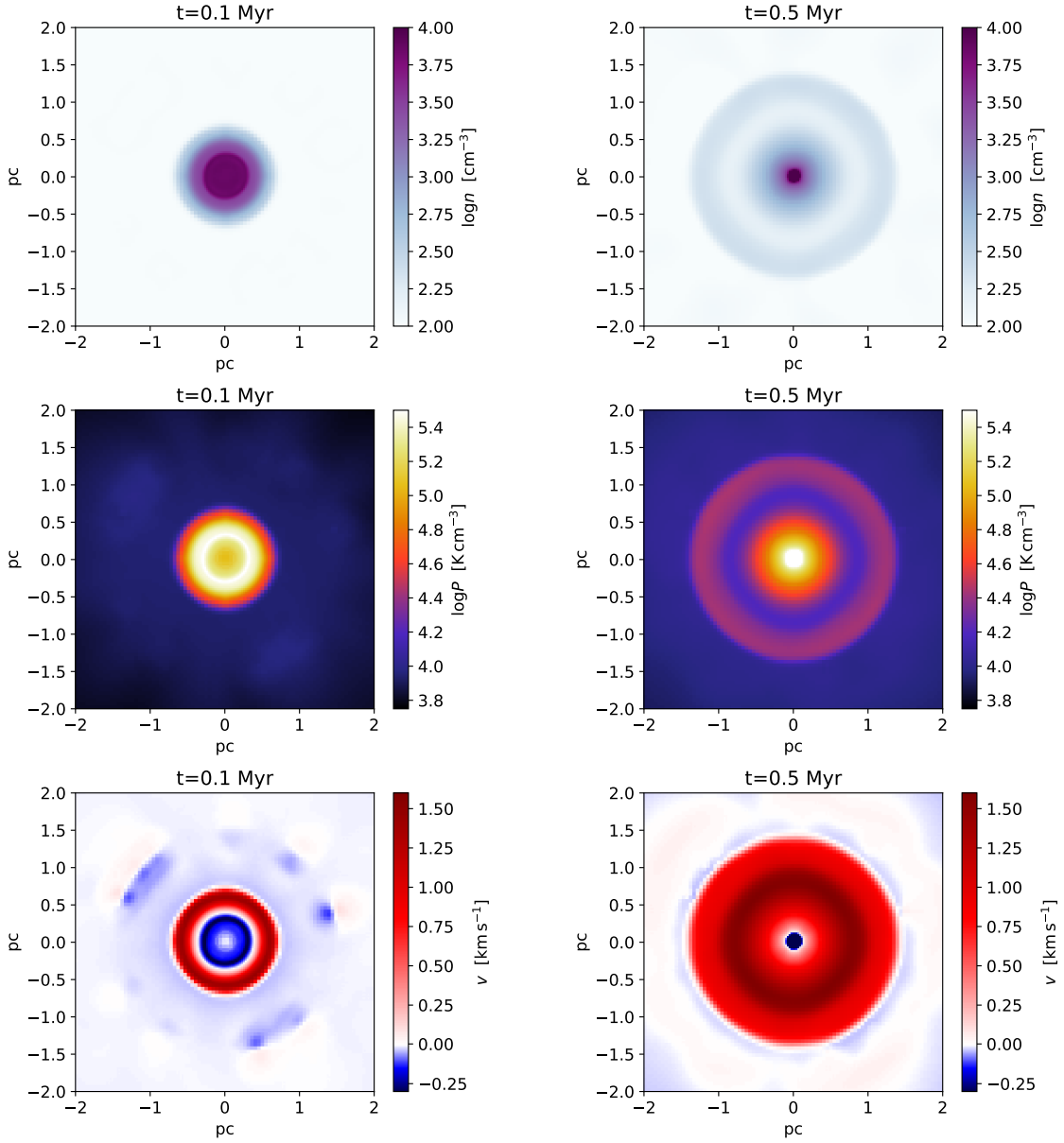

Figure 4.6: Snapshots of the simulation `clump_M50_G2e3` at times $t = 0.1$ Myr (left) and at $t = 0.5$ Myr (right), obtained by slicing the computational box through its centre. **Upper panels**: gas density (baryon number density n); for visualization purposes the colour range in the right panel is reduced with respect to the maximum density, $n_{\max} \simeq 6 \times 10^6$ cm^{-3}. **Central panels**: gas pressure normalized by the Boltzmann constant. **Bottom panels**: gas radial velocity, with the convention that gas flowing towards the centre has negative velocity, and outflowing gas has positive velocity.

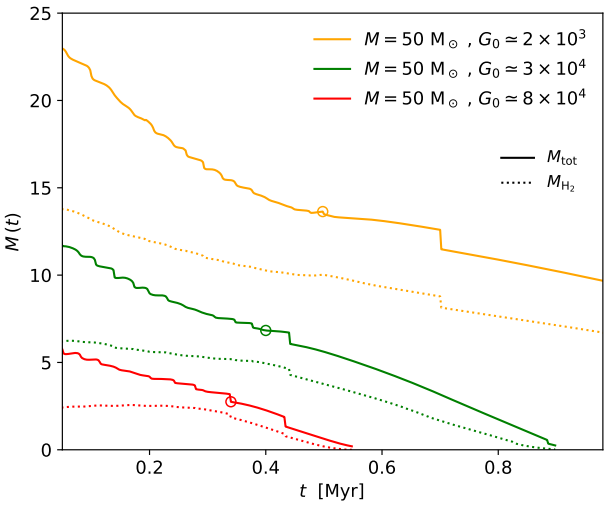

Figure 4.7: Total clump mass (solid line) and molecular mass (dotted line), as a function of time, for the the runs of a 50 $M_\odot$ clump with radiation. The simulations are stopped when the clumps reach a minimum radius and gravitational collapse begins.

$n_c \simeq 6.6 \times 10^3$ cm^{-3}. We run a simulation with no external radiation source, to be used as a control case. We then perform three simulations introducing a nearly isotropic radiation field with different intensities G_0.

The clump radius is defined as the distance from the centre where the 99.7% of the molecular gas mass is enclosed. In the run with no radiation, all the box is fully molecular, so we had to adopt a different definition of radius, namely where the H_2 density reaches 10% of its maximum value at the centre.

4.4.1 Run with no radiation

In Fig. 4.5, the clump without radiation sources is shown with grey lines: the plot tracks the evolution of the radius (left panel) and the central density (right panel). The radius decreases by a factor of 100 during the collapse, leading to an increase of the maximum core density by 3 orders of magnitude. The clump reaches the minimum radius slightly before the free-fall time $t_{\rm ff}$ (shown by the vertical dotted line in the right panel), and the maximum compression state is indicated by the grey circle. As opposed to works on protostellar accretion (Larson, 1969; Shu, 1977), we do not follow the clump evolution after the collapse, since our aim here is only to compare the implosion phase with that of clumps exposed to radiation.

4.4.2 Runs with different impinging flux

We now want to compare the gravity-only simulation with the simulations where radiation is impinging on the clump surface. For the three simulations `clump_M50_G2e3`,

`clump_M50_G3e4` and `clump_M50_G8e4`, the Habing flux G_0 through the clump surface is $\simeq 2 \times 10^3$, 3×10^4, and 8×10^4, respectively.

Slices of number density, thermal pressure and radial velocity for the $G_0 = 2 \times 10^3$ run are shown in Fig. 4.6, at times $t = 0.1$ Myr and $t = 0.5$ Myr. In the first snapshot ($t = 0.1$ Myr), it is possible to see that a thick layer of gas ($n \sim 500$ cm^{-3}) is pushed away at high velocity (Mach number $\mathcal{M} = 1.5$), due to the underneath high-pressure gas ($P \sim 3 \times 10^5$ K cm^{-3}). This is due to radiation heating the clump surface, so that the pressure is increased and drives an expansion of an outer shell of gas. On the other hand, the overpressure (seen as the highest pressure layer in the first snapshot) also drives a shock inward. The shocked gas is flowing towards the centre at a velocity that is higher than the rest of the clump gas, which is undergoing gravitational collapse. The qualitative behaviour of the gas is the same found in Decataldo et al. (2017), albeit that work considered the effect of ionizing radiation but no gravity. Nevertheless, the effect of the FUV radiation is qualitatively the same: a surface layer of the clump is heated, so that it expands and drives a shock towards the centre of the clump. In the second snapshot, the clump is collapsed to a dense small core, while the photoevaporating flow has reached a higher distance from the centre.

4.4.3 Radius and density evolution

In Fig. 4.5, the evolution of clump radius and clump central density are shown for all the four runs. The radius decreases suddenly from the initial value, because of the photodissociation front moving into the cloud as an R-type front: the molecular hydrogen is thus photodissociated and the gas remains almost unperturbed, until the flux is attenuated (both because of photodissociation and dust absorption) and the front stalls. This phase lasts few kyrs (see Eq. 4.3). After that, the front drives a shock front compressing the gas ahead of it (D-type shock front, Spitzer, 1998), so that the clump shrinks further because of the radiation-driven shock wave. Even if the flux is different in the 3 runs with radiation, the temperature at which the clump surface is heated does not vary much (200-250 K), hence the clump contraction proceeds almost at the same speed. The simulations are then stopped when the clump radius reaches a minimum of $\lesssim 2\Delta x_{\rm min}$, i.e. when the clump collapses to a size below the adopted resolution.

The right panel of Fig. 4.5 shows the clumps central density at different times. For the coloured lines, a circle marks the moment in which the clump has reached the minimum radius (i.e. about the size of a cell), and it corresponds to the higher compression state of the clump. The density reached in the implosion phase is lower when the radiation is stronger. This happens because for the simulations with strong flux the dissociated shell in the R-type phase is thicker, hence the remaining molecular collapsing core is less massive.

4.4.4 Mass evolution

In order to compare the efficiency of the photoevaporation process with different radiation intensities, we plot in Fig. 4.7 the total clump mass $M_{\rm tot}$ (solid line) and the H_2 mass M_{H_2} (dotted line) as a function of time.

The lines start from the time $t_{\rm R}$ which marks the end of the R-type dissociation front propagation. Subsequently, photodissociation continues at the surface of the clump, generating a neutral flow such that both $M_{\rm tot}$ and M_{H_2} decrease with time. Notice that the ratio $M_{\rm tot}/M_{H_2}$ is not constant, since the clump molecular fraction x_{H_2} changes with time, even in the interior of the clump.

In particular, x_{H_2} is lower just after the R-type phase, when clumps have lower density. Indeed, both the bins [6.0, 11.2] eV (bin a) and [11.2, 13.6] eV (bin b, corresponding to Lyman-Werner band) play a role in the dissociation of H_2, as we have verified in some test simulations with only one radiation bin: the bin b dissociates the H_2 through the Solomon process, while the bin a causes an increase of the gas temperature, hence increasing the collisional dissociation of H_2. While the absorption of radiation in the bin b is very strong because of H_2 self-shielding, radiation in the bin a is basically absorbed by dust only* and can penetrate even in the clump interior. At later times, clumps become denser and the gas cools more efficiently. As a result, H_2 formation is promoted, yielding the maximum value $x_{H_2} \simeq 0.76$ within the clump.

4.4.5 Stability of the molecular core

We have explicitly verified that the molecular core of the clumps is Jeans unstable when the simulations are stopped, implying that the clump could eventually collapse. This conclusion does not depend on the resolution of the simulation, as we have verified by running the simulation `clump_M50_G8e4` with 2× and 4× the standard resolution (see Sec. 4.4.6). Hence, the final clump mass is an upper limit to the final stellar mass $M_\star$. For the 50 $M_\odot$ clumps, we find $M_\star \simeq 15\,M_\odot$ in the lowest flux case ($G_0 = 2 \times 10^3$) and about $M_\star \simeq 3\,M_\odot$ in the highest flux case ($G_0 = 8 \times 10^4$). Following the standard Shu classification (Shu et al., 1987; André, 1994; André & Motte, 2000), star formation proceeds through an early accretion phase from the surrounding envelope ($t \simeq 1$ kyr), a late accretion phase via a disk ($t \simeq 0.2-1$ Myr) and a protostellar phase ($t \simeq 10$ Myr). We cannot investigate the effect of photoevaporation during these phases with the resolution and physics considered in our simulation suite, but we expect that the mass that goes into stars will be in general lower than $M_\star$ due to photoevaporating gas from the protostellar system.

*With the absorption cross sections adopted, the optical depth in the bin a is $\tau_a = 1$ when $N_{\rm H} = 7 \times 10^{20}\,{\rm cm}^{-2}$, while for LW radiation $\tau_b = 1$ when $N_{\rm H} = 10^{15}\,{\rm cm}^{-2}$

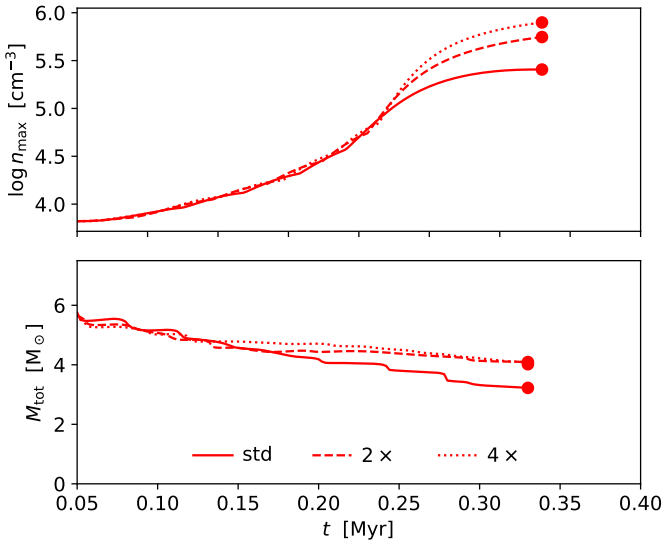

Figure 4.8: Maximum density in the clump (upper panel) and total clump mass (lower panel) as a function of radius, for a $50\,M_\odot$ clump subject to a FUV radiation field with $G_0 = 8 \times 10^4$. The three lines are obtained by running the simulation with different maximum resolution.

4.4.6 Convergence test

The standard resolution of our simulation suite is $\Delta x \simeq 0.047$ pc, refining up to $\Delta x \simeq 0.023$ pc according to a H_2 density gradient criterion. Due to radiation-driven implosion and gravitational instability, all the clump mass collapses to one cell at some time t_c which depends on the initial mass and the intensity of the radiation field. We stop our simulations at t_c, since the later time evolution of the clumps would be unresolved.

We argue that – despite the resolution limit – t_c is a good estimate of radiation-driven implosion duration and, being the final clump Jeans unstable. Its mass at t_c represents an upper limit to the gas mass that collapses and forms stars. To show this point, we perform a convergence test: we take the $50\,M_\odot$ (with $G_0 = 8 \times 10^4$) clump as a reference and we run the two additional simulations: (1) we increase the resolution by a factor 2 in a central region with radius 0.1 pc; (2) we add a further level of refinement in a region with radius 0.05 pc.

Fig. 4.8 shows the time evolution of the maximum density (upper panel) and the clump mass (lower panel) for the runs with different resolution. Simulations are stopped at the time t_c when the clump reaches the minimum resolvable size (1-2 cells): t_c is roughly the same in the three cases. In fact, by increasing the resolution, we can resolve the clump collapse to a later stage, but since the timescale for collapse becomes shorter, the clumps reach the minimum size in almost the same time. The lower panel confirms that the final clump mass is not affected by numerical resolution, implying that the estimate of the

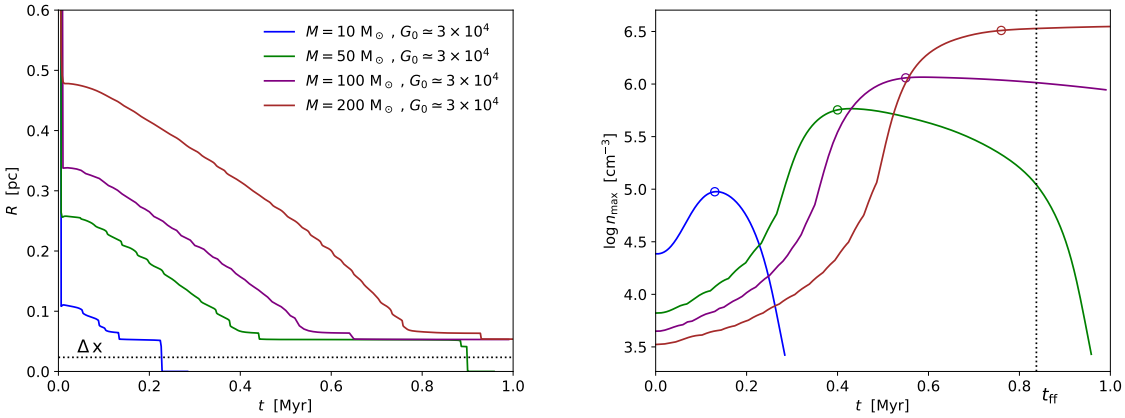

Figure 4.9: Comparison of the evolution of the clump in the four simulations with the same impinging flux: `clump_M10_G3e4`, `clump_M50_G3e4`, `clump_M100_G3e4` and `clump_M200_G3e4`. **Left**: variation with time of the clump radius, defined as in Fig. 4.5. **Right**: variation with time of the clump maximum density, with the same symbols used in Fig. 4.5

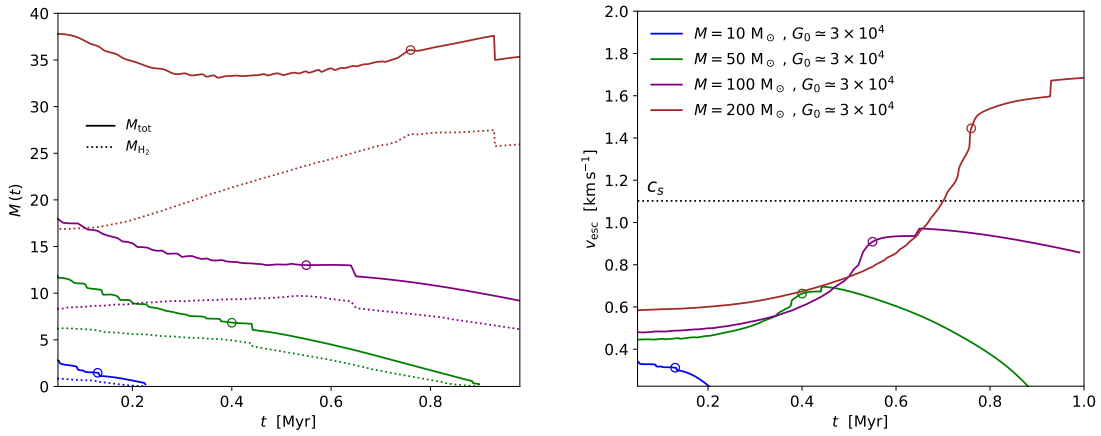

Figure 4.10: **Left:** Total clump mass (solid line) and molecular mass (dotted line), as a function of time, for the the four simulations with the same impinging flux: `clump_M10_G3e4`, `clump_M50_G3e4`, `clump_M100_G3e4` and `clump_M200_G3e4`. The circles mark the time when the clump has reached the minimum radius in the simulations, and gravitational collapse begins. **Right:** Escape velocity from the surface of the molecular core, as a function of time. The dotted horizontal line marks the typical sound speed in the heat atomic layer of the clump, which approximates the speed of the photoevaporative flow.

clump mass at the end of the RDI is reliable.

4.5 Results - Clumps with different masses

After focusing on clumps with mass $50\,M_\odot$, we also analyse the effect of photoevaporation on clumps with lower (10 $M_\odot$) and higher (100 and 200 $M_\odot$) masses, with an initially impinging flux of $G_0 \simeq 3 \times 10^4$ (see Tab. 4.1).

In the left panel of Fig. 4.9 the clump radius is plotted as a function of time. Clumps with larger masses take more time to collapse, as they have a lower initial density and hence longer free fall time. The maximum density $n_{\rm max}$ as a function of time is shown in the right panel, with higher values reached by more massive clumps.

In Fig. 4.10 (left panel), the total mass and the H_2 mass in the clumps are plotted. The $10\,M_\odot$ and $50\,M_\odot$ have the same trends seen in Sec. 4.4, with both total and H_2 mass decreasing during the implosion phase. Instead, the behaviour is different for the $100\,M_\odot$ and $200\,M_\odot$ clumps:

- $100\,M_\odot$: M_{H_2} increases slightly (by 25%) during the implosion, while $M_{\rm tot}$ decreases slowly.
- $200\,M_\odot$: M_{H_2} increases substantially (by 50%) during the RDI, while $M_{\rm tot}$ does not decrease considerably and shows a slight raise after 0.4 Myr.

The different behaviour of M_{H_2} in the two more massive clumps, before the gravitational collapse, is due to the effect of radiation in the bin [6-11.2] eV. Photons in this band make their way to the clump interior, which is less dense in the centre with respect to smaller clumps, and increase the gas temperature so that the H_2 decreases in the centre. Nevertheless, when the clump collapses, the gas self-shields from this radiation and H_2 abundance increases again in the centre. This boost of the H_2 abundance compensates for the photoevaporative loss.

In the final part of the RDI, the two massive clumps behave differently, with $M_{\rm tot}$ raising for the 200 $M_\odot$ clump. This is due to the fact that the escape velocity from the $200\,M_\odot$ becomes higher than the typical velocity of the outflowing gas. Fig. 4.10 (right panel) shows the time evolution of the escape velocity $v_{\rm esc}$ from the surface of the clump, for the four simulations with similar impinging flux. We have marked with a horizontal line the isothermal sound speed c_s at a $T \simeq 250$ K, which is a typical temperature of the heated atomic surface of the clumps. The circles mark the time when clump collapse. Only the 200 $M_\odot$ clump has $v_{\rm esc} > c_s$ at the end of the implosion phase, clarifying why this clump can accrete further in spite of the radiation impinging on its surface.

The same considerations of Sec. 4.4.5 hold: clumps are Jeans unstable at the end of the RDI, hence the remaining mass in the clump is an estimate of the mass going to form stars. Considering that photoevaporation can also remove mass from the protostellar

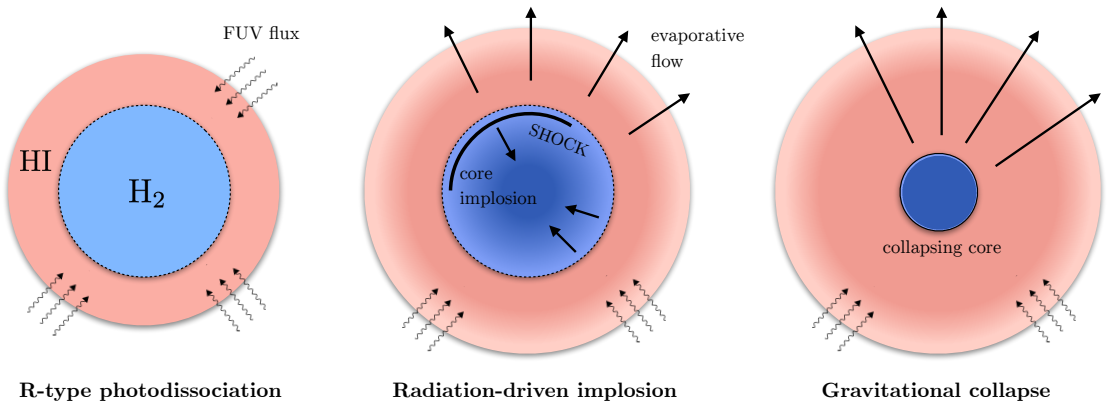

Figure 4.11: Sketch of the 3 main phases of the photoevaporative process. From left to right: (1) FUV radiation penetrates as an R-type photodissociation front, turning a clump shell to atomic form, without any dynamical effect on the gas; (2) the clump undergoes an implosion phase, because of the high pressure of the photodissociated shell, while the atomic gas flows into the surrounding ISM; (3) the clump implodes to a Jeans unstable core, which undergoes gravitational collapse and star formation, if its mass is sufficient.

system, such final mass should be regarded as an upper limit to the stellar mass. While the clump mass is generally reduced by photoevaporation during the RDI, thanks to its self-gravity the most massive clump in our set of simulations ($200\,M_\odot$) manages to retain its core mass after the R-type propagation of the dissociation front. Hence in this case photoevaporation is completely inefficient in limiting star formation.

4.6 General picture of photoevaporating clumps

The 3D simulations that we have run show that photoevaporating clumps undergo three main evolutionary phases, summarised in Fig. 4.11:

- R-type dissociation front propagation: FUV radiation penetrates the clump as an R-type front, with the clump density structure unaltered;
- radiation-driven implosion: the heated atomic shell drives a shock inward, so that the clump implodes;
- gravitational collapse: the molecular core is Jeans unstable, so it undergoes a gravitational collapse, with photoevaporation regulating the mass going into stars.

In the following, we analyse the details of these phases, trying to generalise the results of the simulations to a range of clump masses and impinging flux.

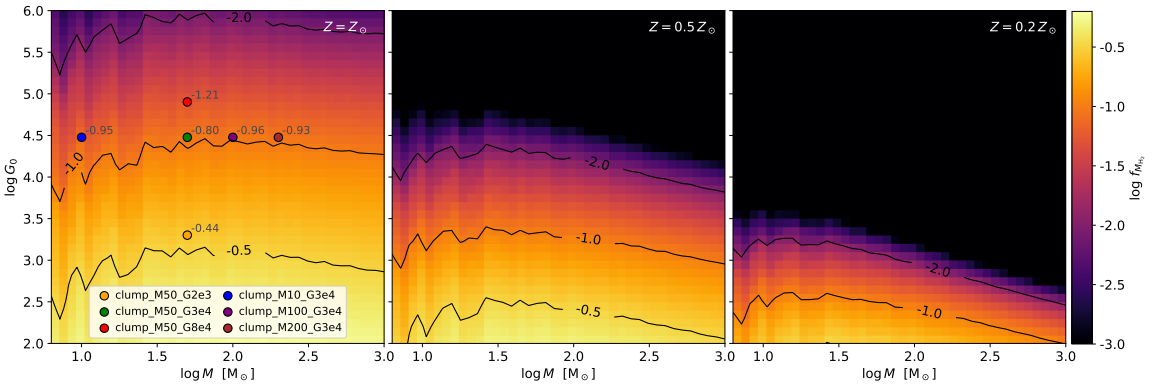

Figure 4.12: Ratio of molecular mass after the R-type dissociation front propagation with respect to the initial value ($f_{M_{H_2}}$), for different clump masses and different impinging FUV fluxes, obtained by running a set of 1D simulations. The three panels show the results for different gas metallicities ($Z = Z_\odot$, $0.5Z_\odot$, $0.2Z_\odot$). In the first panel, the results from the 3D simulations are reported with dots, together with the corresponding $f_{M_{H_2}}$ measured from the simulations.

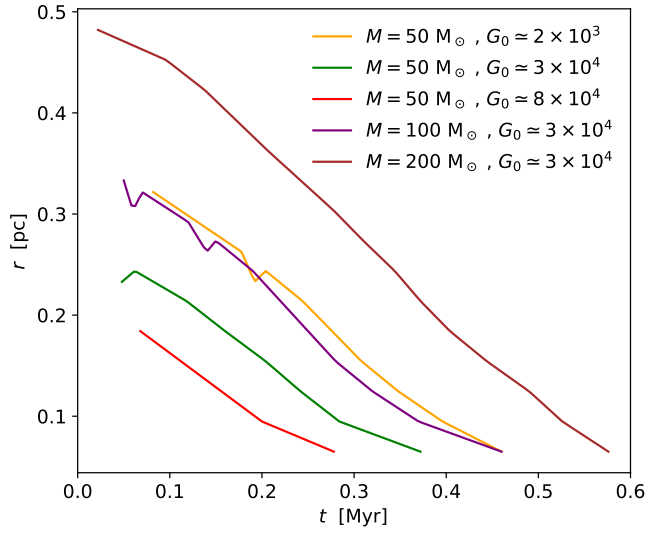

Figure 4.13: The solid line tracks the shock position (radial distance from the centre of the clump) as a function of time, for the simulations `clump_M50_G2e3`, `clump_M50_G3e4`, `clump_M50_G8e4`, `clump_M100_G3e4`, `clump_M200_G3e4`. The shock position is found by producing the radial profile of velocity in the computational box and taking the position of the maximum negative velocity.

4.6.1 R-type dissociation front propagation

The first phase of the photoevaporative phenomenon is the dissociation of clump molecules by the propagation of the dissociation front (DF) as an R-type front. During this phase, a clump shell is converted in atomic form during the DF propagation, without any dynamical effect on the gas. This phase is very short (less than 0.02 Myr), and it is responsible for the sudden decrease of $M_{\rm H_2}$ with respect to its initial value, as we already pointed out in Fig. 4.7 and Fig. 4.10.

This phase determines substantially the fate of a clump. In fact, if the remaining H_2 mass is very small, the clump can be quickly eroded in the following photoevaporative phase. To make a prediction of the H_2 mass in the clump after the R-type dissociation front propagation, we have run a set of 1600 1D simulations, with clump masses varying between 6 and $10^3\,{\rm M}_\odot$ and FUV fluxes in the range $G_0 = 10^{2-6}$. As initial setup of the 1D simulations, we have considered a 1D stencil passing through the centre of a 3-dimensional clump. Hence, radiation is injected from both sides of this 1D box, with the prescribed flux. The results are shown in Fig. 4.12 (leftmost panel), where the colours mark the ratio of molecular mass after the R-type dissociation front propagation to the initial molecular mass ($f_{M_{\rm H_2}}$). With respect to the results of the 3D simulations, the 1D simulations slightly understimate $f_{M_{\rm H_2}}$, because of the different geometry. The plot shows that the fraction $f_{M_{\rm H_2}}$ depends only weakly on the initial clump mass (apart from the low mass clumps, $M < 30{\rm M}_\odot$), so that a relation between $f_{M_{\rm H_2}}$ and G_0 can be derived by fitting the data:

$$\log(f_{M_{\rm H_2}}) = -0.85\log^2 G_0 + 0.22\log G_0 - 0.38 \tag{4.6}$$

We also notice that for the range of masses and fluxes that we have chosen, no clump is suddenly dissociated by the FUV radiation, hence all the analysed clumps will eventually undergo the implosion phase.

We investigate the dependence of gas metallicity on the efficiency of photoevaporation. We run two additional sets of 1D simulations (2×1600) with lower values of Z, i.e. $0.5Z_\odot$, $0.2Z_\odot$. The results for $f_{M_{\rm H_2}}$ are shown in the central and right panel of Fig. 4.12. Since the dust abundance is assumed to be proportional to Z, the low-Z gas is more transparent to radiation, and molecular gas is dissociated more efficiently. Clumps are fully photodissociated by the R-type dissociation front for $Z = 0.5Z_\odot$ ($Z = 0.2Z_\odot$) when $G_0 > 3 \times 10^4$ ($G_0 > 3 \times 10^3$). This finding agrees with results from Vallini et al. (2017) and Nakatani & Yoshida (2018), both pointing out that photoevaporation is more rapid in metal poor clouds, i.e. the ones expect in high redshift galaxies (e.g. Pallottini et al., 2017b, 2019).

4.6.2 Radiation-driven implosion

Clumps that are not completely dissociated by the propagation of the DF, will then attain a configuration with a molecular core surrounded by an atomic heated shell (this is the case for all clumps considered in this work). Since the latter has a higher pressure with respect to the molecular core, a shock propagates inward compressing the clump. This phase is generally called radiation-driven implosion (RDI).

In Decataldo et al. (2017) we have developed an analytical solution for the propagation of the shock towards the centre of the clump. In that work, the shock parameters (as mach number and compression factor) are computed as a result of the discontinuity between the cold molecular core and the heated atomic shell. The backup pressure from the atomic shell is kept constant during the evolution, which is equivalent to assume a constant heating of the shell by radiation. Hence, the shock velocity $v_{\rm shock}$ changes only because of spherical convergence, causing an increase with radius as $v_{\rm shock} \sim r^{-0.394}$. Nevertheless, the present work shows that radiation is absorbed in the photoevaporative flow, hence the heating of the atomic gas is reduced and its pressure decreases accordingly. This effect acts in the opposite direction than the spherical convergence, reducing the shock speed.

In Fig. 4.13, the shock radial distance from the centre is plotted as a function of time. The simulation `clump_M10_G3e4` has been excluded because the resolution is too low to resolve the shock position properly. The initial position of the shock is determined by the clump radius at the end of the DF propagation (cfr. left panel of Fig. 4.5 and 4.9). The plot shows that the shock speed is almost constant in time, implying that there is a balance between absorption of radiation which is backing up the shock, and spherical convergence of the shock. The simulations show that the shock Mach number (with respect to the gas ahead of the shock) is $\mathcal{M} = 2.0 \pm 0.3$, with a shock speed about half of the speed of sound in the heated clump shell ($c_{\rm PDR}$). This is in contrast to Gorti & Hollenbach (2002) assumption, where the shock speed is approximated to be exactly $c_{\rm PDR}$.

Finally, we notice that the RDI lasts more than the time needed for the radiation-driven shock to reach the centre of the clump, in contrast with Gorti & Hollenbach (2002) assumption that the clump stops contracting when the shock has reached the centre. This is evident especially for massive and larger clumps, and it is due to the fact that the shock moves towards the centre with a higher speed than the collapsing clump surface. Thus, when the shock has reached the centre, the surface is still moving inward.

During the RDI, two effects changing the H_2 mass are competing: (1) the clumps loses mass from its surface, (2) the central density increases, raising the H_2 abundance. The second effect dominates for clumps massive enough ($M \geq 100\,{\rm M}_\odot$). Furthermore, self-gravity inhibits the photoevaporative flow of even more massive clumps ($M \geq 200\,{\rm M}_\odot$), showing that in this case photoevaporation is not effective in reducing the total clump

mass during the RDI.

4.6.3 Gravitational collapse

After the RDI, the molecular core is still Jeans unstable, thus we expect it to undergo a gravitational collapse with possible star formation (if the molecular mass of the core is sufficient). We do not include star formation routines in our simulations, as done for instance via seeding of a protostellar object and by following its accretion (Dale et al., 2007c; Peters et al., 2010).

Other works on photoevaporation (Gorti & Hollenbach, 2002; Decataldo et al., 2017) do not include clump-self gravity in their analysis. As a result, in those works the clump reaches a minimum radius where thermal pressure balances the pressure of the shell heated by radiation. In this scenario, gas continues to photoevaporate from its surface, until all the molecular gas is dissociated. This is not seen in our simulations, since gravity leads to the clump self-collapse after the RDI.

The clump mass at the end of the R-type dissociation front propagation (Fig. 4.12) is in general an upper limit to the mass $M_\star$ going into stars. In fact during the RDI, a fraction of the mass flows away from the clump. However, this does not happen for clumps with sufficiently large masses in which self-gravity prevents the gas from escaping the clump.

4.7 Summary

We have studied the photoevaporation of Jeans unstable clumps by Far-Ultraviolet (FUV) radiation, by running 3D RT simulations including a full chemical network which tracks the formation and dissociation of H_2.

The simulations have been run with the adaptive mesh refinement code RAMSES (Teyssier, 2002) by using the RAMSES-RT module (Rosdahl et al., 2013), in order to perform momentum-based on-the-fly RT. The RT module has been coupled with the non-equilibrium chemical network generated with KROME (Grassi et al., 2014), in order to consider photo-chemical reactions, as the dissociation of H_2 via the two-step Solomon process. We have run seven simulations of dense clumps, embedded in a low density medium ($n = 100$ cm^{-3}), with different clump masses ($M = 10 - 200\,M_\odot$) and different impinging FUV radiation fields ($G_0 = 2\times10^3 - 8\times10^4$). These clumps have central number densities $n_c \simeq 6\times10^3 - 2\times10^4$ and total column density $N_{H_2} \simeq 5\times10^{21}$cm^{-2}.

In all the cases, we find that the evolution a clump follows three phases:

1) R-type DF propagation: the density profile remains unaltered while most of the H_2 mass is dissociated ($40 - 90\%$ of the H_2 mass, depending on G_0).

2) RDI: the heated shell drives a shock inward ($\mathcal{M} \simeq 2$) promoting the clump implosion; at the same time, the heated gas at the surface evaporates with typical speed $1.5 - 2\,\mathrm{km\,s^{-1}}$.

3) Gravitational collapse of the core: the clump collapses if the remaining H_2 core is Jeans unstable after the RDI; if M_{H_2} is significantly higher than 1 $M_\odot$, than we expect it to form stars.

During the RDI, both the molecular mass M_{H_2} and the total mass M decrease for the 10 and $50\,M_\odot$ clumps. However, we find that M_{H_2} tends to increase by $\sim 25 - 50\%$ for more massive clumps, due to the fact that previously dissociated H_2 recombines when the clump collapses and the density increases. For the most massive clump only ($200\,M_\odot$), photoevaporation is inefficient even in reducing the total mass M, since during the RDI the escape velocity becomes larger than the outflowing gas speed (comparable to the HI sound speed).

All the H_2 cores are still Jeans unstable after the RDI. This shows that FUV radiative feedback is not able to prevent the gravitational collapse, although it regulates the remaining molecular gas mass. All the simulated clumps manage to retain a mass $M > 2.5\,M_\odot$, hence suggesting that star formation may indeed take place. The evolution of low-mass clumps follows what expected from analytical works (Bertoldi, 1989; Gorti & Hollenbach, 2002; Decataldo et al., 2017). However, our analysis clarifies that self-gravity has a non negligible effect for massive clumps ($\simeq 100 M_\odot$), limiting the mass loss by photoevaporation.

The dynamics of photoevaporating clumps can also have important consequences for their Far-Infrared (FIR) line emission (Vallini et al., 2017), [C II] in particular. In fact, a strong G_0 increases the maximum [C II] luminosity, as FUV radiation ionizes carbon in PDRs, albeit short-lived clumps may contribute less significantly to the parent GMC emission. To understand the effect of photoevaporation on line luminosity, simulations accounting for the internal structure of GMCs are required. This would allow to track the contribution of many clumps with different masses and subject to different radiation fields.

Finally, we point out that photoevaporation is also a crucial effect in regulating the molecular mass in ultra-fast outflows launched from active galaxies. Indeed, dense molecular gas ($n \sim 10^{4-6}$ cm^{-3}) is observed up to kpc scale (Cicone et al., 2014; Bischetti et al., 2018; Fluetsch et al., 2019), and its origin and fate are currently under investigation (Ferrara & Scannapieco, 2016; Decataldo et al., 2017; Scannapieco, 2017; Richings & Faucher-Giguère, 2018a). In addition to FUV radiation, these clumps are also subject to a strong EUV field (not considered in this work), causing a fast photoevaporative flow of ionized gas and a stronger RDI. Since radiation is coming from the nuclear region of the active galaxy, the radiation field seen by the clump is non-isotropic, affecting only the side of the clump

facing the source. Moreover, clump masses are generally larger ($10^{3-4}\,M_\odot$, see Zubovas & King 2014; Decataldo et al. 2017) and high turbulence is reasonably expected within the outflow. Nevertheless, clumps will still follow a similar evolutionary path, with R-type dissociation/ionization, RDI, and gravitational collapse if the imploded core is Jeans unstable. This can be relevant to explain the observed molecular outflow sizes, which depends on the lifetime of clumps undergoing photoevaporation. Moreover, in this scenario the recent hints of star formation inside the outflow (Maiolino et al., 2017; Gallagher et al., 2019; Rodríguez del Pino et al., 2019) seem plausible, in view of our finding that most clumps manage to retain a sufficient amount of mass to collapse and form stars.

Chapter 5

Numerical simulation of a Giant Molecular Cloud

5.1 Introduction

The structure of giant molecular clouds (GMC) is determined by the effect of different phenomena. Initial turbulence can be be established during the formation process, possibly inherited from large scale turbulence present in the arms of the parent galaxy (Brunt et al., 2009; Elmegreen, 2011b; Hughes et al., 2013; Colombo et al., 2014; Dobbs, 2015; Walch et al., 2015). Then gravity kicks in, fostering the formation of dense clumps and filaments, and at the same time leaving behind low density regions devoid of gas. The gas keeps collapsing in overdense regions, until the density is high enough for star formation to occur. Stars with larger masses (above 10 $M_{\odot}$) have a dramatic impact over the surrounding interstellar medium (ISM), interacting with it through different mechanisms: radiation (Whitworth, 1979), winds (Castor et al., 1975; Weaver et al., 1977) and supernova explosions (Sedov, 1958; Ostriker & McKee, 1988). Hence, the effect of stellar feedback is crucial in determining the structure of GMCs, and a proper modelling is needed in order to understand their evolution.

Stellar feedback is indeed invoked to explain many of the observed cloud properties. For example, observations show that GMCs in our Galaxy have in general a very low star formation efficiency (SFE) and star formation rate (SFR), converting only a few percent of the gas mass to stars (Williams & McKee, 1997; Carpenter, 2000; Krumholz & McKee, 2005; Evans et al., 2009; García et al., 2014; Lee et al., 2016; Chevance et al., 2019). A possible explanation is that GMCs are indeed short-lived, and gas is quickly heated and dispersed by stellar feedback, therefore quenching completely star formation in less then 10 Myr (Elmegreen, 2000; Hartmann et al., 2001). This picture is supported by the recent analysis of the CO-to-Hα ratio, which is an indicator of the co-spatiality of the GMC molecular phase and young stars (Kruijssen et al., 2019; Chevance et al., 2019). On the

other side, the existence of long-lived GMCs would require stellar feedback to increase the turbulence in order to provide pressure support, without dispersing the cloud (Federrath & Klessen, 2012; Padoan et al., 2012).

High-mass stars ($M > 5\,M_\odot$) emit an important fraction of photons in the far ultraviolet (FUV, $6\,eV < h\nu < 13.6\,eV$) and extreme ultraviolet bands (EUV, $h\nu > 13.6\,eV$). FUV photons can dissociate molecules like CO and H_2, determining the formation of molecular-to-atomic transition regions (photodissociation regions, PDR) heated up to 10^3 K (Tielens & Hollenbach, 1985; Kaufman et al., 1999; Le Petit et al., 2006; Bron et al., 2018); EUV photons ionize hydrogen and helium (HII regions), rising the gas temperatures to 10^{4-5} K depending on the luminosity of the star (Strömgren, 1939; Anderson et al., 2009). Since hot gas has higher pressure relative to the cold molecular ISM, shocks propagate ahead of dissociation/ionization fronts, compressing the gas and driving turbulent motions (Kahn, 1954; Williams et al., 2018). Gas photoevaporates from dense clumps, hence reducing their molecular mass, but at the same time the radiation-driven implosion can trigger star formation (Kessel-Deynet & Burkert, 2003; Bisbas et al., 2011; Decataldo et al., 2019).

Stars larger then $10 - 12\,M_\odot$ eject mass with a rate of about $10^{-7} - 10^{-5}\,M_\odot\,yr^{-1}$, with terminal velocities up to $3000\,km\,s^{-1}$ (Leitherer et al., 1992). The ejected gas shocks and sweeps away the surrounding medium, leaving a hot low density bubble around the star, with temperatures as high as $T \sim 10^{6-7}$ K (Weaver et al., 1977; McKee & Cowie, 1977; Cioffi et al., 1988; Ostriker & McKee, 1988). Both radiation and winds keep injecting energy in the ISM for the whole lifetime of the star, hence resulting in a large energy input (10^{50-52} erg for a $10^6\,L_\odot$ star living about 3 Myr). However, it is still unclear which of the two feedback mechanisms is more effective, due to the different coupling efficiency with the gas (Matzner, 2002; Walch et al., 2012; Haid et al., 2018b). Supernova explosions occur at the end of stellar life, releasing about 10^{51} erg in a very short time. The coupling of the supernova blast with the cloud gas strongly depends on the density structure, since dense gas cools efficiently radiating away all the energy input (Thornton et al., 1998; Dwarkadas & Gruszko, 2012; Walch & Naab, 2015).

Pioneer analytical works (Whitworth, 1979; Williams & McKee, 1997; Matzner, 2002) have analysed the problem of an HII region expanding in a molecular cloud, estimating the amount of ionized/dispersed gas. EUV radiation has been identified as the main responsible for cloud destruction and hence star formation inefficiency. In order to account for the complex structure of a realistic GMC, numerical simulations have been recently employed to study their evolution under the effect of stellar feedback. Early simulations have used approximated recipes to account for stellar photoionization, without the inclusion of radiative transfer calculations: for example, a common approach is to compute the ionization state of the gas and then the corresponding temperature (Dale et al., 2005, 2007b; Ceverino & Klypin, 2009; Gritschneder et al., 2009), or to account for photoioniz-

ation feedback by injecting thermal energy at stellar locations (Vázquez-Semadeni et al., 2010). Nevertheless, these models managed to reproduce the main features of typical observed structures, as pillars and bright-rimmed clumps, and they assess the effect of triggered star formation due to radiation feedback (see review by Elmegreen, 2011a).

More recent works have adopted coupled hydrodynamics and radiative transfer schemes to account for gas-radiation interaction. Walch et al. (2012) study the effect of radiation from one massive star placed at the centre of a fractal $10^4\,\mathrm{M}_\odot$ GMC, getting a speed up of star formation with respect to a control case with no radiation, while the overall star formation efficiency (SFE=$M_\star/M_{\rm GMC}$, i.e. the ratio between the stellar mass and the initial GMC mass) is reduced. Raskutti et al. (2016) follow the evolution of many GMCs with different mass, radius (hence different gas surface density Σ) and initial amount of turbulence. Star formation is implemented via sink particles (each representing a stellar cluster), which emit radiation with intensity proportional to their mass. They find SFEs of the order of $0.1-0.6$, increasing proportionally to $\log\Sigma$; for all the clouds most of stars form in a time shorter than one free-fall time $t_{\rm ff}$. They define the lifetime of a cloud as the time t_ℓ at which the virial parameter $\alpha=5$, corresponding to a sheer drop of the star formation rate, yielding $t_\ell/t_{\rm ff}\sim 1.2-1.9$.

A similar analysis is carried out by Howard et al. (2017), finding that radiation feedback reduces the SFE more consistently for more massive clouds ($10^4-10^6\,M_\odot$) with respect to smaller clouds ($\sim 10^3\,M_\odot$), since massive clouds manage to form a richer population of massive stars. In their simulations SFE $\sim 0.3-0.6$, suggesting that radiation feedback alone is not enough to suppress the SFE to the generally observed values ($\sim 1-10\%$ Lada et al., 2010; Murray et al., 2010; Lada, 2015; Lee et al., 2016; Ochsendorf et al., 2017). However, other models show that a lower SFEs can be obtained by including magnetic fields in the simulation (Geen et al., 2016, 2018; Kim et al., 2018; Haid et al., 2018a; He et al., 2019). In this Chapter, we make a further step in the accuracy of GMC simulations, including several novel features:

- multi-bin radiative transfer, sampling radiation in the near-infrared, far-ultraviolet and extreme-ultraviolet bands;
- non-equilibrium chemical network coupled with the radiative transfer scheme;
- simultaneous inclusion of different stellar feedback mechanisms: photo-ionization/dissociation, radiation pressure, winds, supernovae;
- stellar particles representing individual stars and not star clusters, each one emitting radiation with a spectrum derived from stellar tracks.

The goal is to understand how stellar feedback alters the structure and the chemical composition of a GMC, determining its final star formation efficiency and lifetime.

Photoreactions	$E_{\rm act}$
$H + \gamma \rightarrow H^+ + e$	13.6 eV
$H_2^+ + \gamma \rightarrow H^+ + H$	2.65 eV
$He + \gamma \rightarrow He^+ + e$	24.6 eV
$H_2^+ + \gamma \rightarrow H^+ + H^+ + e$	30.0 eV
$He^+ + \gamma \rightarrow He^{++} + e$	54.4 eV
$H_2 + \gamma \rightarrow H + H$ (direct)	14.2 eV
$H^- + \gamma \rightarrow H + e$	0.76 eV
$H_2 + \gamma \rightarrow H + H$ (Solomon)	11.2 eV
$H_2 + \gamma \rightarrow H_2^+ + e$	15.4 eV

Table 5.1: List of photochemical reactions included in our chemical network, and corresponding activation energy.

The Chapter is organised as follows. In Sec. 5.2, we describe the numerical method and the simulations suite, in particular the inclusion of radiation (Sec. 5.2.3), winds (Sec. 5.2.4) and SN (Sec. 5.2.5). In Sec. 5.3, snapshots of the clouds are shown (Sec. 5.3.1 and 5.3.2), and its features are analysed with time, focusing on the evolution of the ionized, atomic and molecular phases (Sec. 5.3.3), the star formation efficiency and the star formation rate (Sec. 5.3.4) and the radiation field (Sec. 5.3.5). Our conclusions are finally summarised in Sec. 5.4.

5.2 Numerical Simulation

We carry out our simulations using a customised version of the adaptive mesh refinement (AMR) code RAMSES-RT (Teyssier, 2002; Rosdahl et al., 2013). The thermochemistry module of RAMSES-RT has been coupled with the package KROME (Grassi et al., 2014) in order to include a complex chemical network accounting for 9 species (H, H^+, H^-, H_2, H_2^+, He, He^+, He^{++} and free electrons). This coupling between RAMSES-RT and KROME , detailed in Sec. 2.4, has been already been tested and used in previous works (Pallottini et al., 2019; Decataldo et al., 2019). In order to have reasonable timesteps in the simulation, we adopt a reduced speed of light $c_{\rm red} = 10^{-3}\, c$, where c is the physical speed of light. This approximation brings to an inaccurate propagation of the ionization front IF only when its speed $v_{\rm IF}$ is larger then $c_{\rm red}$ (Deparis et al., 2019; Ocvirk et al., 2019), which in our simulation happens only close to very massive stars. Photoreactions are also listed in Tab. 5.1 for conveniency, with the corresponding activation energies $E_{\rm act}$. We adopted the same rates as in citetBovino2016, with the exception of H_2 formation on dust grains, for which we use the improved rate explained in Sec. 1.2.2, assuming $T_d = 30$ K for the dust temperature).

We track radiation using 10 energy bins, which have been chosen to cover the energies of interest for the 9 photoreactions included in the chemical network. Radiation is absorbed

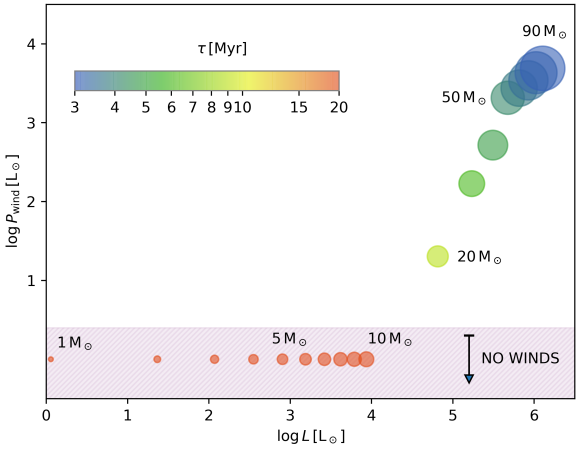

Figure 5.1: Overview of properties of stars on the main sequence. Circles represent stars of different masses, with the diameter of the circle proportional to the mass. The color of each circle corresponds to the time interval (also encoded in the colorbar) a star spends on the main sequence, with red circles standing for times longer than 20 Myr. On the x and y axis the bolometric luminosity and wind kinetic power are shown, both expressed in units of solar luminosities. Stars with mass $< 12 M_{\odot}$ do not produce significant winds.

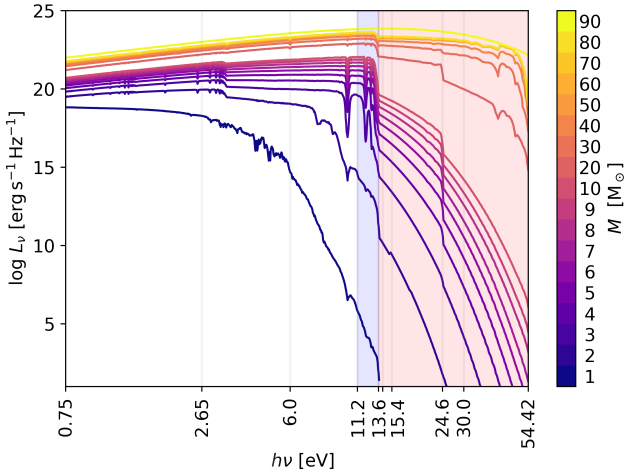

Figure 5.2: Spectra of stars with different masses, the same considered in Fig. 5.1. The vertical grey lines delimit the energy bins adopted in the our simulation suit. The blue and red areas highlight the LW and the EUV bands, respectively.

independently in each bin, taking into account (1) photons taking part in chemical reactions, (2) H_2 self-shielding and (3) dust absorption (for details on the implementation, see Sec. 2.4). The adopted H_2 self-shielding factor by LW radiation is taken from Richings et al. (2014b), while opacities for dust absorption are taken from Weingartner & Draine (2001). We have used the Milky Way size distribution for visual extinction-to-reddening ratio $R_V = 3.1$, with carbon abundance (per H nucleus) $b_C = 60$ ppm in the log-normal populations*.

5.2.1 Initial conditions

The GMC is initially a uniform spherical cloud with mass $M = 10^5\,\mathrm{M}_\odot$ and radius $R = 20$ pc, implying a number density $n = 120\ \mathrm{cm}^{-3}$ and a free fall time $t_{\rm ff} = \sqrt{3\pi/32G\rho} \simeq 4.7$ Myr. In the MW distribution of GMC properties, these kind of clouds are the most abundant (Heyer et al., 2009; Grisdale et al., 2018). The GMC is placed at the centre of a cubic box with size 60 pc, immersed in a uniform background medium with number density $n_{\rm ISM} = 1\ \mathrm{cm}^{-3}$. The gas has the same chemical composition through all the box, with helium abundance of 25 per cent and hydrogen in fully molecular form. The initial temperature is set to 10 K everywhere.

We add a turbulent velocity field in the initial conditions. We generate an isotropic random Gaussian velocity field with power spectrum $P(k) \propto k^{-4}$ in Fourier space, normalising the velocity perturbation in the following way: inside the GMC, the velocity field is such that the cloud virial parameter $\alpha_{\rm GMC} = 5\,v_{\rm rms}^2\,R_{\rm GMC}/G\,M_{\rm GMC} = 2$, so that the cloud is initially unbound; in the background medium, the velocity field has a root mean squared value which is $(n_{\rm ISM}/n_{\rm GMC})^2$ higher than the one in the cloud; this ensures that the ram pressure $P = \rho v^2$ reaches equilibrium at the cloud boundary. In three dimensions, the chosen power spectrum gives a velocity dispersion that varies with scale as $\ell^{1/2}$, i.e. in agreement with Larson's scaling relations (Larson, 1981).

The coarse resolution is 2^6 cells for the background medium (corresponding to a cell size of $\Delta x \simeq 0.9$ pc) and 2^8 cells for the cloud ($\Delta x \simeq 0.2$ pc). The resolution in the cloud is increased by two further levels of refinement ($\Delta x \simeq 0.06$ pc), according to a Lagrangian strategy: a cell at level l is refined if the gas mass contained exceeds $M_l = \mathrm{k}_l M_{\rm SPH}$, where $M_{\rm SPH} \simeq 10^{-4}\,\mathrm{M}_\odot$, $\mathrm{k}_9 = 32$ and $\mathrm{k}_{10} = 24$. In this way, the resolution is increased in denser regions, such as clumps and filaments which are expected to form during the gravitational collapse and due to the effect of stellar feedback.

5.2.2 Star formation

We enable star formation in the GMC after 3 Myr (corresponding to $\sim 0.6\,t_{\rm ff}$), when the dense filaments and clumps have formed within the cloud because of gravitational

*www.astro.princeton.edu/~draine/dust/dustmix.html

instabilities. Hence, we define the evolutionary time of the cloud t as the time elapsed since $t_0 = 3$ Myr. Since we are mostly interested in the effect of feedback by UV radiation and stellar winds over the GMC, we neglect the process of gas accretion onto seed particles, and stars are formed directly with their zero-age main sequence mass. For a given cloud mass $M_{\rm GMC}$ and a given local star formation efficiency η, star formation is implemented in the following steps, which will be detailed below:

(1) we generate a list of stars before starting the simulation;

(2) at each timestep, a star formation episode is triggered in a cell with a probability proportional to the local SFR;

(3) the next star in the list is placed in the cell where a star formation episode has occurred.

The list includes stars for a total stellar mass equal to the GMC mass ($M_{\rm stars} = M_{\rm GMC} = 10^5\,{\rm M}_\odot$), but we do not expect to actually form all the stars in the list, due to the effect of feedback reducing the mass available for star formation.

The star masses in the list are drawn from a Kroupa Initial Mass Function (Kroupa, 2001), until $M_{\rm stars}$ is reached. From this list of stars, we remove the stars with mass lower than 1 ${\rm M}_\odot$, since these stars have weak emission in the UV, no winds and they do not explode as supernovae. Hence, we can save computational time by not tracking these stars in the simulation. A factor $f_\star$ is then introduced in the star formation routine, to keep the SFR consistent (see eq. 5.3 below).

Given the list of stars, they are placed in the GMC one by one at runtime, by deciding which cells host a star formation event in the following way. The local star formation rate density (SFRd) is taken to be proportional to the gas density (ρ) (Schmidt, 1959; Kennicutt, 1998), which has been shown to hold for clouds in the Milky Way (Krumholz et al., 2012):

$$\mathrm{SFRd} = \eta\,\frac{\rho}{t_{\rm ff}}\ , \tag{5.1}$$

where η is the local star formation efficiency, and $t_{\rm ff}$ is the local free-fall time. η takes into account unresolved physical processes as jets, winds and outflows launched during the process of stellar birth, which limit the gas accretion into stars. Its value is very uncertain, and can span from 0.01 (Krumholz & McKee, 2005) to 0.3-0.5 (Alves et al., 2007; André et al., 2010), and in this work we assume $\eta = 0.1$. Then it follows that the star formation rate associated to a cell with mass $M_{\rm cell}$ is

$$\mathrm{SFR}_{\rm cell} = \eta\,\frac{M_{\rm cell}}{t_{\rm ff}}\ . \tag{5.2}$$

According to such relation, at every timestep Δt of the simulation each cell is assigned a probability of forming a star, given by

$$\mathcal{P} = f_\star \frac{\mathrm{SFR}_{\mathrm{cell}}\,\Delta t}{\langle M_\star \rangle} \,, \tag{5.3}$$

where $\langle M_\star \rangle \simeq 3.37\,\mathrm{M}_\odot$ is the IMF-averaged mass of the stars and $f_\star$ is a correction factor correcting taking into account that we do not include stars below $1\,\mathrm{M}_\odot$ ($f_\star = N(m > 1\,\mathrm{M}_\odot)/N_{\mathrm{TOT}} \simeq 0.57$). We also set an H_2 density threshold n_{th} for star formation, so only cells with density $n_{\mathrm{H}_2} > n_{\mathrm{th}}$ are considered for star formation. The efficiency is then rescaled (η') so that the total number of stars formed in a timestep does not depend on the chosen threshold:

$$\eta' = \eta \left(\sum_i \frac{M_{\mathrm{cell},i}}{t_{\mathrm{ff},i}} \right) \left(\sum_{n_i > n_{\mathrm{th}}} \frac{M_{\mathrm{cell},i}}{t_{\mathrm{ff},i}} \right)^{-1} \,. \tag{5.4}$$

To ensure mass conservation when a star formation episode occurs, we remove the corresponding star mass from all the cells of the cloud (selected as those with $n_{\mathrm{H}_2} > 10\ \mathrm{cm}^{-3}$), in the following way:

$$m'_{\mathrm{cell}} = m_{\mathrm{cell}} \left(1 - \frac{M_\star}{N_{\mathrm{cell,GMC}}} \right) \tag{5.5}$$

where m_{cell} and m'_{cell} are the cell gas mass before and after the removal, $M_\star$ is the mass of the newly formed star and $N_{\mathrm{cell,GMC}}$ is the total number of leaf cells in the cloud. In this way, we remove in total a mass $M_\star$ from the cloud avoiding gas mass depletion in cells.

The choice of this star formation routine is alternative to the implementation of sink particles, which form at a minimum mass m_{seed} and then accrete mass from the surroundings. Using sink particles presents additional complications: i) it is not obvious that the correct IMF is recovered, and ii) a reasonable choice for radiation emitted by pre-MS stars have to be made. Since our main goal is to analyse the effect of feedback, and not the star formation process itself, we opted for this simplified recipe.

Finally, we notice that, as we do not track the formation of low-mass stars ($M < 1\,\mathrm{M}_\odot$), we do not properly account for the corresponding gas mass depletion. Indeed, such stars are very numerous, and working out the calculation with a Kroupa IMF we obtain that the mass ratio of stars with $M_{<1\mathrm{M}_\odot}$ and $M_{>1\mathrm{M}_\odot}$ is

$$f_{<1\mathrm{M}_\odot} = \frac{M_{<1\mathrm{M}_\odot}}{M_{>1\mathrm{M}_\odot}} \simeq 0.94$$

This means that the H_2 mass in the simulation is generally overestimated. Therefore, we apply the following correction to the H_2 mass and the stellar mass to the results of the simulation:

$$M'_{\mathrm{H}_2} = M_{\mathrm{H}_2} - f_{<1\mathrm{M}_\odot} M_\star$$
$$M'_\star = M_\star + f_{<1\mathrm{M}_\odot} M_\star$$

where M_{H_2} and $M_\star$ are the values obtained from the simulation, and M'_{H_2} and $M'_\star$ are the corrected values.

5.2.3 Radiation from stars

Newly formed star particles emit radiation as point sources. Every timestep, photons are injected in the cells where stars reside, with an energy spectrum sampled with 10 bins (see Sec. 5.2). We neglect the protostellar phase, the pre-main sequence, the red giant branch and following phases, due to their short duration in comparison to the main sequence (Kippenhahn & Weigert, 1990). Since both bolometric luminosity and spectrum change with time during the main sequence, for simplicity we take values time-averaged over the lifetime of a star, as detailed below.

We employ the stellar evolutionary tracks for a wide range of star masses from the PARSEC code (Bressan et al., 2012). For each mass in the catalogue, we compute the average bolometric luminosity L_{bol} during the main sequence and then we interpolate to find L_{bol} for the stars in our list. Finally, the stellar spectra are extracted from the Castelli-Kurucz Atlas of stellar atmosphere models (Castelli & Kurucz, 2003) for the different masses and L_{bol}. For reference, on the x axis of Fig. 5.1 we report L_{bol} for a range of stellar masses, from 1 $M_\odot$ to 90 $M_\odot$. The corresponding spectra are shown in Fig. 5.2, with coloured regions highlighting the H_2-dissociating (LW, blue) and HI-ionizing (EUV, red) bands. A star with mass between 3-5 $M_\odot$ contributes little both to the LW and EUV; a star with mass of 5 $M_\odot$ starts to contribute non-negligibly to the LW photon budget, with $L_{LW} \simeq 50\,L_\odot$, and for larger masses ($M \geq 20\,M_\odot$) the luminosity in the LW saturates to $L_{LW} \simeq 5 \times 10^4\,L_\odot$; finally, only stars with masses larger than 20 $M_\odot$ have a significant EUV emission, settling to $L_{EUV} \simeq 2 \times 10^5\,L_\odot$ for $M \geq 30\,M_\odot$.

5.2.4 Stellar winds

Besides radiation feedback, massive stars also inject energy in the surrounding ISM through winds. The mass loss rate ($\dot{M}_w$) and the wind kinetic power (P_w) for the stars in our list are taken from PARSEC, averaging over the main sequence. Fig. 5.1 shows $\dot{M}_w$ and P_w as a function of mass, for the stars in our sample, color-coded by the time they spend on the main sequence. Stars with mass lower than 10 $M_\odot$ do not significantly lose mass, so they are not included in the plots. On the other hand, mass loss from very massive stars ($M > 50\,M_\odot$) is about $10^{-5}\,M_\odot\,yr^{-1}$, resulting in a kinetic power of $\sim 10^{37}\,erg\,s^{-1}$ over the their entire lifetime. Assuming an average lifetime of 3 Myr for one of these very massive stars, the total mass loss is $10\,M_\odot$ with a total energy injection in the ISM around 10^{51} erg. Hence the energy output is comparable to that of a supernova, and about 40 times the gravitational binding energy of the GMC, showing that stellar winds have potentially enough energy to disrupt the cloud.

Our implementation of stellar winds consists in the injection of mass and energy in the cells adjacent to the star particle, as generally done in grid-based codes (Geen et al., 2016; Gatto et al., 2017; Haid et al., 2018a). At each timestep Δt of the simulation, and for each star in the box, a mass $\Delta M_{\rm w} = \dot{M}_{\rm w}\Delta t$ is subtracted from the stellar particle and injected in the 27 neighbouring cells (i.e. the 3^3 cube surrounding the particle host cell) and an energy $\Delta E_{\rm w} = P_{\rm w}\Delta t$ is likewise distributed to those cells. Each cell j receives a different amount of mass (ΔM_j) and energy (either in the form kinetic energy $\Delta E_{{\rm kin},j}$ or thermal energy $\Delta E_{{\rm th},j}$), in order to ensure that the wind is spherically symmetric around the source. For the particle host cell, we inject mass and energy only in the form of thermal energy, since i) we do not resolve the dynamics of the wind inside the cell, and ii) the thermal energy injection is isotropic:

$$\Delta M_{\rm host} = \frac{\Delta M_{\rm w}}{27} \qquad \Delta E_{\rm th,host} = \frac{\Delta E_{\rm w}}{27} \tag{5.6}$$

Instead for the other 26 neighbouring cells, we inject mass and kinetic energy by

$$\Delta M = f_j \frac{\Delta M_{\rm w}}{27} \qquad \Delta E_{\rm kin} = f_j \frac{\Delta E_{\rm w}}{27} \tag{5.7}$$

where f_j is the factor accounting for the solid angle covered by the j-th cell when seen from the source. If we consider that all the neighbouring cells are always kept at the maximum refinement level, and we enforce

$$\sum_{j=1}^{26} f_j = \frac{26}{27}, \tag{5.8}$$

we obtain

$$f_j = \frac{39}{22}\left(\frac{\Delta x}{r_j}\right)^2 \tag{5.9}$$

where Δx is the cell size and r_j the distance from the host cell. These cells receive a kick in velocity in the direction of the line joining the centres of the j-th cell and of the host cell.

5.2.5 Supernovae

Stars with mass larger than 8 $\rm M_\odot$ explode as Type II (Smartt, 2009) supernovae at the end of their life. For simplicity, we neglect all the stellar evolution phases following the main sequence (as the red giant branch, the horizontal branch and the asymptotic giant branch), that are expected to represent only a short fraction of the total stellar lifetime, and we assume that stars explode just after the main sequence. The main sequence time is taken from the evolutionary tracks in PARSEC. When a star with mass M explodes as a supernova, it injects in the surrounding cells a mass $M_{\rm ej} = M - M_{\rm rem}$, where $M_{\rm rem} = 1.4\,\rm M_\odot$ is the mass of the remnant (the Chandrasekhar limit, Chandrasekhar, 1939). After the explosion, we set the particle mass to $M_{\rm rem}$ and assume no further radiation is released.

The ejecta are distributed among the 27 neighbouring cell in the same fashion of the winds, but with a total energy input of 10^{51} erg: 1/27 of the energy is injected as thermal energy in the host cell of the star, and the remainder 26/27 as kinetic energy in the surrounding cells.

5.3 Results

5.3.1 Overview of cloud evolution

Images of the cloud are represented in Fig. 5.3, showing snapshots taken at regular intervals up to $t = 2.5$ Myr (we recall that time is counted starting from $t_0 = 3$ Myr, the time at which star formation is enabled). The four columns, from left to right, show the total gas surface density and the surface density of H_2, HI and HII.

At $t = 0$ Myr, the cloud has developed a complex structure of filaments and clumps, forming where the initial turbulent field produces an enhancement in the gas density. Then, stars form stochastically in the overdense cells, according to the probabilistic recipe described in Sec. 5.2.2. Low-mass stars (1-2 $M_\odot$) are able to form small partially ionized gas bubble around them, with a thick transition region to neutral and molecular hydrogen. Most massive stars ($> 30\,M_\odot$) form large HII regions which are clearly visible in the surface density plots. In particular, notice the main bubble found in the $t = 0.5$ Myr snapshot, centred in (6.5 pc, -2 pc), due to the formation of a 40 $M_\odot$ star. The area inside the bubble is quickly emptied, due to the combined effect of radiation and winds.

As the cloud evolves ($t \geq 1.5$ Myr), the high density gas which has managed to resist feedback keeps collapsing towards the centre of the box, while less dense filaments protrude at larger distances. Since SFR is proportional to gas density, it increases to very high values during the final stages of the simulations ($\sim 0.1\ M_\odot\,yr^{-1}$), consuming very rapidly the gas content of the most dense clumps. Hence, feedback and star formation are the two mechanisms decreasing the amount of molecular gas, consuming it all by $t \simeq 2.8$ Myr. Since even the most massive stars in the simulations have a lifetime of about ~ 3 Myr, the cloud has already ceased to exist before any supernovae get the chance of exploding.

While from $t = 1.5$ Myr the molecular gas is only concentrated in clumps in the central region of the cloud, HI maps show that the atomic hydrogen is not collapsing towards the centre. Maps at $t = 1.5$ Myr and $t = 2.0$ Myr show indeed the an HI cloud with radius > 10 pc persists, as the gravitational collapse prevented by the high temperature of FUV-heated gas ($T \simeq 10^3$ K). However, in the last snapshot ($t = 2.5$ Myr), the dense molecular clumps are completely dissociated and ionizing radiation is free to propagate in the whole cloud. As a result, the HI gas is almost completely ionized at the end of the simulation.

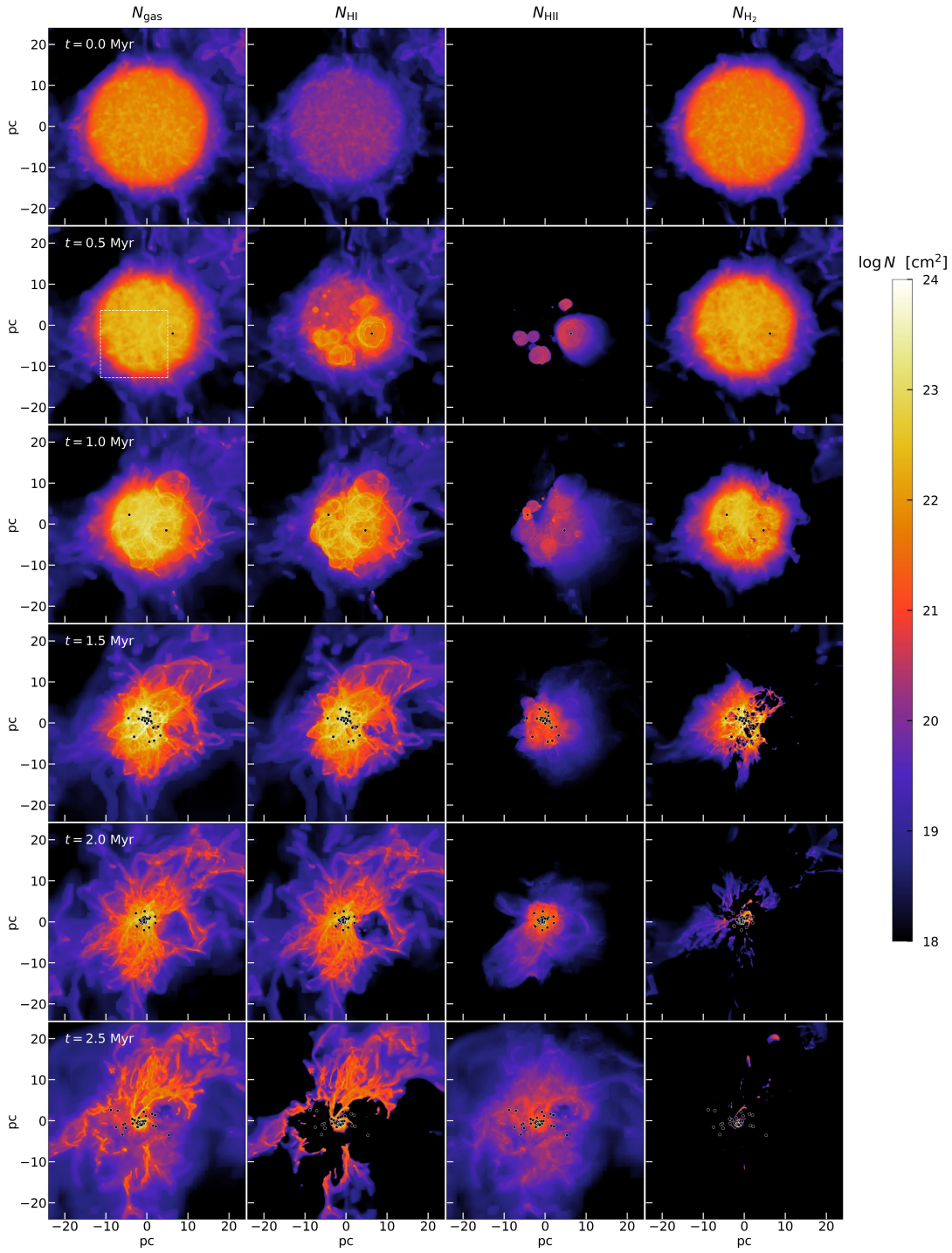

Figure 5.3: Evolution of the molecular cloud since the epoch t_0 of the formation of the first star. The four columns show respectively the total, HI, HII and H_2 column densities at different times (t = 0, 0.5, 1.0, 1.5, 2.0, 2.5 Myr). The black dots represent the locations of stars more massive than 30 $M_\odot$. As stars form, molecular gas is converted in atomic form, and ionized in proximity of massive stars, with the result that the cloud is destroyed around 2.5-3 Myr. The dashed white square in the second left panel is the zoomed region in Fig. 5.4.

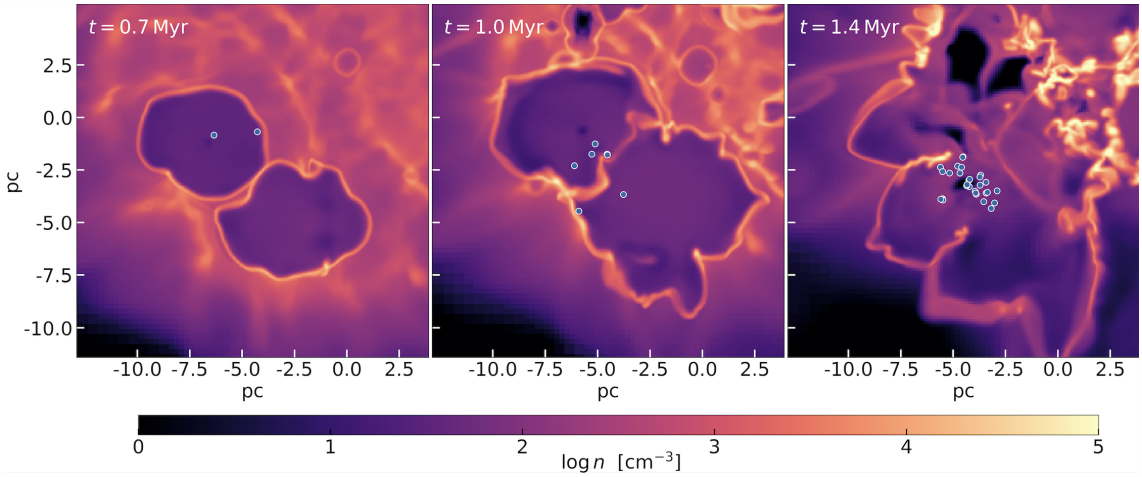

Figure 5.4: Slices of the cloud at different times (t = 0.7 Myr, 1.0 Myr and 1.4 Myr), zoomed to show the evolution of two HII regions (the zoomed area is marked with a white dashed square in Fig. 5.3). The maps are color-coded according to the gas number density, and the dots show stars of any mass within 0.1 pc from the slice. From left to right, we can see the formation of two HII regions, the development of instabilities at the edges, and the formation of dense clumps with a prolonged tail.

5.3.2 Structure of HII regions

In order to study the structure of HII regions, we show in Fig. 5.4 density slices centreed around two close-by massive stars (25 $M_\odot$ and 40 $M_\odot$) forming at t = 0.02 Myr and $t = 0.32$ Myr. All the stars within 1 pc from the cut are shown as black dots. The slices are taken at different times, to show the evolution of the dense shell of gas developing at the edge of HII regions and the formation of clumps with size < 0.1 pc.

In the leftmost slice (t = 0.7 Myr), the HII region are already well developed. Fully ionized gas in the bubbles has a density around $n \sim 100$ cm^{-3}, while gas at the edge reaches around 2000 cm^{-3}, due to the piling-up of gas pushed by the radiation-induced shocks and the winds. This shell is HI-rich, and represents indeed a PDR, formed thanks to FUV radiation getting through the ionized region and dissociating H_2. From the slice, it is evident that the dense shells are not regular in shape and density, due to inhomogeneities in the gas prior to the ionization front propagation.

In the second slice ($t = 1.0$ Myr) the shells fragment due to instabilities, triggered also by the collision between the two close-by shells, inducing the formation of small and dense clumps characterized by a dense and compact head followed by a tail. These clumps move towards the centre of the box due to gravitational potential of the cloud (rightmost slice, $t = 1.4$ Myr). Due to their high density, stellar feedback is ineffective in destroying such clumps, resulting in their rapid conversion into new stars, a process that slowly consumes all the available molecular gas.

Another noticeable effect seen in the simulation is the formation of stars in the compressed shell around HII regions, as seen in both in the first and in the second slice. Since the probability of forming star is proportional to gas density, the formation of dense shells around HII regions fosters the birth of new stars. This scenario of self-propagating (or triggered) star formation has been frequently investigated in previous works, both from an observational point of view (Lada et al., 1999; Zavagno et al., 2006; Deharveng et al., 2006, 2010; Beerer et al., 2010; Liu et al., 2016; Yep & White, 2020) and from simulations (Hosokawa & Inutsuka, 2005, 2006a,b; Dale et al., 2007b,a; Walch et al., 2013).

5.3.3 ISM phases evolution

The evolution of different gas phases in the whole computational box can be studied with density-temperature phase diagrams, shown in Fig. 5.5. Different rows correspond to simulation snapshots at $t = 0$ Myr, $t = 1$ Myr and $t = 2$ Myr. Colors represent the normalized PDF, weighted by the mass of H_2, HI, and HII, respectively. At $t = 0$ Myr, the gas in the box is $\simeq 70\%$ molecular, with the rest being either in atomic ($\sim 5\%$) or ionizd form. This happens because gas compression (shocks and gravitational collapse) increases the temperature, fostering collisional dissociation of H_2 and ionization of HI. On the other side, the gas filling the box outside the cloud has $n < 10^2$ cm^{-3} and $T \simeq 10^{3-4}$ K, either in atomic or ionized form.

The row at $t = 1$ Myr shows features due to the presence of stars, heating the gas via both radiation and winds. At this stage, most molecular gas ($\sim 75\%$ of the total molecular gas) is present in the form of cold ($T < 30$ K) and dense ($n > 10^{3-4}$ cm^{-3}) clumps, even if there is some less dense molecular gas at $n < 10^3$ cm^{-3}. The $M_{\rm HI}$-weighted map is populated mainly by gas in the range $n = 10^3 - 10^4$ cm^{-3}, with temperatures varying from 10^2 K to 10^4 K. Two horizontal branches ($T \simeq 10^3$ K and $T \simeq 10^4$ K) are visible, and correspond to the edges of HII regions, where the gas is compressed by radiation-driven shocks and EUV photons are not able to penetrate. Warm medium with $T < 500$ K is associated with PDRs, and contains around 20% of HI. The $M_{\rm HII}$-weighted map shows a clear horizontal line at $T \simeq 4 \times 10^4$ K, due to photoionization heating of hydrogen and helium. These ionized regions have densities ranging from 10 cm^{-3} to 10^3 cm^{-3}. Gas is heated to even higher temperatures ($T \simeq 10^{5-6}$ K) around massive stars, due to the kinetic energy injection by winds.

The last row ($t = 2$ Myr) shows an advanced evolutionary stage of the cloud, where most of molecular gas has been dissociated. H_2 survives only in very dense clumps ($n > 10^4$ cm^{-3}) and a few patches of low density gas, which are shadowed from radiation. Also, HI is much less abundant than in the previous snapshot, due to photoionization. Indeed, the horizontal branch in the $M_{\rm HII}$-weighted map is much more extended in this case (up to 10^4 cm^{-3}).

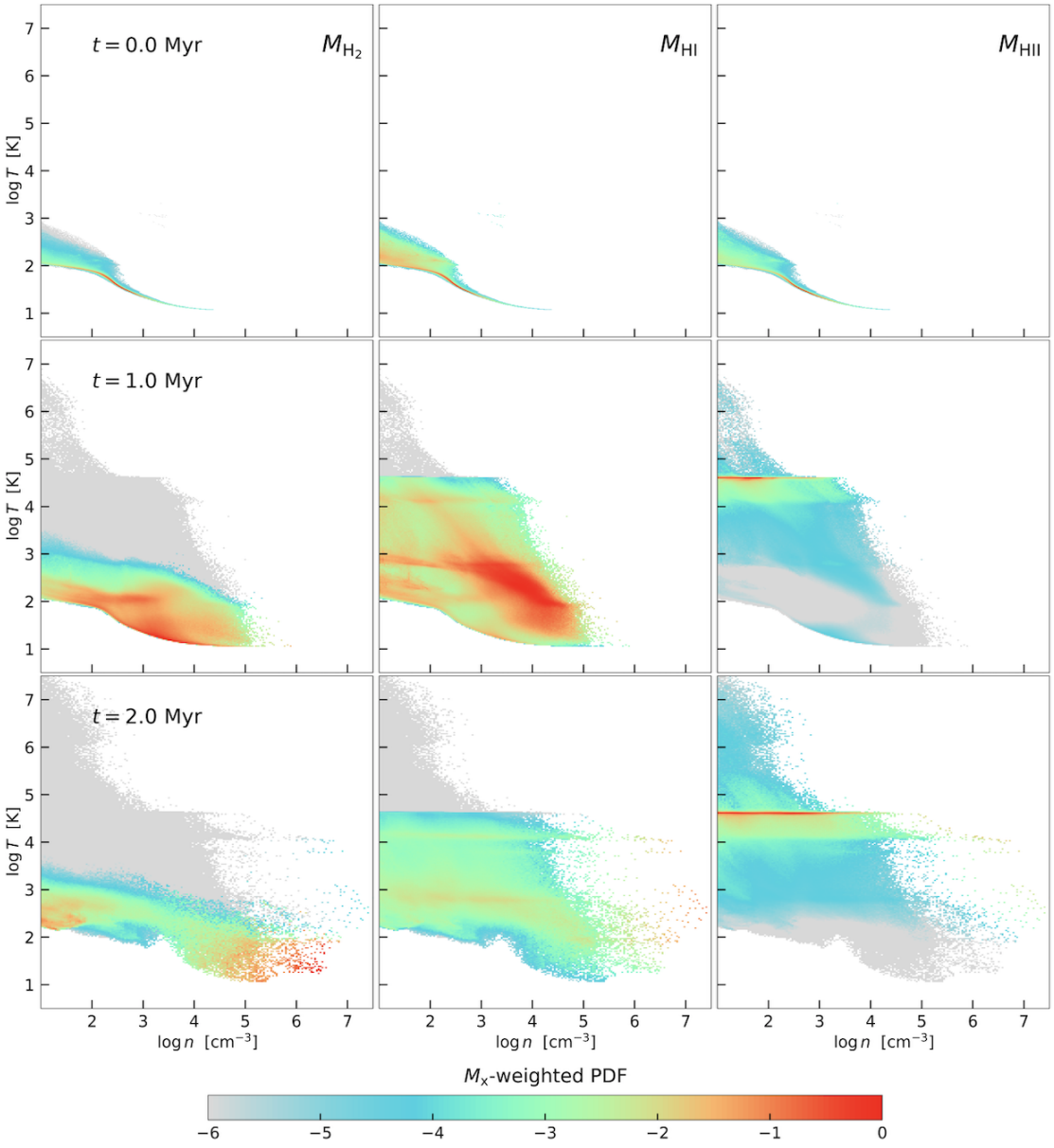

Figure 5.5: Phase diagrams of the gas in the cloud. The three rows show different evolutionary stages, at $t = 0$, 1 and 2 Myr respectively. Each panel shows a $M_{\rm x}$-weighted PDF in the density-temperature ($n - T$) plane, where $M_{\rm x}$ is the mass of the species X. The three columns correspond to the species H_2, HI and HII. As the cloud evolves with time, molecular gas is converted into atomic and ionized gas.

5.3.4 SFE and SFR

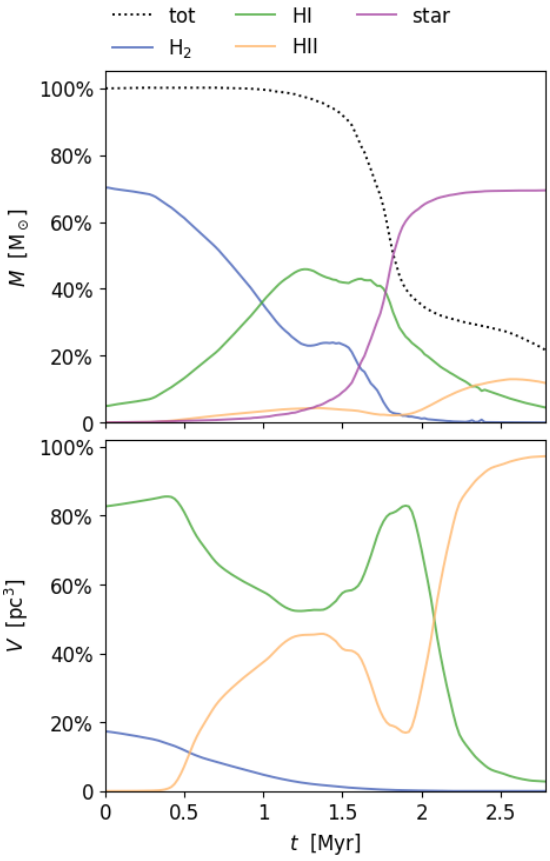

Figure 5.6: **Upper**: Time evolution of H_2 mass, HI mass, HII mass, stellar mass and total gas mass (including also helium) in the whole computational box (hence including both the cloud and the surrounding low density medium). **Lower**: Time evolution of the volume occupied by H_2, HI and HII in whole box; a cell is included in one phase if more than 50% of its mass is in such a phase.

The upper panel of Fig. 5.6 shows the time evolution of gas mass in the box in the different phases (M_{H_2}, M_{HI} and M_{HII}), together with the total gas mass M_{tot} (including also all the other species, as He) and the stellar mass $M_\star$. All masses include all the gas in box, so both the GMC and the surrounding gas.

As the cloud evolves, molecular gas has two possible fates: (1) it is converted into atomic and ionized gas by stellar feedback, (2) it goes into stars. This means that the efficiency of stellar feedback determines the molecular gas mass which remains available for star formation. M_{H_2} goes to zero around $t_{ev} \simeq 2.2$ Myr, marking the complete evaporation of the GMC. HI mass increases as H_2 is dissociated, peaking between 1.2 and 1.7 Myr. Later, HI is ionized and hence its mass tends to zero. HII mass grows as more ionizing flux is produced, and at the end of the simulation the mass is either in in stars or HII, with a small percentage in HI.

The volume occupied by the different gas phases is shown in the lower panel of Fig. 5.6. The volume occupied by the species X (HI, HII or H_2) is defined as the sum of the volume of all cells where the mass fraction $\mu_x = M_x/(M_{HI} + M_{HII} + M_{H_2})$ is larger than 50% *. At $t = 0$ Myr, the gas in the cloud is in fully molecular form ($\sim 20\%$ of the total volume, while the surrounding ISM is in atomic phase. Then, the volume of the molecular phase decreases with time, both because of dissociation by LW photons and gravitational collapse. In the meantime, the external medium is ionized, explaining the decrease in HI volume and the increase in

*We have verified that changing the threshold to 75% or 90% does not yield any significant difference in the trend. We also obtain a similar result by removing the threshold and weighting the volume of the cells by μ_x.

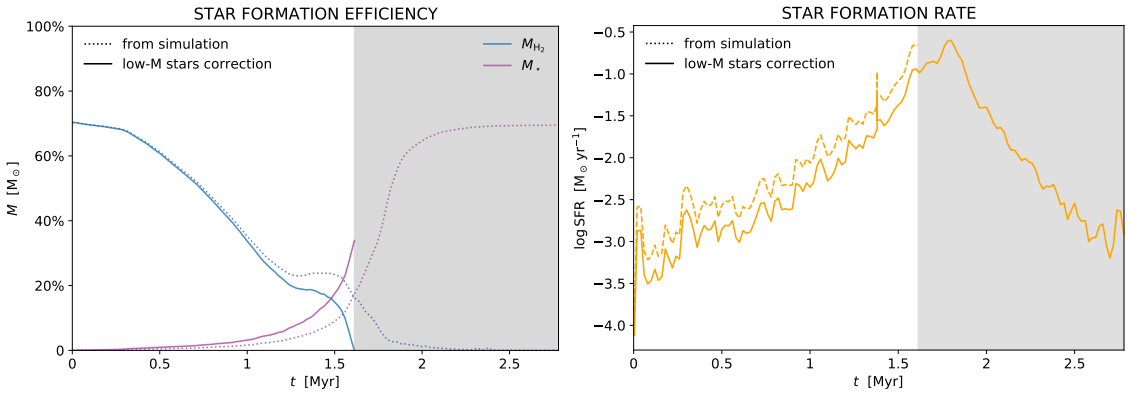

Figure 5.7: **Left**: time evolution of H_2 mass and stellar mass, and relative correction accounting for low mass stars ($M < 1\,M_\odot$), which are not included in the simulation. Accounting for this correction, the cloud is destroyed in a shorter time ($t \simeq 1.6$ Myr), and the final SFE is lower ($\sim 36\%$). **Right**: time evolution of the star formation ionizrate, again plotted together with the low mass star correction. The shaded area mark the times at which the cloud is destroyed (i.e. there is no H_2 left) according to the low-M star correction.

HII volume between $t = 1$ Myr and $t = 1.5$ Myr. Since the gravitational collapse proceeds and more dense clumps form (where the gas is self-shielded from radiation), $t = 2$ Myr marks a phase in which HII volume decreases. On the other side, the HI volume presents a new peak in this phase, while its mass remains almost constant. From the N_{HI} map in Fig. 5.3 we can see that this is due to the gas being more spread out, being pushed away by radiation. After 2 Myr, dense clumps are consumed by star formation, and ionizing radiation can again propagate in the whole computational box, filling almost all the volume.

When the cloud is completely evaporated, the total stellar mass is $M_\star \simeq 7.4{\times}10^4 M_\odot$, which means a global SFE $= M_\star/M_{GMC} \simeq 74\%$. Nevertheless, the correction for the fact that we neglected the formation of low-mass stars (and hence the corresponding mass removal) must be applied, as detailed at the end of Sec. 5.2.2. The left panel of Fig. 5.7 shows with dotted lines the values of H_2 mass and stellar mass straight from the simulation, and the corrected values with solid lines. We can see that the corrected value M'_{H_2} approaches zero around $t = 1.6$ Myr, and by this time the total stellar mass is $M'_\star \simeq 3.6 \times M_\star$, or SFE$\simeq 36\%$.

Recent works on GMC simulations (Geen et al., 2016; Raskutti et al., 2016; Howard et al., 2017; Kim et al., 2018; He et al., 2019) find SFE$\simeq 10 - 20\%$ for clouds with similar properties to this work ($M = 10^5\,M_\odot$, $\bar{n} = 120$ cm^{-3}), despite not including all feedback mechanisms simultaneously (photoionization/dissociation, radiation pressure, winds). This is mainly due to a few significant differences with respect to our setup, which result in more spread and less dense clouds: (1) most works relax the cloud in a

non-turbulent surrounding medium, (2) gravity is turned off or a reduced gravitational constant is used in the relaxation stage, (3) different initial cloud profiles are adopted (isothermal profiles, Bonnor-Ebert spheres, etc.). As a consequence, these clouds are less star forming and more subject to gas evaporation by stellar feedback. Instead, in our simulation, we have an initially uniform, self-gravitating cloud, confined by a turbulent surrounding medium. Star formation is enabled after 3 Myr, when the cloud gas is denser and has already started collapsing towards the centre of the box. Hence, it is natural to expect a more rapid star formation and a higher SFE in our case. In addition, stellar feedback is sometimes implemented in a different way. For instance, He et al. (2019) assume a constant light-to-mass ratio for sink particles, hence overestimating the UV photons emitted by low mass stars (as shown in Fig. 5.2, only stars with mass $M > 10\,\mathrm{M}_\odot$ have a relevant contribution both in the FUV and the EUV).

Nevertheless, it is interesting to notice that both in this and previous theoretical works, the SFE is typically larger than what typically observed ($\sim 1-10\%$ Lada et al., 2010; Murray et al., 2010; Lada, 2015; Lee et al., 2016; Ochsendorf et al., 2017) in local GMCs in the Milky Way, despite the accurate implementation of stellar feedback. A possible explanation is the absence of turbulence driving in our simulation, meant to mimic external shear and compression due to the environment in which the cloud could be embedded in (turbulent motion in the spiral arms of the galaxy, supernova explosions in the neighbourhood of the GMC, etc.).

In addition, the inclusion of magnetic fields could also decrease the SFE of the cloud, since magnetic pressure entails lower clump densities. As a result, clumps are less star forming and more easily dissolved by radiation. Federrath & Klessen (2013) have analysed the impact of different effects on star formation, finding that the effect of an increase of the turbulence is twofold: (1) the increase of α_{vir} stabilizes the cloud against collapse, decreasing the SFE, (2) compressive modes with higher Mach number $\mathcal{M}$ foster star formation by creating local compression; moreover, the presence of solenoidal modes (keeping $\mathcal{M}$ constant) decreases the SFE at least of an order of magnitude, while magnetic fields with Alfvenic turbulence with $\mathcal{M}_{\mathrm{A}} \sim 1.3$ decrease the SFE by a factor of two. Hence, the inclusion of turbulence driving and magnetic fields in our simulation would help to obtain lower values for the SFE, that are closed to the observed ones. We plan to address this issue in a future work.

5.3.5 Radiation in the GMC

Fig. 5.8 shows the maps of photon density-weighted Habing flux G_0, photon density-weighted ionization parameter (U_{ion}, defined as the ratio between photon density and gas density) and gas mass-weighted temperature T at $t = 1.0$ Myr. The flux is high in the neighbourhood of massive stars, but it has not leaked yet from the whole cloud. Typical

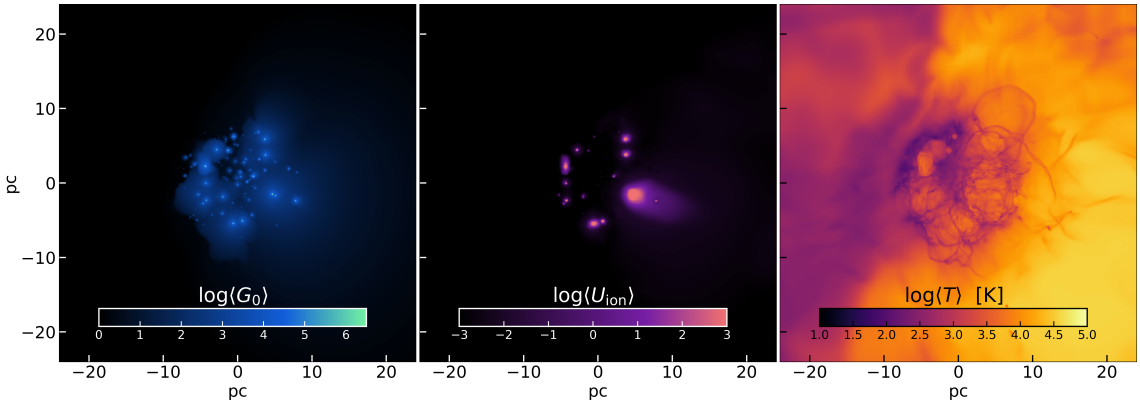

Figure 5.8: Snapshots of the cloud properties at $t = 1.0$ Myr: from left to right, projections of (a) FUV flux G_0 weighted by photon number, (b) ionization parameter $U_{\rm ion}$ weighted by photon number and (c) temperature T weighted by gas mass. At this stage, photons have not leaked yet from the cloud, and the flux is high only close to massive stars or stellar clusters.

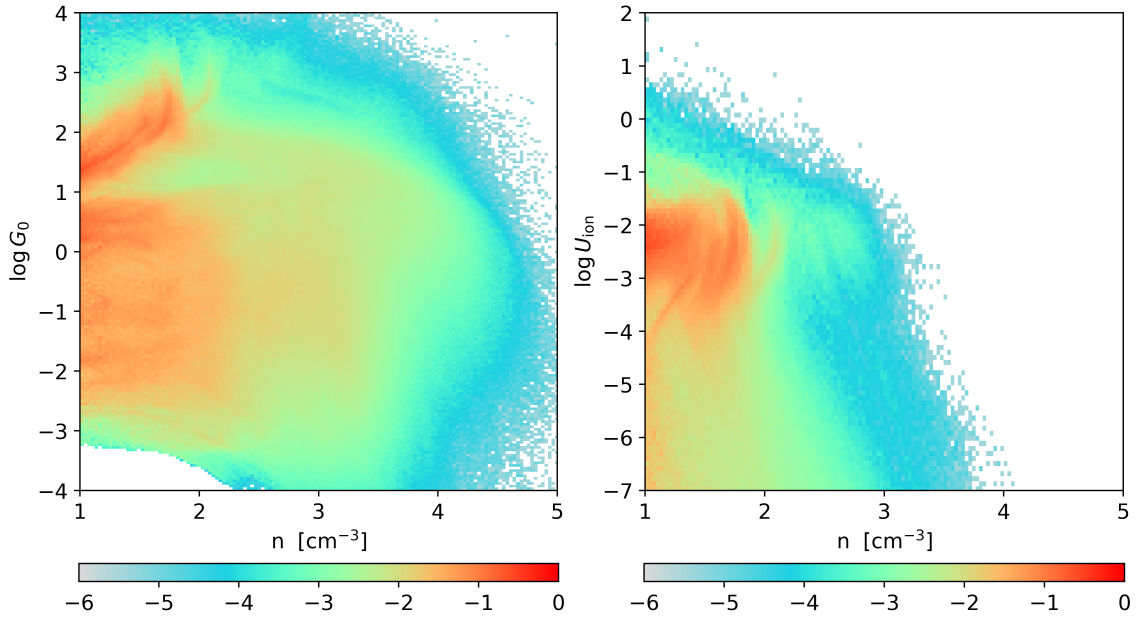

Figure 5.9: $G_0 - n$ (left) and $U_{\rm ion} - n$ (right) phase-diagrams. The PDF are volume-weighted and then normalized. Regions with the density ($n > 10^3$) may have a high FUV flux ($G_0 > 10^2$), while they are completely self-shielded from ionizing radiation. At low gas densities ($n < 10^2$), G_0 can assume a variety of values from 10^{-3} to 10^3, while the ionization parameter is generally $> 10^{-3}$.

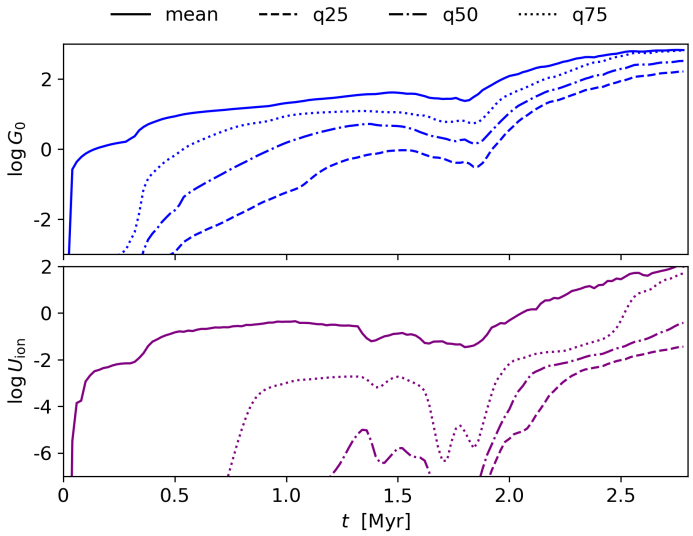

Figure 5.10: Time evolution of G_0 (**upper** panel) and $U_{\rm ion}$ (**lower** panel) in the cloud. The solid line shows the evolution of the volume-weighted average value, while the dashed, dotted-dashed and dotted lines show the 25th, 50th and 75th volume-weighted percentiles respectively (q_{25}, q_{50} and q_{75}). The larger scatter of the $U_{\rm ion}$ distribution indicates that the ionization field is more patchy than the Habing one.

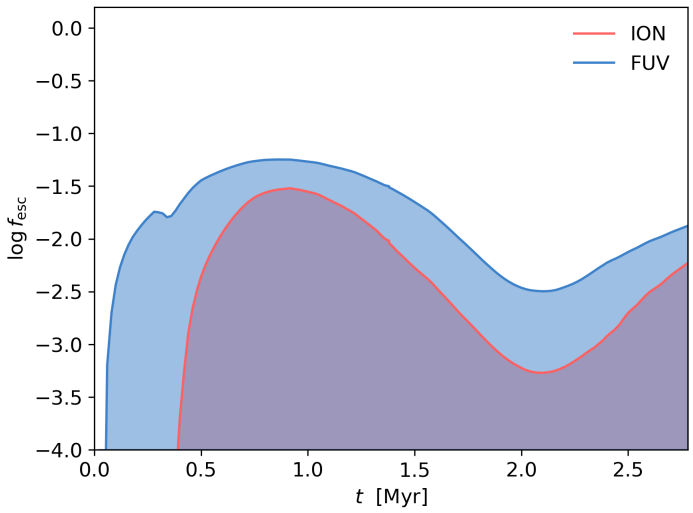

Figure 5.11: Time evolution of the escape fraction (see definition in eq. 5.10) of FUV (blue line) and ionizing (red line) photons.

values of G_0 are 10^{4-5} and $U_{\rm ion} \simeq 10^3$ in the immediate proximity of massive stars, as they have devoided of gas their surrounding. The map shows mass-weighted temperatures of 3000 K inside the cloud, however the maximum temperatures inside HII regions can reach values of 10^{7-8} K near very massive stars, because of the mechanical feedback.

An analysis of the radiation field in molecular clouds is particularly relevant for cosmological simulations of galaxy formation, where generally it is possible only to marginally resolve the internal structure of molecular clouds (Leung et al., 2019). With a typical resolution of tens of parsecs (Rosdahl et al., 2018; Pallottini et al., 2019), a cell represents a whole GMC and therefore its properties are averaged, so local inhomogeneities cannot be taken into account. GMC emission properties – in particular far-infrared lines, as [CII], [NII], and [OIII] and CO – has been shown to be sensitive to their internal density structure (Vallini et al., 2017, 2018), while the radiation field is typically assumed to be constant. In particular, [CII] emission depends on G_0, while [NII] and [OIII] are strongly affected by $U_{\rm ion}$. Hence, the approximation of an average uniform $U_{\rm ion}$ (due to resolution limits) can lead to an incorrect estimation of line emission (see discussion in Olsen et al. 2018 and Pallottini et al. 2019).

In Fig. 5.9 we plot the $G_0 - n$ and $U_{\rm ion} - n$ phase diagrams at $t = 1$ Myr, showing the normalized volume-weighted PDF. High density gas ($n > 10^3$ cm^{-3}) has $U_{\rm ion} \simeq 0$, being able to self-shield from ionizing radiation, while G_0 can attain large values $G_0 > 10$. On the other hand, low density gas ($n < 10^2$ cm^{-3}) typically shows $G_0 > 10 - 100$ and ionization parameter $U_{\rm ion} \simeq 10^{-2}$, as this gas is associated with HII regions. According to Pallottini et al. (2019) [CII] emission mostly comes from regions in which $n \simeq 2 \times 10^2$ cm^{-3}, $G_0 \simeq 20$, and $U_{\rm ion}$ is relatively low, implying that they are neutral (see also Ferrara et al., 2019). Lines as [NII] and [OIII] are instead emitted from ionized regions with densities around 50-100 cm^{-3} and $U_{\rm ion} > 10^{-3}$.

The time evolution of G_0 and $U_{\rm ion}$ in the cloud are shown in Fig. 5.10: the different lines show the volume-weighted average and the 25th, 50th, and 75th volume-weighted percentiles. The average values of both G_0 and $U_{\rm ion}$ increase almost steadily during the simulation, showing a slight drop around $t \simeq 1.5 - 2$ Myr, corresponding to the increase in HI seen in Fig. 5.6. At the end of the simulation, the volume-weighted $\langle G_0 \rangle$ stabilizes at a value of $\sim 10^3$, and $\langle U_{\rm ion} \rangle$ reaches 10^2. The spread in the percentiles evolution is narrower for G_0 than $U_{\rm ion}$: defining the relative spread between percentiles as $\delta X = (q_{75} - q_{25})/q_{50}$, we have $\delta U_{\rm ion}$ larger than δG_0 by a factor 10^7 at $t = 1$ Myr and by a factor ~ 100 for $t > 2$ Myr. This means that the distribution of G_0 at a given time is more peaked, while the distribution for $U_{\rm ion}$ is more spread with a larger variance. Hence, prediction on the intensity of [NII] and [OIII] lines will be strongly affected by the actual distribution of $U_{\rm ion}$, and the assumption of a uniform ionizing field appears not to be satisfied in our cloud. A more detailed analysis of emission properties from our simulated GMC is postponed to a

subsequent work.

Finally, we briefly discuss the time evolution of the escape fraction. This is defined in band X, at time t, as the ratio

$$f_{\rm X,esc}(t) = \frac{N_{\rm X,esc}(< t)}{N_{\rm X,prod}(< t)} \tag{5.10}$$

where:

- $N_{\rm X,esc}(< t)$ is the total number of photons in band X which have crossed the spherical surface of radius $R_{\rm s} = 20$ pc (i.e. the initial cloud radius) up to time t;
- $N_{\rm X,prod}(< t)$ is the total number of photons in band X produced by all stars in the cloud up to time t.

In Fig. 5.11 we show the escape fractions in the FUV band (blue line) and in the ionizing band (red line). FUV photons manage to escape earlier from the cloud, with $f_{\rm FUV,esc} > 0.01$ already around $t \simeq 0.2$ Myr, since they are able to propagate to larger distances in molecular gas before being absorbed. For the same reason, $f_{\rm FUV,esc}(t) > f_{\rm ion,esc}(t)$ at any time. The drop in $f_{\rm esc}$ in both bands around 2 Myr corresponds to the increase in mass and volume of the neutral phase, apparent from Fig. 5.6. Later on, $f_{\rm esc}$ increases again, and we expect it to increase monotonically to large values while neutral gas is progressively ionized. Note, however, that the ionizing photon production goes to zero when massive stars (the main contributors to $N_{\rm ion,prod}$) explode as SNe ($t \simeq 3$ Myr). We find that throughout the evolution $f_{\rm ion,esc} \lesssim 0.03$, also in agreement with similar studies (Howard et al., 2018; Kimm et al., 2019; He et al., 2020).

5.4 Summary

We have studied the evolution of a typical Giant Molecular Cloud (GMC) by running a 3D radiative transfer (RT), zoom hydro-simulation, including a full chemical network tracking H_2 formation and dissociation, and following individual stars forming inside the cloud. Multiple feedback mechanisms, such as photodissociation/ionization, radiation pressure, stellar winds and supernovae, are included simultaneously.

The simulation has been run with the RT version of the RAMSES code (Teyssier, 2002; Rosdahl et al., 2013), by coupling the RT module with the non-equilibrium chemical network generated with KROME (Grassi et al., 2014) in the same fashion as Decataldo et al. (2019) and Pallottini et al. (2019). We have implemented a stochastic star formation recipe, drawing stars from a Kroupa (2001) Initial Mass Function (IMF) and placing them in the simulation already in main sequence. To save computational time, we consider

only stars with masses larger than $1\,M_\odot$ and then apply a correction to account for the mass consumption by low-mass star formation. Each star emits radiation with a spectrum depending on its mass, sampled with 10 photon bins, and injects momentum isotropically in the interstellar medium via winds. The simulated GMC has a mass $M = 10^5\,M_\odot$, radius $R = 20$ pc and initial virial parameter $\alpha_{\rm vir} = 2$, meaning that the cloud is initially unbound.

The cloud presents dense clumps and filaments before star formation, due to turbulence and gravitational instabilities. When stars form, they affect the surrounding environment. Thanks to the inclusion of different mechanisms, and the accurate treatment of radiation and chemistry, it has been possible to identify different phases in the cloud evolution. In a first phase (up to $t = 1$ Myr), we assess the effect of radiation and winds on the structure and composition of the cloud. Ionized bubbles develops around massive stars (with densities $n \simeq 100$ cm^{-3} and $T \simeq 4 \times 10^4$ K) with dense edges ($n \simeq 10^3$ cm^{-3}) corresponding to photo-dissociation regions (PDRs). The molecular content of the cloud decreases by 50% because of the effect of radiation, even if dense molecular clumps ($n > 10^4$ cm^{-3}) are able to self-shield. At the end of this phase, the cloud presents an extended HI structure, whose collapse is prevented by the heating effect of non-ionizing radiation. Later, we identify a second phase in which dense clumps are consumed by rapid star formation (SFR$\simeq 0.1\,M_\odot\,{\rm yr}^{-1}$), so that radiation is free to escape and ionize the atomic gas in the computational box.

After applying the correction for the formation of stars with mass $< 1\,M_\odot$, we obtain that all the molecular gas in the cloud is exhausted in 1.6 Myr, and the final star formation efficiency (SFE) is 36 per cent. The short cloud lifetime that we found supports the picture of short-living GMCs (Elmegreen, 2000), which has also been supported by recent observations (Chevance et al., 2019). The obtained SFE efficiency is higher than the generally observed one, which is around 1-10% (Lada et al., 2010; Murray et al., 2010; Lada, 2015; Lee et al., 2016; Ochsendorf et al., 2017), despite the accurate implementation of stellar feedback. In fact, the initial turbulence is rapidly dissipated in our simulations and the cloud collapses under its own self-gravity entailing an high star formation rate (SFR$_{\rm max} = 0.1\,M_\odot\,{\rm yr}^{-1}$). The inclusion of turbulence driving, in order to effectively account for large-scale phenomena injecting kinetic energy in the ISM, would certainly help to sustain the turbulence level in the cloud, and hence decrease the SFE. We plan to add this feature to our simulations in a future work.

We have then analysed the radiation field inside the GMC, in the Habing and the ionizing bands. G_0 is rather homogeneous throughout the cloud, attaining a value around 10^2 at the end of the simulation. On the other hand, the ionization parameter $U_{\rm ion}$ shows a broader distribution, and hence a larger spatial modulation inside the cloud. This is crucial for the interpretation of emission from galaxy simulations, where generally individual GMCs are

not resolved, and therefore their properties are averaged. The distribution of the radiation field strongly affects line emission calculations, and the sub-grid patchiness of $U_{\rm ion}$ should be taken into account when computing the intensity of lines as [NII] and [OIII] (Olsen et al., 2018; Pallottini et al., 2019). Finally, we find that throughout the evolution the escape fraction of ionizing photons from the cloud is $f_{\rm ion,esc} \lesssim 0.03$, also in agreement with similar studies (Howard et al., 2018; Kimm et al., 2019; He et al., 2020).

Conclusions

The main goal of my Ph.D. has been to study the effect of mechanical and radiation feedback from different sources, as stars and quasars, on the molecular component of the interstellar medium. We have tackled the problem both with an analytical approach and numerical simulations, comparing the results with recent observations. The main conclusions are summarized in the following sections.

Molecular clumps in ionized regions

In Chapter 3, we have developed a semi-analytical model for the evolution of a dense molecular clump, affected by strong UV radiation impinging on its surface.

We have shown that the clump attains a layered structure, that we denote iPDR, with a thin ionized surface layer ($T \sim 10^4$ K) due to the effect of extreme-UV radiation, and a thick atomic layer ($T \sim$ few 10^2 K) due to the far-UV flux (Fig. 3.2). The inner core is self-shielded, and hence it remains cold and molecular. The pressure difference between the layers causes the propagation of shock and rarefaction waves in the clump, inducing the collapse of the core, while the ionized layer expands and disperses in the surrounding medium. Since gravity is not included in this model, the clump collapse is followed by an expansion phase, in which density decreases and radiation finally dissolves the whole clump.

As a first application of our model, we have studied the fate of a clump located inside the HII region of a massive (class OB) star. Clumps with mass $M = 0.1\,\mathrm{M}_\odot$ at 0.3 pc from the source evaporate in 0.01 Myr for the brightest star considered ($L = 10^5\,\mathrm{L}_\odot$) and 0.06 Myr for the $10^3\,\mathrm{L}_\odot$ star (Fig. 3.8). Furthermore, we notice that evaporation times are shorter by a factor 2-4 when ionizing radiation is included, with respect to photoevaporation induced only by FUV. The evolution of photoevaporating clumps has consequences on the emission properties of the ISM, in particular far-infrared lines (e.g.

[CII], [OIII], [NII]). This is relevant in the context of galaxies at high-z, where FIR lines are the primary observational tool.

We have then studied the evolution of molecular clumps embedded in quasar outflows analysing the photoevaporation effect due to quasar radiation. Photoevaporation times range from 0.2 Myr to 0.5 Myr for quasars with luminosity $L = 10^{45-47}\,\mathrm{erg\,s^{-1}}$ and clumps with mass $10^3\,\mathrm{M_\odot}$ (Fig. 3.10). Considering that these clumps are moving at the outflow speed, we can obtain an estimate for the maximum distance travelled by molecular gas before being evaporated. We obtain radii compatible with observed distance at which molecular gas is observed in quasar outflows ($\simeq 0.1 - 1$ kpc), hence suggesting that photoevaporation could be the main mechanism regulating the extension of molecular outflows (Fig. 3.11).

Numerical simulations of photoevaporation of clump

In Chapter 4, we have shown numerical simulations of photoevaporating clumps, focusing on the effect of far-UV radiation on molecular clumps located in photo-dissociation regions around massive OB stars.

We have run AMR simulations featuring coupled hydro, radiative transfer and a non-equilibrium chemical network. We focus on reactions involving hydrogen and helium, tracking in particular the formation and destruction of H_2. We run seven simulations of dense clumps with different masses (in the range $M = 10 - 200\,\mathrm{M_\odot}$) and with different impinging fluxes (in the range $G_0 = 2 \times 10^3 - 8 \times 10^4$ in Habing units).

We identify three phases in the clump evolution (Fig 4.11): (1) the photodissociation front travels as an R-type, leaving the density of the clump unaltered and dissociating most of the H_2 (40-90 % depending on G_0); (2) the molecular core of the clump implodes, while the heated gas at the surface expands; (3) the core collapses under its self-gravity, hence undergoing star formation if the mass is enough.

All the clumps considered manage to retain some molecular mass ($> 2.5\,\mathrm{M_\odot}$), sufficient to form stars, hence showing that photoevaporation is not able to prevent star formation, although it regulates the amount of mass going into stars (Fig. 4.5). In particular, in the case of massive clumps ($> 100\,\mathrm{M_\odot}$), dissociated gas is not able to escape from the surface because of its self-gravity, limiting the mass loss by photoevaporation (Fig. 4.9). In the context of photoevaporating clumps in quasar outflows, our results suggest that star formation within the outflow is a plausible scenario, as hinted by recent observations (Maiolino et al., 2017; Rodríguez del Pino et al., 2019).

Mechanical and radiative feedbacks on Giant Molecular Clouds

In Chapter 5, we have shown a numerical simulation of a Giant Molecular Cloud (GMC), with the goal of studying the effect of radiation and winds from newly formed stars inside the cloud.

In the simulation, we follow the formation and the kinematics of individual stars, including different feedback mechanisms: photodissociation/ionization, radiation pressure, stellar winds and supernovae. Radiation emitted by stars is tracked with 10 photon bins, spanning from the mid-infrared to the extreme ultraviolet bands. Stars are formed via a stochastic recipe, with a probability following the Schmidt-Kennicutt relation.

The evolution of the cloud is dictated by the effect of radiation, carving bubbles and inducing the formation of clumps and filaments (Fig. 5.3 and 5.4). The molecular content is decreased by 50 % in $\sim$ 1 Myr, and only dense clumps ($n > 10^4$ cm^{-3}) are able to self-shield from radiation. In a later phase, these dense clumps are consumed by rapid star formation, and there is no molecular gas left at $t \sim 2$ Myr.

Our results support the picture of short-lived GMCs (Elmegreen, 2000), also corroborated by recent observations. Despite the accurate implementation of feedback, we find a star formation efficiency SFE $\simeq$ 36% (Fig. 5.7), which is higher than generally observed ($< 10\%$). This is probably due to the initial setup, in which the spherical cloud is globally collapsing under its self-gravity, entailing higher densities and hence (1) high star formation rate and (2) more efficient self-shielding from radiation.

Finally, we have analysed the radiation field due to stars forming inside the GMC. The far ultraviolet flux G_0 is rather homogeneous, attaining a value $G_0 \simeq 2$ at the end of the simulation. On the other hand, the ionizing field shows a patchy distribution (Fig. 5.10). This is crucial when interpreting the results of galaxy-scale simulations, where GMCs are not resolved in general. In fact, without resolving the actual radiation field in the individual cells, average values are used and this could affect e.g. line emission calculations.

Bibliography

Aalto S., Garcia-Burillo S., Muller S., Winters J. M., Van Der Werf P., Henkel C., Costagliola F., Neri R., 2012a, Astronomy & Astrophysics, 537, A44

Aalto S., Muller S., Sakamoto K., Gallagher J. S., Martín S., Costagliola F., 2012b, Astronomy & Astrophysics, 546, A68

Aalto S., et al., 2015, Astronomy & Astrophysics, 574, A85

Abel T., Anninos P., Zhang Y., Norman M. L., 1997, New Astronomy, 2, 181

Adams F. C., Hollenbach D. J., Laughlin G., Gorti U., 2004, The Astrophysical Journal, 611, 360

Alatalo K., et al., 2011, The Astrophysical Journal, 735, 88

Alves J. F., Lada C. J., Lada E. A., 2001, Nature, 409, 159

Alves J., Lombardi M., Lada C. J., 2007, Astronomy & Astrophysics, 462, L17

Anders E., Grevesse N., 1989, Geochimica et Cosmochimica Acta, 53, 197

Anderson L. D., Bania T. M., Jackson J. M., Clemens D. P., Heyer M., Simon R., Shah R. Y., Rathborne J. M., 2009, The Astrophysical Journal Supplement Series, 181, 255

André P., 1994, in The Cold Universe. p. 179

André P., Motte F., 2000, in Star Formation from the Small to the Large Scale. p. 219

André P., et al., 2010, Astronomy & Astrophysics, 518, L102

Aubert D., Teyssier R., 2008, Monthly Notices of the Royal Astronomical Society, 387, 295

Bakes E. L. O., Tielens A. G. G. M., 1994, The Astrophysical Journal, 427, 822

Bally J., Langer W. D., Stark A. A., Wilson R. W., 1987, The Astrophysical Journal, 312, L45

Barnes P. J., Hernandez A. K., Muller E., Pitts R. L., 2018, The Astrophysical Journal, 866, 19

Bedijn P. J., Tenorio-Tagle G., 1984, Astronomy & Astrophysics, 135, 81

Beerer I. M., et al., 2010, The Astrophysical Journal, 720, 679

Bell E. F., McIntosh D. H., Katz N., Weinberg M. D., 2003, The Astrophysical Journal Supplement Series, 149, 289

Bell E. F., et al., 2004, The Astrophysical Journal, 608, 752

Bell T. A., Viti S., Williams D. A., Crawford I. A., Price R. J., 2005, Monthly Notices of the Royal Astronomical Society, 357, 961

Bergin E. A., Snell R. L., Goldsmith P. F., 1996, The Astrophysical Journal, 460, 343

Bertoldi F., 1989, The Astrophysical Journal, 346, 735

Bertoldi F., McKee C. F., 1990, The Astrophysical Journal, 354, 529

Bertoldi F., McKee C. F., 1992, The Astrophysical Journal, 395, 140

Beuther H., Schilke P., Menten K. M., Motte F., Sridharan T. K., Wyrowski F., 2002, The Astrophysical Journal, 566, 945

Bialy S., Sternberg A., 2016, The Astrophysical Journal, 822, 83

Bisbas T. G., Unsch R., Whitworth A. P., Hubber D. A., Walch S., 2011, The Astrophysical Journal, 736, 142

Bisbas T. G., Bell T. A., Viti S., Yates J., Barlow M. J., 2012, Monthly Notices of the Royal Astronomical Society, 427, 2100

Bisbas T. G., Papadopoulos P. P., Viti S., 2015, The Astrophysical Journal, 803, 37

Bischetti M., Maiolino R., Fiore S., Carniani F., Piconcelli E., Fluetsch A., 2018, preprint (arXiv:1806.00786)

Black J. H., 1981, Monthly Notices of the Royal Astronomical Society, 197, 553

Blitz L., 1993, in Protostars and Planets III. pp 125–161

Bohlin R. C., Savage B. D., Drake J. F., 1978, The Astrophysical Journal, 224, 132

Bolatto A. D., Leroy A. K., Rosolowsky E., Walter F., Blitz L., 2008, The Astrophysical Journal, 686, 948

Boltzmann L., 1872, Sitzungsberichte der Kaiserlichen Akademie der Wissenschaften in Wien, mathematisch-naturwissenschaftliche Classe, 66, 275

Bonnor W. B., 1956, Monthly Notices of the Royal Astronomical Society, 116, 351

Bouwens R. J., et al., 2016, The Astrophysical Journal, 833, 72

Bovino S., Grassi T., Capelo P. R., Schleicher D. R. G., Banerjee R., 2016, Astronomy & Astrophysics, A15, 1

Bressan A., Marigo P., Girardi L., Salasnich B., Dal Cero C., Rubele S., Nanni A., 2012, Monthly Notices of the Royal Astronomical Society, 427, 127

Bron E., Agúndez M., Goicoechea J. R., Cernicharo J., 2018, preprint (arXiv:1801.01547)

Brunt C. M., Heyer M. H., Mac Low M.-M., 2009, A&A, 504, 883

Bryan G. L., et al., 2014, The Astrophysical Journal Supplement Series, 211, 19

Burke J. R., Hollenbach D. J., 1983, The Astrophysical Journal, 265, 223

Burton M. G., Hollenbach D. J., Tielens A. G. G. M., 1990, The Astrophysical Journal, 365, 620

Calzetti D., Armus L., Bohlin R. C., Kinney A. L., Koornneef J., Storchi-Bergmann T., 2000, The Astrophysical Journal, 533, 682

Cappi M., et al., 2006, Astronomy & Astrophysics, 446, 459

Carniani S., et al., 2017, Astronomy & Astrophysics, 605, A42

Carpenter J., 2000, The Astronomical Journal, 120, 3139

Castelli F., Kurucz R. L., 2003, Modelling of Stellar Atmospheres, 210, A20

Castor J. I., Abbott D. C., Klein R. I., 1975, ApJ, 195, 157

Cen R., 1992, The Astrophysical Journal Supplement Series, 78, 341

Ceverino D., Klypin A., 2009, The Astrophysical Journal, 695, 292

Champion J., Berné O., Vicente S., Kamp I., Petit F. L., Gusdorf A., Joblin C., Goicoechea J. R., 2017, Astronomy & Astrophysics, 604, A69

Chandrasekhar S., 1939, Chicago

Chevance M., et al., 2019, Monthly Notices of the Royal Astronomical Society

Cicone C., Feruglio C., Maiolino R., Fiore F., Piconcelli E., Menci N., Aussel H., Sturm E., 2012, Astronomy & Astrophysics, 543, A99

Cicone C., et al., 2014, Astronomy & Astrophysics, 562, A21

Cicone C., et al., 2015, Astronomy & Astrophysics, 574, A14

Cioffi D. F., McKee C. F., Bertschinger E., 1988, The Astrophysical Journal, 334, 252

Colella P., 1990, Journal of Computational Physics, 87, 171

Colombo D., et al., 2014, ApJ, 784, 3

Combes F., et al., 2013, Astronomy & Astrophysics, 558, A124

Costa T., Sijacki D., Haehnelt M. G., 2014, Monthly Notices of the Royal Astronomical Society, 444, 2355

Couch W. J., Sharples R. M., 1987, Monthly Notices of the Royal Astronomical Society, 229, 423

Da Cunha E., et al., 2013, The Astrophysical Journal, 766, 13

Dale J. E., Bonnell I. A., Clarke C. J., Bate M. R., 2005, Monthly Notices of the Royal Astronomical Society, 358, 291

Dale J. E., Bonnell I. A., Whitworth A. P., 2007a, Monthly Notices of the Royal Astronomical Society, 375, 1291

Dale J. E., Clark P. C., Bonnell I. A., 2007b, Monthly Notices of the Royal Astronomical Society, 377, 535

Dale J. E., Ercolano B., Clarke C. J., 2007c, Monthly Notices of the Royal Astronomical Society, 382, 1759

Dale J. E., Ercolano B., Bonnell I. A., 2012a, Monthly Notices of the Royal Astronomical Society, 424, 377

Dale J. E., Ercolano B., Bonnell I. A., 2012b, Monthly Notices of the Royal Astronomical Society, 427, 2852

Dalgarno A., McCray R. A., 1972, Annual Review of Astronomy & Astrophysics, 10, 375

Dame T. M., Hartmann D., Thaddeus P., 2001, The Astrophysical Journal, 547, 792

Dasyra K. M., Combes F., 2012, Astronomy & Astrophysics, 541, L7

Dayal P., et al., 2020, arXiv:2001.06021 [astro-ph]

Decataldo D., Ferrara A., Pallottini A., Gallerani S., Vallini L., 2017, Monthly Notices of the Royal Astronomical Society, 471, 4476

Decataldo D., Pallottini A., Ferrara A., Vallini L., Gallerani S., 2019, Monthly Notices of the Royal Astronomical Society

Decataldo D., Lupi A., Ferrara A., Pallottini A., in prep., Monthly Notices of the Royal Astronomical Society

Deharveng L., Lefloch B., Massi F., Brand J., Kurtz S., Zavagno A., Caplan J., 2006, Astronomy & Astrophysics, 458, 191

Deharveng L., et al., 2010, Astronomy & Astrophysics, 523, A6

Demircan O., Kahraman G., 1991, Astrophysics and Space Science, 181, 313

Deparis N., Aubert D., Ocvirk P., Chardin J., Lewis J., 2019, Astronomy & Astrophysics, 622, A142

Dobbs C. L., 2015, MNRAS, 447, 3390

Draine B. T., 1978, The Astrophysical Journal Supplement Series, 36, 595

Draine B. T., 2011, Physics of the Interstellar and Intergalactic Medium by Bruce T. Draine. Princeton University Press, 2011. ISBN: 978-0-691-12214-4

Draine B. T., Bertoldi F., 1996, The Astrophysical Journal, 468, 50

Draine B. T., Salpeter E. E., 1979, The Astrophysical Journal, 231, 438

Draine B. T., et al., 2007, The Astrophysical Journal, 663, 866

Dressler A., Gunn J. E., 1983, The Astrophysical Journal, 270, 7

Dwarkadas V. V., Gruszko J., 2012, Monthly Notices of the Royal Astronomical Society, 419, 1515

Dwek E., Foster S. M., Vancura O., 1996, The Astrophysical Journal, 457, 244

Dyson J. E., 1968, Astrophysics and Space Science, 2, 461

Dyson J. E., 1973, Astronomy & Astrophysics, 27, 459

Dyson J. E., Williams D. A., 1997, The physics of the interstellar medium. Edition: 2nd ed. Publisher: Bristol: Institute of Physics Publishing, 1997. Edited by J. E. Dyson and D. A. Williams. Series: The graduate series in astronomy. ISBN: 0750303069

Ebert R., 1955, Zeitschrift für Astrophysik, 37, 217

Elmegreen B. G., 2000, ApJ, 530, 277

Elmegreen B. G., 2011a, EAS Publications Series, 51, 45

Elmegreen B. G., 2011b, The Astrophysical Journal, 737, 10

Evans N. J., et al., 2009, The Astrophysical Journal Supplement Series, 181, 321

Faber S. M., et al., 2007, The Astrophysical Journal, 665, 265

Federrath C., Klessen R. S., 2012, The Astrophysical Journal, 761, 156

Federrath C., Klessen R. S., 2013, The Astrophysical Journal, 763, 51

Ferland G. J., Korista K. T., Verner D. A., Ferguson J. W., Kingdon J. B., Verner E. M., 1998, Publications of the Astronomical Society of the Pacific, 110, 761

Ferrara A., Scannapieco E., 2016, The Astrophysical Journal, 833, 46

Ferrara A., Tolstoy E., 2000, Monthly Notices of the Royal Astronomical Society, 313, 291

Ferrara A., Vallini L., Pallottini A., Gallerani S., Carniani S., Kohandel M., Decataldo D., Behrens C., 2019, Monthly Notices of the Royal Astronomical Society, 489, 1

Ferrarese L., Merritt D., 2000, The Astrophysical Journal Letters, 539, L9

Feruglio C., Maiolino R., Piconcelli E., Menci N., Aussel H., Lamastra A., Fiore F., 2010, Astronomy & Astrophysics, 518, L155

Feruglio C., Fiore F., Piconcelli E., Cicone C., Maiolino R., Davies R., Sturm E., 2013, Astronomy & Astrophysics, 558, A87

Feruglio C., et al., 2015, Astronomy & Astrophysics, 583, A99

Field G. B., 1965, The Astrophysical Journal, 142, 531

Finkelstein S. L., et al., 2012, The Astrophysical Journal, 756, 164

Fischer J., et al., 2010, Astronomy & Astrophysics, 518, L41

Fluetsch A., et al., 2019, Monthly Notices of the Royal Astronomical Society, 483, 4586

Fryxell B., et al., 2000, The Astrophysical Journal Supplement Series, 131, 273

Gallagher R., Maiolino R., Belfiore F., Drory N., Riffel R., Riffel R. A., 2019, Monthly Notices of the Royal Astronomical Society, 485, 3409

García-Burillo S., et al., 2015, Astronomy & Astrophysics, 580, A35

García P., Bronfman L., Nyman L.-Å., Dame T. M., Luna A., 2014, The Astrophysical Journal Supplement Series, 212, 2

Gatto A., et al., 2017, Monthly Notices of the Royal Astronomical Society, 466, 1903

Gebhardt K., et al., 2000, The Astrophysical Journal Letters, 539, L13

Geen S., Hennebelle P., Tremblin P., Rosdahl J., 2016, Monthly Notices of the Royal Astronomical Society, 463, 3129

Geen S., Watson S. K., Rosdahl J., Bieri R., Klessen R. S., Hennebelle P., 2018, Monthly Notices of the Royal Astronomical Society, 481, 2548

Genzel R., Stutzki J., 1989, ARA&A, 27, 41

Glover S. C. O., Abel T., 2008, Monthly Notices of the Royal Astronomical Society, 388, 1627

Glover S. C. O., Jappsen A.-K., 2007, The Astrophysical Journal, 666, 1

Gnedin N. Y., Hollon N., 2012, The Astrophysical Journal Supplement Series, 202, 13

Godunov S. K., 1959, Matematicheskii Sbornik, 47(89), 271

González-Alfonso E., et al., 2010, Astronomy & Astrophysics, 518, L43

González-Alfonso E., et al., 2017, The Astrophysical Journal, 836, 11

González M., Audit E., Huynh P., 2007, Astronomy & Astrophysics, 464, 429

Gorti U., Hollenbach D. J., 2002, The Astrophysical Journal, 573, 215

Grassi T., Bovino S., Gianturco F. A., Baiocchi P., Merlin E., 2012, Monthly Notices of the Royal Astronomical Society, 425, 1332

Grassi T., Bovino S., Schleicher D. R. G., Prieto J., Seifried D., Simoncini E., Gianturco F. A., 2014, Monthly Notices of the Royal Astronomical Society, 439, 2386

Grisdale K., Agertz O., Renaud F., Romeo A. B., 2018, Monthly Notices of the Royal Astronomical Society, 479, 3167

Gritschneder M., Naab T., Burkert A., Walch S., Heitsch F., Wetzstein M., 2009, Monthly Notices of the Royal Astronomical Society, 393, 21

Guderley G., 1942, Luftfahrtforschung, 19, 302

Gutcke T. A., Macciò A. V., Dutton A. A., Stinson G. S., 2017, Monthly Notices of the Royal Astronomical Society, 466, 4614

Habing H. J., 1968, Bulletin of the Astronomical Institutes of the Netherlands, 19, 421

Haffner L. M., et al., 2009, Reviews of Modern Physics, 81, 969

Haid S., Walch S., Seifried D., Wuensch R., Dinnbier F., Naab T., 2018a, Monthly Notices of the Royal Astronomical Society

Haid S., Walch S., Seifried D., Wünsch R., Dinnbier F., Naab T., 2018b, Monthly Notices of the Royal Astronomical Society, 478, 4799

Häring N., Rix H.-W., 2004, The Astrophysical Journal Letters, 604, L89

Harten A., Lax P. D., Van Leer B., 1983, SIAM Review, 25, 35

Hartmann L., Ballesteros-Paredes J., Bergin E. A., 2001, ApJ, 562, 852

Harvey D. W. A., Wilner D. J., Lada C. J., Myers P. C., Alves J. F., Chen H., 2001, The Astrophysical Journal, 563, 903

He C.-C., Ricotti M., Geen S., 2019, preprint (arXiv:1904.07889)

He C.-C., Ricotti M., Geen S., 2020, Monthly Notices of the Royal Astronomical Society, 492, 4858

Herschel W., 1785, Philosophical Transactions of the Royal Society of London Series I, 75, 213

Hester J. J., et al., 1996, The Astronomical Journal, 111, 2349

Heyer M., Krawczyk C., Duval J., Jackson J. M., 2009, The Astrophysical Journal, 699, 1092

Hindmarsh A. C., 1983, IMACS Transactions on Scientific Computation, 1, 55

Hobson M. P., 1992, Monthly Notices of the Royal Astronomical Society, 256, 457

Hockney R. W., Eastwood J. W., 1981, Computer Simulation Using Particles. New York

Hollenbach D. J., 1989, Symposium-International Astronomical Union, 135, 227

Hollenbach D., McKee C. F., 1979, The Astrophysical Journal Supplement Series, 41, 555

Hollenbach D., McKee C. F., 1989, The Astrophysical Journal, 342, 306

Hollenbach D., Salpeter E. E., 1971, The Astrophysical Journal, 163, 155

Hollenbach D. J., Tielens A. G. G. M., 1999, Reviews of Modern Physics, 71, 173

Hopkins P. F., 2015, Monthly Notices of the Royal Astronomical Society, 450, 53

Hosokawa T., Inutsuka S.-i., 2005, The Astrophysical Journal, 623, 917

Hosokawa T., Inutsuka S.-i., 2006a, The Astrophysical Journal, 646, 240

Hosokawa T., Inutsuka S.-i., 2006b, The Astrophysical Journal Letters, 648, L131

Howard C. S., Pudritz R. E., Harris W. E., 2017, Monthly Notices of the Royal Astronomical Society, 470, 3346

Howard C. S., Pudritz R. E., Harris W. E., Klessen R. S., 2018, Monthly Notices of the Royal Astronomical Society, 475, 3121

Howe J. E., et al., 2000, The Astrophysical Journal, 539, 137

Huggins P. J., Forveille T., Bachiller R., Cox P., Ageorges N., Walsh J. R., 2002, The Astrophysical Journal Letters, 573, L55

Hughes A., et al., 2013, ApJ, 779, 46

Inoue A. K., et al., 2016, Science, 352

Janssen A. W., et al., 2016, The Astrophysical Journal, 822, 43

Jura M., 1975, The Astrophysical Journal, 197, 575

Kahn F. D., 1954, Bulletin of the Astronomical Institutes of the Netherlands, 12, 187

Kahn F. D., 1969, Physica, 41, 172

Kamp I., Bertoldi F., 2000, Astronomy & Astrophysics, 353, 276

Kauffmann G., et al., 2003, Monthly Notices of the Royal Astronomical Society, 346, 1055

Kaufman M. J., Wolfire M. G., Hollenbach D. J., Luhman M. L., 1999, The Astrophysical Journal, 527, 795

Keeton C. R., Kochanek C. S., 1998, The Astrophysical Journal, 495, 157

Kennicutt R. C., 1998, Annual Review of Astronomy & Astrophysics, 36, 189

Kennicutt R. C., Evans N. J., 2012, Annual Review of Astronomy & Astrophysics, 50, 531

Kessel-Deynet O., Burkert A., 2003, Monthly Notices of the Royal Astronomical Society, 338, 545

Kim J.-G., Kim W.-T., Ostriker E. C., 2018, The Astrophysical Journal, 859, 68

Kimm T., Blaizot J., Garel T., Michel-Dansac L., Katz H., Rosdahl J., Verhamme A., Haehnelt M., 2019, Monthly Notices of the Royal Astronomical Society, 486, 2215

King A. R., 2003, The Astrophysical Journal, 596, L27

King A. R., 2010, Monthly Notices of the Royal Astronomical Society, 402, 1516

King A. R., Pounds K. A., 2003, Monthly Notices of the Royal Astronomical Society, 345, 657

King A., Pounds K., 2015, Annual Review of Astronomy & Astrophysics, 53, 115

Kippenhahn R., Weigert A., 1990, Stellar Structure and Evolution, XVI, 468 pp. 192 figs.. Springer-Verlag Berlin Heidelberg New York. Also Astronomy & Astrophysics Library

Kormendy J., Ho L. C., 2013, Annual Review of Astronomy & Astrophysics, 51, 511

Kravtsov A. V., Klypin A. A., Khokhlov A. M., 1997, The Astrophysical Journal Supplement Series, 111, 73

Kriek M., Conroy C., 2013, The Astrophysical Journal Letters, 775, L16

Krips M., et al., 2011, The Astrophysical Journal, 736, 37

Krolik J. H., McKee C. F., Tarter C. B., 1981, The Astrophysical Journal, 249, 422

Kroupa P., 2001, Monthly Notices of the Royal Astronomical Society, 322, 231

Kruijssen J. M. D., et al., 2019, Nature, 569, 519

Krumholz M. R., McKee C. F., 2005, The Astrophysical Journal, 630, 250

Krumholz M. R., Tan J. C., 2007, The Astrophysical Journal, 654, 304

Krumholz M. R., McKee C. F., Tumlinson J., 2009, The Astrophysical Journal, 699, 850

Krumholz M. R., Klein R. I., Mckee C. F., 2011, The Astrophysical Journal, 740, 74

Krumholz M. R., Dekel A., McKee C. F., 2012, The Astrophysical Journal, 745, 69

Lada C. J., 2015, Proceedings of the International Astronomical Union, 10, 8

Lada C. J., Alves J., Lada E. A., 1999, The Astrophysical Journal, 512, 250

Lada C. J., Lombardi M., Alves J. F., 2010, The Astrophysical Journal, 724, 687

Larson R. B., 1969, Monthly Notices of the Royal Astronomical Society, 145, 271

Larson R. B., 1981, Monthly Notices of the Royal Astronomical Society, 194, 809

Le Petit F., Nehmé C., Le Bourlot J., Roueff E., 2006, The Astrophysical Journal Supplement Series, 164, 506

Le Teuff Y. H., Millar T. J., Markwick A. J., 2000, Astronomy & Astrophysics Supplement Series, 146, 157

Lee E. J., Miville-Deschênes M.-A., Murray N. W., 2016, The Astrophysical Journal, 833, 229

Lefloch B., Lazareff B., 1994, Astronomy & Astrophysics, 289, 559

Leitherer C., Robert C., Drissen L., 1992, The Astrophysical Journal, 401, 596

Leung T. K. D., et al., 2019, The Astrophysical Journal, 871, 85

Levermore C. D., 1984, Journal of Quantitative Spectroscopy and Radiative Transfer, 31, 149

Lis D. C., Schilke P., 2003, The Astrophysical Journal, 597, L145

Liu H.-L., et al., 2016, The Astrophysical Journal, 818, 95

Liu M., Tan J. C., Cheng Y., Kong S., 2018, The Astrophysical Journal, 862, 105

Luhman K. L., Engelbracht C. W., Luhman M. L., 1998, The Astrophysical Journal, 499, 799

Mac Low M., Klessen R. S., Heitsch F., 1999, ASP Conference Series, 188

Madgwick D. S., et al., 2002, Monthly Notices of the Royal Astronomical Society, 333, 133

Maiolino R., et al., 2005, Astronomy & Astrophysics, 440, L51

Maiolino R., et al., 2012, Monthly Notices of the Royal Astronomical Society, 425, L66

Maiolino R., et al., 2017, Nature, 544, 202

Mäkelä M. M., Haikala L. K., 2013, Astronomy & Astrophysics, 550, A83

Marconi A., Testi L., Natta A., Walmsley C. M., 1998, Astronomy & Astrophysics, 330, 696

Maselli A., Ferrara A., Ciardi B., 2003, Monthly Notices of the Royal Astronomical Society, 345, 379

Mathis J. S., Rumpl W., Nordsieck K. H., 1977, The Astrophysical Journal, 217, 425

Matzner C. D., 2002, The Astrophysical Journal, 566, 302

Maxwell J. C., 1860, The London, Edinburgh, and Dublin Philosophical Magazine and Journal of Science, 19, 19

McKee C. F., Cowie L. L., 1977, The Astrophysical Journal, 215, 213

Mellema G., Iliev I. T., Alvarez M. A., Shapiro P. R., 2006, New Astronomy, 11, 374

Mendis D. A., 1968, Monthly Notices of the Royal Astronomical Society, 141, 409

Mihalas D., Mihalas B. W., 1984, New York, Oxford University Press, 1984, 731 p.

Minamidani T., et al., 2011, The Astronomical Journal, 141, 73

Molina F. Z., Glover S. C. O., Federrath C., Klessen R. S., 2012, Monthly Notices of the Royal Astronomical Society, 423, 2680

Morganti R., Frieswijk W., Oonk R. J. B., Oosterloo T., Tadhunter C., 2013, Astronomy & Astrophysics, 552, L4

Morganti R., Oosterloo T., Oonk R. J. B., Frieswijk W., Tadhunter C., 2015, Astronomy & Astrophysics, 580, A1

Mortlock D. J., et al., 2011, Nature, 474, 616

Mueller K. E., Shirley Y. L., Evans N. J., Jacobson H. R., 2002, The Astrophysical Journal Supplement Series, 143, 469

Murray N., Quataert E., Thompson T. A., 2010, The Astrophysical Journal, 709, 191

Nakanishi H., Sofue Y., 2003, Publications of the Astronomical Society of Japan, 55, 191

Nakanishi H., Sofue Y., 2006, Publications of the Astronomical Society of Japan, 58, 847

Nakatani R., Yoshida N., 2018, preprint (arXiv:1811.00297)

Narayanan D., Krumholz M. R., Ostriker E. C., Hernquist L., 2012, Monthly Notices of the Royal Astronomical Society, 421, 3127

Nayakshin S., Zubovas K., 2012, Monthly Notices of the Royal Astronomical Society, 427, 372

Netzer H., 2015, Annual Review of Astronomy & Astrophysics, 53, 365

Neufeld D. A., Lepp S., Melnick G. J., 1995, The Astrophysical Journal Supplement Series, 100, 132

Nieten C., Neininger N., Guélin M., Ungerechts H., Lucas R., Berkhuijsen E. M., Beck R., Wielebinski R., 2006, A&A, 453, 459

Ochsendorf B. B., Meixner M., Roman-Duval J., Rahman M., Evans N. J., 2017, The Astrophysical Journal, 841, 109

Ocvirk P., Aubert D., Chardin J., Deparis N., Lewis J., 2019, Astronomy & Astrophysics, 626, A77

Oesch P. A., et al., 2012, The Astrophysical Journal, 759, 135

Oey M. S., et al., 2007, The Astrophysical Journal, 661, 801

Olsen K., et al., 2018, Galaxies, 6, 100

Osterbrock D. E., Ferland G. J., 2006, Astrophysics of Gaseous Nebulae and Active Galactic Nuclei., second edn. University Science Books, Sausalito, California

Ostriker J. P., McKee C. F., 1988, Reviews of Modern Physics, 60, 1

Padoan P., Nordlund A., 2002, The Astrophysical Journal, 576, 870

Padoan P., Nordlund A., 2011, The Astrophysical Journal, 730, 40

Padoan P., Haugbølle T., Nordlund Å., 2012, The Astrophysical Journal Letters, 759, L27

Pallottini A., Gallerani S., Ferrara A., Yue B., Vallini L., Maiolino R., Feruglio C., 2015, Monthly Notices of the Royal Astronomical Society, 453, 1898

Pallottini A., Ferrara A., Gallerani S., Vallini L., Maiolino R., Salvadori S., 2017a, Monthly Notices of the Royal Astronomical Society, 465, 2540

Pallottini A., Ferrara A., Bovino S., Vallini L., Gallerani S., Maiolino R., Salvadori S., 2017b, Monthly Notices of the Royal Astronomical Society, 471, 4128

Pallottini A., et al., 2019, Monthly Notices of the Royal Astronomical Society, 487, 1689

Parsons H., Thompson M. A., Clark J. S., Chrysostomou A., 2012, Monthly Notices of the Royal Astronomical Society, 424, 1658

Peters T., Banerjee R., Klessen R. S., Mac Low M., Galván-Madrid R., Keto E. R., 2010, The Astrophysical Journal, 711, 1017

Pineda J. L., Langer W. D., Velusamy T., Goldsmith P. F., 2013, Astronomy & Astrophysics, 554, A103

Pounds K. A., Reeves J. N., Page K. L., Wynn G. A., O'Brien P. T., 2003, Monthly Notices of the Royal Astronomical Society, 342, 1147

Raga A. C., Cantó J., Rodríguez L. F., 2012, Monthly Notices of the Royal Astronomical Society, 419, L39

Rankine W. J. M., 1870, Philosophical Transactions of the Royal Society of London, 160, 277

Rasera Y., Teyssier R., 2006, Astronomy & Astrophysics, 445, 1

Raskutti S., Ostriker E. C., Skinner M. A., 2016, The Astrophysical Journal, 829, 130

Raymond J. C., Cox D. P., Smith B. W., 1976, The Astrophysical Journal, 204, 290

Reipurth B., 1983, Astronomy & Astrophysics, 117, 183

Richings A. J., Faucher-Giguère C.-A., 2018a, Monthly Notices of the Royal Astronomical Society, 474, 3673

Richings A. J., Faucher-Giguère C.-A., 2018b, Monthly Notices of the Royal Astronomical Society, 478, 3100

Richings A. J., Schaye J., Oppenheimer B. D., 2014a, Monthly Notices of the Royal Astronomical Society, 440, 3349

Richings A. J., Schaye J., Oppenheimer B. D., 2014b, Monthly Notices of the Royal Astronomical Society, 442, 2780

Rodríguez del Pino B., Arribas S., Piqueras López J., Villar-Martín M., Colina L., 2019, Monthly Notices of the Royal Astronomical Society, 486, 344

Röllig M., et al., 2007, Astronomy & Astrophysics, 467, 187

Rosdahl J., Blaizot J., Aubert D., Stranex T., Teyssier R., 2013, Monthly Notices of the Royal Astronomical Society, 436, 2188

Rosdahl J., et al., 2018, Monthly Notices of the Royal Astronomical Society, 479, 994

Sakamoto K., Aalto S., Combes F., Evans A., Peck A., 2014, The Astrophysical Journal, 797, 90

Saltzman J., 1994, Journal of Computational Physics, 115, 153

Sawada T., Koda J., Hasegawa T., 2018, The Astrophysical Journal, 867, 166

Sazonov S. Y., Ostriker J. P., Sunyaev R. A., 2004, Monthly Notices of the Royal Astronomical Society, 347, 144

Scannapieco E., 2017, The Astrophysical Journal, 837, 28

Schaerer D., Charbonnel C., Meynet G., Maeder A., Schaller G., 1993, Astronomy & Astrophysics Supplement Series, 102, 339

Schmidt M., 1959, The Astrophysical Journal, 129, 243

Schneider N., et al., 2015, Astronomy & Astrophysics, 575, A79

Scoville N. Z., Good J. C., 1989, The Astrophysical Journal, 339, 149

Sedov L. I., 1958, RvMP, 30, 1077

Shapley A. E., Steidel C. C., Pettini M., Adelberger K. L., 2003, The Astrophysical Journal, 588, 65

Shu F. H., 1977, The Astrophysical Journal, 214, 488

Shu F. H., Adams F. C., Lizano S., 1987, Annual Review of Astronomy & Astrophysics, 25, 23

Smartt S. J., 2009, Annual Review of Astronomy & Astrophysics, 47, 63

Sommovigo L., Ferarra A., Pallottini A., Carniani S., Gallerani S., Decataldo D., in prep., Monthly Notices of the Royal Astronomical Society

Spergel D. N., et al., 2003, The Astrophysical Journal Supplement Series, 148, 175

Spitzer L., 1998, Physical Processes in the Interstellar Medium. Wiley-VCH, Weinheim, Germany

Spoon H. W. W., et al., 2013, The Astrophysical Journal, 775, 127

Springel V., Yoshida N., White S. D. M., 2001, New Astronomy, 6, 79

Stahler S. W., Palla F., 2004, The Formation of Stars, wiley-vch edn. Weinheim, Germany, doi:10.15713/ins.mmj.3

Steidel C. C., Giavalisco M., Pettini M., Dickinson M., Adelberger K. L., 1996, The Astrophysical Journal Letters, 462, L17

Stephens T. L., Dalgarno A., 1973, The Astrophysical Journal, 186, 165

Sternberg A., Dalgarno A., 1989, The Astrophysical Journal, 338, 197

Sternberg A., Le Petit F., Roueff E., Le Bourlot J., 2014, The Astrophysical Journal, 790

Stoerzer H., Stutzki J., Sternberg A., 1996, Astronomy & Astrophysics, 310, 592

Stone J. M., Gardiner T. A., Teuben P., Hawley J. F., Simon J. B., 2008, The Astrophysical Journal Supplement Series, 178, 137

Stone M., Veilleux S., Meléndez M., Sturm E., Graciá-Carpio J., González-Alfonso E., 2016, The Astrophysical Journal, 826, 111

Strömgren B., 1939, The Astrophysical Journal, 89, 526

Sturm E., et al., 2011, The Astrophysical Journal Letters, 733, L16

Sutherland R. S., Dopita M. A., 1993, The Astrophysical Journal Supplement Series, 88, 253

Takahashi S., Ho P. T. P., Teixeira P. S., Zapata L. A., Su Y.-N., 2013, The Astrophysical Journal, 763, 57

Taylor S. D., Hartquist T. W., Williams D. A., 1993, Monthly Notices of the Royal Astronomical Society, 264, 929

Tenorio-Tagle G., 1977, Astronomy & Astrophysics, 54, 517

Teyssier R., 2002, Astronomy & Astrophysics, 385, 337

Thornton K., Gaudlitz M., Janka H.-T., Steinmetz M., 1998, The Astrophysical Journal, 500, 95

Tielens A. G. G. M., Hollenbach D. J., 1985, The Astrophysical Journal, 291, 722

Tombesi F., Cappi M., Reeves J. N., Palumbo G. G. C., Yaqoob T., Braito V., Dadina M., 2010, A&A, 521, A57

Toro E. F., 2009, Riemann Solvers and Numerical Methods for Fluid Dynamics: A Practical Introduction, third edn. Springer-Verlag, Berlin Heidelberg, doi:10.1007/b79761

Tremonti C. A., et al., 2004, The Astrophysical Journal, 613, 898

Tsai J. C., Mathews W. G., 1995, The Astrophysical Journal, 448, 84

Vallini L., Gallerani S., Ferrara A., Pallottini A., Yue B., 2015, The Astrophysical Journal, 813, 36

Vallini L., Ferrara A., Pallottini A., Gallerani S., 2017, Monthly Notices of the Royal Astronomical Society, 467, 1300

Vallini L., Pallottini A., Ferrara A., Gallerani S., Sobacchi E., Behrens C., 2018, Monthly Notices of the Royal Astronomical Society, 473, 271

Van der Werf P., Goss W. M., Heiles C., Crutcher R. M., Troland T. H., 1993, The Astrophysical Journal, 411, 247

Vázquez-Semadeni E., Colín P., Gómez G. C., Ballesteros-Paredes J., Watson A. W., 2010, The Astrophysical Journal, 715, 1302

Veilleux S., et al., 2013, The Astrophysical Journal, 776, 27

Verner D. A., Ferland G. J., 1996, Astrophysical Journal Supplement, 103, 467

Verner D. A., Yakovlev D. G., 1995, Astronomy & Astrophysics Supplemente Series, 109, 125

Wadsley J. W., Stadel J., Quinn T., 2004, New Astronomy, 9, 137

Walch S., Naab T., 2015, Monthly Notices of the Royal Astronomical Society, 451, 2757

Walch S. K., Whitworth A. P., Bisbas T., Wünsch R., Hubber D., 2012, Monthly Notices of the Royal Astronomical Society, 427, 625

Walch S., Whitworth A. P., Bisbas T. G., Hubber D. A., 2013, Monthly Notices of the Royal Astronomical Society, 435, 917

Walch S., et al., 2015, Monthly Notices of the Royal Astronomical Society, 454, 238

Walter F., et al., 2017, The Astrophysical Journal, 835, 265

Weaver R., McCray R., Castor J., Shapiro P., Castor J., 1977, The Astrophysical Journal, 218, 377

Webber W. R., 1998, The Astrophysical Journal, 506, 329

Weingartner J. C., Draine B. T., 2001, The Astrophysical Journal, 548, 296

Whitham G. B., 1958, Journal of Fluid Mechanics, 4, 337

Whitworth A., 1979, Monthly Notices of the Royal Astronomical Society, 186, 59

Williams J. P., McKee C. F., 1997, The Astrophysical Journal, 476, 166

Williams J. P., de Geus E. J., Blitz L., 1994, The Astrophysical Journal, 428, 693

Williams R. J. R., Bisbas T. G., Haworth T. J., Mackey J., 2018, Monthly Notices of the Royal Astronomical Society, 479, 2016

Wolf C., Meisenheimer K., Rix H.-W., Borch A., Dye S., Kleinheinrich M., 2003, Astronomy & Astrophysics, 401, 73

Wolfire M. G., Hollenbach D., McKee C. F., Tielens A. G. G. M., Bakes E. L. O., 1995, The Astrophysical Journal, 443, 152

Wolfire M. G., McKee C. F., Hollenbach D. J., Tielens A. G. G. M., 2003, The Astrophysical Journal, Volume 587, Issue 1, pp. 278-311., 587, 278

Wong T., et al., 2008, Monthly Notices of the Royal Astronomical Society, 386, 1069

Wood K., Hill A. S., Joung M. R., Mac Low M., Benjamin R. A., Haffner L. M., Reynolds R. J., Madsen G. J., 2010, The Astrophysical Journal, 721, 1397

Wyder T. K., et al., 2007, The Astrophysical Journal Supplement Series, 173, 293

Yep A. C., White R. J., 2020, The Astrophysical Journal, 889, 50

Yue B., Ferrara A., Salvaterra R., Xu Y., Chen X., 2013, Monthly Notices of the Royal Astronomical Society, 433, 1556

Yue B., Ferrara A., Pallottini A., Gallerani S., Vallini L., 2015, Monthly Notices of the Royal Astronomical Society, 450, 3829

Zavagno A., Deharveng L., Comerón F., Brand J., Massi F., Caplan J., Russeil D., 2006, Astronomy & Astrophysics, 446, 171

Zel'dovich Y. B., Raĭzer Y. P., 2002, Physics of Shock Waves and High-Temperature Hydrodynamic Phenomena. Dover Publications, Mineola, New York

Zhang Z., Papadopoulos P. P., Ivison R. J., Galametz M., Smith M. W. L., Xilouris E. M., 2016, Royal Society Open Science, 3600, 25

Zubovas K., King A. R., 2012, Monthly Notices of the Royal Astronomical Society, 426, 2751

Zubovas K., King A. R., 2014, Monthly Notices of the Royal Astronomical Society, 439, 400

Zubovas K., Nayakshin S., 2014, Monthly Notices of the Royal Astronomical Society, 440, 2625

Zurita A., Rozas M., Beckman J. E., 2000, Astronomy & Astrophysics, 363, 9